Escola de Postgrau
Universitat Autònoma de Barcelona

Departament de Fisica

Detectors for Quality Assurance in Hadrontherapy

Doctoral Thesis

30th May 2013

Director:
Prof. Ugo Amaldi

Tutor:
Prof. Enrique Fernandez

Author:
David A. Watts

0.1 Executive summary

Hadrontherapy is currently a clinical reality in radiation oncology and a proven technique in the fight against cancer. In the world today, hadrontherapy is being more and more widely employed for treating patients with non-operable deep-seated or radio-resistant tumours because of its advantage in delivering a highly conformal dose to the tumour volume. This offers an increased likelihood of tumour control and a better sparing of healthy surrounding tissue as compared with traditional radiotherapy which use photon beams. Despite the fact that 35 centers are currently treating patients, hadrontherapy is still considered to be an emerging clinical technique. One of the persisting challenges to hadrontherapy is the verification of the dose delivered to the patient since the physical properties of hadrons are only beneficial for therapy if they can be delivered precisely to the tumour volume.

Quality assurance can be achieved using novel diagnostic techniques which make use of radiation detectors similar to those developed for high-energy physics experiments and already used in medical imaging. Proton radiography can be used to verify the patient setup prior to irradiation, using a diagnostic proton beam of higher energy and lower intensity, but can also provide directly the information needed for accurately computing the range of hadrons in the patient tissues. Range calculations currently rely on X-ray CT data, and are characterized by a small but non-negligible uncertainty. During irradiation with the therapeutic beam, the activation of the patient tissues caused by nuclear interactions with the hadron beam can be visualized by PET detectors, making it possible to perform *in-vivo* dosimetry during irradiation and in the minutes immediately following.

In this context, this thesis presents an expansive study of novel radiation detectors which have been developed for quality assurance in clinical hadrontherapy. Three distinct detector solutions are described, a proton radiography instrument and two detectors technologies which could be used for performing *in-vivo* dosimetry of the delivered treatment plan.

In the case of proton range radiography (PRR), a novel instrument called the PRR10 has been built having 10x10 cm^2 active area and covering a residual range of 10 cm water-equivalent path length (WEPL). The PRR10 has been extensively tested with proton beams at the Paul Scherrer Institute (PSI) in Villagen, Switzerland and at the *Centro Nazionale di Adroterapia Oncologica* (CNAO) in Pavia, Italy. A residual range resolution of 1.6 mm WEPL has been measured as well as a spatial resolution better than 1 mm. The PRR10 currently sits at the CNAO center awaiting further testing while a new instrument, the PRR30, which has an active area of 30x30 cm^2, is reaching a final stage of completion. The PRR30 will allow full-size PRR images to be made and is scheduled for testing with proton beams at PSI and the CNAO by the end of 2013.

To perform *in-vivo* dosimetry, two different PET technologies have been studied. The first is based on inorganic scintillators (crystals) coupled to a photodetector, having many similarities to conventional PET hardware for nuclear medicine. The design for a unit PET detector based on crystal follows the trends in current PET research allowing for the depth-of-interaction (DOI) to be measured as well as the time-of-flight (TOF) between the coincidence photons. Both techniques result in a higher effective sensitivity and a better rejection of noise, and therefore higher quality PET images. Two prototypes have been assembled and tested, built using 12x60x30 cm^3 LYSO crystals and a multi-anode Multi-Channel Plate (MCP) photodetector. An excellent localization of the photon interaction, 1.2 mm in the transverse direction and $\sim$15 mm in DOI, have been demonstrated with an energy resolution of 13% FWHM. The coincidence TOF resolution has been measured as 810 ps.

The second PET technology we have studied makes use of multi-gap Resistive Plate Chambers (MRPCs), which are highly unusual in PET because of their low detection efficiency to 511 keV gammas. Compact MRPC modules have been built and tested, having 7x10 cm^2 and 12x30 cm^2 active area. The design and assembly procedure has been shown to be suitable for mass-production, a requirement for overcoming the intrinsic low efficiency.

A 4-gap 7x10 cm^2 MRPC module has been tested and shown to have an efficiency of (0.66$\pm$0.01)% to 511 keV gammas. In addition, the timing between ends of the strip readout at either side of the module has been measured as 3.8 ps, enough to allow an interaction localization of 3.5 mm. The single-detector TOF resolution between two single-gap RPCs and two 4-gap MRPCs has been measured as 310 ps and 370 ps, respectively with a coincidence resolution of $\sim$150 ps expected shortly.

To compliment the experimental results, Monte-Carlo simulations of both LYSO-MCP and MRPC-based PET scanners have been carried out using the GATE toolkit. Two commercial detectors, the Philips Gemini and Siemens HiRez, have also been included in the study as a benchmark for the results. The full-ring LYSO-MCP scanner has been shown to have a 57% higher sensitivity than the Gemini to a 70 cm long line source, a consequence of the increased depth (30 mm) of the LYSO crystals used in our design. An MRPC-PET scanner, after performing a sensitivity optimization of various parameters, has been shown to be a factor of 2.5 higher than the Gemini. Although considerable development will be required to build such a MRPC-PET scanner, the gains in sensitivity over existing commercial scanners, coupled with their excellent TOF resolutions, make this technology an exciting alternative to crystals, whether for hadrontherapy quality assurance, or whole-body PET imaging.

Contents

Chapter 1

Introduction

This thesis describes novel radiation detectors designed for quality assurance in clinical hadrontherapy. Generally speaking, hadrontherapy is a particular kind of radiotherapy used in the treatment of cancer, often synonymously referred to ion therapy or particle therapy. In recent years, most notably in Japan, Europe and the United States, a significant number of hospital-based facilities, constructed uniquely for the purpose of delivering therapeutic beams of protons and carbon ions, are treating patients with very promising clinical results [1].

As hadrontherapy is still an emerging clinical technique, research and development in domains both medical and technical are needed to support the ever-growing community of scientists and medical practitioners engaged in the field. New facilities wishing to add protons or carbon ions to their arsenal require novel and compact accelerator solutions which are both economically viable and capable of the most advanced treatment techniques. In this context, the Italian research foundation for Oncological Hadrontherapy (TERA) is developing fast-cycling and compact accelerators, called cyclinacs, which consist of a fixed energy cyclotron and a high-gradient radio-frequency linear accelerator operating with a high-repetition rate. Cyclinacs have the unique property of allowing fast electronic beam-energy variation which opens the way for active scanning and tumour multi-painting, currently the state-of-the-art in hadrontherapy beam delivery.

Besides the field of accelerator physics, TERA is also engaged in research of radiation detectors applied to instrumentation and imaging in hadrontherapy. In hadrontherapy just as in conventional radiotherapy, detectors play a primary role at all stages of cancer therapy. Imaging detectors are widely used by oncologists in the diagnostic and staging phases and detectors for instrumentation ensure the precise delivery of the beam used for irradiation. For example, X-ray detectors used for Computerized Tomography (CT) are fundamental not only for locating and delineating the tumour site, but also to the medical physicist whose treatment plan relies on the anatomical data

of the patient tissues mapped precisely by the planning CT. Detectors for nuclear medicine, such as Positron Emission Tomography (PET), play a role in the diagnosis and follow-up stages and are proving useful for predicting levels of tumour hypoxia. Cone-beam CT is used in the treatment room before each fraction to accurately locate the patient with respect to the beam isocenter.

The presence of the hadron beam, however, presents unique opportunities for diagnostics, imaging and quality control. In later chapters of this thesis we present novel detectors which have been designed to exploit this new niche and provide quality assurance beyond that which is available from existing detector technologies designed for conventional radiotherapy. Carried out by the Advanced QUality Assurance (AQUA) group of the TERA Foundation in Geneva, Switzerland, several types of detectors are under study in which a different detection modality is utilized [2]. Broadly speaking, the detectors can be classified by those which make use of a *diagnostic* beam of low intensity (ensuring a negligible dose) which traverses the patient entirely, and those which detect the secondary radiation emitted from the body during or immediately following irradiation by a *therapeutic* beam.

For a diagnostic beam of protons passing through the body, Proton Range Radiography (PRR) can provide anatomical information about the tissues in the field-of-view of the beam. Additionally, using a diagnostic beam of 700-800 MeV protons, elastic proton-proton scattering between the beam and the patient tissues can be exploited to map the hydrogen density in the body, using a modality known as Nuclear Scattering Tomography (NST).

During irradiation with a therapeutic beam of protons or carbon ions, detectors for in-beam PET based on either crystal-scintillators or Resistive Plate Chambers are proposed, both of which would allow real-time *in-vivo* monitoring of the dose as it is being delivered. Also with the therapeutic beam, *in-vivo* dosimetry can be performed by tracking charged particles which are produced in abundance during irradiation and escape the body. Detection of these secondary tracks can be used to reconstruct the vertex of the interaction along the beam line using the method known as Interaction Vertex Imaging (IVI).

Figure 1.1 shows a schematic representation of these projects which are proposed by TERA and under study by the AQUA group [3].

In this dissertation, the design, construction and test of novel radiation detectors for two of TERA's proposed projects, Proton Range Radiography and in-beam PET, will be described in detail. Because this requires a review of the basic physics of particle interaction in matter as well as an overview of the workings of detectors for physics instrumentation, these subjects will be reviewed before delving into the precise details of the laboratory work and simulations that constitute the unique aspect of this research. Though the technologies and techniques employed have been derived from experimental

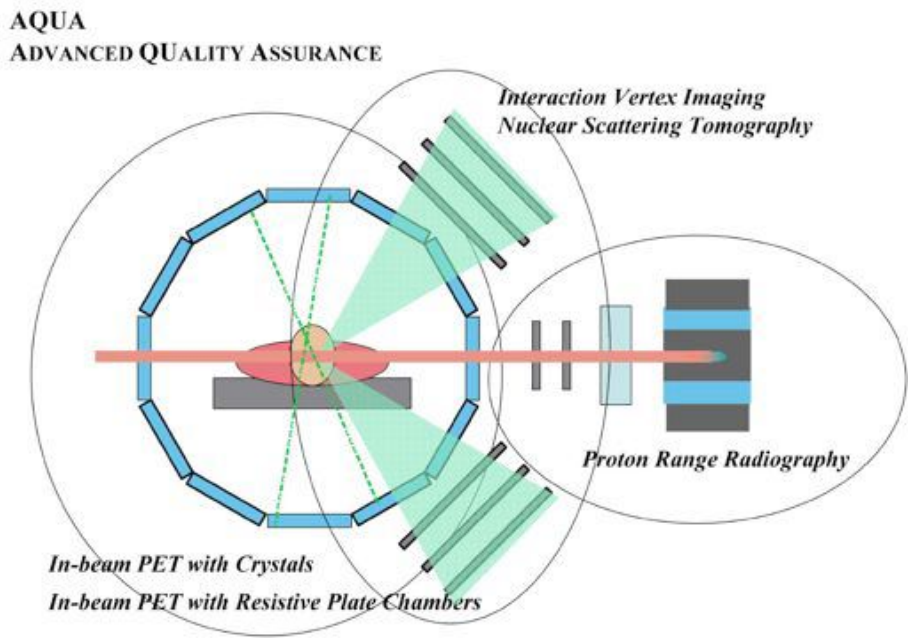

Figure 1.1: A illustration of various detector solutions for hadrontherapy QA proposed by the AQUA group of the TERA Foundation.

high-energy physics (HEP), the application to a hadrontherapy environment requires that the detector designs be very different from what is needed in fundamental scientific research. To appreciate the specific requirements and challenges that that entails, I felt it necessary to touch upon a variety of topics outside the realm of HEP in the next chapter, including the basics of radiobiology and radiotherapy, the case for using protons and carbon ions over photons as in conventional radiotherapy, and a discussion about the need for quality assurance and how such detectors can provide it.

Chapter 2

The rise of hadrontherapy

2.1 Cancer in the 21st century

Present day statistics rate cancer as the second most likely cause of death in developed countries and in 2008, 7.6 million people died of cancer accounting for 13% of all deaths worldwide [4]. On average, one in three adults in the course of their lives will develop cancer.

Cancer can be defined as a broad variety of diseases in which a group of cells exhibits unregulated growth or cell division. A group of cells divide and grow forming what is known as a malignant tumour. Initially, the tumour produces no symptoms, however, as it grows it eventually impinges on neighboring tissues causing complications. For example, lung cancer can cause blockage of the lung passages resulting in coughing and shortness of breath; cancers of the brain can lead to headaches and seizures as the tumour size creates pressure on the normal tissues. As a tumour grows, it can also invade nearby parts of the body leading to further loss of organ function and when left untreated, death of the patient. In some cases, the cancerous cells may also spread to more distant parts of the body, either through the bloodstream or lymphatic system in a process known as metastasis.

Understanding the cause of cancer is complex, and in practice determining the exact reason for why an individual has developed a specific cancer is impossible since even the most healthy individuals are at risk. That being said, it is long been known that certain environmental factors are associated with an increase in cancer occurrence. The main factors are tobacco and alcohol use, lack of physical activity, poor diet, infections and environmental pollutants. It is stated that more than 30% of cancers could be prevented by not using tobacco, maintaining a healthy diet and active lifestyle and by preventing cancer causing infections [5]. Regardless of the cause, it is expected that the overall incidence of cancer will continue to rise in the future mainly as a result of improvements in early detection methods and an increase in the average life expectancy of the population. The incidence

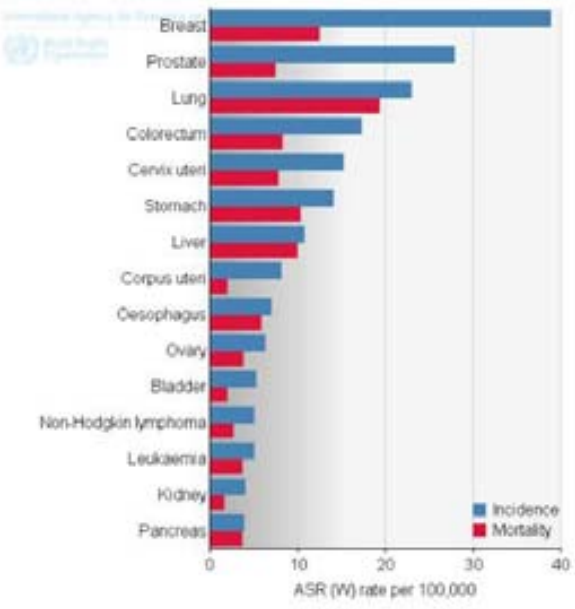

Figure 2.1: Average occurrence and mortality per 100,000 individuals of different cancers in both males and in females [4].

and mortality per 100,000 individuals of the most common types of cancer is given in figure 2.1.

Fortunately, with modern medical practice, cancer is a very curable disease. The majority of cancers can be treated, often to the point of remission using a variety of techniques. The four main types of treatments are: surgical removal of the tumour tissue, radiotherapy, chemotherapy, and immunotherapy. The exact method of treatment depends strongly on the type of cancer and its stage of development at the time of diagnosis. In 42% of new cancer patient cases, the cancer has metastasized beyond the primary tumour and the disease is already generalized about the body. Surgery and radiotherapy are of little use (except for palliative treatment) in such cases and only about 12% (5% of the total) of patients can be cured, usually by chemotherapy. In 58% of new cases, the disease is localized in a well-defined volume and the prognosis for such patients is considerably higher: about 70% of patients having local disease will be cured (40% of the total). The percentage of cured patients by treatment technique is shown in figure 2.2. Presently, nearly 50% of new cancer patients are cured by one or a combination of the treatments discussed above. In 90% of successful cases, a cure is achieved by a *loco-regional* control of the primary tumour, either by the surgical removal of the tumour itself or the destruction of the tumour cells *in-vivo* using radiotherapy [6]. These two loco-regional treatments are normally accompanied by chemotherapy. Since the ability to cure a cancer

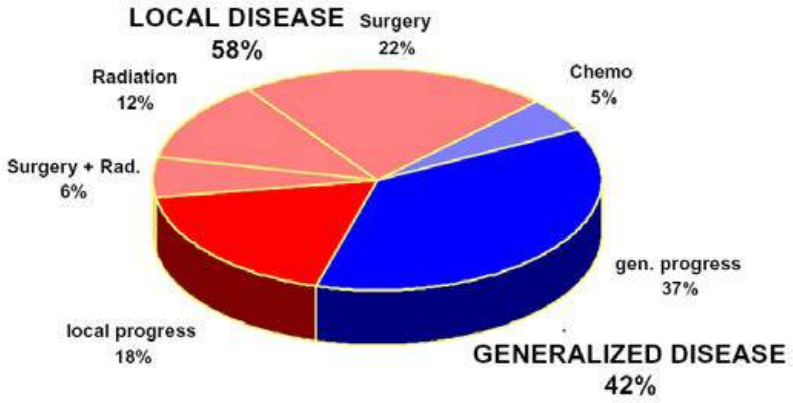

Figure 2.2: Distribution of cancer therapy methods [7].

is strongly dependent on the progression from local to general disease, it can be expected that improvements in early diagnosis of cancer will greatly improve the overall rate of cure.

Surgery is currently the most generally successful method of cancer therapy. In clinical practice, the aim is to remove all cancerous cells from the body entirely while minimizing the negative impact to the patient's well-being. The primary tumour must be removed and no cancerous cells must remain in the tumour bed. Since most cancers metastasize by dividing and proliferating beyond the primary tumour, a margin of normal tissues immediately surrounding the primary tumour is usually removed along with the primary tumour during surgery. Because it is an invasive therapy, surgery always implies a recovery period of the patient whose severity depends on the difficulty of the intervention. In fact, the main limitation of the surgical approach is the complications to the healthy tissues of the body that the operation would imply. This is particularly important for deep-seated tumours or tumours in the vicinity of vital organs where it's risky to intervene surgically. For instance, head and neck tumours are often in-operable since they require intervention around the skull base and in the vicinity of critical organs such as the brain stem or spinal cord.

Radiotherapy is the most commonly used type of treatment, given to about half of all cancer patients, either exclusively or in conjunction with chemotherapy and surgery. Its popularity owes to the fact that unlike surgery, it is entirely non-invasive: the irradiation procedure itself is painless and in most cases the only discomfort to the patient is minor burning of the skin that develops in the weeks following treatment at the entry and exit channels of the radiation field. In addition, radiotherapy is cheaper than surgery when taking into account the associated costs of patient hospital-

ization needed for recovery after an intervention. The reality today is that radiotherapy is a very desirable option for cancer treatment, especially when surgery would be highly invasive or risky. These days, the tumour control probability and related side-effects can be reasonably predicted thanks to ever-growing clinical data affording patients a real, and often preferable, option over surgery when deciding the course of their therapy with oncologists. Here we refer to conventional radiotherapy, that which uses beam of high-energy photons (used in 95% of cases) or electrons (used in 5% of cases), in order to make the distinction with hadrontherapy which will be discussed shortly.

In some cases, surgery and radiotherapy are combined by exposing the tumour site through surgical intervention and then directly irradiating the tumour and tumour bed by a beam of electrons. This technique, called Intra Operative Radiation Therapy (IORT), has reached quite a high level of precision in recent years and commercial machines which allow the doctor to perform the surgery and deliver the radiation while being guided by sophisticated imaging are becoming more and more available in hospitals. In a somewhat similar technique known as brachytherapy, radioactive sources are inserted either surgically or with the aid of needles into the tumour volume where they deliver a very localized dose over the course of their lifetime or until they are removed.

When a cancer has metastasized, the disease has progressed to a point in which the cancer is general throughout the body. In these cases, neither surgery nor radiotherapy is an option for cure and rather a systemic drug-based treatment is required. Because cancer cells are rapidly proliferating, they are more sensitive to certain cytotoxic drugs than regular cells which selectively destroy the cancer rather than the healthy tissues. However, because such drugs need be diffused into the entire body, patients usually experience a wide range of side-effects. For this reason, the use of chemotherapy on its own is limited to very specific types of malignancies which make up only a very small fraction (4%) of total tumour incidence. In most cases when used exclusively, chemotherapy serves primarily as a palliative treatment. One the other hand, most patients receive chemotherapy after surgery and radiation to control any possible metastasis that may have already spread beyond the tumour site.

Providing optimal treatment for cancer patients often requires a multidisciplinary effort that involves combinations of the various treatment methods described. Each cancer case is unique and many factors are considered when deciding on the right course of treatment. The patient's age, health and genetic heritage, as well as the cancer's progression and histology, must all be taken into account when deciding the exact course of treatment chosen by the patient, following the advice and guidance of their oncologist.

2.2 The basics of radiobiology

The study of radiobiology focuses on the biological effect of ionizing radiation in living tissues. It is well known that cell death can be attributed to DNA damage, caused either directly by ionizations of the DNA molecule or indirectly through the action of reactive oxygen species (ROS) formed by ionizations in the vicinity of the DNA molecule. Both may result in damages to the DNA in various forms: base damage, protein cross-links, single-strand breaks, double strand breaks, and/or a combination of all (see figure 2.3). Though all living cells have mechanisms for DNA repair, damage to the DNA molecule can lead to the destruction of the cell. In some cases, the damage is not correctly repaired and yet the cell is able to divide, propagating a mutation in the DNA which is inherited by daughters of the parent cell. At very low doses, damages leading to single-strand breaks (SSBs) do not result in cell death or mutation since they are readily repaired by the cell before cell division (mitosis) since a copy of the DNA exists in the undamaged half of the chromatin. At higher doses, breaks occurring on opposite sides of the DNA or separated by only a few base pairs can lead to double strand breaks (DSBs), in which the chromatin is broken entirely at one point along the helix. DSBs, unlike SSBs, are more difficult to repair and can lead to what are called chromosomal and chromatid aberrations as the cell attempts repair and instead fuses incorrectly with another DSB in the vicinity. While some of these aberrations are non-lethal and can be passed on to the progeny, many lead to cell death during mitosis. In general, there is significant evidence that the majority of fatal lesions are caused by DSBs rather than SSBs. Specifically, the likelihood of cell death is strongly correlated to the quantity of DNA aberrations which are the result of incorrectly repaired damage caused by *pairs* of DSBs which are not well isolated from each other.

A crucial aspect of radiobiology is the quantification of the sensitivity to ionizing radiation exhibited by both malignant and normal cell lines. Though the precise modeling of biological endpoints (cell death, carcinogenesis and mutation) as the result of double-strand breaks induced by ionizing radiation is an active subject of research in radiobiology, the diversity and variation in the biological response of cells to radiation has historically rendered a more empirical approach to cell survival prediction. The data relies on very large samples of well-controlled experiments which must be carried out on a wide variety of cells types. In standard studies of cell lines *in-vitro*, the cells are isolated and seeded into a number of culture flasks. The flasks are then irradiated with a known dose and the surviving fraction of cells measured by counting the number of cell colonies that develop after a given incubation period. The surviving fraction from each flask is then typically plotted on a log-linear graph as a function of dose. Figure 2.4 shows such a plot for several types of human and rodent tumour cells. Given the

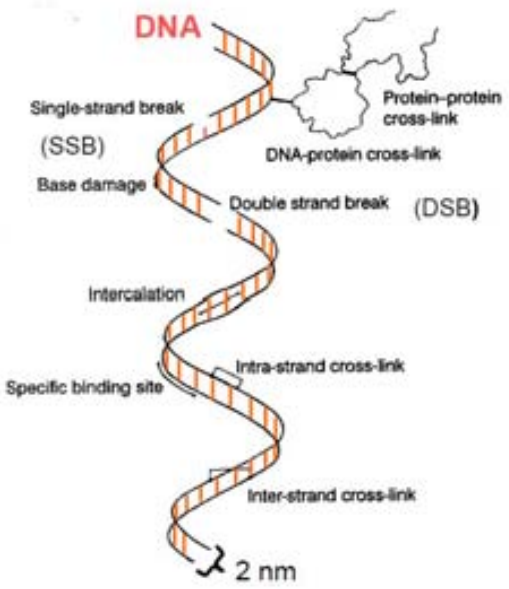

Figure 2.3: Schematic of DNA damages produced by ionizing radiation.

variability seen in biological response of cells from different specimens and of different types (illustrated by the different shapes of the survival curves shown in figure 2.4), prediction of cell survival is usually associated with some uncertainty. For this reason, survival studies must also be carried out considering a range of factors such as the specimens health and genetic heritage.

Though there are more sophisticated models which are more accurate, the most widely accepted model for cell survival is the linear-quadratic model, represented by the equation

$$S = e^{-\alpha D - \beta D^2}$$

where S is the surviving faction, D the dose and α and β the components that describe the shape of the shoulder characteristic of the curve on a log-linear plot. The behavior can be understood if we recall that the likelihood of cell death is proportional to the production of aberrations arising from two DSBs in close vicinity. The interpretation is probabilistic: the chance to create a nearby DSB pair from a single ionization event depends linearly with dose while the chance to produce a pair by two separate ionization events depends on the dose squared. This concept is illustrated in figure 2.5.

The aim of all radiotherapy treatments is to maximize the dose delivered to the treatment volume (and thus the probability of control) while maintaining a tolerable level of side-effects. Generally speaking, a treatment is

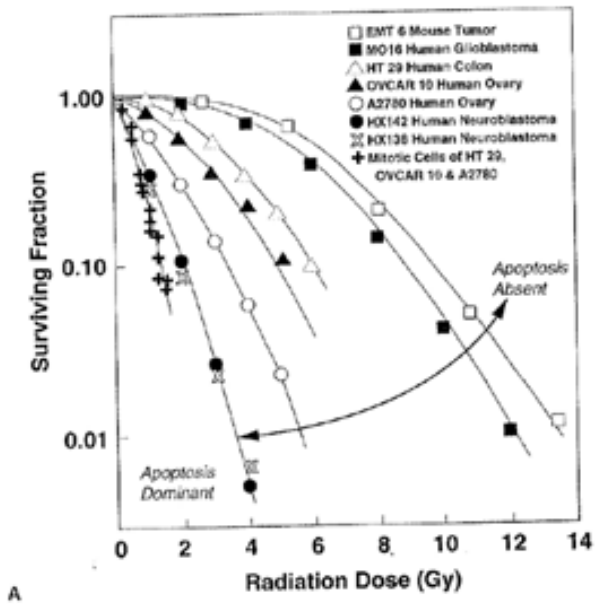

Figure 2.4: Cell survival curves for a number of cell cultures of human and rodent origin. There is a wide range of radio-sensitivities [8].

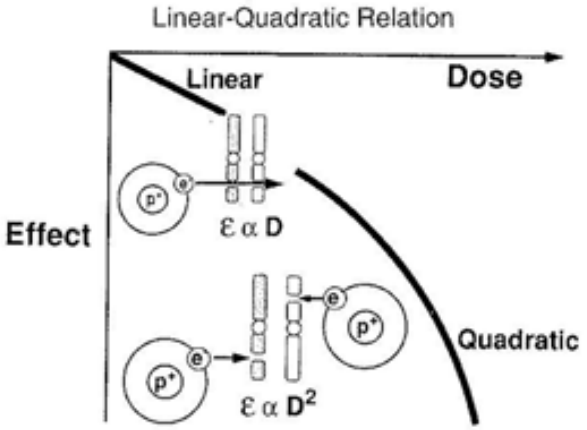

Figure 2.5: An illustration of the linear-quadratic relationship of biological effect of cell killing as a function of dose [8].

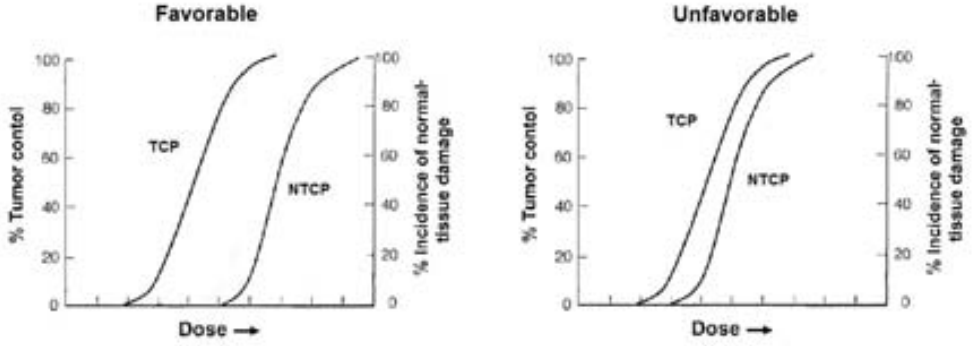

Figure 2.6: A sketch of the tumour Control Probability (TCP) and the Normal Tissue Complication Probability (NTCP) for two different radiotherapy cases, one which is favorable for radiotherapy (left) and one which is unfavorable (right) (adapted from [8]).

considered optimum if it maximizes the tumour control probability (TCP) and simultaneously minimizes the normal tissue complication probability (NTCP). Typically, this is achieved with a TCP $> 50\%$ and a NTCP $< 5\%$ [9]. Figure 2.6 shows an example of two different cases for radiotherapy. On the left, the treatment is favorable thanks to the large separation between the TCP and the NTCP (i.e.: it is possible to achieve a very high level of tumour control with a very low level of side-effects.) On the right, is an unfavorable case since the TCP and NTCP are very similar and only a low value of TCP can be achieved for a tolerable level of side-effects. The ability to make such predictions, and thus to facilitate the highest patient care, relies on both the existing knowledge of the radio-sensitivity of malignant and healthy cell lines and a precise estimation of the volumetric dose which would be delivered to the patient by a beam of irradiation.

The reason radiotherapy is so effective as a treatment for cancer owes to the fact that most cancerous cells are more sensitive to ionizing radiation than healthy tissue cells. This is the case for nearly 90% of cancerous cell lines, while about 10% are radio-resistant. The exact reasons for the higher sensitivity of most cancerous cell lines over healthy ones are complex but are similar in many ways to that which is exploited in chemotherapy. Loosely speaking, the more rapidly proliferating a cell line the more sensitive it is to radiation. This inherent benefit effectively widens the gap between TCP and NTCP making it possible to treat tumours when a dose to healthy surrounding tissues is unavoidable. Furthermore, the sensitivity of cells to radiation can be modified with certain drugs known as sensitizers and protectors.

The situation can be further improved by delivering the radiation in

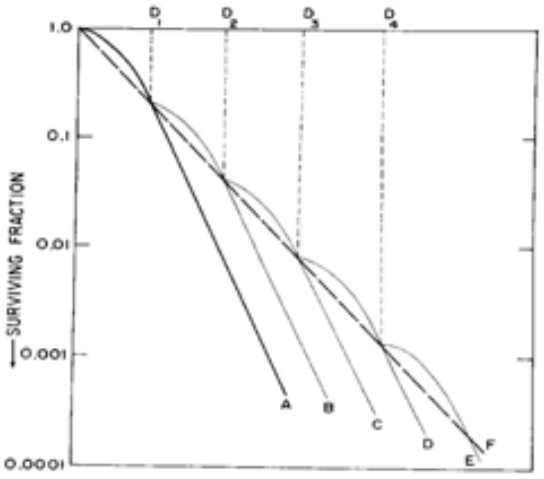

Figure 2.7: Cell survival for a single irradiation and fractionated radiotherapy scheme. In the fractionated scheme the dose is delivered at intervals separated by a time which allows the repair of sub-lethal DNA damage.

fractions allowing time for the healthy tissues to repair. For most cell lines, if the entire dose is given in a single fraction, the cell survival is much lower than what it would be if the dose is built up allowing the time for the cell to repair. This is illustrated by the cell-survival curve shown in figure 2.7 in which the initial shoulder of the linear-quadratic at low doses is effectively repeated with each fraction. Because of the higher sensitivity of malignant cells which exhibit a steeper slope as compared with healthy cells, fractionation then preferentially spares healthy cells and further improves the separation of TCP and NTCP.

2.3 Conventional radiotherapy: electrons and photons

The main principle behind radiotherapy treatment is to deliver collimated beams of ionizing radiation precisely onto a predefined volume within the body. Though the early days of radiotherapy delivery were crude, mainly relying on the application of radioactive sources directly onto the diseased tissues, modern techniques allow the deposition of a volumetric dose which is highly conformal to the tumour volume.

In current radiotherapy practice, the majority of treatments employ photon beams, referred to by physicians as X-rays. Though X-rays are also used in imaging, to be useful for radiotherapy they are produced at much higher energies and intensities. Therapeutic X-ray beams are generated by focusing a beam of high-energy electrons onto a target, usually a tungsten alloy.

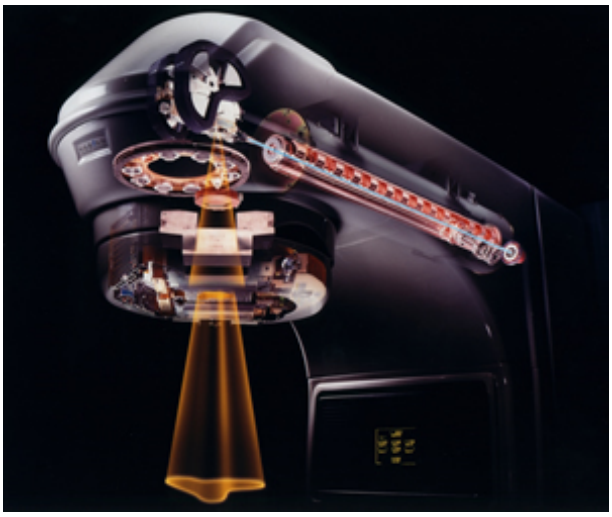

Figure 2.8: A conventional radiotherapy machine. An electron accelerator is used to irradiate a tungsten target which produces X-rays with a broad energy spectrum which can be used for therapy.

This produces photons with a broad energy spectrum with a maximum energy of the incident electron beam and an "effective" energy which is about one third of this maximum. The photons are collimated and can then be directed towards the patient. In most devices, the target can be removed to allow the electron beam itself to be used in therapy. Electrons, however, are used only in a small fraction of radiotherapy cases, mainly with superficial lesions near the skin surface and in IORT.

Figure 2.8 shows a schematic of a typical electron accelerator used in modern conventional radiotherapy. The electron accelerator has been highlighted along with the target and collimator. In the world today there are nearly 20,000 such accelerators used exclusively for cancer therapy treating nearly 4 million patients per year.

In the case of irradiation by photons or electrons, the largest fraction of the dose is deposited several centimeters below the surface. The depth-dose curves for electrons and photons in water is shown in figure 2.9; in both cases the dose profile peaks just below the surface and then decreases gradually with depth. Electrons, because of their limited penetration, are used in the treatment of lesions in a range of between 1-5 cm below the skin (water equivalent). This range can be controlled by varying the beam energy which for radiotherapy is typically between 4-20 MeV. Photons on the other hand, in an energy range of about 4 to 25 MeV are used to treat deep-seated tumours within the body because of their deeper penetration into tissue.

With each delivered photon, there is always a certain amount of dose

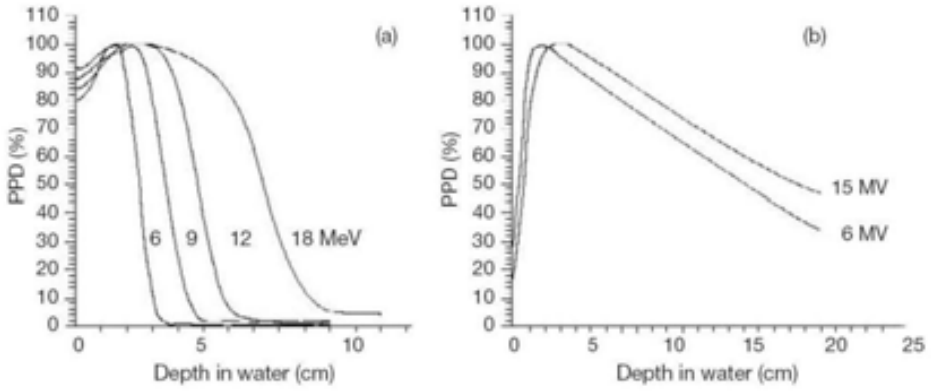

Figure 2.9: Depth-dose curves for electrons and photons in water [9].

which is given to the healthy tissues both before the tumour and after it. Despite the selective sensitivity exhibited by many types of cancer cells to radiation damage and the advantage of fractionation, the use of a single beam (or field) is usually limited when considering the healthy tissue complications that would result. Indeed, the role of the medical physicist is to give the highest dose to the volume delineated by the oncologist while maintaining a tolerable level of dose to the healthy tissues. This is often not possible using a single field, especially when the treatment volume is located deep within the body or in the vicinity of organs-at-risk (OAR). To overcome this challenge, several irradiation fields can be delivered, impinging the body at different angles such that the overlap of the fields corresponds to the target volume. The shape of each field can also be uniquely contoured using a device called a multi-leaf collimator which can be adjusted rapidly by electronic control. In this way, the cumulative dose of many fields is made highly conformal to the target volume. This technique is known as Intensity Modulated Radiation Therapy (IMRT). Figure 2.10 shows a typical treatment plan using the technique of IMRT for a prostate case in which the tumour site is irradiated using 5 fields entering the body at different angles.

2.4 The hadrontherapy advantage: the Bragg peak

Conventional radiotherapy will always be challenged by the fact that for each individual radiation beam, the largest fraction of the dose is deposited only a few cm from the surface (see figure 2.9). This arises from the physics of the interaction of photons with matter. Though the position of the peak can be adjusted somewhat by selecting the beam energy, a significant fraction of the dose is always deposited both before and after the peak. This

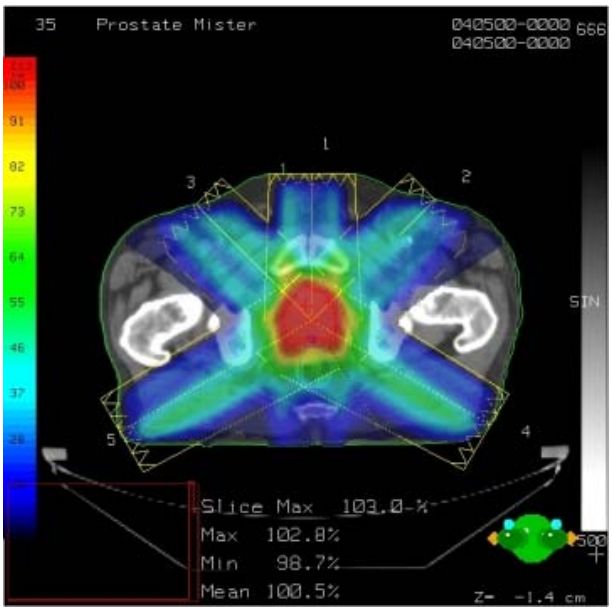

Figure 2.10: A prostate treatment plan using Intensity Modulated Radiation Therapy [10].

physical limitation makes it problematic to treat deep-seated tumours without severe side effects induced by irradiated healthy tissues or OARs. This drawback can be somewhat overcome by building up the dose with many fields as in IMRT, by the use of chemical protectors and sensitizers, and with fractionation, as we've discussed. Still, the gradual fall-off of the dose profile for photons at greater depth makes it very difficult to spare sensitive healthy tissues, and particularly OARs, in the vicinity of the planned treatment volume. Despite its having achieved a remarkable level of precision, conventional radiotherapy will always be limited by this basic principle.

The profile of energy deposition for protons and light ions interacting in matter is characteristically different than for photons or electrons. Instead of the maximum dose being deposited some cm from the surface, it is highly localized at the end of the particle range which can be readily controlled by varying the beam energy. Specifically, a rapid increase in linear energy transfer (LET typically measured in keV/μm) at the end of the hadron beam range, known as the Bragg peak, effectively focuses the bulk of the energy deposited at depth rather than near the surface. This characteristic is similar for most charged particles containing quarks, which includes protons and ions. Consider figure 2.11 in which the relative dose for a beam of photons, protons and carbon ions (of two energies) is indicated as a function of its depth in water. We can easily appreciate the advantage presented by the profile for protons and carbon ions in treating a tumour site at the end of

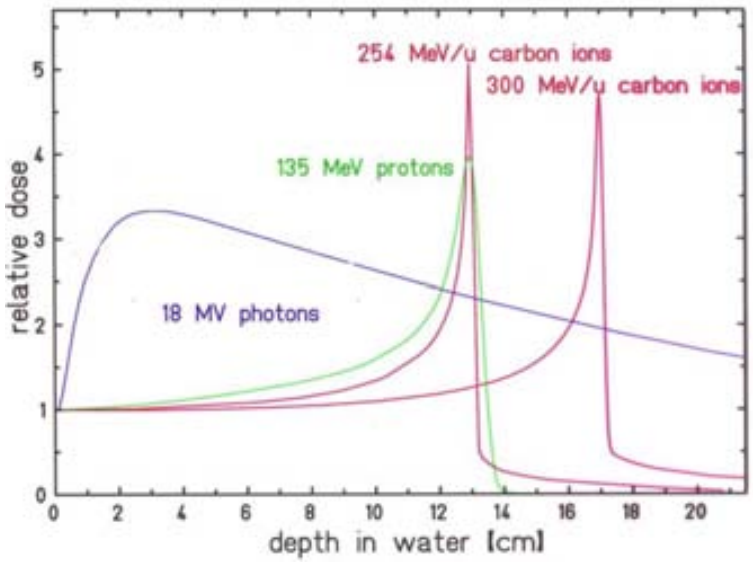

Figure 2.11: The dose-depth distribution of photons, protons, and carbon ions at typical therapeutic energies (courtesy of GSI).

their range; the narrow peak allows a very high dose to be delivered to the target while both before and beyond the target the dose is significantly lower than with photons.

In practice it is necessary to irradiate a volume of tissue uniformly and so the energy of the proton or ion beam must be modulated such that the dose is uniform with depth. This point is illustrated in figure 2.12 where a number of hadron beams of different energies are superimposed to create a uniform dose profile (in depth) referred to as the Spread-Out-Bragg-Peak (SOBP). Since the dose is cumulative, the most distal edge of the tumour site must be irradiated more, while the proximal edge is irradiated less since it receives a portion of dose from the beams penetrating to the distal edge. Such energy modulation can be achieved using passive absorbers inserted between the beam nozzle and the patient, or preferably, by controlling the energy of the beam in the accelerator.

2.5 The case for carbon ion therapy: LET and RBE

In comparing the dose-depth profiles shown in figure 2.11, we can see that the peak for carbon is narrower than for protons and the fall-off beyond the peak more rapid. Not illustrated in figure 2.11, since its vertical scale is only relative, is that the absolute value of the LET in the Bragg peak is many times higher for charged ions than for protons. On average, the LET of a

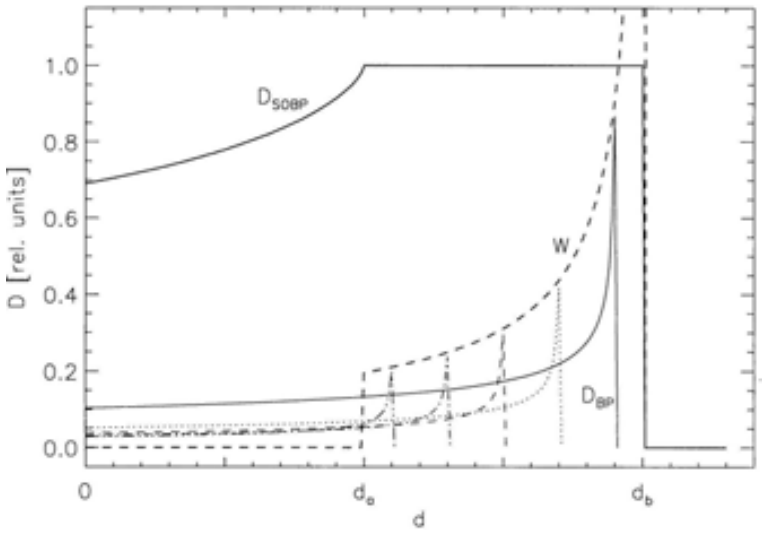

Figure 2.12: The use of several hadron beams of different energies leads to the flat-topped dose profile known as the Spread-Out-Bragg-Peak (SOBP) [11].

carbon ion is about 25 times larger than the LET of a proton having the same range. The significance to medicine is that the higher LET causes a more devastating effect on cells. Specifically, high LET radiation, in the vicinity of a DNA molecule, results in a high concentration of double-strand breaks and thereby a greater likelihood of cell death. This is illustrated in figure 2.13 where the concentration of ionizations on the nanometer scale is shown for a single proton and a single carbon ion with a DNA molecule added for scale. In radiobiology, the biological impact of LET is quantified by the radio-biological effectiveness (RBE), a measure of the increased effectiveness for cell killing induced by ions as compared to the energetic electrons put in motion by X-rays. Precisely, RBE is defined as the ratio of the dose needed for 1 MeV photons to the dose needed for ions which would give the same probability of cell survival for a given cell line. RBE then, depends not only on the species of ion in question, but also on the chosen biological end-point. Figure 2.14 illustrates the definition of the RBE for a certain particle species and at a survival probability of 10%.

The RBE in the Bragg peak for protons (at 10% survival) for most cell lines is roughly 1.1 - 1.2 but can be in a range of 3-5 for carbon ions [12]. For ions heavier than carbon the RBE in the Bragg peak begins to decrease again. Even though the LET is higher, the RBE for an equivalent dose is lower. This is because if we consider a volume of tissue or a given number of cells, fewer high-LET particles are required to deposit the same amount of energy or dose. The probability of striking a cell nucleus thereby

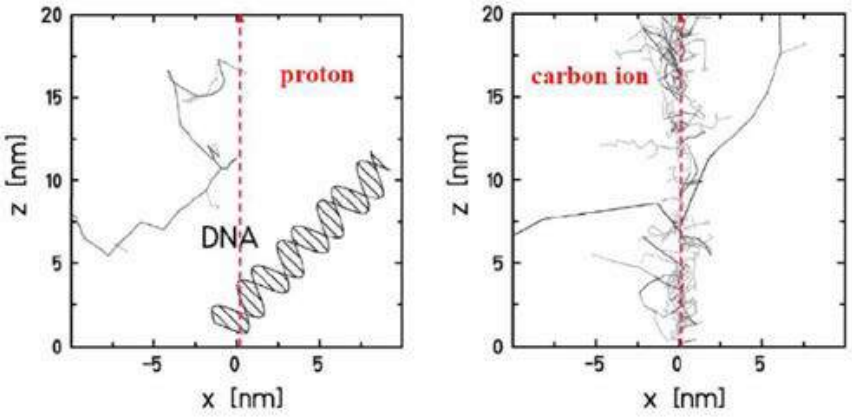

Figure 2.13: An illustration on the nanometer scale of the concentration of ionization or LET for proton and carbon ions [12].

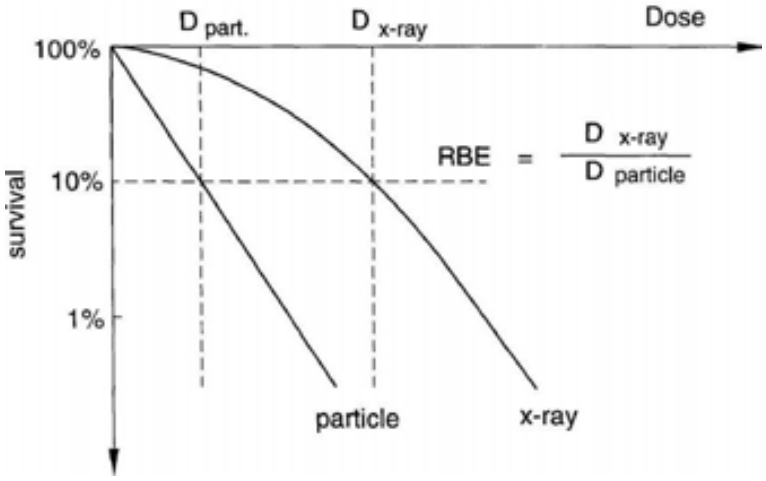

Figure 2.14: Cell survival curves under particle and X-ray irradiation. The RBE is defined as the ratio of doses needed to achieve the same level of cell survival [13].

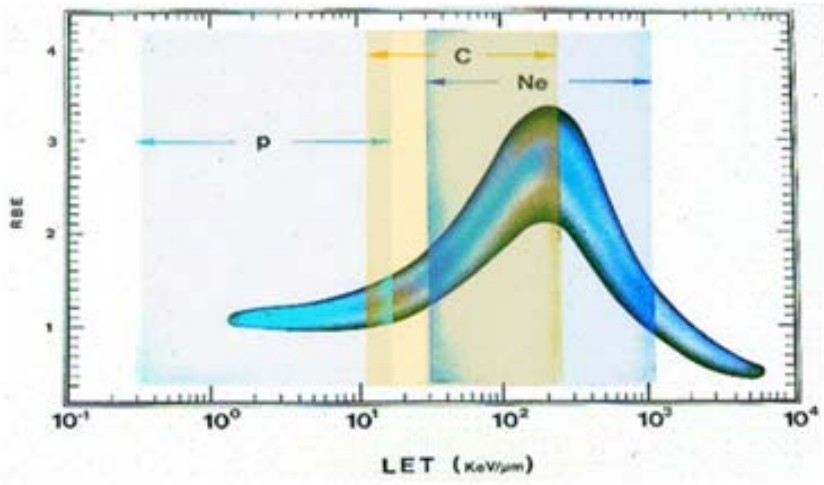

Figure 2.15: The relative biological effectiveness as a function of LET. Several particle types are shown in which the range of LET from the entry energy to the Bragg peak are indicated.

decreases with higher LET and, for ions heavier than carbon, this effect dominates such that the RBE decreases. Furthermore, for ions heavier than carbon the LET in the entrance channel is large enough to increase the RBE thereby causing more damage to the traversed healthy tissues. A schematic representation of the RBE as a function of LET is shown in figure 2.15; the range of LET which spans from the entry energy to the end of the Bragg peak is indicated for protons, carbon ions and neon ions. The figure clearly shows why carbon ions are being chosen for therapy: the RBE at the end of the Bragg peak is maximal while it is not too large at the entrance in the patient body.

Another reason ions heavier than carbon are unfavorable is that they are more likely to deposit their energy through nuclear interactions. The fission fragments of such reactions, which generally have a higher range due to their lower charge, penetrate beyond the Bragg peak, adding a substantial fall-off in the dose-depth profile.

For light ions and carbon ions especially, the higher RBE and the narrower profile of the Bragg peak permit an even better conformity of the effective dose to the target volume. Figure 2.16 shows a comparison of the dose distribution for the best possible treatment plan for a head-and-neck tumour using two beams of carbon ions and IMRT. As this comparison illustrates, there is strong preference to use carbon ions when dealing with cases involving deep-seated tumours near OARs.

Another advantage of carbon ion therapy applies to cases of hypoxic

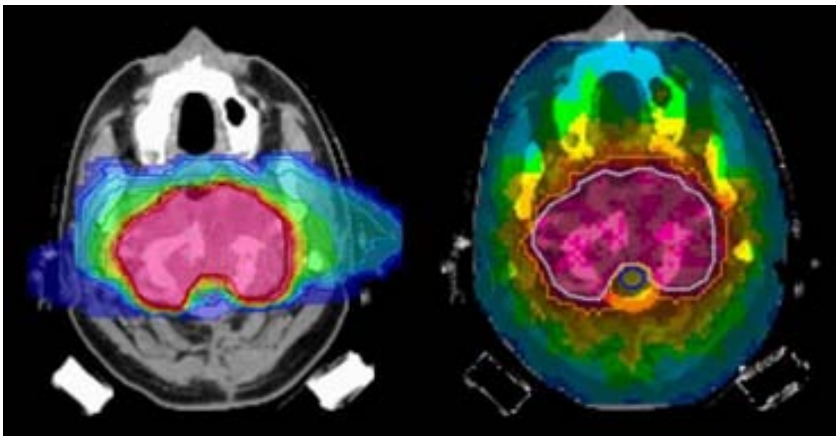

Figure 2.16: Comparison of the dose distribution for a carbon treatment (left) with the best possible conventional IMRT dose distribution (right) [14].

and radio-resistant tumours, the latter of which make up about 10% of the total. Tumours with hypoxia, in which the tissue of the tumour has become oxygen deficient, are notably less sensitive to radiation damage and thus more difficult to control; the center regions of large tumours are very often hypoxic and resist treatment by protons and conventional radiotherapy. The use of ions with an enhanced RBE, such as carbon, is yielding positive results with hypoxic and radio-resistant tumours and this is an exciting area of research in present-day clinical hadrontherapy. In line with this advancement and because of the advantages we have seen, most modern-day hadrontherapy centers are designed to deliver both protons and carbon ion beams and are known as "dual" centers.

2.6 Historical and present perspectives

The treatment of cancer using protons was first proposed in 1946 by Robert R. Wilson. In a seminal paper, he outlined the basic principles illustrating the inherent benefit of the proton's depth-dose profile for targeting malignant disease [15]. He also mentioned the use of helium and carbon ions. The details of his proposal are remarkably illuminated if we consider that the imaging techniques and accelerators required were only a dream at that time. Beginning with the pioneering work at Berkeley in 1954 and at Uppsala in 1957, physicists and radiation oncologists began performing clinical studies using proton beams. In the decades that followed, most notably the study at the Harvard cyclotron involving over 9000 patients having intercranial legions, eye tumours or head-and-neck tumours, much of the basis for future clinical and technological developments were established. Though

neutrons were used for a brief period during the pioneering era of the 70's and 80's, they were abandoned to the more positive clinical results achieved with protons.

Until recently in history, the clinical use of protons, and light ions were confined to academic facilities having research-oriented particle accelerators capable of delivering beams with sufficient energy and intensity to be used therapeutically. This owes to the much greater challenge in accelerating and delivering charged ions as opposed to electrons. For comparison, medical linear electron accelerators are typically installed, operated and maintained by only a handful of people and have been in use since the 1950's as medical radiation sources. This technological challenge is arguably the main reason conventional radiotherapy developed so rapidly into a routine clinical technique during the 70's and 80's, while proton therapy remained largely experimental until the 90's. That being said, by the end of the 80's some 14000 patients had been treated with either protons or helium-ions in facilities dedicated to nuclear or particle physics research. In 1990, the first hospital-based proton facility, the Loma Linda University Medical Center in California, began treating patients. The center featured a rotating gantry designed for routine treatment. Over the last twenty years, a number of dedicated hadrontherapy centers have been constructed exclusively for treating patients, mainly in the US, Europe and Japan.

In 2012, sixty-six years after the proposal by Wilson, hadrontherapy has matured to the point that it can be routinely used therapeutically and is now a modern-day reality in the fight against cancer. Thirty-five centers dedicated to delivering therapeutic beams of protons and carbon ions are currently in operation and many more are nearing completion or are foreseen in the near future. Several commercial companies are involved, namely Hitachi, IBA, Mitsubishi, Siemens, Varian/Accel, and Mevion, all of them offering complete turn-key proton-therapy centers. As of the end of 2011, about 110,000 people have undergone hadrontherapy in the world, over 100,000 treated with protons and over 9000 with carbon ions [16]. During the 2012 alone, the total number has increased by 10%. Although clinical trials are still ongoing, in particular for carbon ions, the growing data for a wide range of malignancies points towards an improvement in local control rates, a better sparing of healthy tissue, reduced side-effects and an overall better prognosis.

Currently, there is a need to bring hadrontherapy more effectively, and economically, to the highest benefit of patients. Because of the challenges inherent in delivering medical beams of protons and ions, particle accelerators are massive and complex machines implying an infrastructure which requires significantly more manpower and investment. Successful operation requires co-operation between doctors, physicists, radiologists, engineers, and administrators. Though finally emerging as a routine clinical practice, hadrontherapy is still in its infancy. In order to best provide patients with

the highest quality of treatment, the community must work together to share ideas, experience and clinical data as it becomes available.

Apart from the logistical and financial challenges, there are a number of technological ones that are active fields of research. On the machine side, compact accelerator components and gantry designs are examples of new developments. In informatics, GRID-based computing infrastructure is allowing for multinational data sharing and providing the computing power needed to produce treatment plans based on Monte-Carlo codes developed for HEP which are more accurate than the analytical ones used currently. In radiobiology, micro-dosimetry and tissue irradiation experiments using exotic and heavy ions are still needed as are validations of modern theoretical models of cell radiosensitivity.

2.7 Quality assurance in hadrontherapy

Of particular importance to the future success and acceptance of hadrontherapy will be the ability to validate the accuracy of the *delivered* treatment plan. Though the accuracy of modern medical ion-beam delivery systems is exceptionally high, the requirement for conformity in ion therapy is much more stringent than in conventional radiotherapy. This is due to the Bragg-peak dose-depth profile characteristic of protons and ion beams. Such particles highly ionize at the end of their range, thus any error in that range, and the dose delivered to healthy tissues could potentially be very large. Similarly, such errors can result in severe under-dosing of the target volume. This point is illustrated in figure 2.17 where the dose from a spread-out-Bragg-peak (SOBP) of ion therapy is compared with one created by photon radiotherapy in the event of a difference in the tissue density along the beam entry path. In both plots the expected dose profile is shown along with the actual delivered profile. The error in dose delivery is low in the case of photons, whereas in the case for ions the tumour will be under-irradiated and healthy tissues over-irradiated. Preventing such errors in hadrontherapy is crucial for both minimizing complications while maintaining tumour control. From one perspective, the use of protons and ions for therapy is a double-edged sword: the very characteristic that makes them favorable for treating tumours, namely the Bragg peak profile at the end of their range, is the same that allows little margin for error.

In modern radiotherapy, the uncertainties in patient setup, beam parameters and treatment-planning calculations typically amount to not more than 3%. Despite this, it is possible for the actual delivered dose to deviate more drastically from the expected one due to changes in the morphology of the tissue before irradiation. Such changes can occur as a result of organ motion, cavity filling or by a reduction or increase of the tumour volume. Because treatment plans are typically based on a single planning X-ray Com-

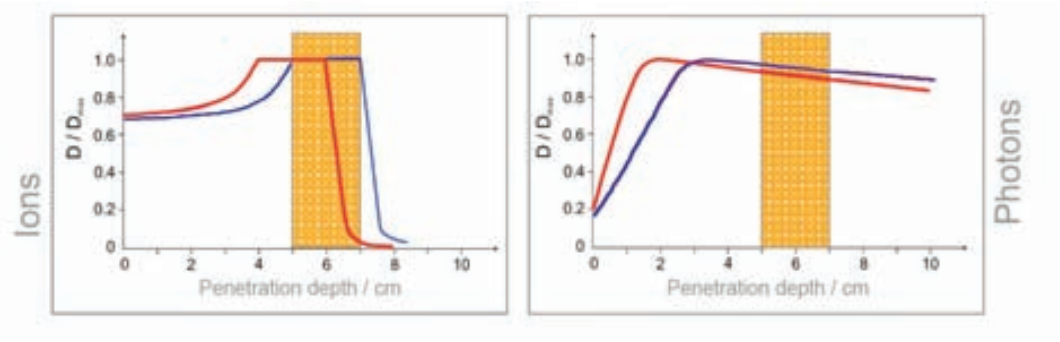

Figure 2.17: The effect of a difference in tissue density on the deposited dose in ion therapy (left) and conventional radiotherapy using photons (right). In each case, the resultant dose when the treatment plans misses the tumour volume is shown.

puterized Tomography (CT) carried out at the beginning of treatment and because treatment schemes are usually fractionated over several weeks, such day-to day changes in morphology can go unchecked and lead to errors of the delivered dose more significant than those encountered routinely. Recently, the use of more frequent CT scans has been introduced.

In hadrontherapy, such errors are more influential to the treatment outcome and patient well-being than they are in conventional radiotherapy. Thus the need for quality control in clinical practice is greater. In the context of this thesis, we refer to quality assurance (QA) as any technique which helps to ensure the accurate delivery of the treatment plan to the treatment volume.

The investigation of novel detectors designed for hadrontherapy QA is the mandate of the AQUA group of the TERA Foundation and the main subject of this dissertation.

Chapter 3

Particle Interaction in Matter

3.1 Charged particles

High-energy charged particles, on their passage through matter, interact with the medium primarily through electromagnetic processes. For charged particles such as protons, alpha particles or any other hadrons, nuclear interactions are also possible and will be considered separately. For the moment, let us consider only interactions arising from the electromagnetic force.

3.1.1 Electromagnetic interactions

When a high-energy charged particle passes through a medium it deposits energy mainly through Coulomb interactions with the atoms or molecules of the material. The interactions with the electrons and the nuclei of the target material gives rise to different effects. Consider a proton colliding with a nucleus. If the mass of the nucleus is much larger than the mass of the proton then little energy loss occurs though the proton can change direction. This is apparent in the expression for the maximum energy transfer of an elastic collision of a proton with mass m on a nucleus of mass M derived from non-relativistic kinematics and given by

$$\triangle E_{max} = \frac{1}{2}mv^2 \left(\frac{4mM}{(m+M)^2} \right) \tag{3.1}$$

In collisions with electrons, however, a large amount of energy can be transferred whereas the direction of the proton will hardly be affected. It thus follows that when a proton interacts with a medium, its energy loss is predominately due to the interactions with the electrons of the medium, while its change in direction is due to interactions with the nuclei. As the proton travels through the medium, the energy transferred to the electrons

results in the atoms of the material being left in either an ionized or excited state. Electrons which are imparted with enough energy to escape the binding forces of the atom are called δ-electrons and can travel a significant distance in the material even leading to further ionizations. Even though not all of the energy deposited along the path of the incident particle will liberate electrons, this kind of energy loss is commonly referred to as *energy loss by ionization*.

The energy deposited per unit distance, dE/dx, by a charged particle having velocity ν, due to interactions with the electrons of a material having ionization potential I and density ρ, is given by the Bethe-Bloch equation

$$\frac{dE}{dx} = \rho\frac{Z}{A}(0.307\,MeVcm^2/g)\frac{Z_{eff}^2}{\beta^2}\left[\frac{1}{2}ln\left(\frac{2m_ec^2\beta^2\gamma^2T_{max}}{I^2}\right) - \beta^2 - \frac{\delta}{2}\right] \quad (3.2)$$

where $\beta = \nu/c$, $\gamma = \frac{1}{\sqrt{1-\beta^2}}$, Z_{eff} is the effective charge of the incident particle, and Z and A are the atomic number and atomic mass of the medium, respectively. The electron rest mass is given in energy units such that $m_ec^2 = 0.511$ MeV and δ is a density-dependent correction term that applies to high energies. T_{max} is the maximum energy transfer to the electron which for all incident particles except the electron itself is $\approx 2m_ec^2\beta^2\gamma^2$. For electrons T_{max} is just the energy of the incident electron.

The Bethe-Bloch equation (equation 3.2) is valid for heavy charged particles at energies above 300 keV; below this value corrections are required. One is the shell correction which includes the fact that the electrons of the medium are bound to the target nuclei. The electrons are polarized either towards or away from the incident particle depending on its charge, either positive or negative. This is known as the Barkas effect and explains why positive particles ionize slightly more than their anti-particle.

Another important correction that occurs at low energy is the decreasing of the effective charge of the incident particle, Z_{eff}. This arises because charged particles (other than protons) can pick up electrons as they travel through the medium. Heavy nuclear fragments exhibit this behavior strongly such that the energy loss actually decreases rather than increases towards the end of the range. Light ion species and alphas, however, only pick-up electrons near the very end of their range.

In working with radiation detectors, it is common to speak of the reduced energy loss (or stopping power) where dE/dx is normalized to the density of the medium, ρ, and expressed in units of MeV cm^2/g. The reason is that for all particles the reduced energy loss obtains a minimum and roughly constant energy-independent value, independent of the material type. This occurs when the velocity of the particle is close to the velocity of light ($\beta \approx 1$). This point is illustrated by the following simplified expression of the Bethe-Bloch equation where

$$\frac{dE}{dx} \approx \rho \left(2MeVcm^2/g\right) \frac{Z_{eff}^2}{\beta^2} \tag{3.3}$$

This minimum value of the reduced energy loss is approximately 2 MeV cm^2/g for particles of unit charge. For particles such as protons, this occurs at energies above 1000 MeV while for electrons, it occurs above 500 keV. At relativistic velocities, where $\beta \to 1$, the energy loss increases only slightly. It follows then that charged particles having near relativistic velocities have a similar reduced energy loss. For convenience, particles in this range of energy are referred to as MIPs (minimum ionizing particles).

In practice sufficient experimental data exists to reasonably predict the energy loss for a given particle energy and detector material. A database of the reduced energy loss for charged particles in many materials has been assembled by the National Institute of Standards and Technology (NIST) and is available for download from their website [17]. A plot of the stopping power for protons traveling through Argon gas at atmospheric pressure taken from the NIST website is shown in figure 3.1.

It should here be mentioned that when considering the biological effects of radiation, we often refer to the linear energy transfer or LET, defined as the average energy deposited in the material per unit length, usually expressed in units of keV/μm. When considering only electromagnetic interactions, the LET is similar to the energy loss discussed above. Indeed, because δ-electrons can travel a significant distance in material, some of the energy lost by the interacting particle is not deposited locally along the trajectory of the particle. Thus, the LET is slightly lower than the energy loss. The LET is important when considering the effective dose delivered to tissue and has an important consequence on the RBE.

As a particle passes through matter, it deposits energy until its energy is depleted and it comes to rest at the end of its path, R. This can be calculated as the integral of the inverse energy loss, or

$$R = \int_{E_0}^{0} (\frac{dx}{dE})^{-1} dE \tag{3.4}$$

Because of the dependence of the energy loss on $1/\beta^2$, charged particles tend to deposit a higher fraction of their energy near the end of their range. The shape of the energy loss as a function of penetration depth has a characteristic shape, shown in figure 3.2. While the velocity of the particle is near to the speed of light, the energy loss profile is a slightly rising plateau corresponding to near the minimum ionization. Close to the end of the range, where the particle has only a fraction of its initial velocity and $\beta \ll 1$, the energy loss increases sharply in what is known as the Bragg peak.

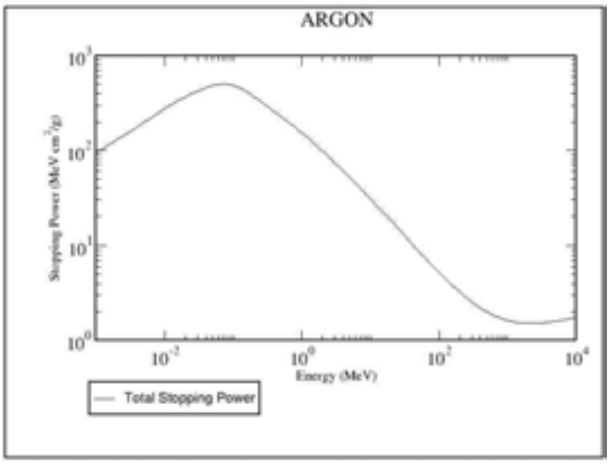

Figure 3.1: The reduced energy loss or stopping power of protons in Argon gas at STP taken from the NIST website.

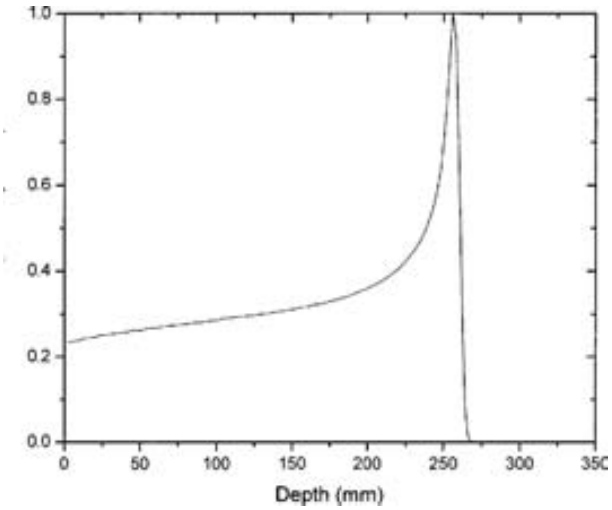

Figure 3.2: The energy-loss profile of a proton traveling through a dense medium. The characteristic rise in energy-loss near the end of the range is known as the Bragg peak.

Material	Radiation Length	
	X_0	
	(g/cm^2)	(cm)
H_2O	36.08	36.1
Al	24.01	8.9
Cu	12.86	1.43
Pb	6.37	0.56
SiO_2	27.05	12.3

Table 3.1: Radiation length of a few common materials [19].

Because of the statistical nature of the energy loss along the particle trajectory not all particles having the same initial energy will have the same range. This variation is called range straggling and amounts to about 1% of the mean range of protons and only 0.3% for carbon ions which have a larger mass. When considering beams of charged particles incident on a target material, range straggling leads to a Bragg peak which is more rounded than it would be for a single particle. In addition, particles do not travel along straight lines as they lose energy. Particles undergo a process known as Multiple Coulomb Scattering (MCS) due to the interactions with the nuclei of the target material which leads to variations in the projected range. Because of kinematics, this is very small when the mass of the projectile is much larger than that of the target. Protons and charged particles are thus only slightly deviated from their path by electromagnetic interactions with electrons and travel very nearly in a straight line through matter before coming to rest. Electrons on the other hand, are deviated strongly, tracing out a chaotic path in which the projected range is much smaller than the actual range.

When considering charged particles (other than electrons) and for small angles of deviation, the change in angle Θ of a particle with charge Z and momentum p traveling through a material of thickness L is roughly Gaussian with a root mean square deviation given by

$$\sqrt{\langle \Theta^2 \rangle} = \frac{13.6MeV}{\beta pc} Z \sqrt{\frac{L}{X_0}} \tag{3.5}$$

where X_0 is the radiation length, a quantity which characterizes how particles interact in a material and depends on the density and charge of the nuclei of the material [18]. The radiation length of a few common materials is given in table 3.1.

Multiple Coulomb Scattering leads to a spread in the lateral beam size which increases with the penetration depth. Figure 3.3 shows the lateral beam width for protons of 148 MeV and carbon ions of 270 MeV/u incident on a water phantom. Though not subject to multiple scattering, the width

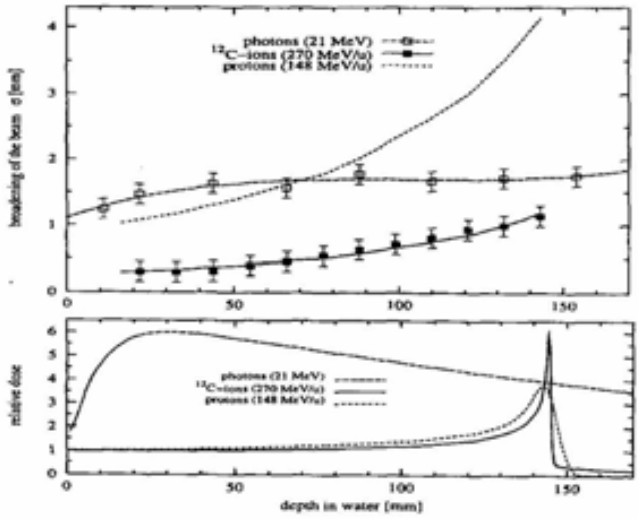

Figure 3.3: The broadening of a beam of protons and carbon ions penetrating into a water phantom caused by multiple scattering. [13]

of a beam of 21 MeV photons is also shown for comparison. The depth-dose profile for the same energies is given for reference (shown below). For protons, the lateral spread increases rapidly with beam depth and becomes greater than for a beam of photons above 7 cm penetration. Carbon ions on the other hand, because of their much higher momentum, undergo much less lateral spreading due to multiple scattering. This effect is important for the conformity of radiotherapy treatment plans and is another advantage of using carbon ions over protons for therapy.

3.1.2 Other electromagnetic processes

Several other interactions, also arising from the electromagnetic force, are also possible with charged particles. These include the Cherenkov effect, transition radiation and Bremsstrahlung. For charged particles such as protons, the energy loss associated with these effects is much smaller than from ionization and so we aim only to summarize these effects for completeness rather than deal with them in detail.

The Cherenkov effect occurs whenever a charged particle travels faster through a medium than the speed of light in that medium, which is given by c/n where n is the medium's index of refraction. The Cherenkov effect is very similar to the way in the which a bow wave is produced in front of a speedboat or the super-sonic bang of a plane going faster than the speed of sound. In the case of a particle, electromagnetic perturbations positively interfere along a wavefront perpendicular to a specific angle from the particle's direction. The angle depends on the ratio between the particle

velocity v and the speed of light in the medium, specifically

$$cos(\theta_c) = \frac{c}{nv}$$

Optical photons are emitted in the direction of the angle θ_c as given above and can be detected if the material is transparent. Though the energy loss from the Cherenkov effect is very small compared with the energy loss due to ionization described earlier, it is an important effect since it depends only on the velocity of the particle. Detectors that exploit the Cherenkov effect by measuring the angle of emission of Cherenkov photons are useful for particle identification and are widely used in high-energy physics experiments.

Transition radiation is another effect which emits photons, though commonly in the soft-X region. It occurs when a charged particle passes a boundary between vacuum and a material. Though it is a very small effect, it can be amplified by using materials with a large number of transitions, such as a stack of thin foils or foam-like structures. Many detector designs exist to exploit this principle and transition radiation detectors are typically also used for particle identification since the magnitude of the energy emitted is proportional to γ.

A further effect that involves the emission of photons is known as Bremsstrahlung. Whenever a charged particle undergoes acceleration, it will emit electromagnetic radiation. This occurs when a charged particle deviates its trajectory from the elastic collision with a nucleus. In practice, the intensity of the radiation is negligible for all particles other than electrons and positrons except at energies above 1 TeV. For electrons the energy loss due to Bremsstrahlung becomes even greater than the energy loss due to ionizations at a critical energy E_c. Indeed, this is the main phenomenon exploited in an electron linac where the electrons hit a heavy target and produce X-rays. The critical energy E_c depends on the nuclear charge of the atoms in the medium and can be approximated by $E_c = 800\,\mathrm{MeV}/(Z + 1.2)$.

3.1.3 Nuclear interactions of charged particles

Charged particles (other than electrons and positrons) can also interact via collisions with the nuclei of the material through the nuclear force. The nuclear cross section can be approximated using geometric principles and can be expressed as

$$\sigma \approx 4 \times 10^{-26}\,(A)^{2/3}\mathrm{cm}^2 \tag{3.6}$$

and the mean free path, often called the *hadronic interaction length* can be shown to be

$$\lambda \approx \frac{A^{1/3}}{\rho} 35\ \mathrm{g/cm}^2$$

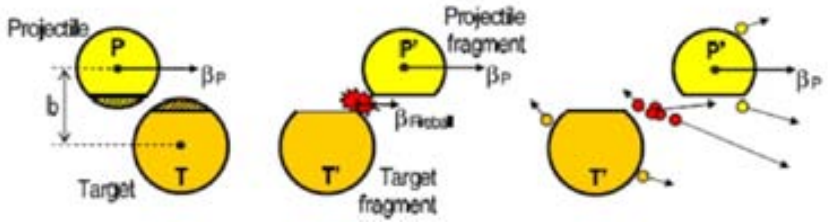

Figure 3.4: An illustration of the collisions of an incident particle with a nucleus of the target material as described by the abrasion-ablation model.

The expression given in equation 3.6 is correct only at high energies, above 1 GeV. At this energy hadrons will on average undergo a nuclear reaction after traveling a distance equal to the hadronic interaction length which is in the range of 10-100 cm in solids. At much lower energies, the actual cross section deviates from the one given above due to quantum mechanical effects. At very low energies below a few hundred keV, the electrostatic repulsion between the incident particle and the nucleus strongly suppresses any nuclear interactions.

In a nuclear interaction, both the incident particle and the target nucleus can be broken up into lighter particles or fragments. A general model which describes the fragmentation process is the abrasion-ablation model, illustrated schematically in figure 3.4. The model applies to peripheral collisions which account for nearly 90% of all nuclear events. In the abrasion-ablation model, the target and projectile nuclei overlap during collision and a fireball is formed on a time scale of 10^{-23} seconds. The excited fireball as well as the nuclei de-excite by emitting nucleons in a process known as evaporation until the energy has fallen below the nucleon barrier potential. This process can take up to 10^{-16} seconds to complete. The emitted nucleons, or fragments, are mainly peaked in the direction of the projectile and can be isotopes of the projectile or target nuclei as well as lower Z ions.

Because heavier elements contain an excess of neutrons as compared with lighter elements, nuclear interactions often lead to the production of a large number of secondary neutrons. A proton of 1 GeV, for example, will on average produce about 25 neutrons in a lead target. Neutron production in this way is referred to as spallation.

3.2 Photons

Photons interact with matter only through electromagnetic processes but, in contrast to charged particles, the interaction occurs as a single spontaneous localized event where the photon is either completely absorbed or re-emitted after depositing some of its energy. Because the interaction is entirely prob-

abilistic, the intensity of a beam of photons passing through a medium of thickness X can be stated simply as

$$I = I_0 e^{-\sigma N X} \tag{3.7}$$

where N is the number density of atoms in the medium and the cross-section, σ, is a measure of the probability of interaction in the medium. The cross-section, whose value depends on both the energy of the photon and specific material, is the sum of the probabilities for several competing processes: photoelectric effect, Compton scattering, and pair-production.

At photon energies in the range of the atomic binding energies of atoms in the medium, the photoelectric effect dominates. Photons in this energy range are often called *soft X-rays*. In the photoelectric effect, the photon, having initial energy E_γ, is entirely absorbed by an electron from an atomic shell of the medium. The electron, now called a photo-electron, is ejected from the atomic shell with kinetic energy E_a, the difference between the photon energy and the binding energy of the shell. The ion successively de-excites by either fluorescence of a photon, having energy E_j, or by the release of an "Auger electron" having kinetic energy E_j. The florescence photon can often leave the detector volume without interacting further and so only the net energy $E_\gamma - E_j$ is deposited in the detector. The probability for fluorescence to occur, expressed as the fluorescence yield, increases with atomic number Z as shown in figure 3.5 [20]. In Argon gas, it occurs only 15% of the time (as compared with roughly 90% in Xenon) and gives rise to an *escape peak* in the deposited energy distribution of events in the detector as we shall see later. Otherwise, the Auger electron, which is released almost immediately upon ionization, is indistinguishable from the photo-electron and the total energy, E_γ, is transferred into the medium.

As the energy of the photon increases, the probability for interaction decreases rapidly. There is a tendency for the photon to liberate electrons held in deeper shells with higher binding energy and this gives rise to a series of characteristic edges visible in a plot of the photoelectric cross-section (see figure 3.6).

At energies above the highest atomic energy level of the medium, (so-called hard X-rays), the photon tends to interact through Compton scattering, a process in which the incident photon, having initial energy $h\nu$, imparts only a portion of its energy to an atomic electron in the medium. The photon, scattered at an angle of θ, continues with a new energy $h\nu'$ such that

$$\frac{1}{h\nu'} - \frac{1}{h\nu} = \frac{1}{mc^2}(1 - cos\theta). \tag{3.8}$$

The energy transferred to the atomic electron, $E_T \equiv h\nu - h\nu'$, can assume any value down to 0 as $\theta \to 0$ and is at a maximum when the scattering

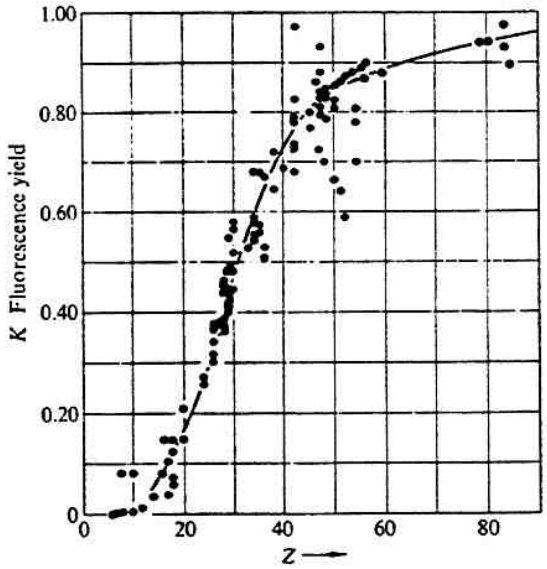

Figure 3.5: The fluorescence yield for different atoms as a function of atomic number [20].

angle is $\theta = 180°$. We can write the maximum transferable energy for the Compton process as

$$E_{T(max)} = h\nu \frac{2h\nu}{mc^2 + 2h\nu}. \tag{3.9}$$

This maximum appears in the spectrum of energy deposited in the medium, if Compton scattering is present, and gives rise to a continuous spectrum leading up to an edge characteristically lower than the observed or expected position of the photo peak.

At energies above 1.02 MeV, equivalent to two electron rest masses, the photon (or gamma ray) interacting with a nucleus can create an electron-positron pair. This process is known as "pair production". Other pairs such as a muon and anti-muon, or a tau and an anti-tau can also be created provided the photon has an energy greater than the total rest mass energies of the pair. In all cases, the energy and momentum is conserved such that the net kinetic energy imparted to the pair increases with the photon energy.

The product σN for lead, which includes the separate contribution of all 3 of the processes discussed above, is shown in figure 3.6 where the thickness X must be applied in g/cm^2.

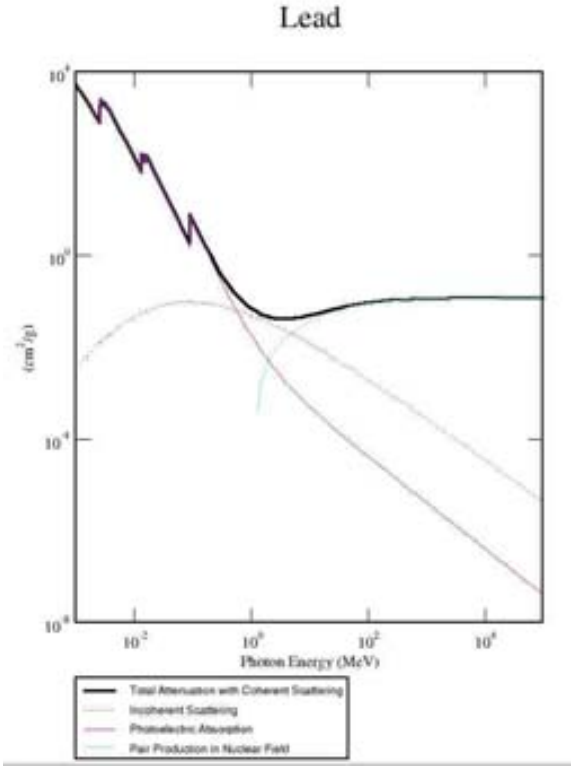

Figure 3.6: The product $N\sigma$ (measured in cm^2/g) for photons in lead [17].

3.3 Neutrons

Neutrons have no electric charge and are therefore not subject to interactions arising from the electromagnetic force. A neutron will penetrate into matter until it undergoes a nuclear reaction due to the strong force. There are three regimes of neutron energy that lead to rather different behavior. It is customary to speak of high-energy neutrons, fast neutrons and slow neutrons depending on their energy.

For high-energy neutrons having energies larger than 1 GeV, the nuclear cross-section behaves in a similar way to that of high-energy protons and the mean free path is of the order of the hadronic interaction length.

Fast neutrons, having energies between 100 keV and 10 MeV, are produced in abundance in nuclear reactors. At these energies, the neutron-nucleus cross section is very different and shows a strong energy dependence as well as pronounced resonances at certain energies which can be orders of magnitude larger than at slightly higher or lower energies.

Fast neutrons typically lose their energy by elastic scattering off the target nuclei until their energy is equal to the thermal energy of the surrounding matter, or $\frac{3}{2}kT$. Other possible interactions are inelastic scattering and neutron capture where the excited nucleus decays either by gamma emission, fission, or by the emission of a charged particle.

Slow neutrons, having an energy less than 0.5 eV, interact either by elastic scattering or neutron capture. They also will lose their energy until matching the thermal energy. For several isotopes, including ^{235}U and ^{239}Pl, the capture cross-section is inversely proportional to the speed of the neutron, because of its wave nature, and becomes very large for thermal neutrons.

Chapter 4

Detectors and Instrumentation

When a particle interacts in a medium, energy is deposited in a variety of forms. In all interactions of energetic particles, the actual energy deposition is miniscule; were it purely converted to heat, the rise in temperature in even a tiny bulk material is practically undetectable. Fortunately for the experimental physicist, other effects are more interesting. In fact, in many materials the energy deposition gives rise to the creation of charges or light which can be extracted in ways which will shall see, allowing the quanta of the energy deposition to be detected. In the field of detector instrumentation in particle physics, the aim is not only to localize the position of the interaction, but also to measure precisely the energy that was deposited. In this way, information about the original particle can be extracted, allowing the deduction of parameters such as its species, energy, direction of incidence, etc. In practice, designing detectors requires an understanding of exactly what is expected to be measured since, as we've seen, particles interact very differently depending on their properties. In this chapter, I summarize the working principles of the different types of detectors: scintillators, photo detectors, and gas detectors, all of which are used in the designs presented in subsequent chapters.

4.1 Gas Detectors

In gaseous mediums, charged particles are most likely to interact via Coulomb interactions leading to ionization or excitation of the gas atoms along the path of the traversing particle. Ionizations result in the creation of electron-ion pairs which provide a signature of the particle's trajectory and form the basis of electronic detection. Photons passing through a gaseous medium on the other hand interact via the photoelectric or Compton process where a single energetic electron is produced which, in turn, produces atomic ioniza-

Gas	Z	ρ (g/cm^3)	I_0 (eV)	W_i (eV)	$(dE/dx)_{min}$ (MeV cm^2/g)
H_2	2	8.38 x 10^{-5}	15.4	37	4.03
He	2	1.66 x 10^{-4}	24.6	41	1.94
Ne	10	8.39 x 10^{-4}	21.6	36	1.68
Ar	18	1.66 x 10^{-3}	15.8	26	1.47
Kr	36	3.49 x 10^{-3}	14.0	24	1.32
Xe	54	5.49 x 10^{-3}	12.1	22	1.23
CO_2	22	1.86 x 10^{-3}	13.7	33	1.62
CH_4	10	6.70 x 10^{-4}	13.1	28	2.21
C_4H_{10}	34	2.42 x 10^{-3}	10.8	23	1.86

Table 4.1: Properties of various gases common to gas detectors.

tions and excitations. In either case, the energy deposited by the interaction liberates electrons with sufficient kinetic energies to ionize further atoms or molecules of the gas volume in a series of successive secondary interactions.

Although the initial ionization electron can assume a variety of kinetic energies depending on the nature of the interaction and even though the primary and secondary interactions are of a statistical nature, the total number of electron-ion pairs produced, called the total ionization, can be calculated to a good approximation as simply

$$n_T = \frac{\Delta E}{W_i} \tag{4.1}$$

where ΔE is the total energy deposited and W_i is the effective energy needed to produce one pair. The relationship is convenient and provides a good estimation for most interactions assuming one takes care to account for any possibilities of secondary particles escaping from the detection volume, such as fluorescence X-rays or delta rays.

Values of the ionization energy, I_0, range between about 10 eV and 20 eV for most gases. The value of W_i, however, is typically about two times larger than the ionization energy. This arises because the energy given to an electron is usually much larger than what is needed to ionize the gas and part of its kinetic energy will be dissipated as heat. Values for W_i have been obtained experimentally and a summary for several gases is given in table 4.1 along with values of the density, ρ, ionization energy, I_0, and stopping power $(dE/dx)_{min}$ for MIPs at atmospheric temperature and pressure.

4.1.1 Charge transport in gases

Once in thermal equilibrium with the surrounding gas molecules, the electron-ion pairs are subject to diffusion which, in the absence of an electric field, will eventually lead to attachment of the electrons with the gas molecules,

charge transfer of the ions to other atoms in the gas, or the recombination of ions and electrons either in the gas medium or on the walls of the detector. If the number of created ion pairs per mm^3 is small, recombination can be easily suppressed in gas detectors in the presence of electric fields which separate the electrons and ions and drift them towards electrodes for charge detection.

In the presence of an electric field the electron-ion pairs are accelerated towards the electrodes and will undergo elastic collisions with the surrounding gas molecules. These elastic collisions effectively prevent the charges to accelerate freely and the effect is that macroscopically the charges appear to move at a constant velocity through the gas, though subject to diffusion. The speed at which they move in the direction of the field, which depends strongly on the field strength, is called the drift velocity.

The cross section for collisions between the ions and gas molecules is independent of the kinetic energy of the ion. This occurs because for the range of electric fields applied in gas detectors, the drift velocity of the ions is always much smaller than the thermal velocity of the gas and as such, the average time between collisions is roughly constant and depends only on the thermal motion of the molecules. The ions then, able to accelerate only briefly between the collisions, move with a drift velocity, w^+, which increases roughly linearly with the applied field, written as

$$w^+ = \mu^+ E \tag{4.2}$$

where the ion mobility, μ^+, depends on the type of ion and surrounding gas composition and is typically on the order of 1 cm^2 V^{-1} s^{-1} in mixtures used in gas detectors. For example, for argon ions traveling through argon gas in a field of 1 kV/cm, the drift velocity is about 15 m/s or 1.5 cm/ms.

During transport, collisions of the drifting ions can result in the transfer of their charge to other gas atoms or molecules having a lower ionization potential. In argon mixtures containing even only a few percent of molecular gases like isobutane or methyl gas, the charge transfer process is highly efficient and all drifting argon ions are quickly replaced by ions of the gas species having the lower ionization potential. This is an important effect that we will discuss later.

Electrons experience a non-linear response of the drift velocity w^- to the applied electric field. The reason is that, in contrast to ions, the electron cross section for collisions on gas molecules is strongly dependent on their kinetic energy. Despite a complex relationship, a simplified one can be written as

$$w_- = \frac{e}{2m} E * \tau(E) \tag{4.3}$$

where $\tau(E)$ is the mean time between collisions, also a function of the electric field. The value of τ is also highly sensitive to the gas composition

Gas	h	t (s)
CO_2	6.2 x 10^{-9}	0.71 x 10^{-3}
O_2	2.5 x 10^{-5}	1.9 x 10^{-7}
H_2O	2.5 x 10^{-5}	1.4 x 10^{-7}
Cl	4.8 x 10^{-4}	4.7 x 10^{-9}

Table 4.2: Coefficient and average time for electron attachment in various gases.

such that small additions of other gases can dramatically change the electron drift velocity. Because the cross section of electrons on gas molecules is also much smaller than for ions, the electron drift velocity is much larger, on the order of a few cm/μs in an electric field of 1 kV/cm.

During transport, the electrons can become attached to molecules in the gas. If the time scale of the attachment process is low enough, then the electrons are soon replaced by negative ions in the gas mixture. The time scale for electron attachment to all noble gases and hydrogen is negligible. It is important for other gases such as CO_2, O_2 and H_2O and in general depends on the electric field applied.

Argon gas is the most common choice as a primary constituent in gas detectors: it is inexpensive, has a fairly high cross-section for interaction, and suffers no loss of electrons from attachment during charge transport. The non-zero attachment coefficient h for gas molecules common in the atmosphere explains why impurities, introduced by leaks in the detector chamber, should be avoided. Table 4.2 summarizes the important parameters for the attachment process is given for several gases.

4.1.2 Electron collection and multiplication

Above a certain value of electric field, the force of recombination is overcome and the electrons are separated from their ion pairs and drifted towards the anode. If the gases are chosen correctly and the chamber is designed to be tight, the loss of electrons by attachment can be kept to a negligible level and all the electrons will be collected on the anode. This allows for a precise measurement of the total ionization in the gas volume which is also a measure of the energy deposited by the initial radiation. Detectors which operate in this way are called *ionization chambers* and are useful for detecting heavily ionizing radiation such as alpha particles. They are also used in applications for detecting radiation which is not heavily ionizing, provided the flux of radiation is sufficiently large. For a constant radiation field this leads to an effectively steady rate of charges created which can be measured as a constant current on the electrodes.

In most single particle interactions, however, the total number of pri-

mary charge pairs produced or the total ionization in the gas is several orders of magnitude too small for detection by charge or current-sensitive preamplifiers connected to the electrodes in the detector. Fortunately, nature provides a mechanism for the amplification of the electrons through a process known as electron avalanche. Since electrons have a mass much lower than that of the ions, in the presence of a strong electric field they can achieve enough energy by acceleration along the mean free path between collisions to create processes other than thermal elastic collisions. Once the electron's energy is higher than the ionization potential of the gas, collision can result in ionization and the creation of a new electron-ion pair. The newly created electron, in turn accelerated by the electric field, can repeat the process of ionization in a repeating cascade known as avalanche multiplication. The process is most generally described using the first Townsend coefficient, α, defined as the number of electrons produced in the path of a single electron having traveled 1 cm in the direction of the field [21] such that the effective gain produced by n primaries over a distance of x is

$$G = e^{\alpha d} \tag{4.4}$$

where d is the thickness of the gas gap. Although the drift velocity of the electrons follows a complex behavior, the multiplicity of the avalanche process can be tuned by a careful adjustment of the electric field and the right selection of the gas mixture. In this way over a range of the applied field the avalanche multiplication factor, or gain G, can be made constant to a good degree independent of the number of primaries and their path of arrival under the influence of diffusion. In this condition the collected charge after amplification is *proportional* to the primary charge deposited in the detector from the ionizing radiation and again a measurement of the collected charge will allow a measurement of the deposited energy by the radiation. Detectors which operate on this principle are called gas *proportional chambers.*

Some important effects which arise during electron avalanche must be noted. De-excitation photons can also be released in the avalanche and can lead to further charge-pair creation. In a gas detector consisting of a pure noble gas, the onset of an electron avalanche will tend to continue unregulated until the entire chamber is effectively ionized from the production and re-absorption of such photons. While pure noble gases are only either excited or ionized, other gases, particularly polyatomic ones, can also be excited into higher rotational or vibrational modes do so by the absorption of the photons produced in the avalanche. The addition of such a gas, also known as a *quencher*, has the effect of limiting the avalanche process before it races out of control by absorbing the photons produced. Polyatomic gases also have an additional quenching effect important to chambers operating in avalanche mode. When a drifting ion reaches the cathode to recombine with an electron, energy is released which can often take the form of an

emission of an electron from the metal surface. Since the electron will in turn drift and experience amplification, the chamber will be caught in an avalanche feedback loop. Polyatomic ions, however, usually dissociate with the energy released upon neutralization instead of provoking an electron to be released from the cathode. If the polyatomic gas has also a lower ionization potential than the primary gas constituent, then all ions arriving on the cathode will be of the polyatomic species effectively preventing any subsequent avalanche.

At very high values of the electric field and in regions of high field gradient, space charge effects from the large number of electron-ion pairs created in the avalanche can distort the local field reducing the amplification factor. Observed is a kind of saturation of the total amount of charge collected on the anode and operation in this region is useful for simple pulse counting but not for energy measurements. Working on this principle is the Geiger-Muller tube, invented by Hans Geiger in 1908 and improved by the help of Walter Muller in 1928 who added alcohol vapor to the gas mixture which acts as an effective quencher.

At extreme fields, especially in the absence of a quencher, the massive build-up of charge carriers localized in a single region effectively adds further to the multiplication process. The avalanche extremities grow in size and extend themselves towards the anode and cathode to form a type of plasma known as a *streamer*. If the streamer grows to touch both the anode and cathode, a current can flow along the conductive plasma channel of the streamer resulting in a short-circuit between the anode and the cathode. This is called a discharge or breakdown and is usually destructive to the detector and electronics. The limit of the gas gain before breakdown and discharge is known as the *Raether limit* and occurs when

$$\alpha d \sim 20 \tag{4.5}$$

where x is the gap distance and α is the inverse of the mean free path for ionization or the first Townsend coefficient presented earlier. Because the electrons in the avalanche have a distribution of energies and because it takes only a few electrons to create breakdown, the Raether limit can be surpassed even at gains of only 10^6 and this sets a practical upper limit on the maximum achievable gain in gas detectors.

Figure 4.1 illustrates the different principles of charge collection and amplification that we have discussed so far. It gives the number of electron-ion pairs collected as a function of the applied voltage for a typical wire cylinder gas detector which makes use of the electron avalanche mechanism. At the left of the curve, when the voltage is zero, the charges quickly recombine and are not collected. At low voltages, in the ionization region, the recombination of the primary charge is overcome and the gain is 1, all ion pairs produced in the gas volume are collected on the electrodes without amplifica-

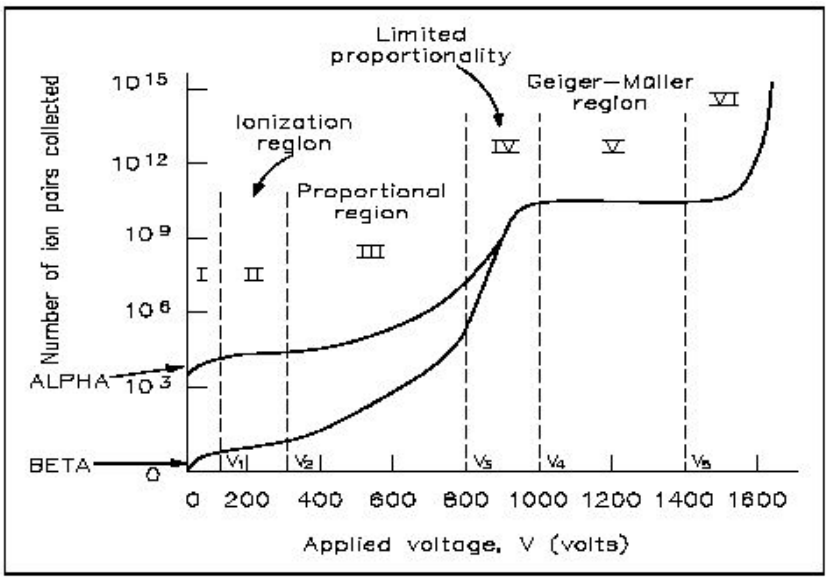

Figure 4.1: Number of electron-ion pairs collected on the electrodes of a typical gas detector as a function of the applied voltage.

tion. At higher voltages, avalanches begin to occur resulting in amplification of the ion pairs with a gain which is independent of the primary ionization. This is the region of proportionality in which most modern detectors for particle physics instrumentation operate. As the voltage increases and the number of ion pairs in the avalanche grows, space charge effects eventually limit the avalanche, and the amplification is no longer proportional. At higher voltages still, space charge effects result in full saturation of the number of ion pairs in the avalanche regardless of the primary ionization. This is the Geiger-Muller region. Resistive Plate Chambers, for example, operate either in the region of limited proportionality or the Geiger-Muller region. At very high voltages, streamers begin to form and breakdown will occur.

4.1.3 Proportional chambers

Gas Proportional Chambers are gaseous detectors operating such that the total number of charge pairs produced in avalanche and collected in the anode is proportional to the total ionization by a constant factor G. Since modern detectors require finely segmented anodes and the charge is shared over several electrodes, the gain must also be constant for all electrodes, regardless of where the radiation interacted in the gas volume. To do this, the amplification zone is typically separated from the interaction volume whose job is only to drift the charges towards the readout. The amplification

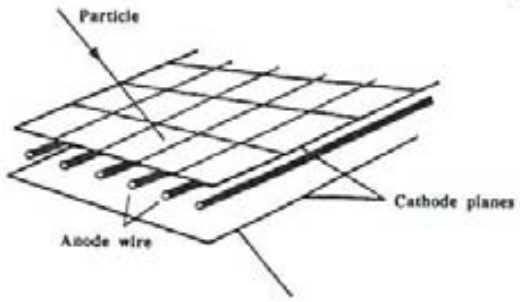

Figure 4.2: A schematic representation of a proportional wire chamber.

is confined to a region very close to the readout plane such that incoming electrons only have a short distance over which to multiply before being promptly collected.

The concept of the Multiwire Proportional Chamber, shown schematically in figure 4.2 and invented by Georges Charpak in 1968, makes use of narrow conductive anode wires, regularly spaced and often in orthogonal axes, which form the segmented anode plane and yield the position information [22]. Operating in the proportional region, the avalanche multiplication occurs very near the surface of the wires, whose diameters range in the tens of microns, where the electric field increases rapidly as $1/r$. This results in a fast-rising signal induced in the wire and a limited region for avalanche that all electrons drifting through the detector volume experience equally. The wires are held under tension and evenly spaced apart in a plane separated from the drift anode in order to provide a uniform field configuration. Charpak eventually received the Nobel prize in 1992 for his invention and wire chambers, forty years later, are still used extensively in high-energy physics and industrial X-ray scanning systems.

4.1.4 Modern micro-Pattern gas detectors

Since the invention of the Multiwire Proportional Chamber (MWPC), there has been a great deal of interest in the field of gaseous detectors and much of the knowledge concerning gas detector operation that we have for a variety of different gases is owed to research following its conception. Some years later, a new design for a proportional gas chamber was introduced by A. Oed called the Micro-strip Gas Chamber or MSGC [23]. It has a similar structure to the MWPC, only instead of wires, two sets of anode and cathode strips, produced on a layer of glass substrate, provide the amplification of charge in a region of high electric field gradient focused near the edges of the strips. Though research on the device was soon abandoned because of problems with discharges, the invention is invaluable as an ex-

ample of applying an old concept using modern technology. The idea to replace the floating wires, prone to mechanical distortions when under voltage and time-consuming to mount mechanically, with strips patterned onto a rigid substrate was the beginning of a new approach, to proportional gas detector design. The lessons learned from trials of the MSGC eventually paved the way for an entire new class of detectors now known collectively as Micro-Pattern Gas Detectors (MPGDs). It was demonstrated that by using photo-lithographic technologies, one could create uniform layers of conductive strips in virtually any desired shape and size on a rigid substrate making the components robust and easy to handle and mount into useful detector assemblies. Furthermore, in a important conceptual development by Yanis Giomataris, came the idea to separate the amplification mechanism from the segmented readout plane. A perforated electrode, held precisely by a patterned insulating layer only several hundreds of microns from the readout plane, could effectively pull electrons from the drift region into a contained region of high electric field for amplification and collection. The MICROMEGAS (MICRO-MEsh GAs Structure) detector makes use of this idea in which a thin metallic foil or mesh, highly perforated by a matrix of holes, is held at a precise distance above a segmented readout plane by insulating spacers whereby a high electric field is created in the gap between mesh and readout such that electrons drifting towards the mesh in the interaction volume are steered through the mesh, amplified and detected on the readout plane [24]. Ions produced in the avalanche process are also mostly absorbed on the mesh due to their low mobility and the result is a faster signal than that of MWPCs. Also, the high-density perforation of the mesh, made possible by the high resolution of photo-lithographic techniques, results in a very uniform amplification over the surface of the detector and thus a high energy resolution. A schematic representation of a MICROMEGAS gas detector is shown in figure 4.3. The spacing between readout and mesh is kept small to limit the avalanche length, typically on the order of hundreds of microns. The beauty of the MICROMEGAS idea is that it allows the production of the mesh to be completely separate from the readout board which can be made of strips or pads in any desired geometry. A schematic drawing of several types of readout board, showing the method for interconnecting the strips or pads in one, two, three axes, or in a pixel matrix, is shown in figure 4.4.

Still, single gap detectors, such as the MICROMEGAS described above, suffer one important drawback: since the amplification occurs in a single stage gap between the mesh and readout, in the unfortunate event of a discharge, all of the charge will be absorbed entirely by the readout anodes as the electrodes release their stored energy upon short-circuiting. The resultant current surge in the input of the preamplifier, many orders of magnitude larger than signals of interest, can be fatal to the electronics. Furthermore, the discharge is also harmful to the thin copper surface of the readout strip

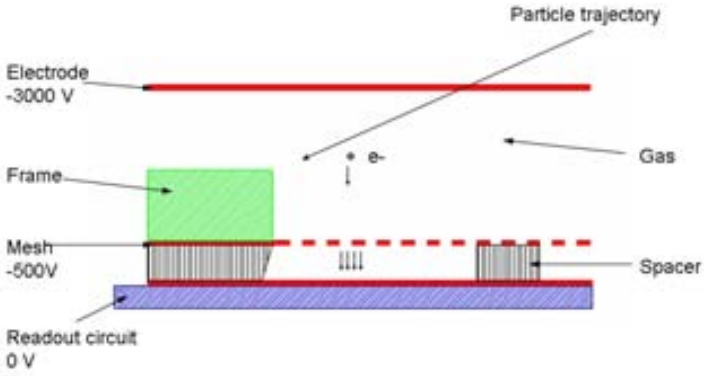

Figure 4.3: A schematic drawing showing a MICROMEGAS gas detector in operation and typical biasing values. The mesh is usually held around 150 μm from the anode plane resulting in a high electric field which causes the avalanche multiplication.

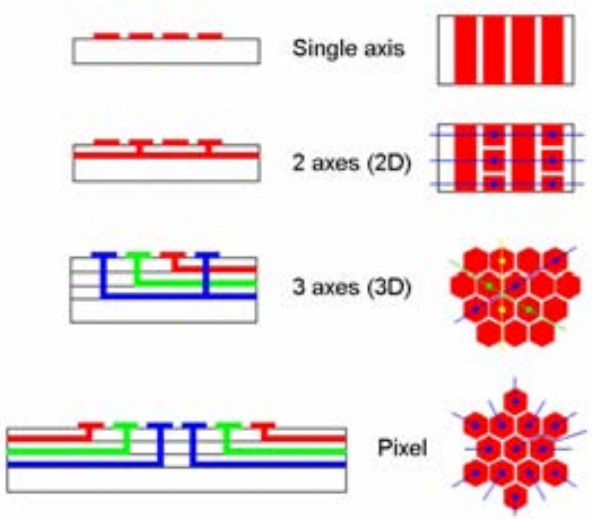

Figure 4.4: A schematic drawing of various possible readout designs for MPGDs.

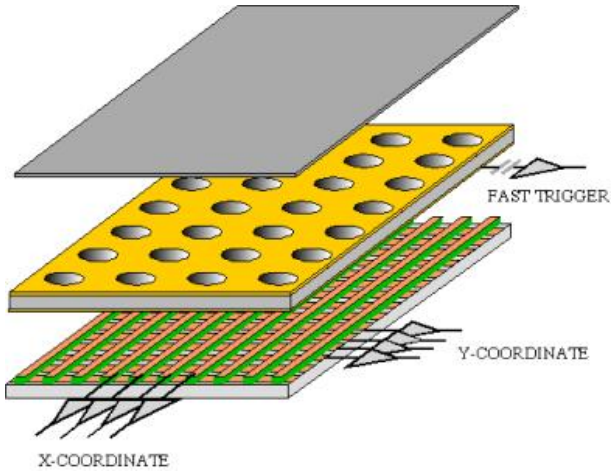

Figure 4.5: Schematic drawing showing a single Gas Electron Multiplier (GEM) gas detector configuration.

or pad. In a clever idea proposed by Fabio Sauli, the region of high electric field needed for amplification is confined to an independent element which can be positioned away from the readout on the order of a few mm. The amplifying element, named the Gas Electron Multiplier (GEM) [25], comprises two electrode layers on two sides of an insulating foil, perforated by a high density of micro-holes (70 μm diameter) spaced apart at regular intervals (140 μm). When a voltage is applied across the electrodes a high electric-field is produced in the holes which provides the avalanche multiplication. A moderate field between the underside of the GEM and readout, also called an extraction field, is used to extract the electrons amplified by the GEM and to transfer them towards the readout. In correct operation, discharges should occur only between the GEM electrodes where a portion of the total charge is absorbed by the GEM itself [26]. A schematic representation of a GEM mounted in a gas detector assembly is shown in figure 4.5.

A GEM can be thought of as a kind of matrix of electrostatic micro-lenses which focuses the ionization charge inside the holes. The electric-field configuration inside a single GEM hole is shown in figure 4.6. Incoming electrons will follow the field lines into the region of high-electric field and be amplified independent of their initial distribution in the drift volume, a necessary condition for good energy resolution. Because the profile of the hole - and thus the field configuration - is spherically symmetrical, electrons are spread out as they exit the GEM structure in much the same way as they come in, preserving the spatial signature of the primary ionization.

The large distance between the bottom of the GEM and the readout plane results in greater diffusion of the exiting charge cluster as it drifts through the extraction gap towards the readout. A wider spatial distribution

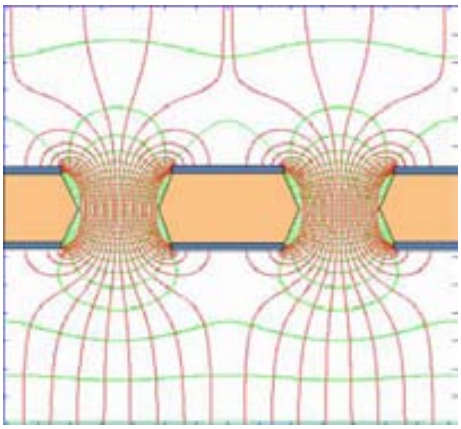

Figure 4.6: The electric field at the center of the hole of the Gas Electron Multiplier. Simulated with Garfield.

of charge is beneficial both for the life of the detector elements and the electronics since the entire charge in discharge is not focused onto few anode strips as in the MICROMEGAS or the MWPC. Although it seems that this added diffusion would result in a poorer spatial resolution, it actually improves it in certain geometries when a center-of-mass algorithm is used to locate the center of the charge shared over many strips or pads. In large area applications where the number of electronic channels must be limited for financial reasons, detectors based on GEMs using relatively large anode dimensions still yield highly accurate position reconstructions. In one application using square anode pads of 2 mm, resolutions of 100 μm have been achieved [28].

As the GEM foil itself is self-supporting and only serves to amplify the charge, there is no restriction for stacking GEMs to increase the amplification. Of course, the maximum effective gain is not limitless and the addition of each GEM increases the diffusion of the charge leading to an eventual loss of position resolution. Still, the use of multiple GEM foils allows operation at voltages less prone to discharges since the work of amplification is shared between each of the GEM structures. Each GEM operates at a lower gain and the total effective gain is just the product of each contribution. Triple-GEM structures, shown schematically in figure 4.7, are widely used in current HEP applications because of their very low discharge probabilities and high achievable gain (up to 2 x 10^5 in Ar:CO_2 gas mixtures) [29].

Multistage detectors, such as the triple-GEM, also have a further advantage over other gas detectors using a single amplification stage. Because the mobility of ions is much lower than electrons, ions produced in each stage of amplification and moving towards the drift cathode are largely absorbed on the bottom layer of the upper GEMs and thus do not feedback into the drift region. This is important for achieving high spatial resolution since

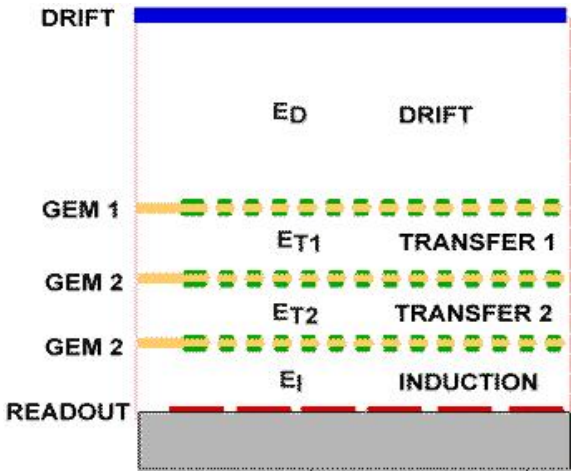

Figure 4.7: Schematic drawing of a triple-GEM detector.

ions in the drift volume effectively modify the field configuration leading to distortions of the drifting ionization. This is especially critical for Time Projection Chambers (TPCs) which use very large drift distances (up to several meters) and precise timing information in order to reconstruct the third dimension of the ionization event; even small field distortions can lead to large errors in the position reconstruction and thus ion feedback must be kept to a minimum. Triple-GEM detectors used in a standard configuration have typically 2% effective ion feedback, defined as the ratio of ions collected on the drift cathode to the electrons collected on the readout anode plane. A recent work describes the use of the uppermost GEM foil as a gate to block the ions which could reduce the value significantly to only 10^{-4} [30].

4.1.5 Resistive Plate Chambers

Another type of gas detector which uses gas amplification, yet not in proportional mode, is the Resistive Plate Chamber (RPC), developed during the 80's by R. Santonico and R. Cardarelli [31, 32]. RPCs are parallel plate chambers (two electrodes or plates separated by a narrow gas-filled gap) in which at least one of the electrodes is made of highly resistive material (between 10^{10}-10^{12} Ω.cm). A large voltage is applied across the plates by means of a resistive coating applied to the electrodes (such as graphite). This generates an electric field of typically about 10-100 kV/cm, and primary ionizations in the gas lead to the creation of large avalanches. On the outside of the chamber, strip electrodes or readout pads, insulated from the high-voltage, collect the induced signal produced by the avalanche within the gap. Figure 4.8 shows a schematic diagram of a simple RPC detector.

RPCs exploit the principle of avalanche multiplication, yet unlike proportional chambers, they operate either in the limited proportionality or

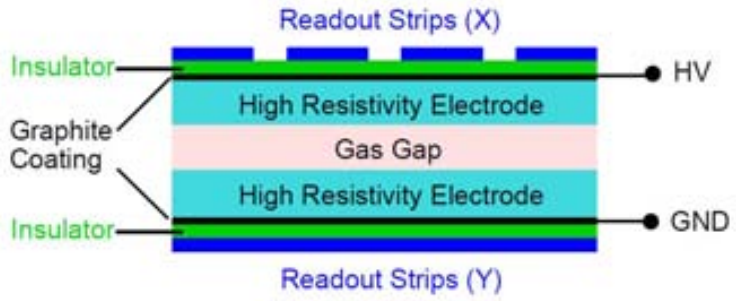

Figure 4.8: Schematic diagram of an RPC chamber [33].

Geiger regime, both of which occur at high fields near the limit of saturation and the onset of streamers. For this reason RPCs have a very poor energy resolution, one limitation to their use. On the other hand, this operation leads to the induction of large signals which puts a lower demand on the sensitivity of the readout electronics as compared with what is needed for gas proportional counters.

The use of resistive electrodes is characteristic of RPCs in contrast to simple parallel plate chambers having conductive electrodes. While parallel plate counters can be used only to detector the passage of a charged particle anywhere between the conductive plates, RPCs allow the localization of the signal since the induced signals created by avalanches are transparent to the high-resistivity electrodes. The high-resistivity electrodes also serve to limit the charge that can be released upon streamer formation and breakdown, which in the case of conductive electrodes, is the entire energy stored capacitively between them. When a breakdown occurs in an RPC, only the charge stored in a small localized region ($\sim$0.1 cm^2) of the resistive bulk of the electrode is available. Since current can pass only slowly through the resistive electrodes (slowly as compared with the short timescale of the avalanche), the electric field in the gas-gap at that location drops as the charges from the avalanche are accumulated, effectively suppressing the current that would otherwise be supplied and minimizing the size of the discharge.

This operation principle has a direct impact on the rate (measured in kHz/cm^2) that can be achieved. Because the electric field drops locally on the electrodes where the charge is accumulated, further avalanches cannot occur until the charges have dissipated through the resistive bulk. This "relaxation" time depends directly on the bulk resistivity of the electrodes though it only affects a region localized about the avalanche, leaving the rest of the detector's active area sensitive detection.

Typical electrode materials for RPCs are float glass, ceramic, or a high-resistivity phenolic resin known as Bakelite. Their properties relevant to RPC design are given in table 4.3. Glass and Bakelite are the cheapest and

Material	Bulk resistivity	Rate
	(Ω.cm)	(kHz/cm^2)
Bakelite	10^{10}-10^{11}	1-10
Glass	10^{12}	< 1
Ceramic	10^9	100

Table 4.3: Properties of common RPC electrode materials.

most common materials in RPC design but allow only modest rates of <1 kHz/cm^2 and 1-10 kHz/cm^2, respectively when operated in streamer mode. Ceramic is more expensive, but can be used for high-rate applications up to 100 kHz/cm^2 because its lower resistivity.

Because they use a narrow gap and work close to Geiger mode, signal formation in RPCs occurs on a very short timescale ($\sim$1 ns), making them attractive for timing applications of charged particles. 1 ns time resolutions are routinely achieved with 2 mm gap RPCs, while resolutions as low as 50 ps are typical of RPCs with narrow gaps of 200-300 μm. The achievable timing resolution depends mainly on the gas-gap thickness but also on the gas mixture. The most common gas used as main component is tetrafluoroethane (TFE), $C_2F_4H_2$, a gas with a high electron affinity which absorbs many of the electrons in the avalanche. This allows higher electric fields to be applied which increases the electron drift velocity and therefore the timing performance. Isobutane (C_4H_{10}) or CO_2 are commonly included as quencher gases to absorb photons and prevent the propagation of the discharge throughout the chamber.

Although the use of a narrow gas gap can improve the timing resolution significantly, it also reduces the detection efficiency since fewer primary charges are created by ionizations with the passage of a charged particle than in a thicker gap. To overcome this challenge, multi-plate Resistive Plate Chambers (MRPCs) were developed, originally in 1996 [34], in which several gas-electrode layers are stacked one on top of the other and readout together, increasing the effective gas thickness and therefore the size of the induced signal. MRPCs can typically achieve timing resolutions down to 50 ps with a detection efficiency of 99% [33]. Figure 4.9 shows a schematic drawing of an MRPC detector.

RPCs (and MRPCs) can be operated in either limited proportional (avalanche) mode or Geiger/streamer mode, depending on their application. For higher rate ($>$ 1 kHz/cm^2), streamers should be avoided since they result in a larger amount of accumulated charge (factor of 10) which requires more time to be dissipated in the electrode bulk. The addition of a small amount of SF_6, also with a high electron affinity, serves to limit the formation of streamers and is often added to the gas mixture for this reason. Operation in the region of limited proportionality rather than in saturation,

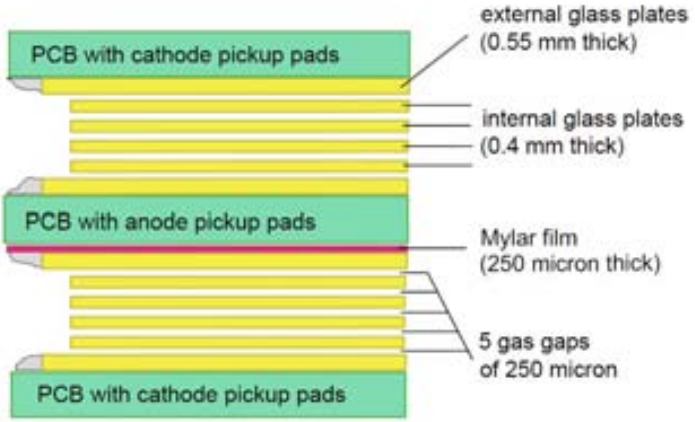

Figure 4.9: Schematic diagram of a multi-gap resistive plate chamber [33].

however, requires the use of more sensitive electronics.

MRPCs are very often chosen for particle tracking and time-of-flight (TOF) due to their excellent timing resolution, insensitive to magnetic fields, and because they are relatively cheap to produce in large surface areas as compared with other detector technologies. For this reason they have been widely used in physics experiments, especially when large surfaces must be covered. The ATLAS experiment, for example, makes use of 2 mm double-gap RPC module for muon triggering over a total surface of 3650 m^2 [35]. A 99% detection efficiency is reached in avalanche mode with a time resolution of 1 ns and up to a particle flux of several kHz/cm^2. The CMS experiment uses similar 2 mm double-gap RPCs and achieves similar efficiency and timing performances as in ATLAS [36]. The ALICE experiment uses multi-gap RPCs with 0.25 mm gas gaps and achieves over 99.5% detection efficiency with 50 ps time resolution [37].

4.2 Scintillators and photodetectors

Ionizing radiation produces free charges in the material that it crosses and most detection techniques work on the principle of the collection of these charges by an electrode where the charge can be extracted and measured. In a gas these charges are easily recuperated using a moderate electric field. In solid materials, the molecules become excited or ionized through interaction with ionizing radiation and collection of the charges is only possible in special materials such as silicon or germanium. In most other solid materials, the free charges are not easy to extract and become either trapped or recombine on a short timescale. However, in certain materials, the charges need not be collected. Instead, when the atoms or molecules excited by the

charges return to their ground state they often emit photons in the visible or near-visible range. This phenomenon is called scintillation, but for most transparent materials the signal is too weak to be exploited. In a few special materials the process is more efficient and these materials are known as scintillators. In a scintillator, it is sufficient that the charges liberated through ionization travel to the nearest luminescence center, which in a scintillator is normally only a few atoms away. Through the excitation of the luminescent molecule and its subsequent de-excitation, the energy of the free charges is converted into light and if the material is transparent at that wavelength, this light can be extracted for detection.

The word luminescence has the general definition of the emission of light by a substance not resulting from heat. The type we are describing is also referred to as radio-luminescence to distinguish it from fluorescence or phosphorescence which are both types of photo-luminescence, a process in which the excitation of the molecule occurs from absorption of light of a shorter wavelength rather than from radiation. Fluorescent materials, also called fluors, are nonetheless used in detector applications for altering the spectrum of light and for this reason fluors are routinely called wavelength shifters. Phosphorescence is photo-luminescence on a time scale of ms to hours. In such materials, called phosphors, the molecules after excitation can become trapped in an energy state which has an unfavorable de-excitation transition. Quantum mechanics allows these transitions to still occur but on timescales that make them impractical for fast detector applications. Phosphors are commonly known as "glow-in-the-dark" materials.

Returning then to luminescent materials for detector physics, we can say that a good scintillator should have the following properties:

- it should be transparent to the wavelength of the scintillation light
- its light production should be large
- its light emission should be as prompt as possible, without much delayed emission
- its light output should be proportional to the energy deposited (no saturation effect)
- its index of refraction should be close to 1.5 to allow the light to be easily extracted

Many types of materials exist which satisfy to varying degrees the requirements of a good scintillator listed above. We can group them into two types: organic and inorganic scintillators. The main difference between them is that organic scintillators are made of low Z materials and inorganic scintillators from high Z ones. For this reason, inorganic scintillators are preferred for X-ray and gamma detection, where the higher Z leads to a higher conversion

Table 4.4: Common properties of polyvinyl-toluene-based plastic scintillator.

Plastic type	Polyvinyl-toluene
Light output	8,000 - 14,000 photons / MeV
Decay time	1 - 5 ns
Emission wavelength	390 - 440 nm
Light attenuation length at 400nm	150 - 400 cm
Density	1.032 g / cm^3
Refractive index	1.58

efficiency. Inorganic scintillators, being of lower Z and less-dense materials, are not efficient in converting gammas but are widely used for detecting charged particles and, in some applications, neutrons with energies between 10 keV and 10 MeV.

4.2.1 Organic scintillators

Three types of organic scintillator exist: organic crystals, organic liquids, and plastic scintillators. Organic crystal scintillators are efficient but expensive compared with plastics and are thus not commonly used. Organic liquids are created by dissolving a solid organic scintillator in a solvent. They are the least expensive and find applications when large amounts of scintillator are required as in the case for radiocarbon dating of archaeological samples.

By far the most common organic scintillator is plastic scintillator. It is made from polymerizable liquids, such as styrene or vinyl-toluene. These materials scintillate in the UV but are also highly absorbing at that wavelength. A wavelength shifting material, or fluor, is typically added at a concentration of 1% in order to absorb the primary scintillation light and re-emit it at a longer wavelength in which the material is more transparent. Production of plastic scintillators is cheap in comparison to other types and fabrication in any desired shape is simple, owning to their popularity for a diverse number of applications; large thin plates and even flexible fibers are commonly used in physics experiments. Table 4.4 summarizes the main properties of the most commonly used plastic scintillator.

4.2.2 Inorganic scintillators

Inorganic scintillators are most commonly ionic crystals, doped with small amounts of impurities or activators. Some examples include the alkali metal halides such as NaI, CsI, and CsF, and also non-alkali halides such as, BaF_2, CaF_2, ZnS, $CaWO_4$, YAG, GSO, and LSO. Because of their density and composition, they are vastly more efficient in converting gamma rays than

organic scintillators but also more expensive to manufacture. Their light output is high, while the decay time of the light is longer than organics, on the order of 100 ns.

When ionizing radiation interacts in an ionic crystal an electron confined in the valence band can be liberated into the conduction band. Since it will generally be put in motion with a energy much larger than the band-gap energy, the primary electron can lift other electrons into the conduction band with a corresponding hole produced in the valence band. This continues until the electrons occupy the lower energy levels of the conduction band. The result is that an X-ray or gamma interaction in the crystal produces a large number of electron-hole pairs on a brief timescale (10^{-12} s). If this were the only effect, the crystal would not be transparent to its own scintillation light; the energy released by transitions of electrons from the conduction band to the valence band would be greater than the band-gap and thus promptly reabsorbed, until dissipated by mechanical energy, in the form of lattice vibrations. However, if luminescent centers are present which have localized energy levels lying within the band-gap of the base lattice, then transitions from these centers releases light which can propagate through the crystal.

The luminescent centers are introduced by doping ions of an impurity species at a few percent level into the crystal. Electrons created from the particle interaction can migrate through the conduction band and fall into the lower energy configurations of the luminescent centers. Cerium and thallium are the most common dopant materials mainly because they have energy levels with favorable transitions that occur on rapid timescales. The re-absorption of the light emitted from the impurity ions by the impurity ions themselves is avoided due to a mechanism known as the *Stokes shift*. The Stokes shift arises due to a relaxation of the lattice configuration immediately after excitation into a higher energy state. This causes the energy associated with the de-excitation to be smaller than that of the excitation resulting in a hysteresis of the energy transitions. The Stokes shift is the energy difference corresponding to this hysteresis and is what allows the crystal to be transparent to the light produced from the luminescence centers.

The timescale of the emission of light from the scintillator is determined by the lifetime of the excited level in the luminescent centers. For this reason, all inorganic scintillators using the same impurity species have similar decay times. Cerium doped scintillators, for example, have decay times of about 40 ns. The time structure of the light emitted from the scintillator follows a decaying exponential due to the rapid collection of charges by the luminescent centers, followed by their slower stochastic de-excitation. In practice, however, the timescale of the scintillation can be much longer than the decay time of the impurity species. This can occur because of imperfections in the crystal which can cause traps for either the electrons or holes. Before reaching the luminescent centers, the charges liberated from

Table 4.5: Properties of some commonly used inorganic scintillators.

Name	Density (g/cm^3)	Emission (nm)	Light yield (γ/MeV)	Decay time (ns)	Radiation length (cm)
NaI:Tl	3.67	410	41000	230	2.59
BGO	7.14	480	4000	300	1.12
CsI:Tl	4.5	565	66000	600	1.68
$PbWO_4$	8.28	480	200	10	0.89
GSO:Ce	6.7	440	8000	60	1.38

the initial interaction can fall into the trap. If the binding energy of the trap is small then the charges can be released due to thermal fluctuations on a timescale that depends strongly on temperature. If this timescale is much larger than the decay time of the crystal, then we will have two components in the time structure of the light yield. This occurs frequently in many kinds of inorganic scintillator and is an important consideration for choosing the right scintillator in critical timing applications.

Table 4.5 lists some of the most common inorganic scintillators and their corresponding properties.

4.2.3 Photodetectors

Scintillators would not be very useful as particle detectors if there were no way to detect the light they emit. In practice, scintillators are coupled to photodetectors which can be described as devices which convert visible light into an electrical signal. By far the most common type of photodetector is the photomultiplier tube (PMT), though recently other devices have been developed such as the multichannel plate (MCP) and silicon photo-multiplier (SiPM).

PMTs, originally developed over 70 years ago, all operate on roughly the same principle. A PMT consists of a photo-cathode and a series of metal dynodes all contained within a vacuum tube. A photo-cathode is a thin layer of a material which emits electrons when absorbing photons in the visible or near-UV range. A large negative voltage is then applied between the photo-cathode and the dynodes in a cascading configuration. A final metal electrode is held at ground for collecting the electrons and is referred to as the anode. The high voltage causes the electrons ejected from the photo-cathode to be accelerated toward the cascading dynode configuration. Under a sufficiently high voltage a single electron emitted from the photo-cathode can acquire enough energy to liberate electrons when striking the first dynode. This multiplication process can continue at each dynode stage. The final result is the collection of a large number of electrons on the anode which in modern PMTs is many orders of magnitude larger than the number of electrons emitted from the photo-cathode, typically 10^6 or more.

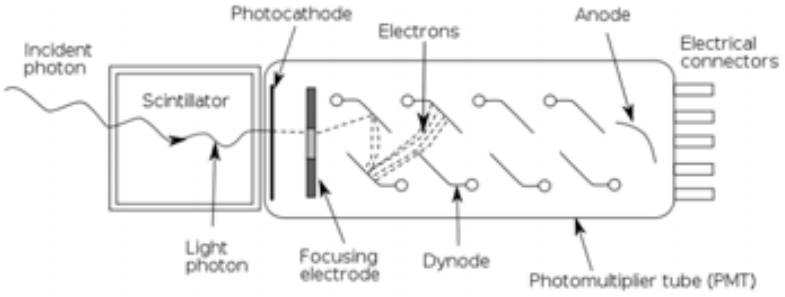

Figure 4.10: Schematic drawing of a scintillator-PMT assembly showing the various components of the PMT such as the photo-cathode, dynodes and anode.

A schematic drawing showing a scintillator and PMT assembly is shown in figure 4.10.

Several factors will affect the performance of the PMT. Obviously, the geometry of the dynodes must be optimized for the best collection of electrons produced at each previous stage and this is determined by the field geometry between the photo-cathode, dynodes, and the anode. Focusing electrodes are often used to guide the electrons produced on the photo-cathode towards the first anode. The yield of secondary electrons from each dynode also depends on the surface of the dynode and its composition. Some common dynode materials include beryllium oxide, magnesium oxide, and gallium phosphide.

In most PMTs, the transit time for an electron to travel from the cathode to the anode is around 20 ns. However, it is the variation in this transit time that is important in timing applications. This variation, known as the transit-time-spread (TTS), is caused by geometrical variations in the path that an electron can follow from the photo-cathode down to the anode and is typically on the order of several ns. Modern PMTs developed for precise timing applications have transit-time-spreads around 200-300 ps.

The choice of photo-cathode is also important in determining the PMT performance. For best results the quantum efficiency (QE) of the PMT's photo-cathode must be matched to the emission spectrum of the scintillator it is to be coupled to; the higher the quantum efficiency the better will be the final electrical signal output. Many materials display the photoelectric effect for UV photons, but the QE is usually very small. Certain semiconductor materials have a large QE for light in the visible range. A thin layer of about 10 μm of this material can be deposited on the inner surface of the PMT window. The best photo-cathodes are the bialkali which have a QE of around 20-30% at 400 nm. One drawback is that materials with a high QE also easily emit electrons from the conduction band due to thermal

fluctuations and as such electrons from these photo-cathodes are produced even in the absence of illumination. This leads to a low level constant current within the PMT known as the dark current. Most photo-cathode materials release between about 10^2 and 10^4 electrons per cm at room temperature which leads to a dark current on the order of a few nA at the anode.

4.2.4 Other photodetectors

Recently some new types of photodetectors have become available. Multichannel plate (MCP) photomultipliers and solid-state photodetectors are examples that will be discussed here.

Multichannel plate photomultipliers are somewhat similar to conventional PMTs except that instead of dynodes, a plate perforated by a high density of holes (or pores) is responsible for the electron multiplication. In an MCP-PMT, photo-electrons emitted by the photo-cathode are steered by the electric field into the pores of the MCP plate. Because the holes are generally cut into the plate at an angle, the electrons are guaranteed to hit the wall, releasing a large number of secondary electrons. In most MCP-PMT designs two MCP plates having oppositely angled holes are placed one after the other in a chevron configuration. This reduces ion feedback and allows higher gains to be reached at the same voltage.

Because of their planar design and their unique amplification mechanism, MCP-PMTs can be produced in large surface areas and are practically insensitive to magnetic fields. In addition, the transit-time-spread of an MCP-PMT is much smaller than that of conventional PMTs making them very desirable for applications in which precise timing is required. A high resolution image of the pores of two different MCP designs is shown in figure 4.11. MCP-PMT producers are currently developing MCPs with smaller pore sizes which promises further improvement in timing properties. Position-sensitive multi-anode MCPs are also available on the market.

Another common type of photomultiplier is the silicon photodiode. The principle of operation is the collection of the electron-holes produced by the interaction of visible light in the depletion region. Since the mean free path of optical photons in silicon is of the order of 0.1 μm at 400 nm and about 5 μm at 700 nm then one electrode of the photodiode must be kept very thin in order to allow the light to reach the depletion region. Silicon photodiodes have a very high quantum efficiency, around 60% at 400 nm and are insensitive to magnetic fields. But, because there is no amplification of the primary charge in the detector, the actual current they produce is usually too small to be useful. As such, silicon photodiodes are only suitable for applications where a large amount of light is available. For example, the light produced by a typical scintillator is too low to be detected by a silicon photodiode.

Avalanche photodiodes (APD) partially solve this problem. The APD is

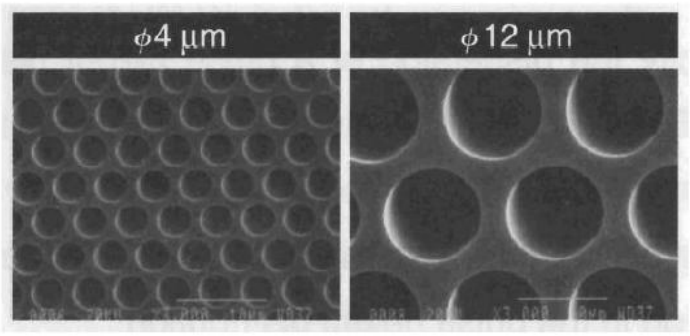

Figure 4.11: Scanning electron microscope image of a MCP. The pore diameters are 4 μm and 12 μm diameter.

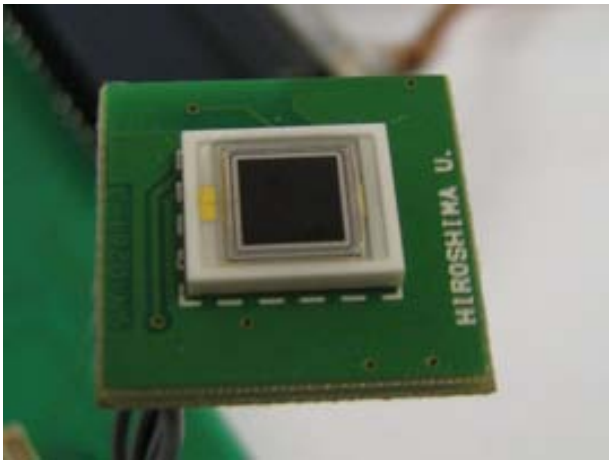

Figure 4.12: An avalanche photodiode mounted on a small prototype PCB having active area of 3x3 mm^2.

a silicon photodiode with internal gain. They consist of a low field region in which the light produces electron-hole pairs and a high-field region in which the charges are accelerated sufficiently to create electron amplification. By this method moderate gains on the order of 100 can be achieved. Increasing further the gain becomes complicated due to stability issues and production techniques; so far the size of APDs is limited to about 10 mm^2. A picture of an APD having 3x3 mm^2 active area is shown in figure 4.12.

Another exciting development in photodetector technology is the silicon-photomultiplier (SiPM) occasionally referred to as the Multi-Pixel-Photon-Counter (MPPC). The device is an array of tiny diodes connected in parallel and arranged over a surface in a pixelated matrix. Each cell is typically only 50x50 μm. Each diode is essentially a photodiode operating with a very

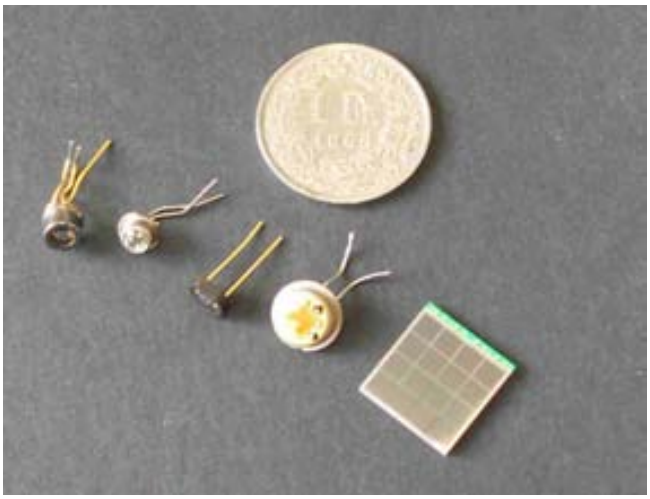

Figure 4.13: A variety of silicon photomultipliers (SiPMs) which have been purchased for study by TERA. The three on the left have 1x1 mm^2 sensitive area, the second to the right has 3x3 mm^2, while on the far right is a 4x4 SiPM array, where each individual sensor has 3x3 mm^2 active area.

large electric field in the amplification region. With the creation of a single electron-hole from the interaction of a photon, the cell goes into discharge. Because each cell is placed in series with a resistor, the discharge is quenched and only the charge stored within the diode is released. Under illumination by photons, a number of pixels will fire simultaneously and because the charge stored by each diode is uniform across the array, the output pulse is highly proportional to the number of pixels fired, at least when the number of incident photons is much lower than the number of total pixels. A gain of 10^6 can be achieved with this technology. Figure 4.13 shows several SiPM devices: the three on the left are single sensors 1x1 mm^2 in active area, second to the right is a 3x3 mm^2 SiPM, while on the far right is a matrix of 16 SiPMs on the same chip, each having 3x3 mm^2 active area.

SiPMs have an excellent energy resolution, high quantum efficiency (around 50-75%) and they are capable of single-photon counting. SiPMs also have timing resolutions on the order of about 100 ps making them very attractive for fast timing applications. Furthermore, they are insensitive to magnetic fields, just like APDs and silicon photodiodes. Their drawbacks are their limited active area (3x3 mm^2 are now commercially available), large noise (roughly 100 kHz single photon threshold), and gain dependence on temperature.

Chapter 5

Proton Range Radiography

5.1 Principles of PRR

A diagnostic beam of protons with energy high enough to pass entirely through the body of the patient can provide anatomical information about the tissues along the beam path. Since it is only a diagnostic beam and not used for therapy, it must be delivered at a much lower intensity as to minimize the dose delivered to the patient. Interesting, many existing medical proton accelerators, particularly synchrontrons, can provide beams of higher energies and low intensities with relatively minor adjustment in the machine parameters. This makes it feasible to image the patient immediately before radiation and from the field of view of the beam itself.

The principle of proton range radiography (PRR) is to measure precisely the residual energy E_R of a mono-energetic proton beam having initial energy E, emerging from an irradiated target. This concept is illustrated in figure 5.1. If the path of the protons and their initial energies are known then the average stopping power of the tissue along the trajectory L can be deduced from the energy loss $\triangle E$ inside the tissue. This is fundamentally different to X-ray radiography in which the attenuation of the number of photons gives a measure of the electron density along their path. Because each proton carries information about the tissue traversed, proton radiographies yield contrast resolutions similar to X-ray radiographies yet with a

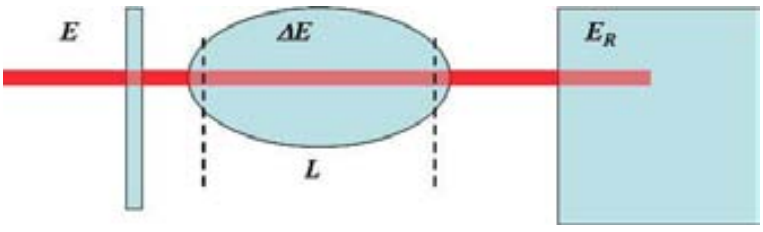

Figure 5.1: Principle of proton range radiography (PRR).

dose given to the patient 50 to 100 times lower [38]. Though this presents a significant advantage over X-ray imaging, proton radiographs suffer from Multiple Coulomb Scattering (MCS) of the protons along their trajectory resulting in rather poor spatial resolution for thicker targets. Initially proposed in the 60's as a modality for imaging, proton radiography was largely later abandoned due to this disadvantage and the requirement of more powerful accelerators than what is needed for therapy (230 MeV for protons).

Nowadays, with the advent of proton therapy, the situation is changing. Though proton radiographies offer poorer spatial resolution, they are significant to quality assurance in hadrontherapy for two reasons. First, a proton radiograph obtained with the accelerator can reduce uncertainties related to patient positioning or beam parameters since it is a true beam's-eye projection of the treatment volume. Second, and more importantly, the range information obtained directly by a proton radiograph is what is needed for accurately computing a hadrontherapy treatment plan. The conversion from CT Hounsfield units to stopping power introduces an uncertainty in the range calculation for protons because of the lack of density resolution characteristic of X-ray CT [39]. This uncertainty has been estimated as between 3-4% of the proton range and is further degraded by the presence of complicated tissue-air and tissue-bone interfaces [40]. Reducing this uncertainty is very important for hadrontherapy and is prompting development towards full proton CT. Though still some years away, many researchers are convinced that future hadrontherapy treatment plans will rely on data provided by proton CT, obtained by the very accelerators that provide the treatment. A detector capable of proton radiography is the logical first step towards full proton CT.

Whether or not the future will see proton CT as the basis for treatment planning, a proton radiography instrument could already provide valuable information for QA in current hadrontherapy practice [40]. Designed for this purpose, the prototype detector shown in figure 5.2, the PRR10, has been constructed and tested by the AQUA group of the TERA Foundation. It uses the technologies of HEP instrumentation to measure the trajectory and residual range of individual protons at a rate of up to 10^4 protons/s. This prototype, capable of producing PRR images up to 10x10 cm^2, has been tested experimentally with protons beams at the Paul Scherrer Institute in Villagen, Switzerland and the *Centro Nazionale di Adroterapia Oncologica* (CNAO) in Pavia, Italy. Excellent spatial and range resolutions have been observed during the beam tests, the results of which will be presented in this chapter devoted to the subject.

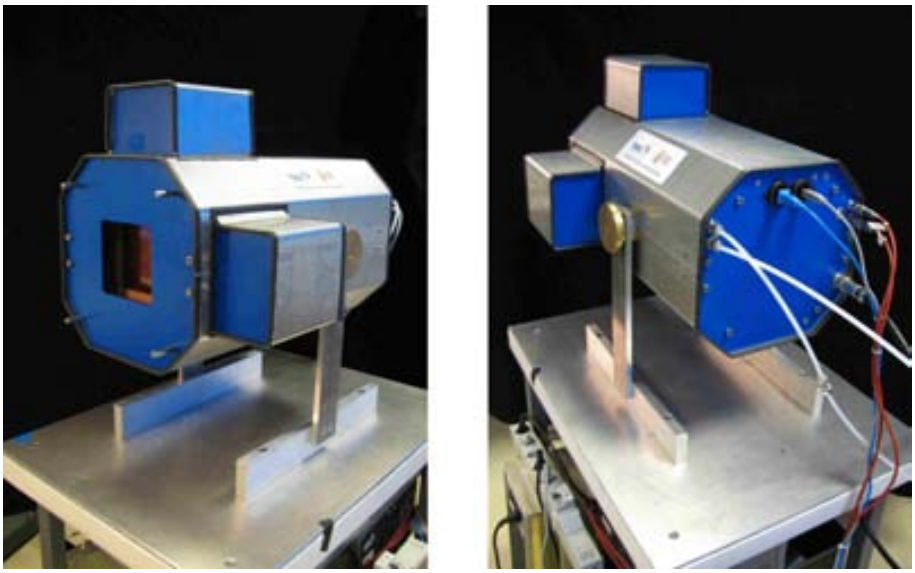

Figure 5.2: The AQUA PRR10 mounted on a portable table.

5.2 The AQUA PRR10

The main requirements for a device capable of performing proton radiography are tracking detectors to record precisely the direction and position of protons emerging from the patient and a calorimeter which measures their residual energy. In order to be useful to clinicians, the position resolution should be better than 1 mm, on the order of the resolution of X-ray images. The energy resolution, which defines the contrast, must be high enough to allow a maximal differentiation between tissues and an accurate computation of the stopping power in the tissues needed for verifying the treatment plan. For a suitable proton radiography destined for clinical application, the required density resolution has been suggested to be better than 0.3% [41], which puts high demands on the energy resolution of the calorimeter.

Measuring the residual energy of a charged particle typically implies stopping it within a detector. Good energy resolutions can be obtained by using large inorganic scintillating crystals, such as CsI or YAG, in which the particle is completely absorbed and the total light output measured by a photodetector, usually a PMT coupled to one face of each crystal [42, 43]. Energy resolutions as low as 1% for protons of 200 MeV have been demonstrated [44]. However, large inorganic scintillators are expensive and in addition, the rather slow decay time of such crystals limits the acquisition rates that can be achieved. Also, the energy resolution of large crystal systems depends on the position of the interaction requiring that a calibration be performed.

Instead of measuring the residual energy of protons with large inorganic

scintillators, we have chosen to measure their range by using a stack of thin plastic scintillators, each read out individually. There are several reasons for choosing to use such a device, which we shall refer to as a range telescope. First, plastic scintillator is far cheaper than inorganic and although it does not have the energy resolution of crystal, it can be used to measure the proton residual range rather than the residual energy. Second, plastic is one of the scintillators with the shortest decay times, making it possible to acquire the radiography faster, leading to shorter exposure times for the patient.

The range of a particle depends roughly on its energy as

$$R(E) \approx \alpha E^p \tag{5.1}$$

where α and p are parameters of the material and the particle in question. This expression is a simplified result of equation 3.4 for charged particles and it applies to protons in the energy ranges used in therapy. By differentiating the above equation we can approximate the relationship between the relative energy and range uncertainties and write

$$(\tfrac{\sigma_R}{R}) \approx p(\tfrac{\sigma_E}{E})$$

Since for protons of medical energies the value of p is typically about 1.8, it follows that a measurement of the range with a 1% uncertainty is equivalent to an energy measurement with 0.56% uncertainty. Measuring the range of protons precisely can be achieved with a range telescope by measuring the light output on each scintillator provided they stop inside the telescope. The range can then be determined in a simple manner by determining the last scintillator hit. The absorbers should be thin and many to ensure both a good range resolution and that the protons stop inside the detector over a wide energy range.

In reality, the uncertainty that one can measure the residual range is limited by several factors, both practical and physical. One is the momentum spread of the beam from the accelerator. Though the momentum variation is typically small for modern accelerators and especially for radiotherapy beams (since this is important in profiting from the rapid fall-off at the distal edge), it can have a significant contribution to the overall uncertainty in a residual energy (or range) measurement. This affects both crystal calorimeters and range telescopes.

Another factor, important at lower energies, arises from the multiple scattering of the protons along their path in the target and detector. The expression given in 5.1 for the range of charged particles should be not be confused with the projected range, which will vary depending on the amount the particle is deviated from a straight line by MCS. Following equation 3.5 given in chapter 3, and for protons traversing 20 cm of water, the MCS angle is roughly 1°. The effect of MCS then, for the energies

associated with proton radiography, contribute only a tiny amount to the uncertainty in the projected range and are generally disregarded. It should be pointed out, however, that although MCS does not strongly affect the range resolution, it does add a significant uncertainty to the proton path through the phantom, which has consequences on the spatial resolution of the density determination. This effect has been observed in beam tests with our own range telescope and is a subject of study currently underway by the AQUA group.

Although MCS can be ignored in predicting the range resolution for protons at medical energies, range straggling due to the statistical nature of the energy-loss cannot. Because the process of energy-loss along the particle path is stochastic, charged particles of the same energy will not all have the same range. For protons, the standard deviation of the variation caused by straggling is about 1.1% of the range in water and this sets a lower limit on the achievable range resolution that a range telescope could have. For a 150 MeV beam of protons, whose range is approximately 15 cm in water, this amounts to about 1.6 mm.

The residual range then, that which would be measured by our scintillator absorbers, will be distributed about a mean value for a number of protons having the same initial energy, even for a perfectly mono-energetic beam. Generally speaking, the measured range resolution will be the result of contributions from range straggling, the momentum spread of the beam from the accelerator (expressed as an equivalent range uncertainty), and the intrinsic range resolution of the device. This can be expressed as

$$(\sigma_R)_{measured} = \sqrt{(\sigma_R)^2_{straggling} + (\sigma_R)^2_{beam} + (\sigma_R)^2_{detector}} \qquad (5.2)$$

The intrinsic resolution of our range telescope will depend on the choice of absorber thickness. If we consider 3 mm thick water-equivalent absorbers, statistics predicts we can measure a range resolution on the order of the absorber thickness divided by $\sqrt{12}$, or about 0.87 mm. Since this is about half the magnitude of the range straggling at this energy, using thinner absorbers will not substantially improve the overall uncertainty. Another reason to avoid making the scintillators too thin is that their light output decreases with thickness for charged particles. Our initial calculations suggested that 3 mm was a good choice for obtaining a reasonable signal even for high energy protons where the energy deposition is 3-4 times lower than in the Bragg peak. A further reason not to choose thinner absorbers is to limit the number needed for spanning a reasonable range of residual energy.

Applying equation 5.2 for a perfectly mono-energetic beam of 150 MeV protons (which have a range of 15 cm in water), it follows that the best range resolution we can hope to achieve with a 3 mm thick range telescope is 1.82 mm. If we add a 1% range uncertainty caused by variations in the beam energy into the calculation (equal to a 0.56% energy variation), we

can expect a range resolution of 2.36 mm. For the beam energy considered here which has a range of 15 cm in water, this amounts to a relative range resolution of 1.6%. This result is equivalent to a 0.89% energy resolution and will improve slightly for higher energy beams since the absolute detector uncertainty is constant. Even including a contribution from beam-energy uncertainty, the example of a range telescope illustrated here for measuring the energy of 150 MeV protons is better than most results reported with crystal systems.

At this stage it is important to recall that in proton range radiography all protons must travel the same water-equivalent path length (WEPL) when considering the combined WEPL of target plus range telescope. As a result, the range resolution for a range telescope is constant for a given energy of the primary diagnostic beam, regardless of the thickness of phantom traversed by each proton. In crystal systems, this is not necessarily the case, since the energy resolution may change with different residual energy of the absorbed proton, especially if its residual energy is small. To avoid this, the highest possible beam energy could be used, which is in practice limited on the order of 250 MeV for most medical accelerators. At any rate, crystal-based PRR systems can suffer from a complex energy resolution dependence on the amount of phantom traversed whereas a range telescope will not. For a range telescope, the maximum WEPL thickness of the target that can be imaged is therefore only limited by the primary beam energy. If the estimation of the uncertainties presented above for a 150 MeV proton beam are reasonably accurate, then a range telescope could have some advantages over crystal calorimeter systems for this reason.

Coming back to equation 5.2, the actual uncertainty in the mean value of the range depends on the number of samples measured and will be $\sigma_R/\sqrt{N}$, where N is the number of protons in each image element. Assuming that the residual range is proportional to the integrated density of the material along the particle path, the uncertainty in the density can be shown to be

$$\sigma_\rho = \frac{\sigma_R}{L\sqrt{N}} \tag{5.3}$$

where L is the thickness of the object whose density must be determined. Using the estimations stated previously for a beam of 150 MeV protons, if 200 events are sampled per pixel, the actual range uncertainty of a range telescope with 3 mm absorbers can be as low as 0.167 mm. This corresponds to a density resolution in near water-equivalent tissues of 0.11% across the full 15 cm WEPL. For an object within the target of 5 cm WEPL, the density can be resolved to nearly 0.3%, in line with the requirements for a clinical proton radiography instrument.

Measuring the density with this precision using a PRR instrument puts a heavy requirement on the data acquisition speed. For a 1x1 mm^2 pixel size and a full image of 30x30 cm^2, acquiring an average of 200 events per

pixel requires processing of more than 10^7 proton tracks in total. To keep patient exposure times to something reasonable, say 10 s, this requires a data acquisition (DAQ) system capable of a 1 MHz read-out rate.

The use of a range telescope for the application in proton radiography has already been proven by a group at the Paul Scherrer Institute [45]. Using plates of plastic scintillator 3 mm thick they have achieved a 0.3% density resolution for a beam of 177 MeV protons traversing a target of 15 cm. In deciding which technology to use for the AQUA PRR prototype, we have adopted to use plastic scintillators in light of the promising results by the PSI group and the reasoning presented above. For measuring the position of the protons we selected GEM detectors because of their excellent spatial resolution and rate capabilities for tracking charged particles. In addition, GEMs are inexpensive to produce in large surface areas as compared with solid-state detectors. A further benefit of using gas-filled detectors is that the material budget is very low, such that their inclusion in the range telescope has little effect on the traversing protons.

A schematic diagram of AQUA's initial proposal for a PRR instrument is shown in figure 5.3. The device is comprised of two main components: a stack of plastic scintillators for measuring the residual range and a pair of GEM detectors for tracking. The first prototype, named the AQUA PRR10, will be described in detail in this section followed by the results of extensive testing with proton beams at PSI and CNAO. For this proof-of-principle prototype, the active area has been chosen to be 10x10 cm^2 in an effect to reduce costs and simplify the assembly. In addition, only thirty 3 mm thick scintillators have been included in the range telescope, covering a total residual range of 9 cm WEPL, somewhat smaller than required for clinical PRR imaging of human patients. A new prototype which has an active area of 30x30 cm^2 and 48 scintillators, named the PRR30, is currently being constructed and will be briefly described at the end of this chapter.

5.2.1 Calorimeter

Scintillators, WLS fiber and SiPM photodetector assembly

In selecting the absorber material for the range telescope, we have chosen to use plastic scintillator, which is based on polyvinyl-toluene and has a density of 1.032 g/cm^3. Thin sheets of this material have been purchased from Saint Gobain Crystals [46], type BC-408, with the dimensions 12x12 cm^2 and a thickness of 3 mm with an allowable tolerance of ± 0.38 mm. The scintillators were procured with polished edges to ensure a maximal light collection and were measured to be thinner than requested, with an average value of 2.63 ± 0.2 mm.

The emission spectrum from BC-408 plastic scintillator is shown on the left of figure 5.4. This peak of the emission spectrum, which occurs at 435

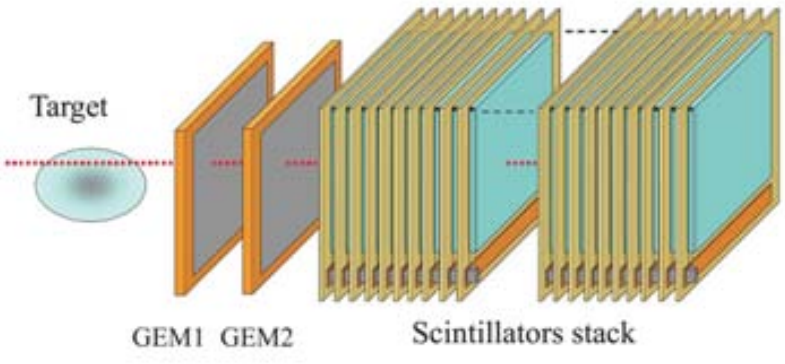

Figure 5.3: A schematic diagram of a detector capable of proton radiography. Two GEM detectors are used for tracking and a stack of plastic scintillators used to measure the residual range.

nm, is well suited for detection by SiPMs, which in recent years are a cheaper alternative to PMTs and readily available from a number of manufacturers. We have chosen SiPMs produced by Hamamatsu [47] as photodetector, MPPC type S10362-11-050C, which have a sensitive area of 1 mm^2 enclosed in a compact package only 6 mm diameter. These devices operate around 70 V and have the photon detection efficiency spectrum shown on the right of figure 5.4, well matched to the light produced by the plastic scintillators.

Collecting the light from the scintillator and transmitting it efficiently to the SiPM required some experimentation. Several methods were evaluated, including a direct coupling of the SiPM to one 3 mm edge of the scintillator plate, however, this resulted in poor light collection and was soon abandoned. Instead, we opted to use a wavelength-shifting (WLS) fiber mounted length-wise along one edge of the scintillator. This resulted in a more efficient collection of the light which was then transmitted - at longer wavelength - to the SiPM. We selected BCF-91F fiber, also from Saint Gobain Crystals, which has the absorption and emission spectra shown in figure 5.5. The peak of its absorption occurs at 425 nm, perfectly matched to the plastic scintillator, while its emission peak occurs at 495 nm giving the fiber its greenish color. At this wavelength the SiPM is 45% efficient, rather than 50%, which was deemed to be a reasonable matching for our purposes.

The WLS fiber, being 1 mm in diameter, contains an exterior cladding which helps the light to be transmitted efficiently along the fiber length. One end of each fiber was aluminized by vapor deposition in order to maximize the amount of light transmitted to the SiPM at the other end. A picture taken through a microscope of several WLS fibers with the aluminum coated ends is shown in figure 5.6.

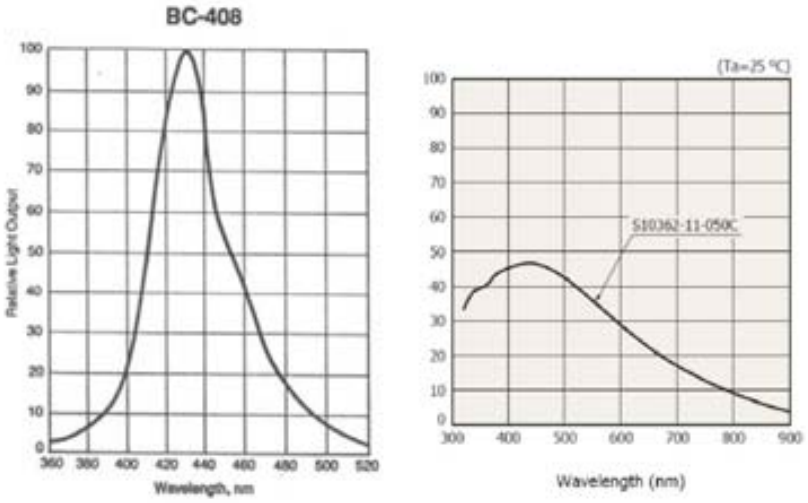

Figure 5.4: On the left, the scintillation emission spectrum of plastic scintillator (BC-408) and on the right, the detection efficiency of the SiPMs (S10362-11-050C) chosen for the AQUA PRR10.

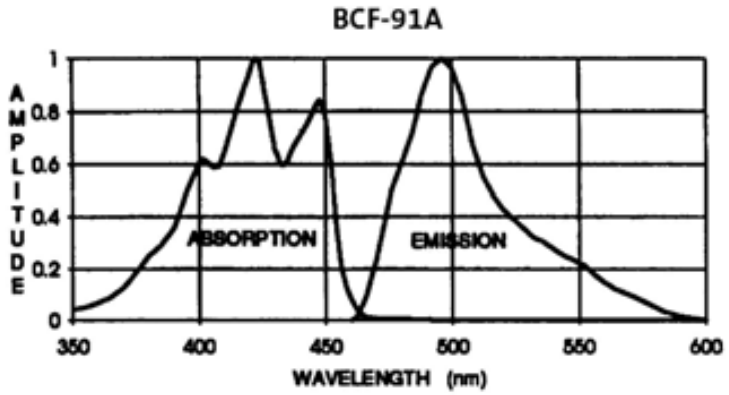

Figure 5.5: Absorption and emission spectrum of BCF-91A wavelength shifting fiber.

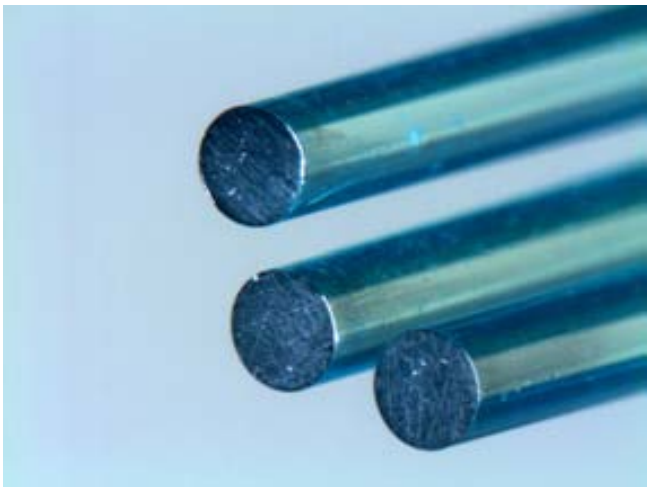

Figure 5.6: Wavelength-shifting fibers (BCF-91F) with aluminized ends for better light collection at the SiPM side.

The fibers were then connected along one edge of the scintillator plates in order to maximize the light collection. Several methods of doing this were tested, including using nylon fishing line to space the fiber slightly away from the plastic with a thin air gap of several hundred microns. The best results, however, were achieved by gluing the fiber into a shallow "v"-shaped groove machined into the edge of the plastic. Optical glue was used having an index of refraction matched to the scintillator.

A picture of all components of the system is shown in figure 5.7 including a custom-built optical box used to hold the SiPM in place with respect to the WLS fiber and the scintillator plate. After gluing all parts in place, the scintillator was covered first with a thin layer of aluminum foil and then with black plastic wrapping made of polyvinyl chloride (PVC). It should be mentioned that this wrapping contributes to the effective thickness of the scintillators. We have measured the total wrapping thickness from both sides to be about 750 μm with a small contribution from the aluminum reflector. Since our wrapping is plastic with a density of about 1.3 g/cm^3, we can say that each scintillator module has an effective thickness of about 3.6 ± 0.2 mm water-equivalent.

To evaluate the light collection of our design, each scintillator module was exposed to irradiation from a ^{90}Sr source and the charge output from the SiPM digitized over a large sample of events. ^{90}Sr is a $\beta-$ emitter with a peak energy of 2.28 MeV, but in practice all $\beta-$ emitters will exhibit electron energies from the peak energy down to zero, resulting in a huge range of energy loss in a given material. In order to restrict the range of energy loss inside the scintillator, we used an additional module placed after for triggering, thereby providing a selection on only the highest-energy electrons

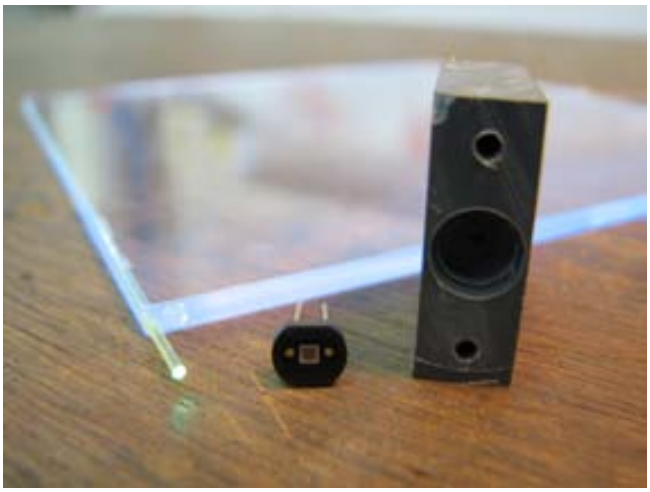

Figure 5.7: Main components of each scintillator slice: the plastic scintillator sheets, the WLS fiber glued along one edge, the SiPM and an optical box for supporting the SiPM with respect to the fiber and scintillator assembly.

which can traverse the 3 mm plastic scintillator under test. Figure 5.8 shows the typical energy spectrum of electrons emitted from a ^{90}Sr source (left) as well as the stopping power of electrons in plastic scintillator (right). Requiring that electrons reach the second scintillator effectively cuts the electrons below a certain energy, indicated by a line on the graph at the left of figure 5.8. This selects the region of stopping power highlighted in the graph on the right in the scintillator under test, which to a good approximation is equivalent to minimum ionizing electrons. The experimental setup is shown in figure 5.9.

Using this approach, pulses from the scintillator-SiPM assembly were digitized using a NIM discriminator (LeCroy 821CL) and a CAMAC ADC (LeCroy 2249A). Data acquisition was performed with a simple program written in LABVIEW. The SiPM bias voltage was set to around 70 V, such that the output signal was within the dynamic range of the ADC. To test the uniformity of the response over the area of the scintillator, several positions were irradiated. The energy spectra for a typical scintillator under test after collection of about 10^3 events is shown in figure 5.10. In green is shown the response at the center of the module while in red is shown the response at one of the corners. Only a small variation of the average pulse height of less than 10% was observed. In addition, the individual photon peaks are clearly visible (testimony to the excellent energy resolution of the SiPMs), conveniently allowing a measurement of the average number of photons detected. In this example, the mean response to energy-selected electrons (roughly MIPs) is 8 photoelectrons. Though this is not a large number, it is sufficient to allow a selection above the single-photon noise of

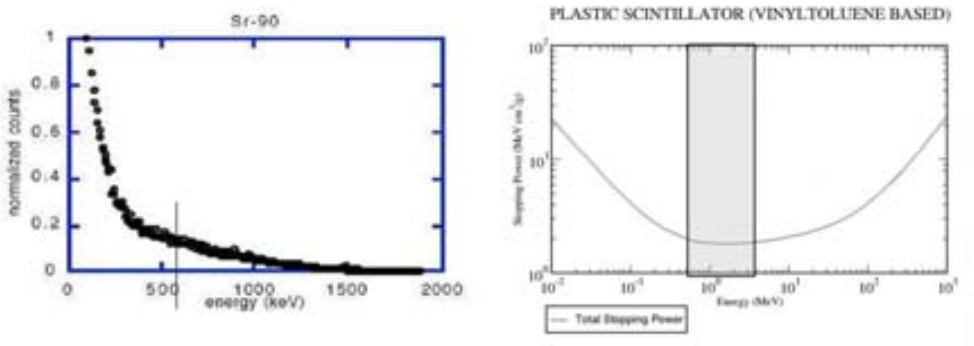

Figure 5.8: The energy spectrum of electrons emitted from a ^{90}Sr source (shown left) with a line indicating the threshold at which electrons have energy enough to traverse 3 mm of plastic scintillator. Shown right is the stopping power for electrons in plastic scintillator. The corresponding selection of electrons which will traverse 3 mm of scintillator is highlighted and nearly equivalent to the minimum ionization.

Figure 5.9: Setup for evaluating the response of the scintillator modules to irradiation by a ^{90}Sr source of electrons. The first module is under test and the second is used for triggering the data acquisition.

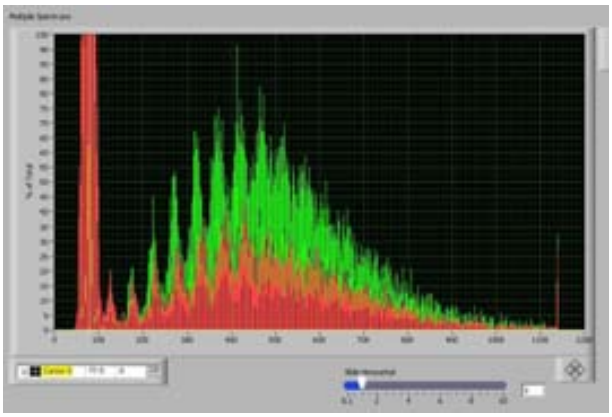

Figure 5.10: Energy spectrum recorded by a PRR10 scintillator module irradiated by high-energy electrons from a ^{90}Sr source (MIPs). Two spectra are shown obtained with the electrons passing through the center of the module (green) and one of the corners (red).

the SiPM and is roughly equal to the reported 10 photoelectrons obtained by the PSI group using a beam of high-energy protons and a similar WLS fiber embedded in bulk of the scintillator plate with PMT as photodetector [45].

Scintillator readout electronics

Beyond the initial tests carried out with conventional NIM and CAMAC electronics, we required a electronics readout solution which could be expanded to many modules and integrated in a compact and portable DAQ system. For each scintillator module, a custom circuit was designed consisting of a two-stage preamplifier with 80 ns shaping time followed by a 12-bit pipeline ADC. Also integrated on the board was a 5 V digital-to-analogue converter (DAC) which allows fine adjusting of the bias voltage of the SiPM. Because the SiPMs require ∼71 V for normal operation, we used a base voltage of 67 V which could also be adjusted. Communication with both the DAC and the ADC was implemented by I^2C protocol, limiting the number of wires needed for each module. In order to restrict the final size of the range telescope, considerable effort was put into optimizing the mechanical design in order to allow the modules to be stacked as close as possible. A picture of one of the scintillator modules mounted in a supporting frame along with the electronics PCB is shown in figure 5.11. All modules are identical, yet they can be piled-up in an alternating configuration thereby optimizing on the use of space and allowing each to be removed independently from the stack. The later point is important in case reparations or debugging are required on a single module. A picture of the mechanical frame which has

Figure 5.11: A pair of scintillator modules mounted on support frames. The design allows the scintillators and readout electronics to be packed tightly, an important requirement for minimizing the size of the full range telescope.

been constructed to support the scintillator modules is shown in figure 5.12. All 30 modules are are shown mounted and each can be removed comfortably from the stack from alternating sides. The module spacing is 8 mm.

All 30 scintillators in the range telescope are controlled by a central DAQ holding an Altera Cyclone III FPGA and a QuickUSB module capable of transmitting data at up to 30 Mbytes/s [48]. The DAQ board sits atop a mezzanine which serves as a fan out for communication with the scintillators. Four ribbon cables allows the readout of up to 48 scintillators, where each cable can be connected to a total of 12 scintillator modules thanks to special addressing which must be set uniquely on each module. The mezzanine also holds 4 high-voltage supplies (one supply per cable) which provide the 67 V base voltage needed for the SiPMs. Programming of the 67 V base voltage, the 5 V DAC for SiPM biasing as well as readout from all modules is handled by the firmware program uploaded to the FPGA and controlled by the user through software written in LABVIEW. Readout of the digitized signals from each module's ADC, when initiated from the central DAQ, occurs in parallel on all modules. The data is then assembled into a single package and stored in a first-in-first-out (FIFO) memory block within the FPGA. After accumulating a large number of events, the contents of the FIFO can be rapidly transferred to the PC through the QuickUSB connection.

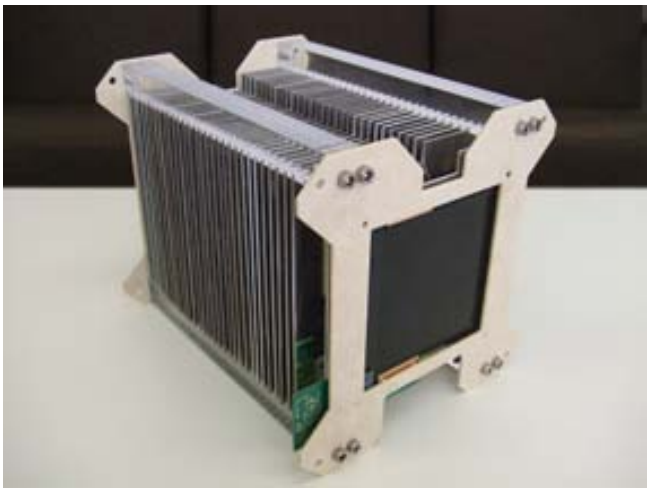

Figure 5.12: Mechanical support for 30 scintillator modules of the range telescope. Each module is fixed to a frame and can be removed easily from the stack for debugging without disturbing the others.

Figure 5.13: The central DAQ for readout of the 30 plastic scintillator modules. The central DAQ holds an FPGA as well as a QuickUSB module and is connected to a mezzanine board which serves as a fan-out for communication with the modules as well as providing the 67 V base voltage needed for the SiPMs.

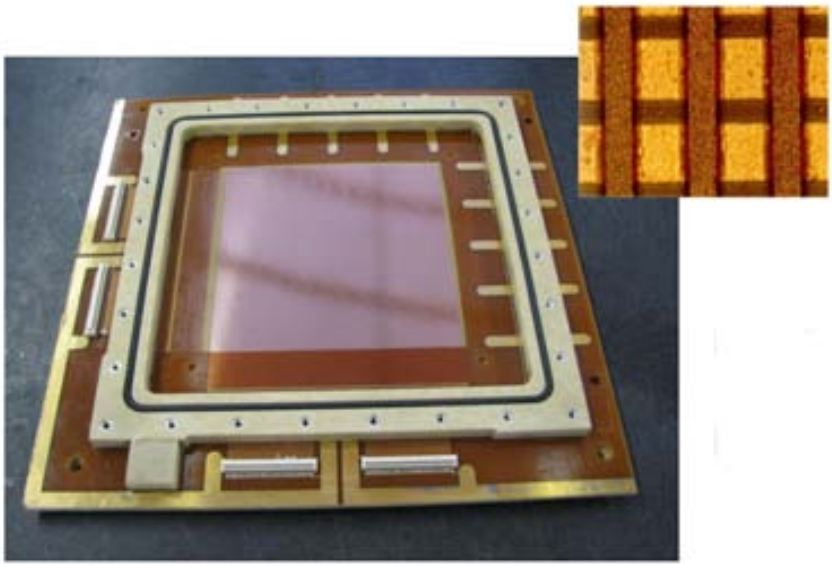

Figure 5.14: Lower half of the gas chamber showing the 2D XY-readout plane used with the triple-GEM detectors. The readout has a pitch of 400 μm for both X and Y planes.

5.2.2 Tracking GEM detectors

TGEM configuration and XY readout

As tracking detectors, we have chosen triple-GEM detectors having an active area of 10x10 cm^2. Each GEM is of the standard geometry described in the previous chapter, having holes of 70 μm diameter, separated by 140 μm in a hexagonal array which is repeated over a polyimide foil of 50 μm thickness. Three such GEMs are placed into a enclosed gas chamber with a 2D XY-readout anode patterned on the upper surface. The XY readout, shown in figure 5.14, consists of strips of 80 μm held at 50 μm above perpendicular strips of 350 μm both at a pitch of 400 μm. This asymmetry yields an equal charge sharing over both X and Y strips.

The GEMs are stacked in the gas chamber as illustrated in figure 5.15. The drift gap is 3 mm and each GEM is spaced at 2 mm from the other and the XY readout. Incorporated into the back of the readout structure is a honeycomb structure which reduces the amount of material in the beam path while maintaining mechanical rigidity. Once assembled, a mixture of Argon (70%) and CO_2 (30%) gas is circulated through the chambers at a rate of about 2-3 L/hr.

All aspects of this configuration, the drift and GEM spacing, the XY-readout geometry, and the gas mixture, are identical to that of triple-GEM

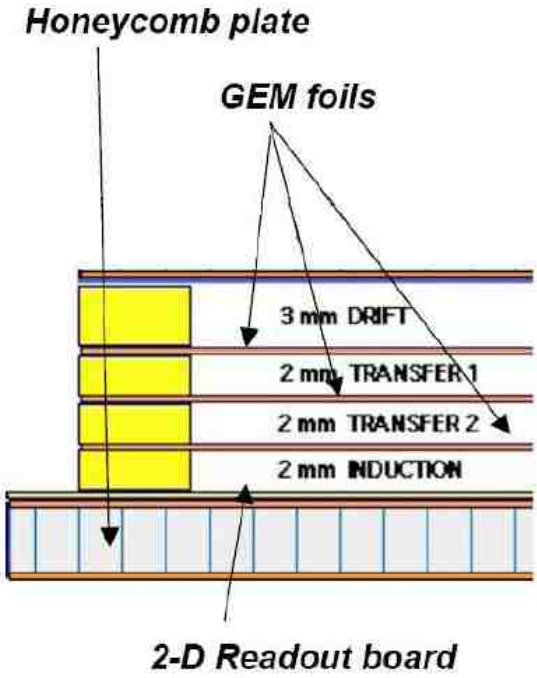

Figure 5.15: Geometry of the triple-GEM stack within the gas chamber.

detectors used in the COMPASS experiment [49] at CERN and considered standard in the use of triple-GEM detectors.

HV control

To apply the high-voltage to both the drift cathode and GEM electrodes, a high voltage distribution circuit was designed consisting of polarization resistors and a voltage divider. This allows a single voltage to be applied to the top of the divider which for normal operation is between -3800 V and -4300 V. Essentially identical to the standard schematic used for triple-GEM detectors in the COMPASS experiment, our HV divider uses resistor values which are ten times larger, effectively reducing the current on the power supply by an order of magnitude. No loss in gain or rate capabilities at the maximum particle flux in our application ($\sim 10^6$) were observed with the use of our low-current HV circuit.

In order to control the HV remotely, a special controller circuit has been designed and implemented. Shown in figure 5.16 is the controller and a compact HV module mounted in the PRR10 detector in the space between the two triple-GEM detectors. The module is made by Matsusada Precision Inc., model J6-5N, and provides voltages up to 5 kV with less than 20

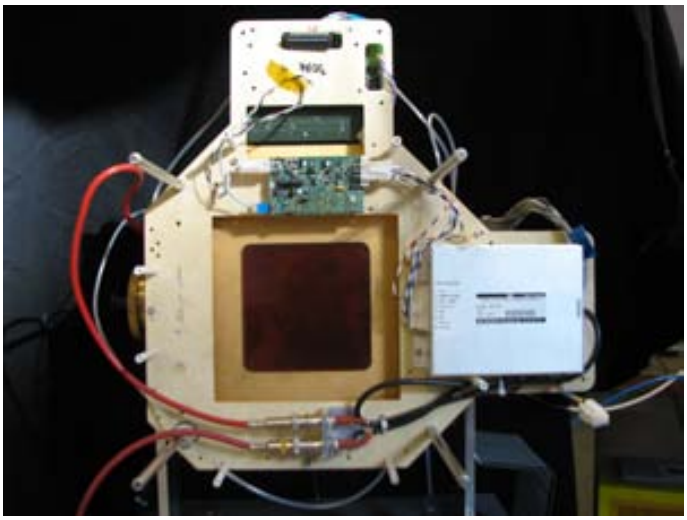

Figure 5.16: GEM HV module and HV controller mounted within the PRR10 detector. A single module powers both GEM detectors. The voltage and current can be set and monitored by software.

mV ripple peak-to-peak. The module also provides a voltage and current monitor which is useful for ensuring the GEMs are operating correctly, even during beam tests when the user must operate the detector remotely. Since the two GEMs are identical, a single controller and HV module have been used for both detectors. With our modified HV distribution, both GEMs draw about 140 μA at -4000 V.

DP-GP5 front-end electronics

For the electronic readout of the GEM detectors, we have made use of a front-end solution developed for fast readout of MPGDs, and extensively tested and characterized in previous studies, the results of which have been reported in a number of publications [50, 51, 52]. Referred to as the DP-GP5, the front-end is based on the 128-channel IDEAS VATAGP5 [53] ASIC (Application Specific Integrated Circuit) and a 128-channel diode-protection ASIC originally developed for the TOTEM experiment [54]. Here we summarize its main features.

The diode protection ASIC, which is a needed component of any gas detector front-end electronics, consists of 128 independent channels, each one having the schematic circuit diagram shown in figure 5.17. The protection ASIC, mounted before the GP5, also serves conveniently as a pitch adapter; wire bonding is made “chip-to-chip” from the output of the protection ASIC to the input pads of the GP5, removing the need for expensive PCB technologies which would have been necessary to match the very fine pitch of

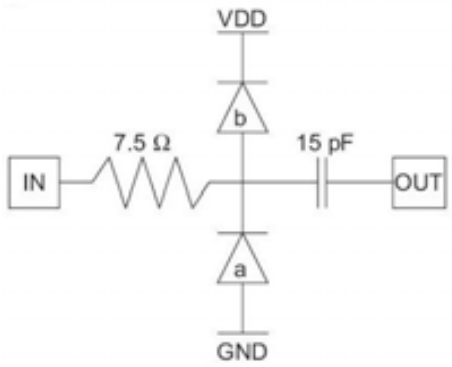

Figure 5.17: Schematic of the circuitry present in each channel of the diode-protection ASIC used to protect the GP5 from discharges [54].

the GP5 input bond pads.

The GP5 has 128 independent channels, each with both a fast 40 ns shaper for producing a trigger and a slow 250 ns shaper which provides a precision amplitude measurement of the integrated charge. An output buffer allows reading all 128 channels in either serial, sparse and sparse-with-neighbors mode. So far, only serial readout has been implemented. Each GP5 channel also contains a built-in trim-DAC which can be used to normalize the trigger threshold on each channel with respect to the global threshold applied to all the chip. A schematic for a single channel of the GP5 is shown in figure 5.18.

Both diode protection ASIC and the GP5 have been mounted and wire-bonded on custom-built hybrids which uses board-to-board connectors for integration between the GEM detector readout and the DAQ. A picture of a fully assembled DP-GP5 hybrid is shown in figure 5.19.

MDAQ and central DAQ

An intermediate board, called the MDAQ, receives two front-end DP-GP5 hybrids and relays them to a central DAQ board. The MDAQ, pictured in figure 5.20, digitizes the analogue voltage levels on the output buffers of the GP5s by means of 16-bit pipeline ADCs. In addition, the MDAQ provides the biasing voltages and programmable thresholds needed for the GP5s as well as interconnection between the FPGA on the central DAQ for setting the GP5 registers and transmitting the ADC data.

The central DAQ for the GEM detectors holds a QuickUSB module and an Altera Cyclone III FPGA and is identical to the central DAQ of the range telescope. Unlike the range telescope DAQ, however, the GEM central DAQ sits on top of a fan-out mezzanine board built to allow connection of up to 4 MDAQs, the requirement for full readout of two triple-GEM detectors, each

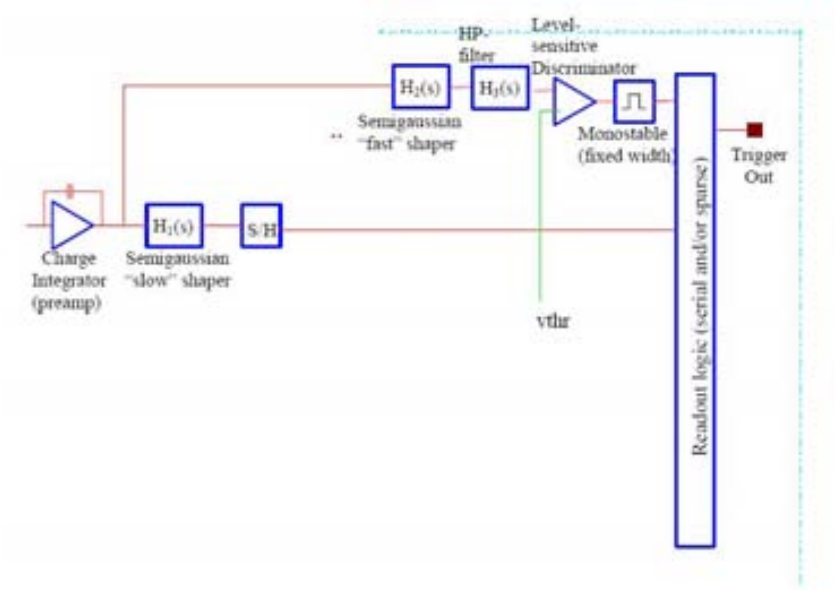

Figure 5.18: Schematic of each channel of the VATAGP5 [53]. A fast shaper is used for generating a trigger while a show shaper is used to obtain an accurate measurement of the integrated charge.

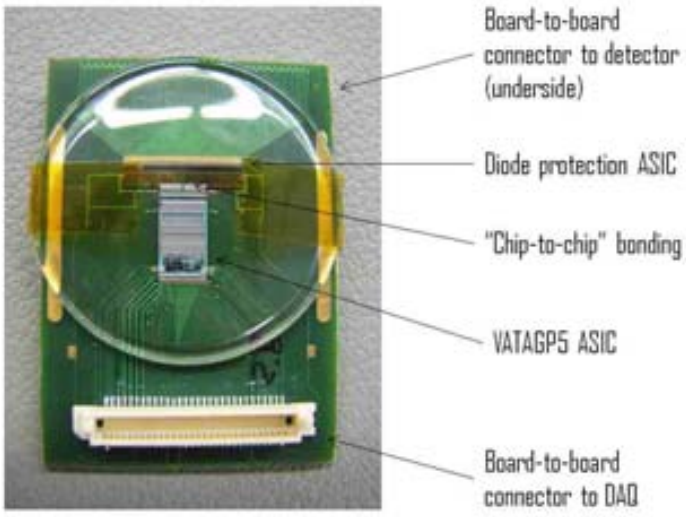

Figure 5.19: The DP-GP5 front-end electronics mounted on a custom hybrid with board-to-board connector for link between the detector and electronics.

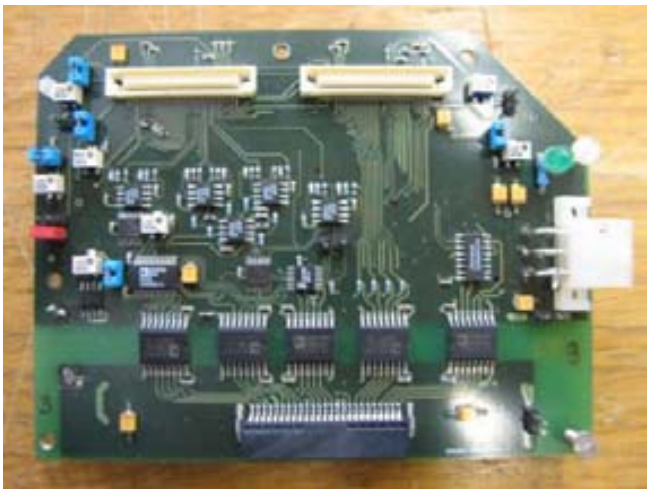

Figure 5.20: The MDAQ intermediate board connecting two DP-GP5 front-end hybrids and a master DAQ. The MDAQ provides biasing for the GP5s and holds pipeline ADCs for digitization of the GP5 analogue output buffers.

having 256 channels per axis, for a total of 1024 channels. Slow control of the GP5 chips (register programming, threshold setting, etc) can be controlled by the user using a software interface written in LABVIEW and the firmware uploaded to the Altera FPGA. Because only serial readout mode has been implemented, the total readout rate for a single 10x10 cm^2 GEM is limited to about 10^3 samples/s. Though too slow for performing radiographies on a timescale useful for clinicians (and comfortable for patients), this solution was adopted for the PRR10 prototype since the DP-GP5 front-end was already available to the AQUA group.

The entire GEM DAQ system can be operated independently in self-triggering mode, making it possible to test the GEMs without the need of the range telescope. This flexibility also make it feasible to consider this double GEM system in other detector applications. One of the AQUA triple-GEM 10x10 cm^2 detectors, fully assembled and equipped with HV distribution, four DP-GP5 hybrids and two MDAQ intermediate boards, is shown in figure 5.21.

GEM and DP-GP5 Calibrations

The DP-GP5 front-end has been calibrated prior to the start of the PRR10 project using a simple charge injection procedure where a square pulse of known voltage is sent to a capacitor connected in series to a input channel of the electronics chain. A high dynamic range and a linear gain of the analogue response with input charge has been observed, up to 1 pC with a non-linearity of less than 10% [52]. The entire system, with the MDAQ

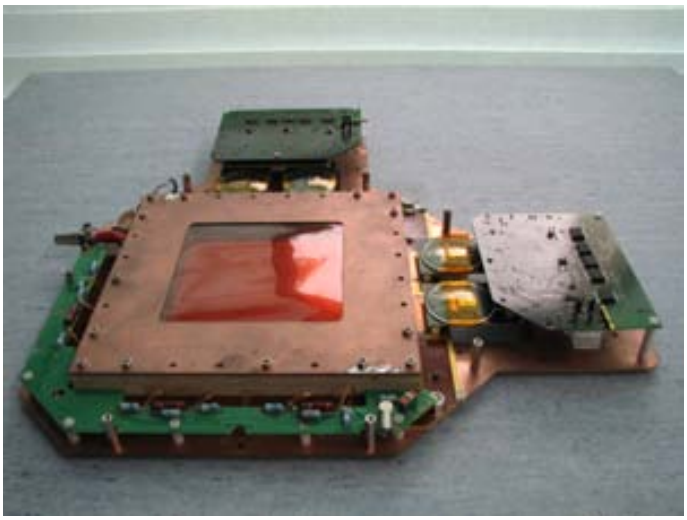

Figure 5.21: A single triple-GEM mounted with GP5 front-end readout electronics and MDAQ boards.

and its 16-bit ADCs, has been calibrated to 31 ADC counts per fC of input charge, a value which has been used to calculate the GEM gain when exposed to a known source of primary ionization.

The noise on the analogue channels outputs of the DP-GP5 front-end has also been characterized and found to be 0.8 fC + 0.25 fC/pF [52]. This is the intrinsic noise of the slow shaping circuit within each GP5 channel and should not be confused with the noise of the fast shaper which is what limits the lowest threshold which can be set in self-triggering mode. In practice, the fast shaper has a much larger noise than the slow shaper because of its fast timing. This has also been characterized by charge injection and for single channel triggering, the lowest threshold that could be set above the noise was measured to be 15 fC. If the trigger is set to logical OR of all 128-channels on the same hybrid, the lowest threshold that can be set is 140 fC, a consequence of the pedestal variations between channels [52]. These values increase slightly when then inputs are connected to the readout strips of a 10x10 cm^2 GEM detector due to the added capacitance of the readout strips.

To verify the correct working of all components, each GEM was exposed to ^{55}Fe, a source of 5.9 keV X-rays. Shown in figure 5.22 are the pulse-height spectra for the X and Y axes on one GEM detector held at -4000 V. The data is shown after pedestal subtraction and after processing with a simple common-mode (CM) noise-rejection algorithm which also sums the charge in each cluster of hit strips. The main peaks in the spectra correspond to the full energy from photoelectric absorption of the 5.9 keV X-rays while the smaller peaks to the 3 keV escape-peak characteristic of gas mixtures with

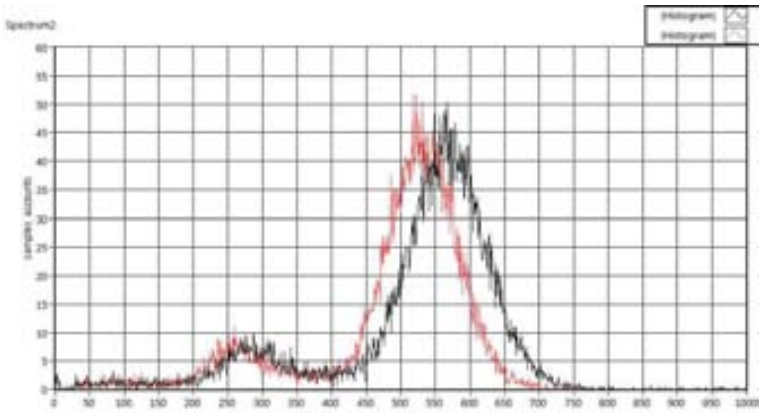

Figure 5.22: Pulse-height spectra of X-rays from an ^{55}Fe source in one of the triple-GEM chambers read out with DP-GP5 electronics. Both X (black) and Y (red) axis spectra are displayed.

Argon predominance. As expected, the position of both X and Y spectra are roughly equal indicating an even charge sharing between X and Y strips of the readout board. The energy resolution is 23% FWHM testimony to the low noise of the analogue measurement from the DP-GP5 and the good working of the CM correction. In addition, the horizontal position of the 3 keV peak at half the 5.9 keV peak indicates a good linearity of the electronic response and that the GEM is working in the proportional regime.

5.9 keV X-rays release about 220 electrons of primary ionization in Argon gas (see table 4.1). Using the DP-GP5 calibration stated above, we can deduce the total charge collected on the XY readout strips from the position of the ^{55}Fe spectra (being sure to apply a factor of 2 since the total charge is shared equally between X and Y). The GEM effective gain is then inferred as the ratio of the total charge to the primary ionization. The effective gain for one triple-GEM detector as a function of the applied voltage at the top of the HV divider is shown in figure 5.23. As expected, the result is in very close agreement with the COMPASS triple-GEM detectors [49].

The GEM detectors were also tested for gain uniformity by measuring the response to an ^{55}Fe source in 5 different locations over the 10x10 cm^2 active area: the center and the four corners. Shown in figure 5.24 is the relative variation of the 5.9 keV peak of the pulse-height spectra over the surface. Less than 16% variation is observed between all locations.

The GEM detectors must have a high detection efficiency for charged particles in order to ensure that we would not miss protons during radiographies. Though protons should release about 2.5 times the energy of MIPs at the entrance of the Bragg curve, we studied the GEM efficiency to MIPs extensively as a worse case scenario before going to a proton beam. MIPs release about 28 electrons of primary ionization in 3 mm of Argon gas, or

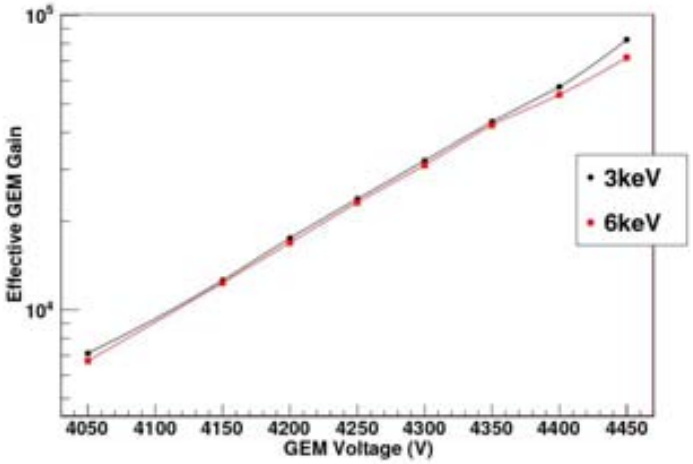

Figure 5.23: The effective gain of a triple-GEM chamber as a function of voltage applied to the top of the voltage divider made using a ^{55}Fe source and a charge injection calibration using 1 nF and 220 nF series capacitors.

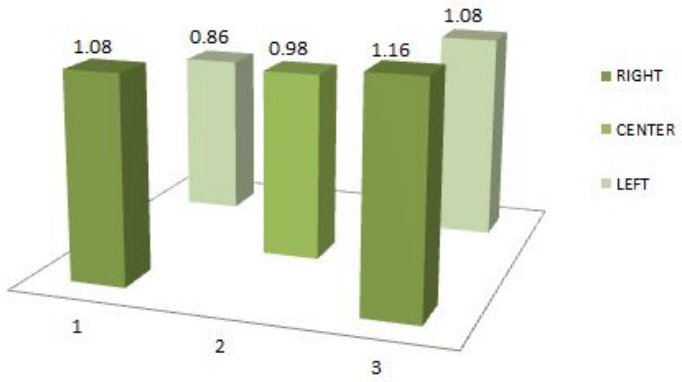

Figure 5.24: Gain uniformity over in the center and four corner of one 10x10 cm^2 triple-GEM detector. The measurement is made at 4300 V and with ^{55}Fe.

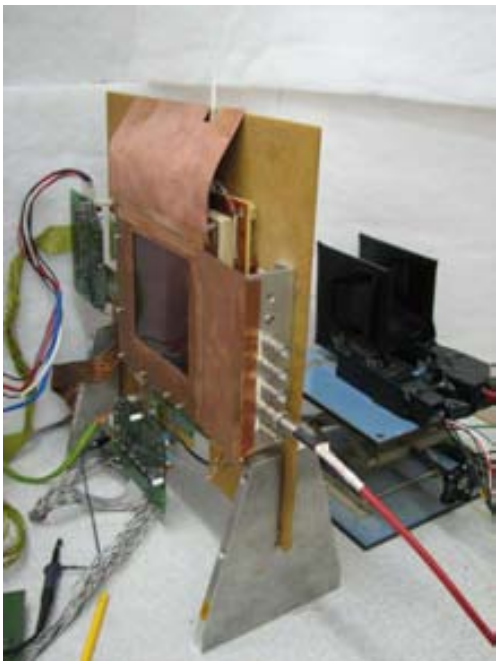

Figure 5.25: The laboratory setup for measuring the GEM efficiency to MIPs in self-triggering mode. A pair of scintillator modules are placed behind the GEM and are required to be in coincidence in order to select only high-energy electrons passing through the GEM.

the equivalent of about 0.73 keV of their energy. At a nominal GEM gain of 10^4, this amount to a total charge of about 350 fC which is shared between X and Y axes and over several strips. Considering that the lowest threshold that can be set on the GP5 for all-channel triggering is 140 fC, it follows that the detector will not reach full efficiency for MIPs in these conditions.

To investigate this limitation experimentally, a pair of scintillator modules were placed after the GEMs and required to be in coincidence when exposing the GEMs to high-energy electrons (produced by a ^{90}Sr source) directed from above, thus selecting near MIPs passing through the GEMs. The setup is shown in figure 5.25. Coincidences were evaluated between the scintillators using a NIM coincidence unit (LeCroy 465). By comparing whether a trigger was received from the GEM detector (at least one X and one Y strip) at the same moment as a coincidence from the scintillators we were able to deduce the GEM efficiency. An efficiency of only 80% could be reached even at high gains of $5\text{x}10^4$ near the onset of discharges as expected for the DP-GP5 front-end in self-triggering mode.

One option for improving the MIP efficiency could be to make use of the trim-DACs for each channel of the GP5s, effectively canceling pedestal differences and giving a normalized global threshold over all channels. In this

way, it is expected that the lowest threshold for all channels could approach that measured for a single channel, 15 fC, likely improving the efficiency significantly. This is one development that could be explored in future studies for DP-GP5 applications which require self-triggering functionality and high efficiency for MIPs. A simpler method is to provide an external trigger to the GP5 and exploit the lower noise of the analogue chain through analysis of the serial data set.

Using the same setup with scintillator pair placed behind the GEM, we delivered the coincidence signal from the scintillators to the GEM-DAQ initiating readout in serial mode. In the initial study, the timing of the coincidence signal with respect to the GEM signal was not considered. Figure 5.26 shows the efficiency of one of our GEM detectors for MIPs as a function of the applied voltage using this external trigger setup. The CM noise-rejection algorithm, which has been routinely applied to the GEM data in analysis, has an effect on the final amplitude of the signal since it must select the hit channels from the pedestal channels in the serial data. The threshold between signal and noise, set between 3, 4 or 5 sigma, determines the number of channels which contribute to the amplitude and must be set prior to analysis. For the 5.9 keV peak presented previously, adjusting the threshold of this CM rejection had little effect on the total amplitude because the signal to noise ratio was large. For small signals such as MIPs, however, the choice of CM threshold impacts the amplitude considerably and therefore the obtainable efficiency. For this reason, the GEM efficiency to MIPs has been reported for 3, 4 and 5 sigma CM rejection thresholds. At 3 sigma, a MIP efficiency of 95% is reached at a voltage of -4150 V, corresponding to a gain of $\approx 10^4$.

5.2.3 Trigger and synchronization

In order to yield a useful radiography, events recorded in the GEM detectors must be matched with events in the scintillator stack. This requires a global trigger signal which initiates the read-out of the scintillator modules and the GEM detectors simultaneously, ensuring events in both correspond to the passage of the same proton. To do this, and to provide a permanent external trigger for the GEM detectors (thereby ensuring their highest efficiency), it was decided to include an additional two scintillator modules located between the GEMs and the scintillator stack for trigger selection. The trigger scintillators are identical to the other scintillators in size and use the same light collection method of WLS fiber and SiPM described above. The electronic circuit, however, has been modified to provide a fast shaping with 40 ns rise time. This was needed in order to bring the trigger in time to digitize the peak amplitude of the analogue signals in the other scintillators, which use a shaping time of 80 ns. A constant-fraction discriminator was implemented to provide the digital trigger signal with a programmable threshold

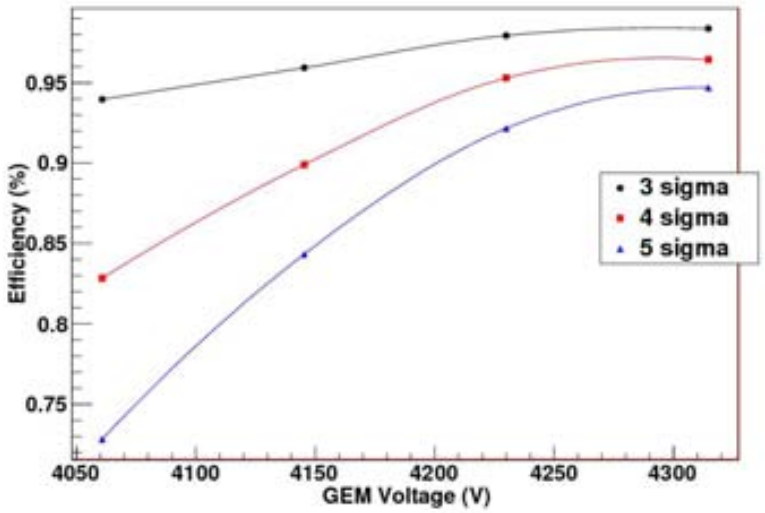

Figure 5.26: Detection efficiency of a triple-GEM detector to MIPs using an external trigger provided by a pair of scintillators located behind the GEM detector.

for selecting events above the intrinsic noise of the SiPM. The circuit also provides a 5 V DAC for fine adjustment of the SiPM bias voltage.

In readout operation, the central DAQ of the scintillator modules monitors the output from the trigger scintillators and selects coincidences. A trigger signal is sent to the GEM DAQ with a delay which can be adjusted in software. This was needed because both the GEM charge collection time and the shaping time of the GP5 analogue chain are longer than the shaping time of the scintillator preamplifiers. In order to find the best setting for the delay, runs were made with the ^{90}Sr source irradiating the GEM detectors from above with the trigger scintillators placed behind. Data was recorded by externally triggering the GEM detectors from coincidences evaluated by the scintillator central DAQ. A wide range of delay values were tested from 0 to 4000 ns. The most probable value (MPV) of the pulse-height spectrum in the GEM detectors was then determined for each run. Shown in figure 5.27 is the result, for 3 and 5 sigma CM rejection threshold. The peak in the MPV occurs with a delay of 300 ns, very close to the slow shaping time of the GP5. To evaluate any improvement using the correct timing, another MIP efficiency scan was made of the GEM detectors over their range of operating voltage using a 300 ns delay. A significant improvement was observed as compared with the efficiency test using NIM electronics where the delay was not measured. Shown in figure 5.28 is the result. With the external trigger arriving with the correct timing to the GEMs, an efficiency of over

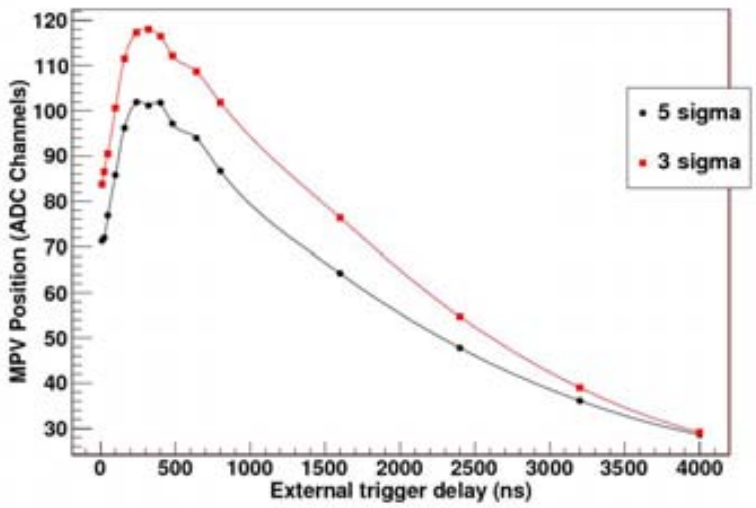

Figure 5.27: The analogue response of the GP5 and GEM detectors triggered externally from the 2 trigger scintillators of the range telescope with a time delay generated within the FPGA on the central DAQ of the scintillators (master) before sending to the GEM central DAQ.

95% was achieved even at a gain of 10^4 and at 4 sigma CM threshold. For 3 sigma CM threshold, which is sufficient to allow an accurate recognition of the hit channels and a good energy resolution, an efficiency of 99% was measured at the same voltage. A delay of 300 ns was used for all subsequent measurements.

With all scintillator and GEM DAQs triggering correctly on single particles, we turn to the analysis of the data delivered to the PC. Because both the GEM and scintillator DAQs communicate by unique USB connections and because USB is a non-synchronous protocol, a time-stamping method was implemented. For each coincidence from the trigger scintillators a unique 24-bit time stamp is generated on the scintillator central DAQ from its main clock running at 48 MHz. The time stamp is bundled together with the range telescope data for transfer to the PC but is also transmitted to the GEM central DAQ (along with the trigger signal) for bundling with the GP5 data. In this way, synchronization of the range telescope data with the GEM tracking data is performed in software by matching the time stamps in both the GEM and scintillator data sets.

The final PRR10, fully assembled yet with cover removed is shown in figure 5.29. All in all, the PRR10 consists of two TGEM detectors, two 3 mm scintillators for triggering, and thirty 3 mm scintillators for measuring the residual range of nearly 10 cm water equivalent. Four stainless steels

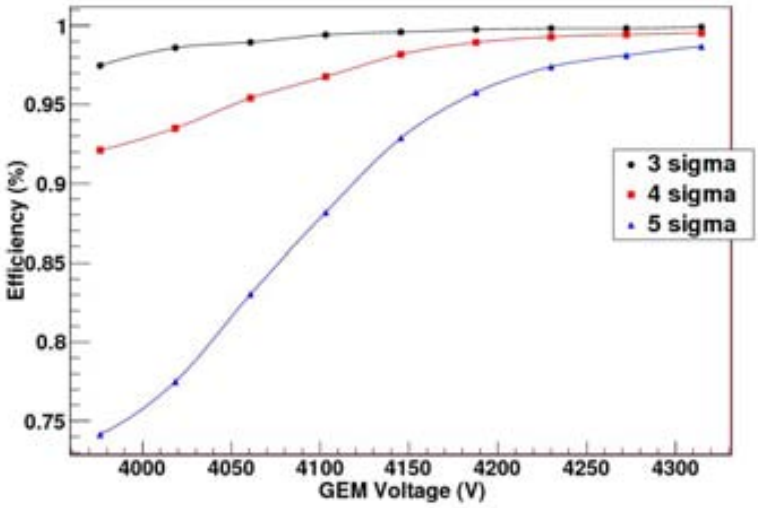

Figure 5.28: Detection efficiency of a triple-GEM detector to MIPs in external trigger mode after trigger synchronization has been optimized.

rods have been used to align the GEM detectors precisely with respect to themselves and the range telescope. The rods have been purposely made longer than required for aligning phantoms and absorbers during the beam tests and for easily adjusting the distance between the GEM detectors if required. During our beam tests, the GEMs have been spaced at 10 cm from each other in order to yield a good angular resolution. The range telescope has a total effective thickness of just over 10 cm (30 scintillators 3.33 mm thick and density 1.032 g/cm^3) and can measure the residual range of protons having energies between about 50 and 130 MeV. This energy range can be adjusted by placing absorbers in front of the telescope, or between the GEM detectors and trigger scintillators.

The PRR10 has been designed to be compact and modular, allowing things to be easily assembled and taken apart for debugging. The two GEM detectors can be removed (as a block or individually) and tested independently. The same is true for the entire range telescope and the scintillator modules. In addition to the fundamental detector components, the assembly provides simple rear-panel connections of the USB cables, the GEM gas inlet and outlet, and low-voltage power for the DAQ boards. Two HV connectors have also been routed to the back panel to allow the GEMs to be optionally powered by an external power supply. A protective cover was also designed and implemented, shown previously in figure 5.2. In order to monitor the temperature, which alters the gain of the SiPM and thus the scintillator response, several temperature sensors have been included which

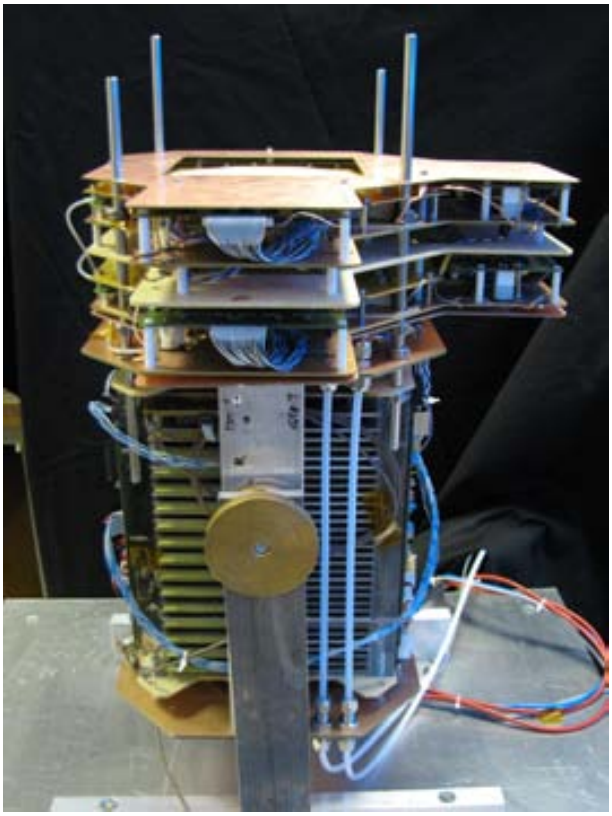

Figure 5.29: The AQUA PRR10 mounted on a portable table and rotated in vertical position for tests with cosmic muons.

communicate through the scintillator central-DAQ. In addition, the entire detector has been mounted on a portable table which holds a PC and all the needed power supplies. This allows for easy transport and for piloting of the device using a remote connection, an important condition for beam testing where the user must be out of the test beam area during irradiation. On the portable table, the PRR10 can be easily rotated into a vertical position for testing with cosmic muons. In the absence of a source of high-energy charged particles which pass through the entire detector, this is useful for verifying the correct operation of all scintillators.

5.2.4 The PRR10 graphical user interface

In order to facilitate the control and operation of the PRR10 prototype during beam tests, an elaborate and custom-built software tool has been developed. All aspects of the software have been programmed in LABVIEW, from the detector control and readout to the analysis and display of the data. LABVIEW was selected mainly because it is highly efficient for creating Graphical User Interfaces (GUI) which allow the user to interactively control the various aspects of the detector (HV, thresholds, etc) as well as navigate through various display options both on-line during data taking and off-line in analysis. LABVIEW is also powerful for parallel data processing which has simplified the task of synchronizing the data from both scintillator and GEM central DAQs.

Thanks to the nice features of the LABVIEW programming environment, the AQUA group has been able to produce a single software package for the PRR10 which provides all the necessary functionality. Although a full description of the PRR10 LABVIEW GUI is beyond the scope of this thesis, many of the images produced during beam tests with the PRR10 are presented as they appear in the software. So that the reader appreciates from where these images have been taken, the most important aspects of the software are described briefly here. For more detailed information and the software and its architecture the reader is encouraged to refer to the PRR10 User Manual or the following reference [55].

Piloting of the PRR10 with the LABVIEW GUI starts with opening the main application, shown in figure 5.30. Before data taking begins, the user can set the thresholds on the trigger scintillators, apply previous calibration settings to the scintillator trim-DACs, change the firmware on the FPGAs of the central DAQs, adjust and monitor the HV on the GEM detectors, and setup the parameters of the data acquisition (such as number of events to be acquired and the file outputs). The temperature can also be recorded at regular intervals and monitored throughout the course of operation.

During data taking, the data is both saved to disk and post-processed in a set of parallel loops which are optimized by LABVIEW automatically during compilation. The on-line mode allows the user to visualize the data in real-

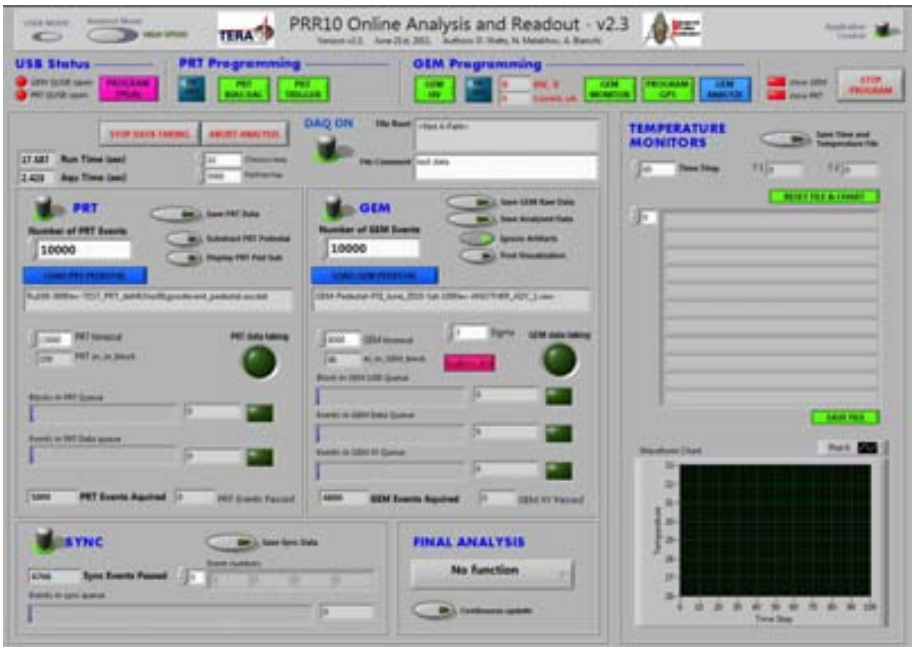

Figure 5.30: The main user interface of the PRR10 software written in LABVIEW.

time as it is being recorded. For example, the response of the scintillators or the tracking of the GEM detectors can be observed at any time during data taking by opening a visualization tool which displays the response from all scintillators for each event. The GEM detector data can also be monitored on-line using a similar visualization tool. This is practical for debugging as well as for quickly positioning the detector correctly in the beam line. In addition, the time-stamp synchronization between scintillator and GEM data sets is also processed on-line (though the raw data can also be saved before synchronization and made off-line) and the assembled data passed to a graphical imaging tool which displays the data as a 2D proton radiography.

In the analysis of the data for imaging, the XY position is first determined in each GEM detector by taking the maximum-hit-channel in each cluster in each axis of the GEM detectors. Although the position could be found more precisely by fitting the center-of-mass of the charge in the serial GP5 data, the simpler maximum-hit-channel method was favored in our tests because it is faster and because it gives a good spatial resolution on the order of the pitch of the GEM XY readout (0.4 mm). Using the XY data, the pixel location of each event can be selected from either GEM, or as the average between the two. For the beam tests presented below we have chosen a pixel size of 400 μm, equivalent to the separation between strips in the XY-readout board of the GEM detectors. A pixel size of 1 mm can also be selected, but we have chosen to use the higher resolution in displaying

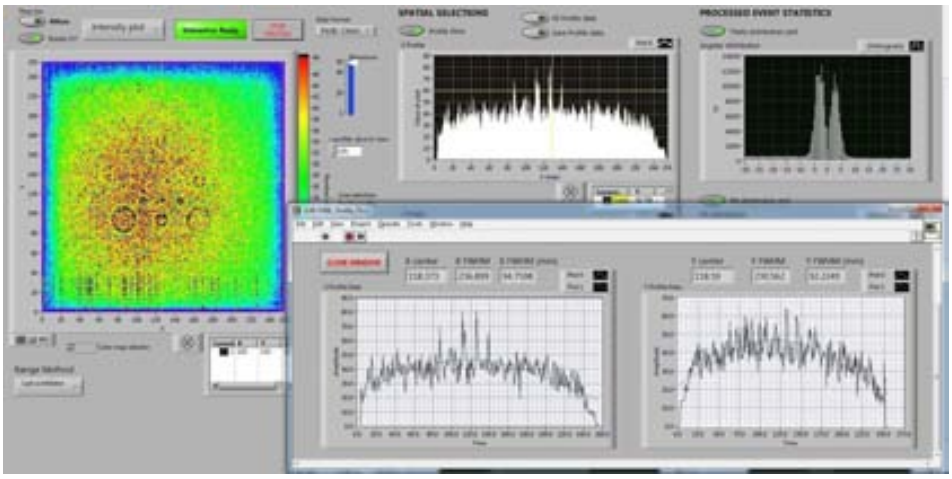

Figure 5.31: A screen-shot of the proton radiography software imaging tool used to analyze the PRR10 data during a run with the hole phantom at PSI. The intensity of the beam in 2D space is been selected for display in the image on the left. Also shown is a pop-up subroutine of a slice in X and Y through the image data, which in this case has been used to measure the beam profile.

image data.

Once the pixel for each event is known, the range is determined from the response of the scintillators. As the data is accumulated, a running average of the range is calculated for each pixel in the image space. This can be expressed as,

$$\overline{R_{n+1}} = \frac{\overline{R_n} n + R_i}{n+1}$$

where n is incremented with each track projected to the pixel x, y. This allows the PRR image to be updated during data taking while keeping the size of the memory for the image space constant. Although the user can observe the radiography as the data is acquired, the synchronized data is also saved in a simplified format so that it can also be re-loaded later using the same program. In off-line analysis mode the user can apply different analysis settings, make various selections of the data in the image space, or chose different display options to features different aspects of the data. For illustration, a screen-shot from the radiography imaging tool is shown in figure 5.31.

5.3 Beam Tests at PSI

The PRR10 was installed at the Paul Scherrer Institute (PSI) in Villagen, Switzerland, for tests with a proton beam. PSI is a physics laboratory where

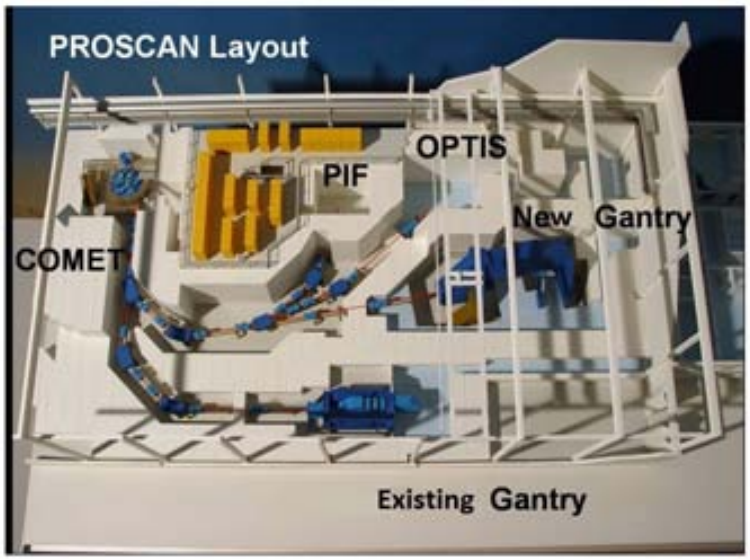

Figure 5.32: Layout of the PROSCAN accelerator at PSI. The COMET cyclotron and the beam line which delivers protons to the PIF are visible. The beam line for the PIF is the same as for the OPTIS project.

clinical proton therapy has been performed for a number of years, active in the treatment of patients with deep-seated tumours. The center is capable of delivering protons of medical energies using a spot-scanning technique. In 2000, the success of the OPTIS project for treating eye cancers led to the birth of the PROSCAN project. Installation and commissioning tests of the COMET 250 MeV superconducting cyclotron completed in 2007 making it possible to treat patients full-time using the existing gantry. A layout of the PROSCAN accelerator is shown in figure 5.32. A new gantry is currently being commissioned.

In addition to therapy, an experimental hall, called the Proton Irradiation Facility (PIF) is available for beam tests. Designed for testing of spacecraft components in collaboration between PSI and the European Space Agency (ESA), the PIF is also available to other users wishing to access a proton beam of medical energies. Since the PROSCAN accelerator is used to serve both gantry room as well as OPTIS, beam-tests at the PIF must be carried out during weekends and night-shifts.

The proton beam, delivered from the COMET cyclotron into the beam transport line passes first through a primary energy degrader which allows the beam energy to be modulated from 230 MeV down to 70 MeV. Preset beam optics setups are available for energies of 230, 200, 175, 150, 100, and 70 MeV, optimized for both wide and narrow beam profiles of between 100 mm and 6 mm FWHM [56]. For energies lower than 70 MeV there is a local

Figure 5.33: The AQUA PRR10 installed in the PSI experimental hall ready for testing with proton beams.

energy degrader located in the experimental hall at the beam exit from the accelerator. When used, the local degrader introduces a large dispersion in the beam energy which degrades the resolution of our range measurements. This has been observed in all of our measurements with a wide beam which is produced by making use of the local energy degrader.

Another important requirement for our tests has been to limit the intensity of the proton beam to below 10^5 protons/s. This has been achieved using passive collimators located within the beam transport line. For all measurements presented here, beams with a rate of about 10^4 protons/s have been used.

Figure 5.33 shows the AQUA PRR10 mounted and awaiting irradiation in the PIF at PSI. The local energy degrader consisting of layers of copper absorber is shown on the far left of the picture, about 1 m from the PRR10 detector. One of the phantoms used for the imaging tests described below is mounted on the alignment rods immediately in front of the GEM detectors. The PRR10 has been removed from its portable table because of space limitations in the PIF experimental hall. The cover was also removed to reduce excess heating which was observed over the course of the beam tests. This has since been improved with the addition of a simple ventilation system which keeps the temperature of the device stable even during long shifts.

5.3.1 GEM verifications

Our first tests have been to verify the correct working of the GEM detectors with protons and to choose a suitable working voltage which gives a

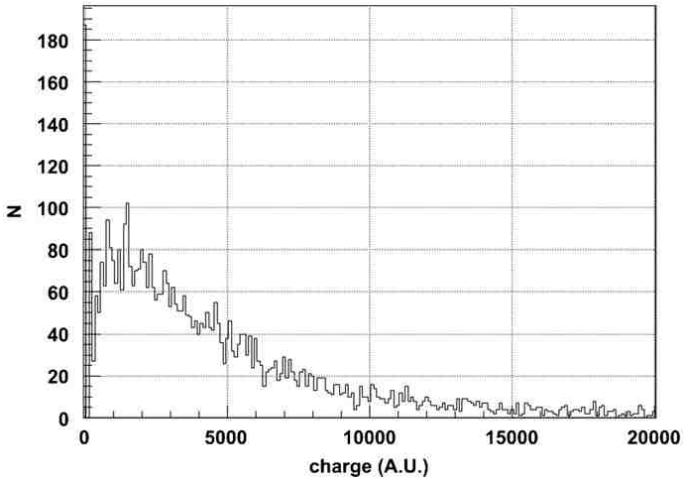

Figure 5.34: Pulse height spectrum in one axis of a triple-GEM chamber irradiated with 230 MeV protons (courtesy of A. Bianchi). The GEM voltage is -3900 V.

minimum chance of discharges while maintaining a good efficiency. This was done by trial-and-error using a beam of 230 MeV protons and using the coincidence trigger generated by the pair of trigger scintillators. A good result was found at a voltage of -3900 V on the GEM detectors. Here, the efficiency of each chamber was found to be greater than 95% (at 3 sigma CM rejection) with practically no discharges or excess noise on any of the channels. For all subsequent measurements, the GEMs were held at -3900 V.

Figure 5.34 shows the pulse height spectrum in one axis of one of the GEM chambers for 230 MeV protons. The spectrum has the distinctive Landau shape, expected for charged particle tracking using gaseous detectors, and the MPV of the distribution is well above the noise (barely visible at the left of peak). Shown in figure 5.35 is the correlation of the pulse height in X and Y for one of the GEM chambers. As expected, there is a nearly one-to-one correlation, indicating that the GEM chambers are functioning well with equal charge sharing between X and Y strips.

The user interface was also tested after the GEM detectors were deemed to be operating in good conditions. Using a beam of 230 MeV protons delivered from the COMET cyclotron to the PIF, the PRR10 was operated in on-line mode, allowing for a verification of the data as it is acquired. Shown in figure 5.36 is a screen-shot from the user interface in the PRR10 Proton Radiography program with the 230 MeV beam. The beam profile is accurately represented in both the image on the left and the two graphs on the right which correspond to a slice through the 2D data set at the position of the cross-hairs in the image on the left. The horizontal and vertical beam

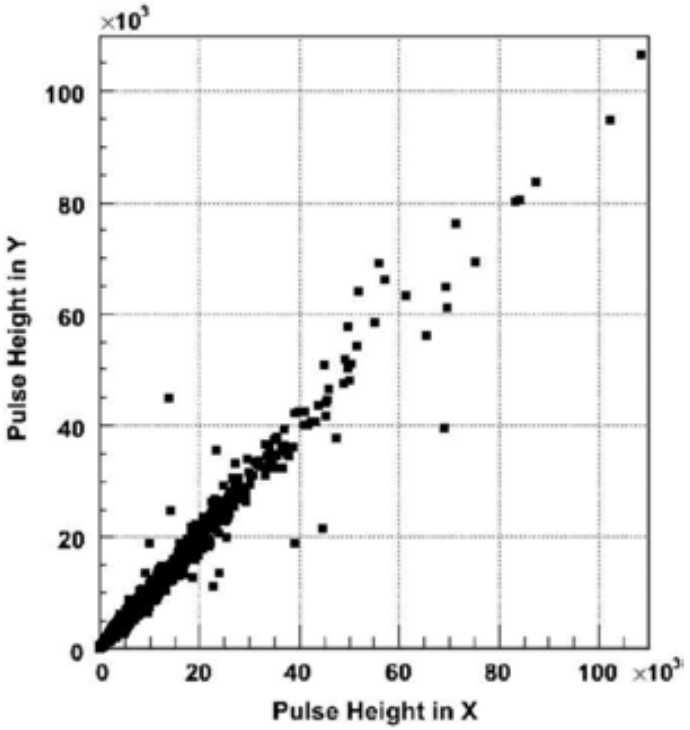

Figure 5.35: Correlation between pulse height measured on the X and Y planes for one of the triple-GEM detectors irradiated with 230 MeV protons (courtesy of A. Bianchi). The GEM voltage is -3900 V.

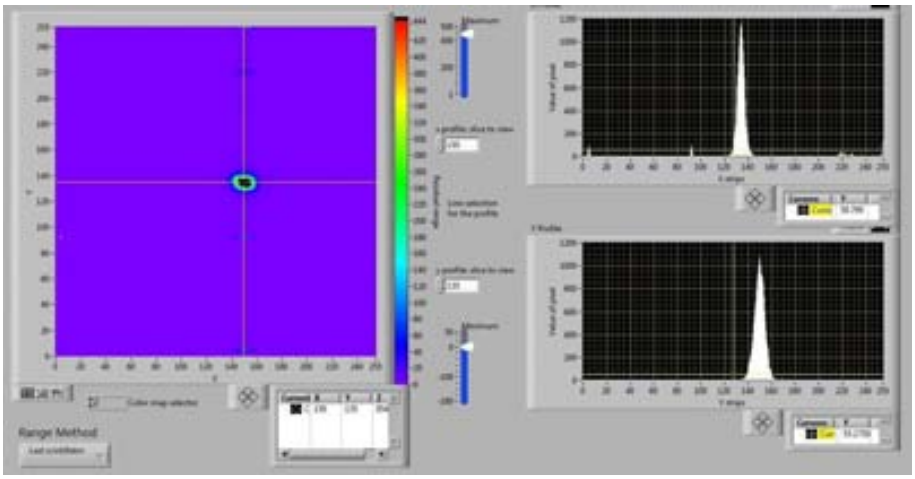

Figure 5.36: Screen-shot from the Proton Radiography user interface for the narrow beam of 230 MeV protons used to calibrate the response of the 30 scintillator modules of the range telescope. The beam profile is 3.7 mm and 2.4 mm FWHM in the horizontal and vertical directions, respectively.

widths are 3.7 mm and 2.4 mm FWHM, respectively.

5.3.2 Range telescope calibration

The next tests that were performed involved calibrating the 30 scintillator modules of the range telescope. Because of the differences in light yield, optical coupling, scintillator thickness, and SiPM gain, all modules have a slightly different response to the same energy deposition at the same SiPM bias voltage. In order to unify this response across all modules, a calibration procedure must be followed and is described here. The calibration should be made with charged particles of the highest energy which pass entirely through the PRR10. During the PSI beam tests, a narrow beam of 230 MeV protons was used for calibrating the scintillators, the highest available energy at the PIF.

Shown for example in figure 5.37 is the pulse height distribution recorded on a single scintillator module with a beam of 230 MeV protons which passes entirely through the PRR10. The response is well above the noise, yet far from saturation, an important criterion considering we wish to visualize the Bragg peak within the stack where the energy deposition will be several times higher than it is here.

The first step of the calibration procedure is to set the trim DACs on all modules to 2.5 V, allowing adjustments to be made in either direction later. Data is then recorded on all 30 modules for a run with the 230 MeV protons beam. After the accumulation of a number of events (10^3 is sufficient), the pulse-height distributions in each scintillator should be checked visually to

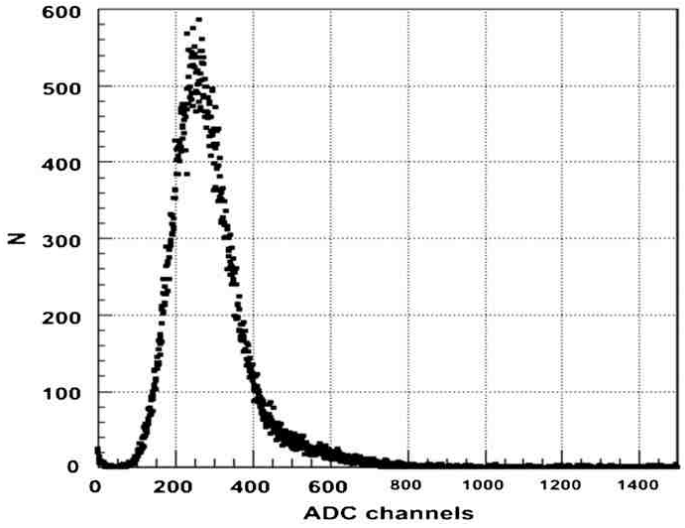

Figure 5.37: Pulse height distribution measured in a single scintillator module with irradiation of 230 MeV protons.

be sure that the MPV is above the noise and far from saturation. The base voltage for each of the 4 scintillator cables of the range telescope can be modified if needed. Runs of 10^3 - 10^4 230 MeV protons are then acquired using several values of trim-DAC voltage applied to all modules. Shown on the left of figure 5.39 is the mean response of all 30 modules to the 230 MeV proton beam using three values of DAC voltage, 1 V, 2.5 V and 4 V. The non-uniformity between modules before calibration is clearly visible. Using a semi-automated method, the target DAC voltages which would give a uniform response over all scintillators are calculated from the 230 MeV calibration data made at several values of bias voltage. This is done by fitting the pulse-height spectrum of each module and using the peak value at each trim DAC voltage to extrapolate the target setting. In the PRR10 software, the fits are made graphically for all scintillators allowing the user to visually verify their integrity and make adjustments if necessary. The calculated target trim-DAC voltages are then programmed on each module and the result of the calibration can be tested immediately with the 230 MeV beam. If the response is not uniform a further iteration can be performed adding the results of the newly calibrated run to the data. In general, we have observed that a single calibration iteration is sufficient for obtaining a uniform response over all scintillators. Once the calibration is deemed satisfactory, the setting can be saved for future reference.

Shown on the right in figure 5.39 is the MPV of the pulse-height spectra in each of the scintillator modules for various proton beam energies after a single calibration iteration has been performed. At 230 MeV the response is flat, the condition of the calibration. Other beam energies were also recorded

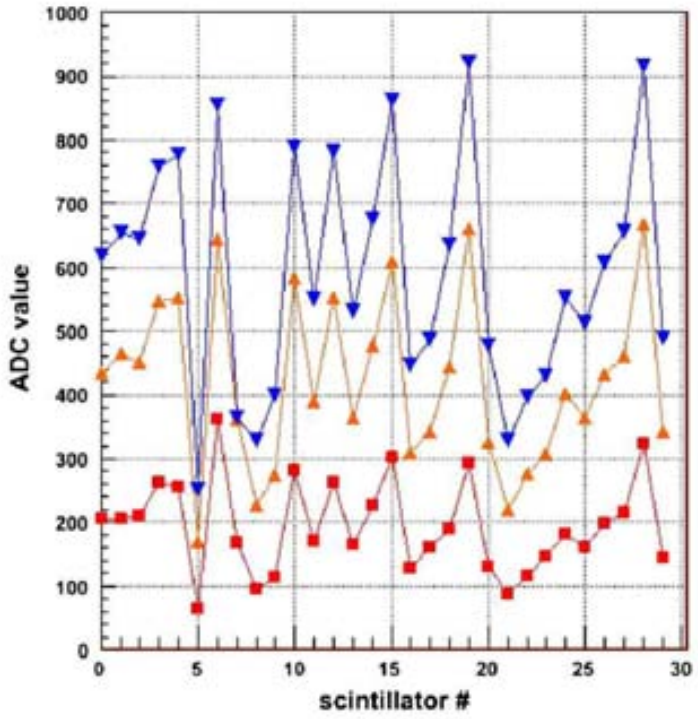

Figure 5.38: The response (MPV) of all 30 scintillator modules to 230 MeV protons at three different bias voltage settings set on all modules (no correction).

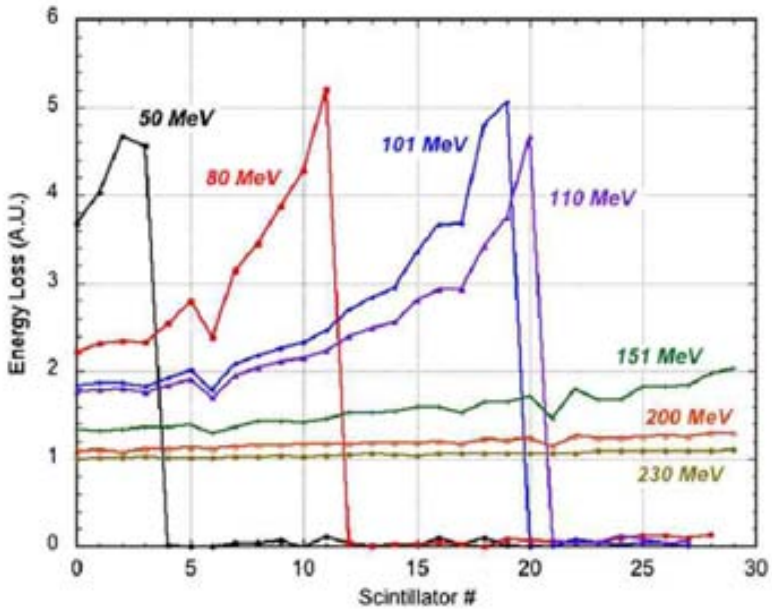

Figure 5.39: The response of all 30 scintillator modules to various proton beam energies after the SiPM bias-voltage corrections have been applied.

after the calibration: 200 MeV, 151 MeV, 110 MeV, 101 MeV, 80 MeV, and 50 MeV. For those beams which stop inside the range telescope, the Bragg peaks are clearly visible.

Range resolution for 99.7 MeV narrow beam

Using a proton beam of 99.7 MeV we have investigated the range resolution that can be achieved by our range telescope. A narrow beam has been selected in order to minimize the momentum spread in the beam itself which can degrade the range resolution according to equation 5.2. At PSI, the beam is generally broadened by introducing a thin scattering foil immediately following the primary energy degrader. Though the exact amount of energy degradation introduced from such a foil is not known, it has been observed to be generally larger for wider beams during the course of our measurements.

Shown in figure 5.40 is a screen-shot of the PRR10 Proton Range Radiography user interface during a run with a centered 99.7 MeV proton beam. The image on the left shows the 2D beam profile, where the color-coded Z-axis represents the beam intensity (number of events recorded for each pixel). The size of each pixel is 400 μm by 400 μm, the pitch of the XY readout in the GEM detectors. The X and Y axes are displayed in units of strips (from 0 to 255) which cover the entire 10x10 cm^2 active area of the

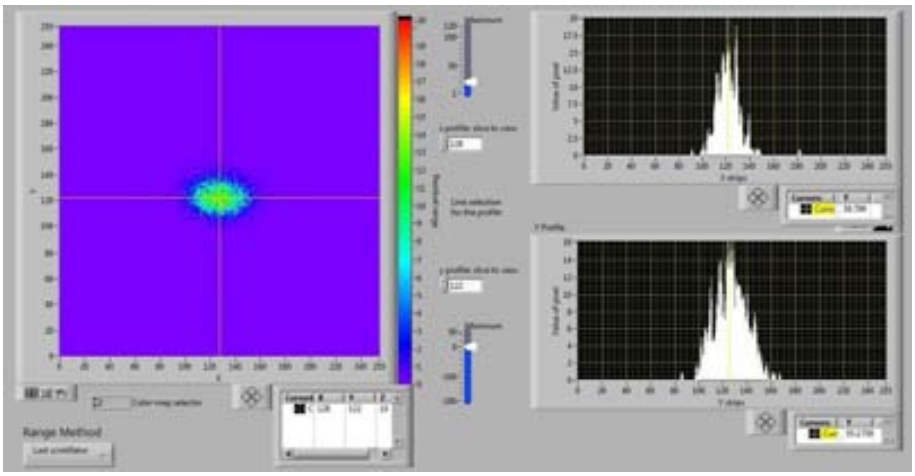

Figure 5.40: Screen-shot from the Proton Radiography user interface for the narrow beam of 99.7 MeV protons used for many of the range telescope calibrations. The beam profile measured is 12 mm and 8 mm FWHM in the horizontal and vertical directions, respectively.

GEM detectors. The beam width measured by the GEM detectors is approximately 12 mm FWHM and 8 mm FWHM in the horizontal and vertical directions, respectively.

Different methods of determining the range resolution have been investigated. The first method that was applied is a purely digital recognition of the last hit scintillator module. For each event, the deepest module which records a signal over threshold is extracted by a simple algorithm which moves through the scintillator data starting with the scintillator closest to the GEM detectors. As soon as the signal falls below threshold, the value of the previous scintillator determines the range of that event. When all events are processed, the distribution of the "last-counter-hit" can be displayed, as shown in figure 5.41 for a run of 10^4 99.7 MeV protons. A Gaussian fit of the data in the peak gives the mean range (in units of scintillator) which, in this case, has been measured to be 17.93 scintillator units. The width of the distribution is 0.4365 scintillator units sigma, which gives the uncertainty in the range measurement for this particular beam run. Applying the effective thickness of the scintillators as 3.64 mm water-equivalent (see the calibration below) we can also express the range uncertainty as 1.59 mm sigma.

It should be noted that the tail on the left of the peak of the range distribution is the result of nuclear interactions where the proton is absorbed by a nucleus of the range telescope material and therefore does not travel its full range as expected from purely electromagnetic interactions. These nuclear interactions occur roughly 20% of the time with proton beams of

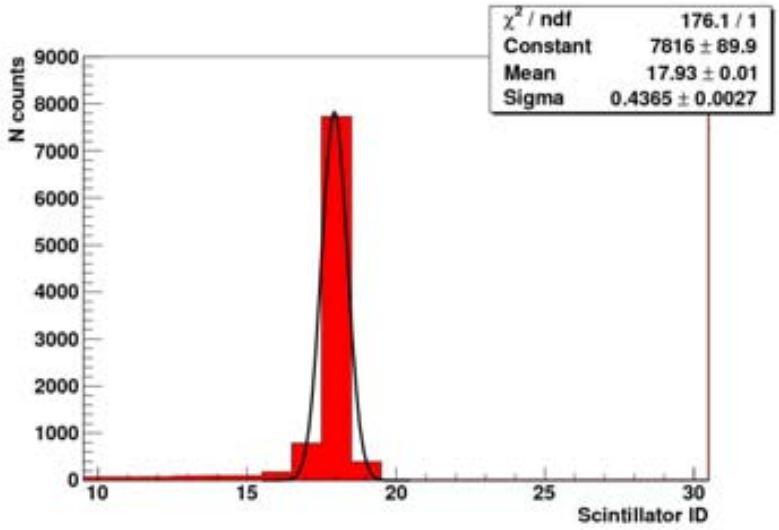

Figure 5.41: Range distribution for a narrow beam of 10^4 99.7 MeV protons. The "last-counter-hit" range determination method has been used for each proton recorded. The standard deviation of the distribution, which reflects the range uncertainty of the PRR10, has been measured at 0.44 scintillator units sigma.

this energy and have an important consequence on the analysis of the data for proton radiography as we shall see.

An alternative approach to measuring the range is to fit the response of the last few scintillators over threshold with a function approximating the shape of the Bragg curve. This can be done for each individual proton track and has been carried out for the same data set of 10^4 99.7 MeV protons shown in figure 5.41. Although this technique was expected to yield a more narrow distribution - albeit with a substantial increase in analysis time - we obtained a standard deviation of 1.58 mm, essentially the same as the simpler (and faster) digital method. For all subsequent measurements and analysis, the "last-counter-hit" range determination has been used.

The range resolution that we have measured, 0.44 scintillator units (or 1.59 mm WEPL), reflects all the uncertainties that were discussed previously and summarized numerically by equation 5.2. Since the mean range sits at 17.93 scintillator units - nearly the middle of the 18^{th} scintillator - and since no phantom has been used, we can say that the measured range is 17.43 scintillators units, or about 19.43 total if we include the two trigger scintillators. The relative range uncertainty is therefore about 0.44/19.43 or $(\frac{\sigma_R}{R})_{measured} = 2.3\%$ for this beam of 99.7 MeV protons.

Using equation 5.2 we can calculate the relative uncertainty $(\frac{\sigma_R}{R})_{beam}$

caused by the energy-spread of the beam by assuming that the contribution from straggling is 1.1% and that our telescope has an intrinsic resolution of 3 mm/$\sqrt{12}$, or 1.11% at this energy of 99.7 MeV. Taking $(\frac{\sigma_R}{R})_{measured} = 2.3\%$ and subtracting quadratically the expected values for the detector and straggling, we can infer a relative range uncertainty in the beam of $(\frac{\sigma_R}{R})_{beam} = 1.7\%$, which corresponds to an energy variation of $(\frac{\sigma_E}{E})_{beam} = 0.9\%$.

This measured value of the relative range uncertainty has been made with a beam of 99.7 MeV protons, which have a range of less than 8 cm water-equivalent, somewhat too small for clinical work with patients. If we extrapolate the measured range uncertainty to a beam having 15 cm WEPL, keeping the relative contributions of the straggling and beam energy variation the same, we expect to measure $(\frac{\sigma_R}{R})_{measured} = 1.9\%$ or $\sigma_R = 2.85$ mm.

In practice, the error in the mean range, when averaged over the number of events, N, in each image element will improve as $1/\sqrt{N}$. For the narrow 99.7 MeV beam measurement above and for 100 events per pixel, the error in the residual range becomes 0.23% or 0.16 mm water-equivalent. For a 150 MeV beam, which could be used to image targets of up to 15 cm WEPL, this error becomes 0.19% or 0.29 mm, assuming the energy variation of the beam can be kept below 1%. In order to provide a contrast resolution for proton radiography over the entire residual energy of such a beam emerging from a patient, however, the telescope must have an equivalent thickness of greater than 15 cm WEPL. For this reason new versions of the AQUA PRR are planned with 48 scintillators, the maximum that can be uniquely addressed electronically on each cable of our scintillator central-DAQ.

The fact that the *relative* range uncertainty decreases with higher energy does not mean that the accuracy in the density measurement of the target improves with higher energy. In fact, the density resolution, σ_ρ, is proportional to the *absolute value* of the range uncertainty, σ_R (as stated in equation 5.3), which clearly increases with higher energy. This implies that the best density measurement for a range telescope will be made with a beam having the lowest possible energy which still traverses the target. Despite this fact, a lower energy of the primary beam does not necessarily lead to a better proton radiography image. The reason is that at lower energy, more MCS occurs within the target leading to a loss in spatial resolution. It follows then that we can expect a trade-off between the density resolution and the spatial resolution of a PRR image as we change the energy of the primary beam. Defining precisely this trade-off is currently being studied by the AQUA group using Monte-Carlo simulation.

Scintillator thickness calibration

The effective thickness of the scintillator modules, measured in WEPL, was also a parameter of the PRR10 that was calibrated during beam tests at PSI. This was accomplished using an approach involving a series of 1 mm absorbers measuring 12x12 cm^2 placed directly in front of the PRR10 detector. The absorbers are made of acrylic glass (PMMA) which has the density 1.18 g/cm^3. In order to calculate the water-equivalent thickness of the scintillator modules precisely, the thickness of the absorbers has been measured accurately using a digital caliper. Stacking five absorbers together and averaging measurements along all sides, we have measured an average thickness of 1.16 mm per absorber. Adding the contribution of the density of PMMA, we can say that each absorber has an average thickness of 1.37 mm WEPL.

The idea of the following tests was to measure the change in the mean range with each added absorber when irradiating the PRR10 with proton beams of fixed energy which stop inside the detector. Two different beams were used: a narrow beam of 99.7 MeV (the same as used in the previous study) and a wide beam of 101 MeV. For the narrow beam, 10^4 protons were recorded for each run, while for the wide beam 10^5 events were acquired per run. The "last-counter-hit" range method has been used to produce the range distributions. Shown for example in figure 5.42 are the distributions for the narrow 99.7 MeV beam with no absorbers and with 5 absorbers present. Fits of the data have been made to determine the mean range and the width of the distributions. Figure 5.43 shows the data with fits for the wider beam of 101 MeV, with 1 absorber and 5 absorbers. A considerable increase in the width of the range distributions can be seen for runs at 101 MeV where a wide beam has been used. For the wide 101 MeV beam, the width has increased to roughly 1.2 scintillator units or about $(\frac{\sigma_R}{R})_{measured} = 6\%$. Applying equation 5.2 as before we can infer that $(\frac{\sigma_R}{R})_{beam}$ has increased from 1.7% to 5.8%, which is equivalent to $(\frac{\sigma_E}{E})_{beam} = 3.2\%$. This increase can be explained by the fact that at the PIF, one of the copper plates of the local degrader must be inserted into the beam to produce a wide beam which is needed for imaging purposes. It also results in a significant increase to the uncertainty of the beam energy and thus a widening of the width of the range distribution as observed. To compensate for this increased uncertainty, more events were recorded for runs with the wider beam at 101 MeV.

By fitting the peak of the range distributions for all runs, the mean range has been determined as a function of the number of absorbers for both the narrow 99.7 MeV beam and the wide 101 MeV beam. The results are summarized in figure 5.44. As expected, the response is linear for both data sets and varies similarly regardless of whether a narrow or wide beam has been used. The slope of the response, derived from a linear fit to each data set, can be used to calculate the effective thickness of the scintillator

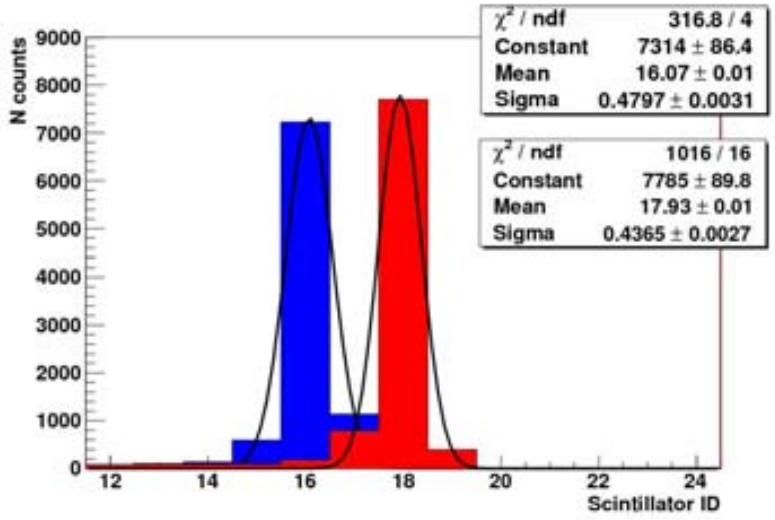

Figure 5.42: Range distributions for 0 mm and 5 mm of PMMA absorber placed directly in front of the PRR10 detector. A narrow beam of 99.7 MeV has been used and 10^4 protons have been recorded for each run.

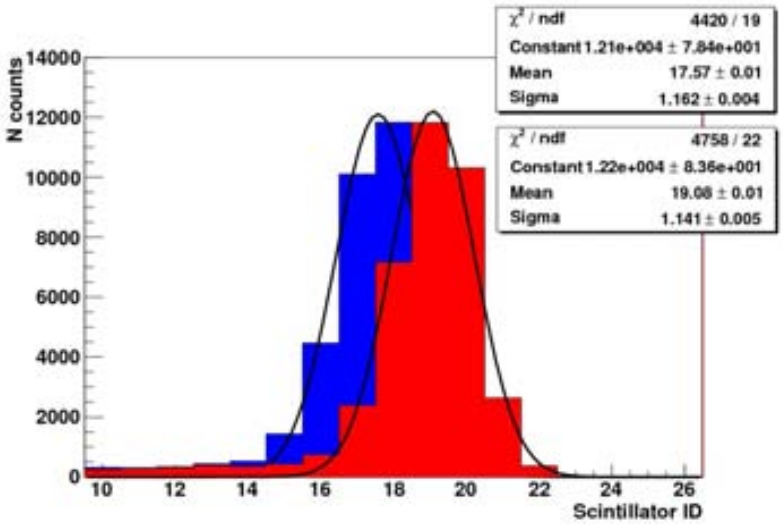

Figure 5.43: Range distributions for 1 mm and 5 mm of PMMA absorber placed directly in front of the PRR10 detector. A wide beam of 101 MeV has been used and 10^5 protons have been recorded for each run. The wide beam has been produced using the local degrader and results in a spread of the beam energy and therefore a wider range distribution.

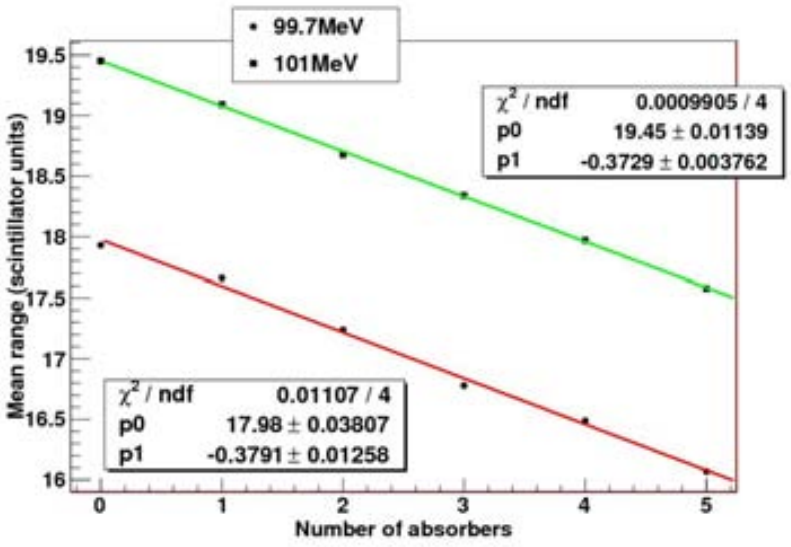

Figure 5.44: A summary of the PMMA absorber tests used to calibrate the effective thickness of the PRR10 scintillators at two different protons beam energies: 99.7 and 101 MeV. The last-counter-over-threshold method has been used to generate the range distributions which are then fit with a Gaussian.

modules knowing the water-equivalent thickness of the absorbers. Using 1.37 mm WEPL for each absorber we can infer an effective water-equivalent thickness of 3.61 mm for the 99.7 MeV data and 3.67 mm for the 101 MeV data. Both are in good agreement to each other and only slightly larger than the initial estimate of the scintillator's effective thickness of about 3.6 mm. For all subsequent calculations and calibrations the average value of the two measurements, 3.64 mm, has been used as the effective water-equivalent thickness of the scintillators.

Absolute water-equivalent range calibration

Using the effective water-equivalent thickness of the scintillator modules calibrated from the previous section, we can convert the measured range from units of scintillator into units of water-equivalent range. Using the data for various energies of the proton beam, 50, 80, 99.7, 101 and 110 MeV, we have first calculated the mean range using the "last-hit-counter" method and then converted the values into equivalent range using the effective scintillator thickness of 3.64 mm WEPL. We have also added the effective thickness of the two trigger scintillators. To be specific, let us consider an example where the peak of the range distribution falls on the 10^{th} scintillator. Since a mean

range of 10.0 means that the beam has stopped in the *middle* of the 10^{th} module, we add 1.5 scintillator units to the mean range data to account for the trigger scintillators and give the total scintillator thicknesses traversed.

Shown in figure 5.45 is the water-equivalent range measured by the PRR10 as a function of the beam energy with all 32 scintillators. In addition, the water-equivalent thickness of each GEM detector has been calculated and included (3.6 mm WEPL each) as well as the contribution from the air between the beam nozzle and the PRR10 (1.5 mm WEPL) which was 1 m. The contribution of both GEMs and the air has also been plotted (in blue) which adds a shift of the data to a higher value. Plotted for comparison is the projected range of protons in water obtained from a Monte-Carlo simulation of a proton beam incident on a water phantom. The experimental data, with GEM and air contributions included, is in fairly good agreement with the simulated data but with a maximum deviation of 4.4 mm WEPL at the energy of 110 MeV, which is nearly 5% of the proton range. A large discrepancy between experimental data and simulation is also observed at 99.7 MeV. One reason for these deviations could be variations in the scintillator thickness which were previously measured as ± 0.2 mm, or about 8% of their thickness. This could cause a discrepancy since a shift in the absolute range may get larger as the number of scintillators traversed increases. The maximum possible uncertainty introduced in the range measurement from variations in scintillator thickness has been displayed along with the data using error bars in the plot given in figure 5.45. The measured and simulated data agree within the maximum tolerances of the scintillator thickness.

Variation in the thickness of scintillators is unlikely to be the sole cause of the differences between the range measured by the PRR10 and simulation, since on average, the variations in thickness will tend to cancel each other out the deeper the protons penetrate into the range telescope. One possibility is that the contribution from the GEM detector and air has been underestimated (here calculated as about 8.7 mm WEPL) or that the variation in the scintillator thickness is larger than measured, especially near the center of the modules. Another explanation may be uncertainties in the actual beam energy for each run. Although the beam parameters are expected to be rather stable at the PIF, the exact energy of each beam was not measured during our beam tests by any other instrument than the PRR10. Instead we relied on measurements that had been made previously for predetermined beam settings, which sometimes made use of the local degrader and other times not. In particular, the large discrepancy between the range data for the 99.7 MeV narrow beam and the 101 MeV wide beam, which should yield nearly identical range measurements, are perhaps an indication that the exact energy was not well recorded during our studies at PSI. Regardless of the cause, this discrepancy between the absolute range measured by the PRR10 and the result expected from theory can be easily calibrated in future beam tests using the methodology described here and

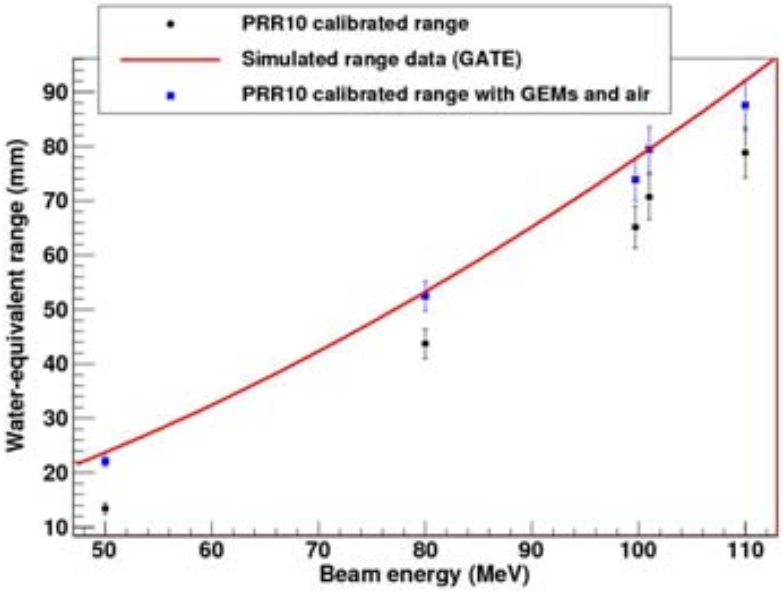

Figure 5.45: Water-equivalent range of proton beams of various energy measured by the PRR10. The range has been calculated using the calibrated thickness of the scintillator absorbers both with and without the water-equivalent contribution from the GEMs and air. The expectation from simulation is also plotted for comparison and matches the corrected data within 3%.

an accurate knowledge of the beam energy.

5.3.3 Measurements with phantoms

In order to study its imaging capabilities the PRR10 was exposed to a proton beam with the addition of phantoms placed immediately in front of the GEM detectors. In most cases a wide beam has been used which covers the entire 10x10 cm^2 active area of the PRR10. Producing the wide beam requires making use of the local energy degrader located in the PIF experimental hall just after the beam exit from the beam line and just 1m in front of the PRR10 detector. This results in a spread in the beam energy which causes an increase in the width of the range distributions as observed earlier.

The intensity profile of the beam can be extracted by the analysis software by making a slice through a horizontal and vertical selection of the image data and plotting the number of events in each pixel along the slice. A subroutine of the imaging software has been created for this purpose which allows the user to quickly and conveniently measure the beam profile. The

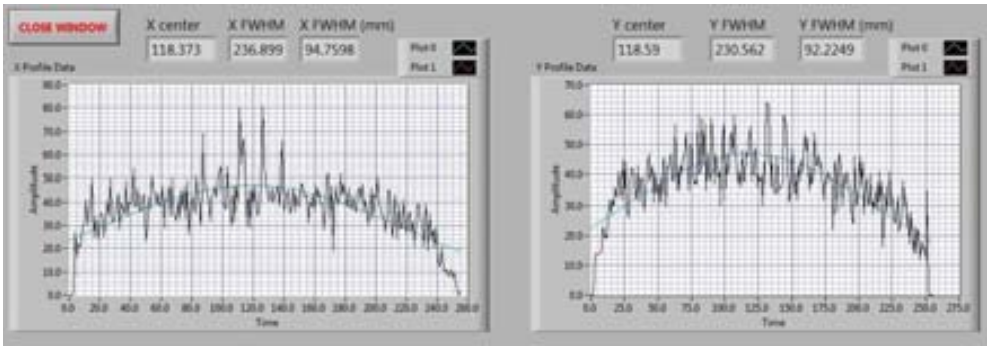

Figure 5.46: A screen-shot of the analysis subroutine used to view the beam profile. Each profile has been made with a slice through the center of the image data plotting the number of events in each pixel. The beam width can be measured using a Gaussian fit. In this example for the wide beam of 100 MeV, a width of about 10 cm FWHM is observed in both vertical and horizontal directions.

user is also free to select the location of both horizontal and vertical slices in order to study different regions of the data. Shown in figure 5.46 is a screen-shot of the beam profile subroutine for slices through the center of the image data for a wide beam run at 101 MeV. The width of the beam is about 10 cm FWHM in both vertical and horizontal directions.

TERA Phantom

Shown in figure 5.47 are two PRR images obtained from a simple phantom designed to test the functioning of all aspects of the device: the GEM detectors, the range telescope, the synchronization between position and range data, and the on-line analysis program. The phantom is a plate of PMMA 20 mm thick with the word "TERA" machined into it at a depth of 10 mm. The word is clearly visibly in both images, testimony to the proper working of all hardware components of the PRR10 as well as the analysis software. The two images display the data from the same beam run but use a different color mapping to represent the average range in each pixel. In addition, the image on the right has been made after applying a cut on the inclination angle of events which can be chosen in the software. The inclination angle is computed using the position of each event recorded by each GEM chamber and knowing that the distance between GEMs is 10 cm. In the image on the right in figure 5.47 a cut above 4 degrees has been applied.

The range information can be extracted from the data in the image in figure 5.47 by selecting limited spatial regions and plotting the range distribution for all events which fall within the selection. Shown in figure 5.48 are the range distributions from three regions with distinct values of the

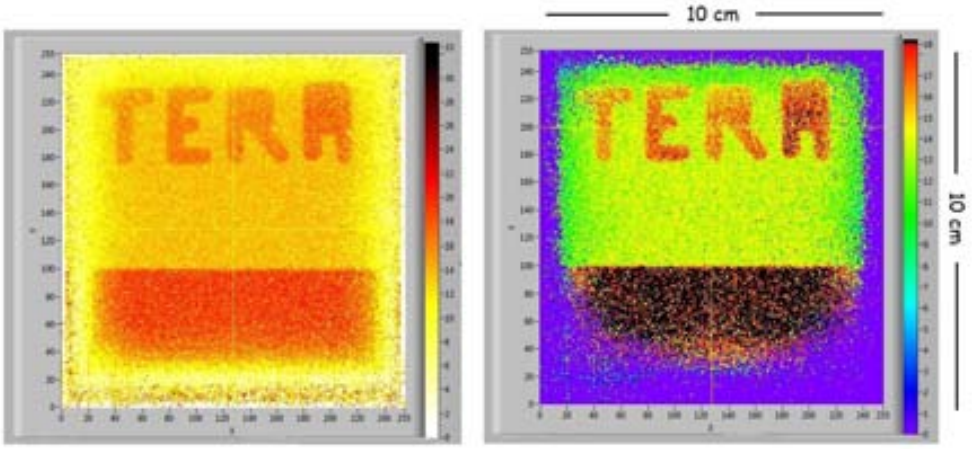

Figure 5.47: Proton radiographies of a simple phantom used to test the correct functioning of the PRR10. The phantom is a 20 mm thick plate of PMMA with the word "TERA" machined into it at a depth of 10 mm. A wide beam of 101 MeV protons has been used. The images shown the same data but the range has been mapped in different color scales. In addition, the right image includes an angular rejection which excludes those events whose inclination angle exceed 4 degrees.

residual range. Furthest to the right (shown in white) at highest residual range is the range data from a region is the lower part of the PRR image 5.47 where the phantom does not cover the detector. The mean range here is 19.48 scintillator units. Furthest to the left (shown in red) is the distribution from a region near the center of the PRR image, where protons have passed entirely through the phantom and the range is 13.17 scintillator units. The central range distribution corresponds to a selection within the "E" in the PRR image. It sits nicely in the middle of the other distributions, as expected since the letters have been machined into the PMMA plate at a depth of about 10 mm.

The difference between the mean values at the two extremes (with and without phantom) is 6.31 scintillator units, or 22.94 mm WEPL if we apply the calibrated water-equivalent thickness of the scintillators. Using the density of PMMA we can infer a phantom thickness of 19.44 mm. To confirm the result the phantom thickness was measured using a precision caliper and found to be 19.5 mm in the region below the word "TERA".

Holes Phantom with wide beam

A more technical phantom is shown in figure 5.49, designed to study the PRR10's ability to distinguish between regions of different WEPL and also

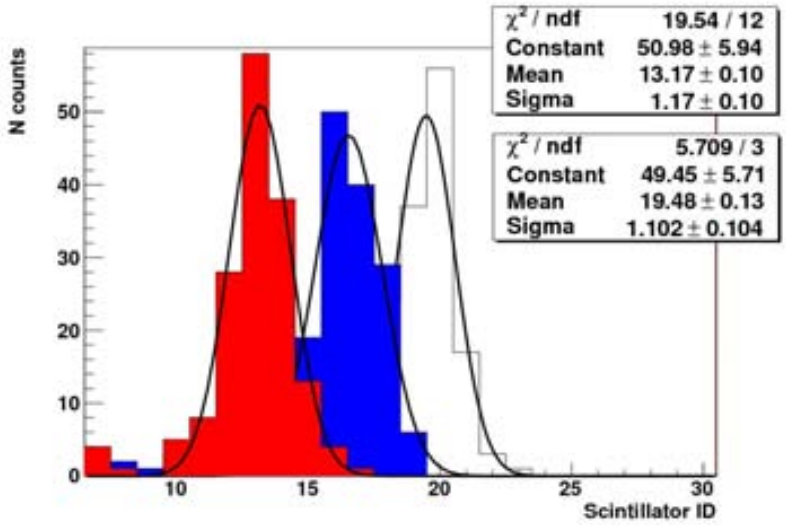

Figure 5.48: Range distributions from three spatial selections in the image data. From highest residual range to lowest: a region outside the phantom, a region in center of the "E", and a region near the center of the image through the entire phantom thickness.

the achievable spatial resolution. The phantom is a 20 mm thick PMMA plate with a series of holes with diameters 1, 2, 3, 5 and 10 mm, drilled to depths of 5 mm, 10 mm, 15 mm, and straight through. The holes were organized in a pattern such that the smaller holes are found near the center and in each quadrant the holes have the same depth. This has been indicated in the picture shown in figure 5.49.

The phantom was first imaged using the wide beam of 101 MeV protons. Shown in figure 5.50 is the PRR image obtained after recording about 10^7 events. The color shades represent the residual range, the scale is shown on the right of each image. The portion of the image which has the largest residual range corresponds to the through holes located in the lower left quadrant of each image. The image shown on the left is without any corrections. The image shown on the right is the same data with a cut on the incidence angle of 3 degrees. In both images the majority of holes are visible. Only the 1 mm diameter hole drilled to a depth of 5 mm is not clearly resolved in either image.

Information about the range resolution using this phantom can be obtained from a plot of the range distributions shown in figure 5.51. Here the range of all events from spatial selections within the 10 mm diameter holes have been plotted for each hole of different depth: 5 mm, 10 mm, 15 mm and straight through. The mean residual range obtained from fits of the

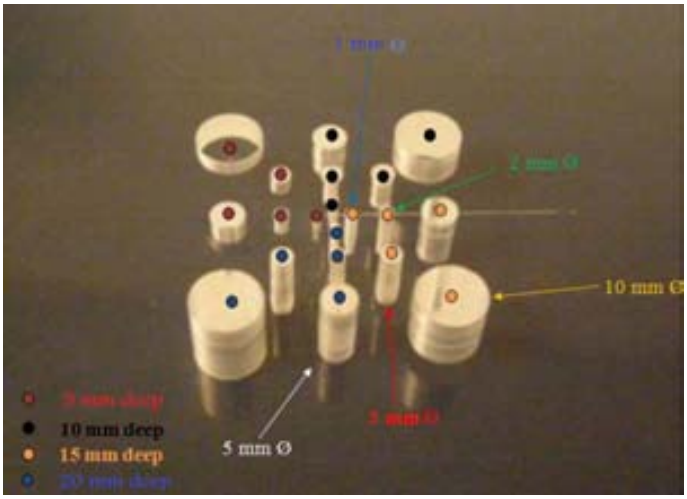

Figure 5.49: The hole phantom used for testing the relationship between the range and spatial resolution of the PRR10. Holes of various diameters (from 10 mm to 1 mm) and of various depths (5 mm, 10 mm, 15 mm and through) have been drilled into a 20 mm thick PMMA plate.

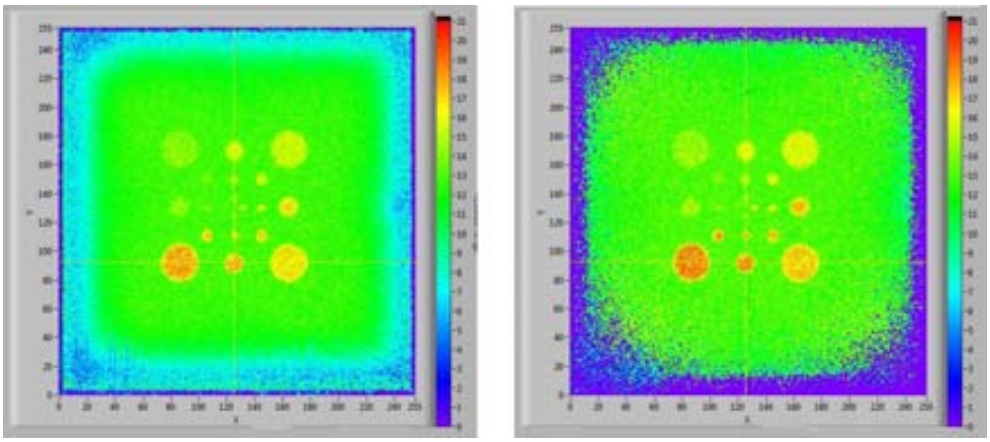

Figure 5.50: Proton radiography of the hole phantom made with a wide beam of 100 MeV protons. The shading corresponds to the average residual range recorded within each pixel. The holes, ranging between 1 and 10 mm in diameter and drilled to a depth of 5 mm, 10 mm, 15 mm and through in a 20 mm thick PMMA plate, are all clearly visible in the image which has a total size of 10x10 cm^2. The image to the right is the same data but with a cut on the incidence angle of 3 degrees.

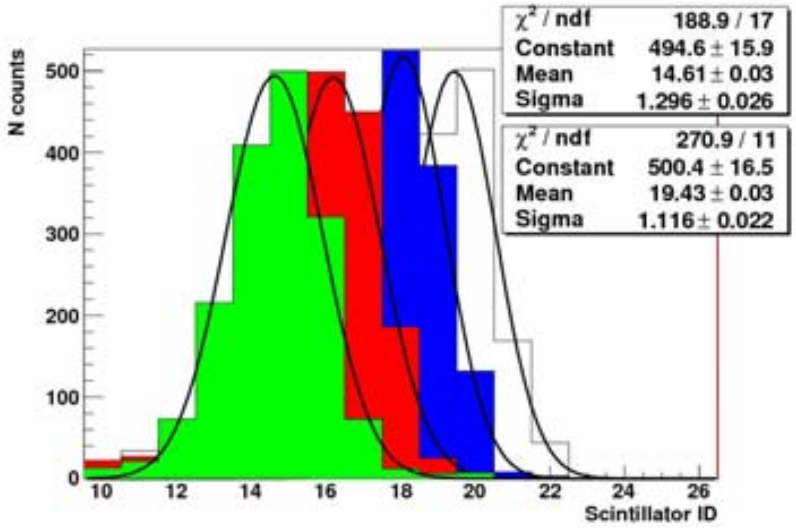

Figure 5.51: Range distributions of all events passing through the 10 mm diameter holes of the hole phantom. The distributions are wider than those obtained previously, reflecting the variation in energy of the wide proton beam used to illuminate the entire 10x10 cm^2 active area of the PRR10.

distributions are 14.61, 16.20, 18.04, and 19.43 scintillator units (only the statistics of two fits are shown in the figure). Taking the through hole at 19.43 scintillator units as the reference (0 mm of phantom) and using the calibrated effective thickness of the scintillators, we can infer a thickness of 5.05, 11.7 and 17.5 mm of WEPL for the 15 mm, 10 mm and 5 mm deep holes respectively, or 4.3, 9.9 and 14.8 mm of PMMA plastic. Considering that the hole depths in this phantom were not controlled with high precision, these results are most likely quite accurate.

Another observation that can be made from figure 5.51 is that the standard deviation of the distributions, on average 1.2 scintillator modules sigma, or about 4.4 mm WEPL, are higher than that measured with the narrow 99.7 MeV beam. This is a consequence of the energy dispersion introduced by the local degrader needed to create the wide beam. More importantly, the width of the distributions is rather constant, regardless of the thickness of phantom traversed. This is in agreement with the argument presented earlier, that for a range telescope the contributions of range straggling of the beam are independent of the phantom traversed since each proton will travel the same water-equivalent range when considering the total of phantom and range telescope.

More information regarding the range and position resolution of the PRR10 device can be extracted from the PRR image data by plotting the av-

erage range in each pixel along a slice through the PRR image data. Shown in figure 5.52 is the result along a horizontal slice at strip 92 of the Y axis which passes through the center of the three holes at the bottom of the image (this is also the position of the cursor in figure 5.50). From left to right, the holes have the diameters 10, 5 and 10 mm. A red line has also been drawn to show the expected location of the holes along with their depths (in scintillator units) and their diameters (in units of GEM strips).

Several observations can be made about the range data along the profile through the PRR image data shown in figure 5.52. The first is that in general, the range values are lower than the expectation values. This may be explained by the fact that to produce the PRR image, the range has been calculated as a running average of all events within each pixel as described previously by equation 5.2.4. This method makes no rejection of nuclear interaction events where the measured range is much shorter than it would be if only electromagnetic processes were involved. These nuclear interactions are not insignificant and occur $\sim$20% of the time. The result is that the average range will be lower than the value obtained by fitting the peak of the distribution in which the contribution from the nuclear interactions (responsible for the characteristic tail to the left of the peak) are ignored. Since the expectation drawn through the data (red line) has been made by fitting the range distribution of all events within the spatial selection and *not* by averaging, this can explain why the average range in each pixel of the PRR image data is consistently lower than the expectation.

Fitting the peak of each range distribution in each pixel is expected to improve the quality of our PRR images. However, this method is likely too computationally intensive to allow a refresh of the image during data taking and instead should be performed once all data is accumulated. For this reason, the running average range method has been implemented in the current version of our analysis software, providing the user with a visual verification without having to wait until the end of the run. An interesting future development may be to include the more advanced range fitting method into the analysis program and evaluate any improvements in the PRR images.

Another observation that we can make considering the data in figure 5.52 concerns the spatial resolution. At the edges of the holes, instead of changing sharply from one range value to another, the range changes progressively over several pixels (or strips). In general, the transition occurs over 3-4 strips which is equivalent to 1.2 to 1.6 mm and defines the spatial resolution of the image. This is only an approximation, however, since the transition depends on the angular cut applied to the data as well as the thickness of the phantom which determines the MCS of the protons before they reach the GEM detectors. In this example, a 3 degree cut on the inclination angle has already been applied.

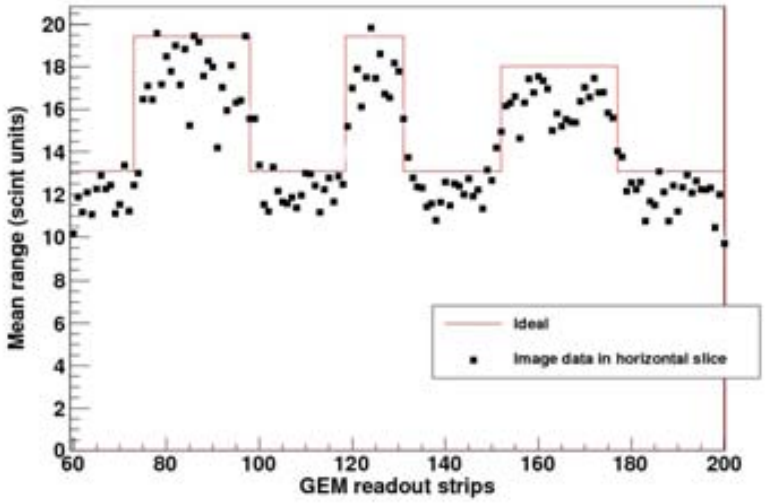

Figure 5.52: Mean residual range per pixel through a horizontal slice at Y=92 through the PRR image data of the hole phantom. The slice crosses through the center of three holes: the 10 mm diameter through hole, the 5 mm diameter through hole and the 10 mm diameter hole drilled to a depth of 15 mm. A line has been drawn at the expected locations and depths of the three holes.

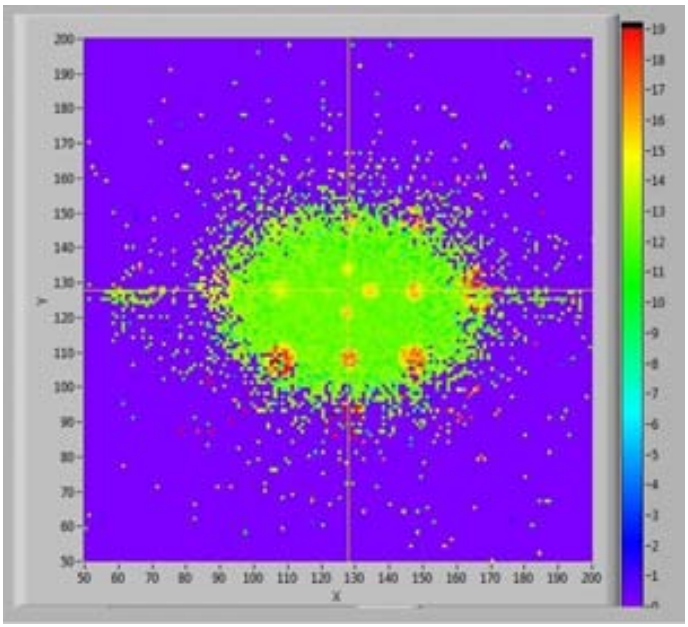

Figure 5.53: PRR image of the hole phantom made with a narrow beam of 99.7 MeV protons. The image has been zoomed to show the details in the 1 mm diameter holes at the center of the image.

Holes Phantom with narrow beam

The hole phantom was also imaged using the narrow beam of 99.7 MeV protons. Figure 5.53 shows the resulting proton radiography of the hole phantom where the central part of the image has been zoomed for convenience. $6x10^4$ events have been collected and no angular cuts applied. The smallest holes of 1 mm are visible at the center of the image though somewhat degraded. The 1 mm diameter hole drilled to the shallowest depth of 5 mm is only barely resolvable.

Shown in figure 5.54 is the average range per pixel along a vertical slice through the center of the PRR image of the hole phantom made with the narrow beam of 99.7 MeV. Shown in figure 5.55 is a similar plot through a horizontal slice through the center of the same image data. Both the horizontal and vertical slices correspond to the location of the cursor in the PRR image of figure 5.53 and fall along the center of the 1 mm diameter holes. A red line has been drawn over the data at the expected location, depth and diameter of the holes crossed by each slice. As before, we observe that in general the range data is lower than the expectation, a consequence of computing the average range of all events in each pixel which includes the contribution of nuclear interactions. In addition, the range data is lower the smaller the diameter of the hole. This can be observed in both the horizontal and vertical slice data for the 1 mm diameter holes. Since we

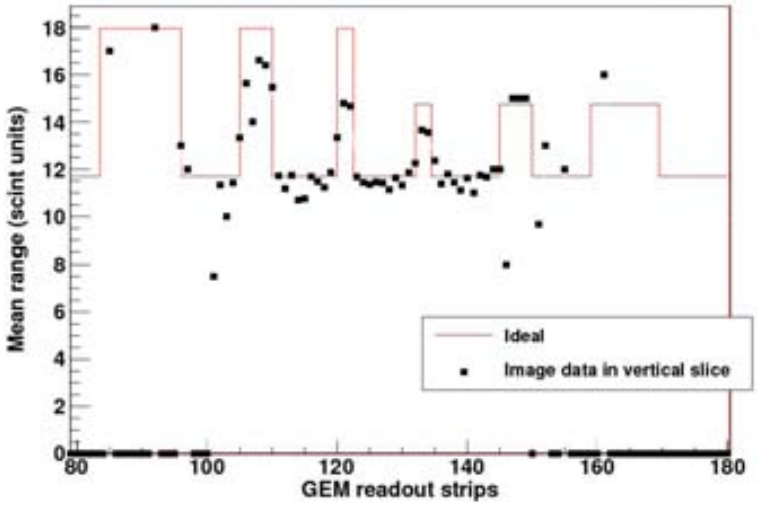

Figure 5.54: Residual range for the narrow beam of the hole phantom through a vertical slice at the center of the PRR image data. The slice crosses through the center of several 20 mm deep holes: 5, 2 and 1 mm diameter, and the center of several 10 mm deep holes: 1, 2 and 5 mm diameter. A line has been drawn at the expected locations and depths of all holes.

have seen before that the transition at range borders occurs over 3-4 strips, this is not surprising since only 2.5 strips of the GEM readout span the 1mm diameter hole.

5.4 Beam tests at CNAO

The PRR10 has also been tested at the *Centro Nazionale di Adroterapia Oncologica* (CNAO) in Pavia, Italy. The CNAO is a hospital-based hadrontherapy center financed by the Italian Ministry of Health and founded by five major hospitals in Milan and Pavia, and by the TERA Foundation. The center received its approval for construction from the Italian health authorities in 2002.

The design of the CNAO accelerator is based on the Proton-Ion Medical Machine Study (PIMMS) carried out between 1996 and 2000 in collaboration between CERN, TERA, Oncology 2000 (Czech Republic) and MedAUSTRON [57]. The goal of the PIMMS study was to produce a complete design for a medical accelerator based on a synchrotron and beam-transport lines optimized for the treatment of deep-seated tumours with protons and light ions up to carbon. In 2004, an adapted version of PIMMS was passed to the

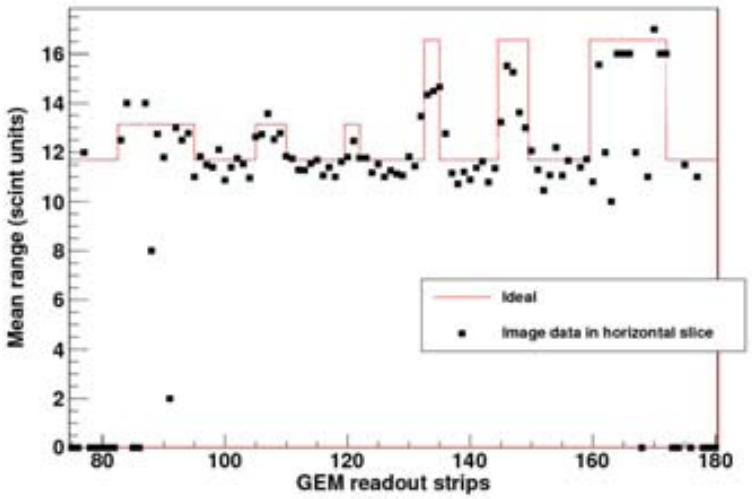

Figure 5.55: Residual range for the narrow beam of the hole phantom through a horizontal slice at the center of the PRR image data. The slice crosses through the center of several 5 mm deep holes: 5, 2 and 1 mm diameter, and the center of several 15 mm deep holes: 1, 2 and 5 mm diameter. A line has been drawn at the expected locations and depths of all holes.

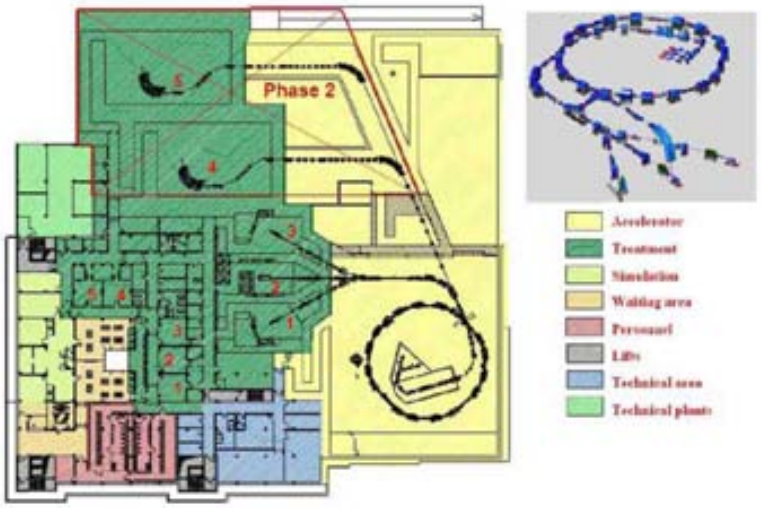

Figure 5.56: Overview of the *Centro Nazionale di Adroterapia Oncologica* (CNAO) hospital-based hadrontherapy center located in Pavia, Italy.

CNAO Foundation by TERA, along with 25 people who make up the core technical group of the CNAO Foundation [58].

Shown in figure 5.56 is the layout of the CNAO accelerator complex and associated hospital infrastructure. Construction of CNAO has been completed at the end of 2009 with a total investment of 125 MEuro, making it the second hospital-based center for proton and carbon ion therapy in Europe after HIT in Heidelberg. In December of 2010 a 230 MeV proton beam was guided to the first treatment room and in January 2012, the first patient was treated with protons.

During two periods in June 2011, the PRR10 was tested using protons at the CNAO facility. Shown in figure 5.57 is the PRR10 mounted near the patient isocenter in the first treatment room where a horizontal beam had recently been made available. The detector is mounted on the portable table and its height matched to the height of the beam line at 150 cm.

5.4.1 Basic Tests

The first tests that were preformed at the CNAO were to observe both a fixed pencil beam of 250 MeV protons as well as a raster-scanned beam. Shown on the left of figure 5.58 is the intensity image of a fixed pencil beam recorded by the PRR10 after about $3x10^4$ events. The beam passes through the center of the detector and has a width of about 7 mm FWHM in both horizontal and vertical directions. Shown on the right in figure 5.58 is the result of a scanned field with the same 250 MeV pencil beam after recording about

Figure 5.57: The PRR10 in one of the treatment rooms with horizontal beam at CNAO.

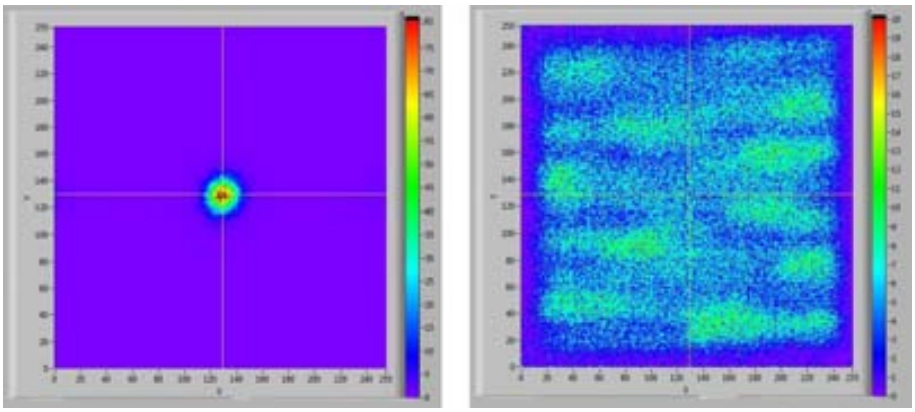

Figure 5.58: Image data of the 2D beam intensity for setup runs with a beam of 250 MeV protons. On the left is a fixed pencil beam whose profile measured by the PRR10 analysis software is 7 mm FWHM. On the right is the same pencil beam raster-scanned across the 10x10 cm^2 active area of the PRR10 made during the setup phase before the scan parameters for a uniform field were obtained.

$3x10^5$ events. On average each pixel in the image of the wide field contains 5 events. This particular wide field image was obtained during the setup phase at the beginning of our beam tests at the CNAO where the machine parameters were tuned to meet our low rate requirements. It was not typical of the uniformity of wide fields that were used for imaging phantoms but has rather been selected to demonstrate the utility of the PRR10 prototype and analysis software for performing basic beam diagnostics. Also during this setup phase, the calibration procedure of the scintillators was performed using the pencil beam of 250 MeV and adjusting the SiPM bias voltages to have a uniform response.

5.4.2 Tests with tissue-equivalent phantoms

Once the machine parameters had been set to provide a low intensity beam, an energy was selected such that the beam stopped within the scintillators of the range telescope. Although the exact energy of this beam was not recorded during our beam run, we were able to carry out phantom studies using tissue-equivalent phantoms made available by our CNAO colleagues. Some of those phantoms are shown in a photograph in figure 5.59. The phantoms are made of epoxy resin and their densities have been calibrated and reported in the manufacturer's datasheet.

Three of the phantoms were selected to test the density resolution of our PRR10 system: lung, breast, and trabecular bone having densities 0.20, 0.99, and 1.16 g/cm^3, respectively. The phantoms were taped to a 1 mm PMMA support plate and positioned directly in front of the active area of

Figure 5.59: Various tissue-equivalent phantoms which have been used in the CNAO beam tests with the PRR10 detector.

the PRR10 as shown in figure 5.60.

The PRR10 and phantoms were then exposed using the proton pencil beam scanned over a wide field which covered the entire active area. A run was made recording 7.5x10^5 events in total. Shown in figure 5.61 is the image data obtained after a 1 degree cut on the incidence angle which leaves only 8x10^4 events in the 2D data set. The image on the left of figure 5.61 shows the number of events per pixel, N, showing the uniformity of the beam intensity over the active area. On average each pixel contains about 3-4 events. On the right, the average range per pixel has been displayed revealing the PRR image of the three phantoms.

In order to evaluate the accuracy of the density determination which can be obtained by the PRR10 several spatial regions of the data have been selected. These regions are indicated with a number in the PRR image at the right of figure 5.61. The lung, breast and trabecular bone phantoms have been labeled 1, 2 and 3, respectively, including a region without phantom, labeled 0, which serves to compute the reference range since the beam energy was unknown. The corresponding range distributions using the "last-hit-counter" range method for a selection from each region have been plotted in figure 5.62 along with a Gaussian fits to the peak of each distribution. The fit statistics corresponding to region 0 and region 3 have been shown for example.

Using the mean of the fits to each range distribution we can infer the density of each sample. Since the relative range shift measured between the region without phantom and the regions with phantom gives a product of the density difference times the length of the sample, we can write

$$\triangle\rho = \frac{\triangle R}{L}$$

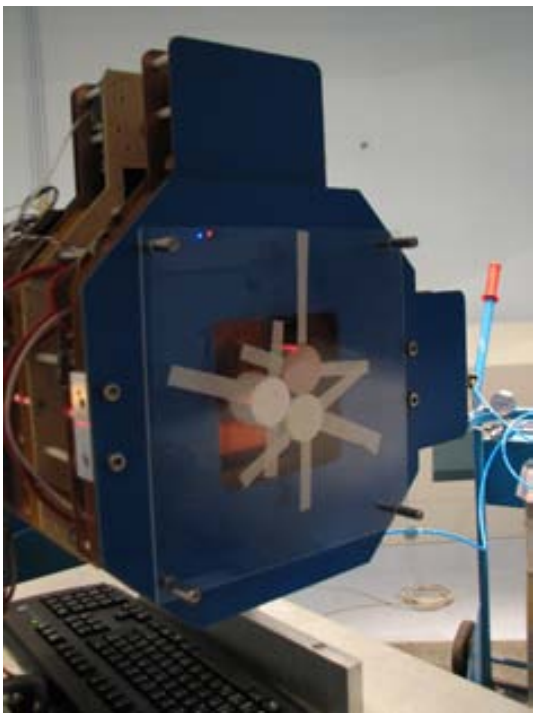

Figure 5.60: Three tissue-equivalent phantoms mounted in the imaging field of the PRR10 at CNAO.

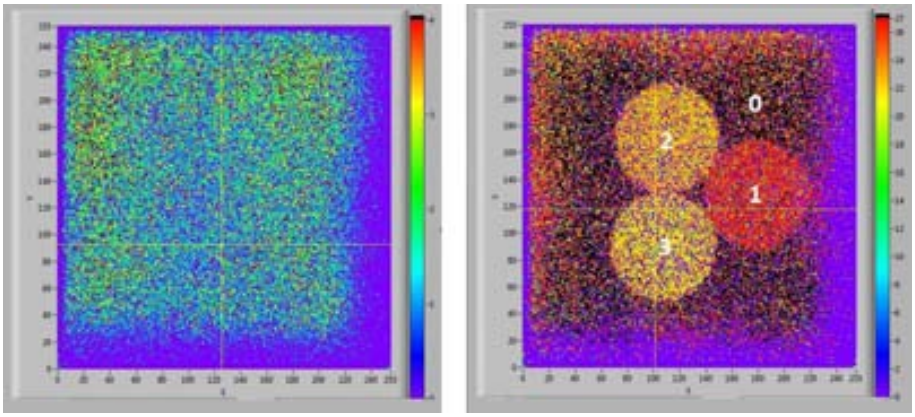

Figure 5.61: Collected image data for the CNAO beam tests with tissue-equivalent phantoms with a scanned pencil beam of protons. On the left: the value N per pixel is displayed giving a 2D image of the beam intensity. On the right: the average range is displayed revealing the three phantoms. A 1 degree cut on the incidence angle has been applied to the data.

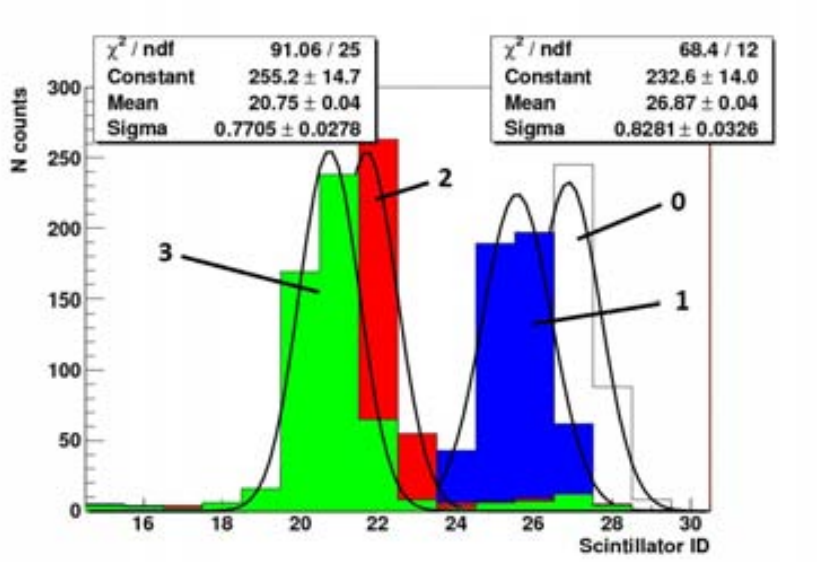

Figure 5.62: Range distributions of selection spatial regions of the PRR data corresponding to the different tissue-equivalent phantoms imaged with a scanned pencil beam at the CNAO. Region "0" corresponds to a selection where no phantom is present. Region "1" is the lung phantom (density 0.2 g/cm^3), region "2" the breast phantom (density 0.99 g/cm^3) and region "3" the trabecular bone phantom (density 1.16 g/cm^3).

	ρ_{real}	L	R	$\triangle R$	ρ_{PRR}
	g/cm^3	mm	scint. units	mm WEPL	g/cm^3
No phantom (ref)	0	-	26.87	0	-
Lung	0.20	24.7	25.50	4.987	0.201
Breast	0.99	18.3	21.69	18.86	1.030
Trabecular Bone	1.16	19.5	20.75	22.28	1.142

Table 5.1: Summary of expected and measured densities of tissue-equivalent phantoms imaged with the PRR10 during the CNAO beam tests.

where L is the thickness of the sample in question and $\triangle R$ is measured in units of mm WEPL. The density of the air can be approximated as zero, and thus the density of the phantom, ρ, is just the range shift from the reference divided by the phantom thickness, or $\triangle R/L$. The effective scintillator thickness must be used to give the measured range shift in units of mm WEPL.

It should be noted that a calibration of this effective thickness using the 1 mm thick PMMA absorbers has not been performed at CNAO using this particular beam energy which stops inside the range telescope near the middle of the 27^{th} scintillator. Because the beam penetrates deeper than the 100 MeV beam at PSI where the calibration was performed (at roughly the 18^{th} scintillator) and because of the uncertainty in the scintillator thickness, we cannot be sure that the effective thickness of 3.64 mm WEPL is accurate here. Nonetheless, the effective scintillator thickness of 3.64 mm WEPL has been applied since no alternative was available. This is one source of uncertainty in the following measurements.

The results of the density calculations are shown in table 5.1. The expected density, ρ_{real}, of each phantom has been taken from the datasheet of the tissue-equivalent phantoms provided by our CNAO collaborators along with the thickness of each phantom, L, measured using a digital caliper. The absolute range within a spatial selection of each phantom, R, is shown as recorded by the PRR10, as well as the corresponding range shift, $\triangle R$, from the reference in units of mm WEPL. Taking the known thickness of each phantom, the measured density, ρ_{PRR}, has been calculated and is reported in the table. The actual deviation from the expected densities are 0.9%, 4.1% and 1.5% for the lung, breast and trabecular bone phantoms, respectively.

5.5 Future developments: PRR30

The AQUA group is currently developing a new PRR detector which has an active area of 30x30 cm^2, large enough to obtain PRR images of clinical relevance with human patients. Because of the excellent results obtained

with the PRR10 prototype during beam tests at the PSI and CNAO, both the GEM technology and the use of 3 mm plastic scintillator absorbers have been selected again, though scaled in size to cover the larger surface area. Apart from an increase in active area, many aspects of the design have been improved with respect to the PRR10. For example, a higher requirement on the manufacturing tolerances from the scintillator suppliers have been requested and a more appropriate wrapping material chosen. Also, a total of 48 scintillators have been included in the range telescope bringing the total up to nearly 15 cm WEPL, the maximum thickness of the target that can be imaged using a single beam energy.

By far the most important undertaking for the new PRR30 prototype has been a re-design of the GEM detector readout electronics. In order to provide PRR images in a time-frame suitable for a hadrontherapy clinical context, a final readout rate of over 1 million-samples-per-second (MS/s) is required. At this rate, the data for an image of 30x30 cm^2 with 1 mm^2 resolution, where each pixel is filled with 100 events, can be acquired in 10 s. To achieve this data through-put, the GEM front-end electronics had to be completely re-designed. In collaboration between the TERA Foundation and the AGH University of Science and Technology in Krakow, Poland, a new front-end ASIC, called the GEMROC, has been designed and fabricated in 0.35 μm CMOS technology [59]. The design of this new ASIC has been been carried out by the Krakow group using the characteristics of 30x30 cm^2 GEM detectors provided by the TERA Foundation.

Because the PRR30 detector is currently under construction by the AQUA group and shall be reported in future dissertations presented by AQUA colleagues, only a basic description of its design and preliminary tests shall be presented here. This includes a description of the GEMROC ASIC and the fast DAQ which has been built by the AQUA group as well as a few details about the scintillators modules which make up the new range telescope.

30x30 cm^2 scintillators

Essentially identical to the scintillator modules of the PRR10, a new production of 30x30 cm^2 plastic scintillator modules for a PRR30 instrument has been carried out. The most important criterion for the new modules has been the thickness tolerance of the scintillators, required to be more stringent than with the previous 10x10 cm^2 prototype. Three samples of 3 mm thick 30x30 cm^2 plastic scintillator have been procured from both Saint-Gobain Crystals and Eljen Technology [60] and have been measured for their thickness uniformity. Following this evaluation, 48 scintillator sheets were purchased from Saint-Gobain and have been measured to have an average thickness of 3.17 mm with a maximum variation of $\pm$0.20 mm.

A 30 cm long 1 mm diameter WLS fiber (the same BCF-91F) has been

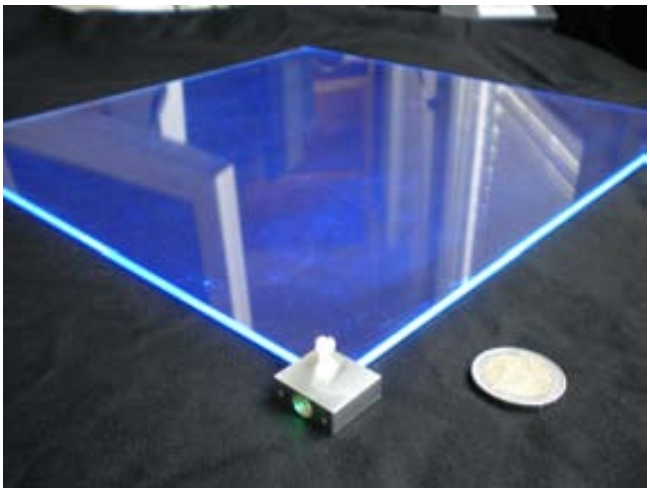

Figure 5.63: One of the 30x30 cm^2 plastic scintillators purchased from Saint-Gobain Crystals. A 1 mm diameter WLS fiber has been glued into a "v"-shaped groove along one edge of the plastic.

glued in a "v"-shaped groove along one edge of the plastic an aluminum optical box fixed with a nylon set-screw. Rather than glue the optical box in place after the wrapping is applied, the optical box has first been fixed to the bare scintillator-fiber assembly such that the fiber end is precisely flush with the optical block's interior surface. It is hoped that this will provide a more uniform transmission of the light from the fiber to the active area of the SiPM which was one factor not carefully controlled in the PRR10 design. After setting the position of the optical block and gluing it in place, each module was wrapped with an aluminized Mylar foil followed by an opaque black plastic. The new wrapping is thinner than the wrapping used for the PRR10 range telescope and has been estimated at less than 100 μm water-equivalent. It has also been tested effective in preventing light leaks. Shown in figure 5.63 is one of the 30x30 cm^2 scintillator modules before the wrapping material has been added.

All 48 scintillator modules have been assembled and are being tested with the same central DAQ used by the PRR10 range telescope. Each of four ribbon cables of the mezzanine card communicates with 12 scintillator modules, the total made possible by the original PRR10 design. Initial tests have shown that a good signal-to-noise from all scintillators can be recorded with cosmic particles as well as a good uniformity of the response over the entire 30x30 cm^2 active area.

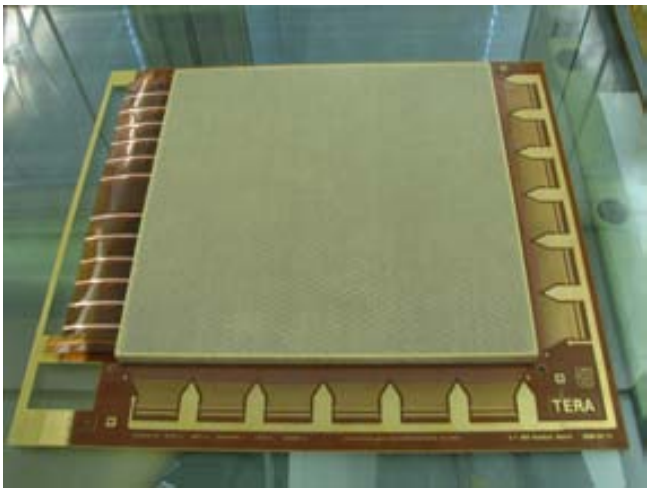

Figure 5.64: One of the two 30x30 cm^2 triple-GEM detectors built by the AQUA group for the new PRR30 prototype.

GEM 30x30 cm^2

Two large surface area triple-GEM detectors have been constructed for the PRR30 prototype each with 30x30 cm^2 active area. The GEM foils, XY readout board, and inter-GEM and drift spacings are exactly the same as in the GEM detectors of the PRR10. One difference is that the GEM foils and drift have been glued into place using a series of epoxy frames rather than being assembled inside a gas chamber which can be re-opened. The assembly procedure that we have followed is the same developed by the COMPASS experiment. Shown in figure 5.64 is one of the two 30x30 cm^2 triple-GEM detectors immediately following their assembly in a clean room. The TERA design is essentially the same as that of COMPASS, except that the connectors for the XY readout have been adapted to the board-to-board connectors of the DP-GP5 front-end. This makes our design compatible with a number of other front-end readout options [52].

Shown in figure 5.65 are the high-voltage distribution boards which has been made for powering the 30x30 cm^2 triple-GEM detectors. The boards use the same low-current voltage divider as the PRR10 except that the GEMs have been segmented and polarized by separate 1 MΩ resistors in order to reduce the capacitance across each GEM foil. This segmentation technique is standard practice in the use of large surface area GEM detectors since it reduces the energy released upon discharge, protecting the GEM foils and readout electronics. The current required is identical to that of the PRR10 HV distribution boards (less than 70 μA per detector), allowing the single HV module and controller circuit of the PRR10 to be re-used in the PRR30.

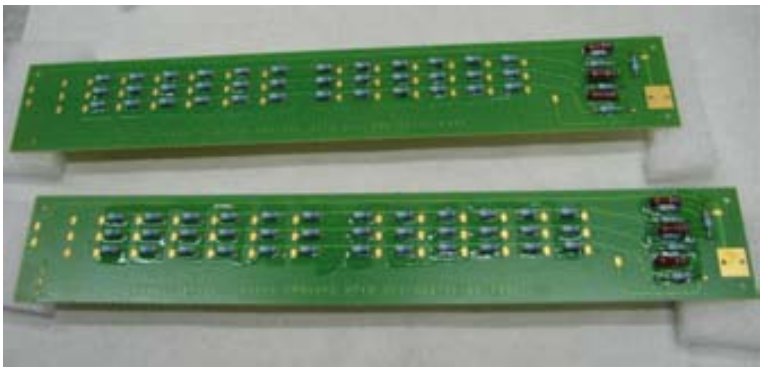

Figure 5.65: HV distribution boards designed by AQUA for powering the two 30x30 cm^2 triple-GEM detectors of the PRR30.

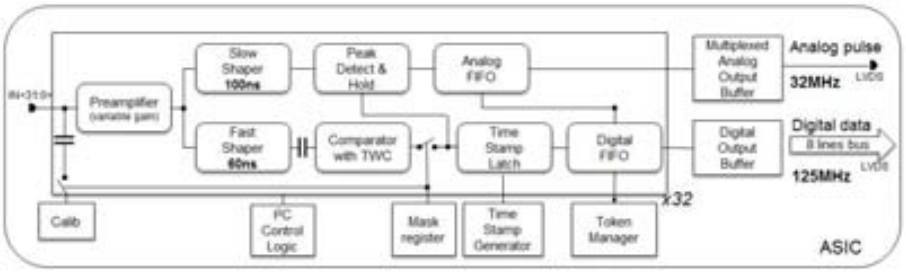

Figure 5.66: GEMROC ASIC block diagram.

GEMROC high-speed front-end

The GEMROC ASIC is a 32-channel preamplifier front-end based on the MSGCROC [61]. A schematic diagram of the chip architecture is shown in figure 5.66. Each channel has two shaping circuits similar in many ways to the GP5: a slow shaper (100 ns) for the analogue measurement of the charge and a fast shaper (60 ns) for triggering. Unlike the GP5, however, the GEMROC provides data only for triggered channels which is transmitted through the output buffer at a rate of 31.25 MHz, allowing a maximum data-throughput of nearly 1 MS/s per channel. Since only triggered channels are transmitted, the data is always received with full zero-suppression, which is similar to the GP5 operated in sparse-readout mode. In addition to the analogue measurement, a 32-bit word is also transmitted over an 8-wire digital bus at a speed of 125 MHz. This digital data contains the channel address as well as a unique time stamp, selectable with 4 or 8 ns precision, which allows for data synchronization with an external system.

To accommodate our 30x30 cm^2 GEM detector design, two GEMROC ASICs have been mounted on a custom hybrid using our board-to-board connectors and a diode protection system identical to that used by the Scal-

Figure 5.67: GEMROC hybrids mounted on the 30x30 cm^2 GEM readout board. Each hybrid reads 64 channels.

able Readout System of the RD51 Collaboration [62]. Shown in figure 5.67 are two GEMROC hybrids mounted on the 30x30 cm^2 GEM. Each hybrid has 64 channels (2 GEMROCs) and 12 hybrids are required for each GEM detector, 2 x 768 = 1536 channels in total.

Although the XY readout board of the 30x30 cm^2 detectors has the same pitch as those of the PRR10 (400 μm), we have opted to connect two strips to each input of the GEMROC ASICs in order to reduce the total number of channels of the entire system. This also increases the maximum data through-put since clusters will contain less hit channels (at the same GEM gain and threshold) as compared with a 400 μm pitch XY readout geometry.

Because we intend to implement a center-of-mass determination of the charge sharing over neighboring channels rather than the maximum-hit-channel method used in the PRR10 software, we still expect a very good spatial resolution even if the strip pitch of the XY readout is effectively 800 μm.

AQUA Fast DAQ system

In order to communicate with the GEMROC hybrids and to receive their data at a rate suitable for proton radiography, the AQUA group has developed a fast DAQ system which will be integrated into the PRR30 instrument. An intermediate board called the GR-DAQ, which communicates with two GEMROC hybrids and a central DAQ, has been designed and implemented. The GR-DAQ contains two dual-channel 12-bit ADCs (Linear Technologies LTC2265) which continuously digitize the analogue output of the GEMROCs at the frequency of the GEMROC output buffer. In order to handle

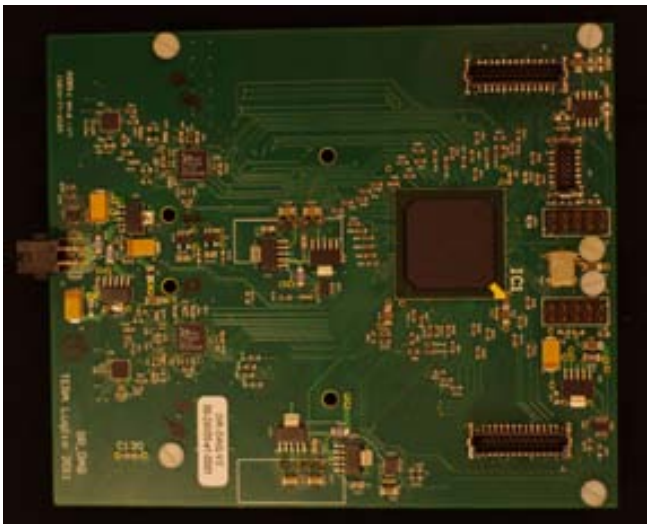

Figure 5.68: The GR-DAQ board which interfaces with two GEMROC hybrids having a total of 128 channels. The GR-DAQ has two dual-channel pipeline ADCs its own Altera FPGA. The firmware handles the data acquisition and assembles the analogue and digital data from the GEMROCs before transmitting them to the central DAQ.

that high data-throughput, an Altera Cyclone III FPGA has also been included which assembles the analogue and digital data from all 4 GEMROCs and also performs the programming of various GEMROC registers. Figure 5.68 shows one of the GR-DAQ boards after production and assembly of all components.

A central DAQ has been developed for communicating with up to 6 GR-DAQ boards, which allows for the full readout and control of one 30x30 cm^2 GEM detector. The central DAQ is the same as that which was used for the GEM detectors and range telescope of the PRR10, except that a new mezzanine card and firmware have been developed specifically for this application. During readout, the firmware programmed onto the FPGA receives the assembled data from each GR-DAQ as it becomes available and stores it in a FIFO whose contents are periodically transmitted to a PC through the QuickUSB module at the maximum rate of up to 48 MBytes/s. Figure 5.69 shows the new GEMROC central DAQ and its custom mezzanine which can communication with up to 6 GR-DAQs.

PRR30 current status

At the time of writing, most aspects of the PRR30 construction are approaching completion. One GEM chamber has already been fully equipped with GEMROC front-end electronics and the fast DAQ as well as analysis

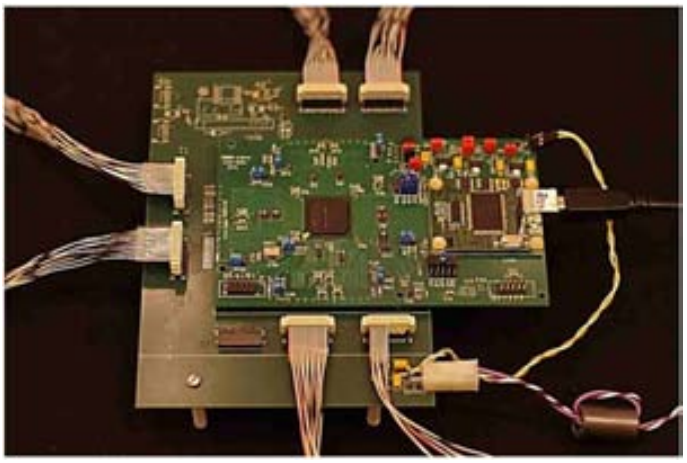

Figure 5.69: The PRR30 central DAQ. The mezzanine board has been adapted for use with up to 6 GR-DAQ boards which are enough to equip an entire 30x30 cm^2 triple-GEM detector.

software are also at a good stage of development. Since the range telescope component of the instrument is essentially identical to the PRR10 design (but with more scintillator modules), the main challenge has been in developing the fast DAQ for the GEM detectors and achieving a total throughput of 1 MS/s.

Using a portable X-ray generator, we have been able to demonstrate an acquisition speed of 1.6 MS/s with data integrity [63]. Shown in figure 5.70 are two X-ray radiographies obtained with our 30x30 cm^2 GEM detectors and readout DAQ based on the GEMROC front-end. Both images contains nearly $1x10^6$ events. The XY position of each recorded X-ray interaction has been determined using a center-of-mass algorithm which has been implemented in a new version of the LABVIEW analysis software for the PRR30.

Shown in figure 5.71 is a picture of the PRR30 in its current state. All 48 scintillator modules, as well as the two trigger modules and scintillator DAQ, have been mounted in a newly designed mechanical frame. The scintillator module spacing has been reduced to 6 mm thanks to a new scintillator support which is more compact, cost efficient, easy to assemble, and lightweight. One of the GEM chambers, that which has been fully equipped with GEMROC hybrids and GR-DAQ boards and recently tested, is shown mounted precisely in front of the range telescope. At the time of writing, several aspects of the design are under development: a second GEM detector is being equipped and tested for data integrity and fast data acquisition with the X-ray source; a clock-and-control board, which synchronizes the time stamp between the separate GEM and range telescope DAQs, has been produced and tested; and a new GUI and software solution, also based on

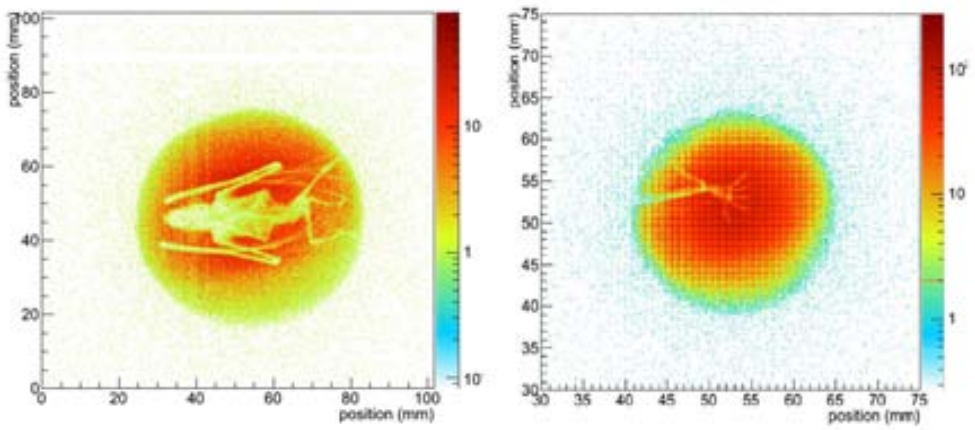

Figure 5.70: X-ray radiographies of a bat made in the AQUA laboratory using one of the 30x30 cm^2 GEM detectors fully equipped with GEMROC hybrids and our fast-DAQ solution. The image on the right has been made with a narrow beam and is zoomed to show the high resolution that can be achieved.

the LABVIEW environment, is being optimized for high-speed on-line data acquisition and analysis. The entire PRR30 instrument is expected to be completed in the near future, with beam tests scheduled for the end of 2013.

Another important aspect of the new PRR30 design is that the clock-and-control board has been designed to be easily scalable, allowing the addition of another pair of GEM detectors to the system. An additional GEM pair can be used to track the protons before they enter the patient which make possible the application of more sophisticated reconstruction techniques. Using the method known as the most-likely path (MLP), the effect of MCS, which leads to the degradation of spatial resolution characteristic of proton radiography, can be somewhat overcome. Rather than being limited to around 3-5 mm, the spatial resolution can be made as low as 1-2 mm using the MLP method [64]. This is another subject of simulation study currently under investigation by AQUA group.

Figure 5.71: The new PRR30 instrument in its current state of development. 48 scintillator modules have been assembled and one GEM detector has been fully equipped and tested with GEMROC front-end electronics.

Chapter 6

In-vivo dosimetry with PET

A highly desirable goal for quality control in hadrontherapy is on-line *in-vivo* dosimetry. Monitoring of the cumulative and volumetric dose as it is delivered by the therapeutic beam would be invaluable for preventing and tracking errors caused by changes in tissue morphology. Always undesirable, these changes can occur for natural reasons (cavity filling: rectum, bladder, sinus, etc.), or by differences in patient immobilization between fractions. Tumour shrinkage in the course of treatment.

One consequence of using a hadron beam for therapy is that a certain fraction of the hadrons will undergo nuclear reactions with the nuclei of the tissues along their trajectory. Nuclear interactions result in the creation of a myriad of secondary particles. Those which are relevant to medicine include gammas, protons, alphas, neutrons, and fission fragments of the projectile or target nuclei, which are produced over a wide range of energies and solid angle. Of these, most are reabsorbed within the body in the vicinity of the primary interaction point, while some of them escape the target entirely.

Accurate knowledge of nuclear processes and the inclusion of the dose that the secondaries contribute is of importance in hadrontherapy treatment planning. For instance, the characteristic tail beyond the Bragg peak in the dose-depth profile for carbon ions is the result of ionization by nuclear fragments. The production rates of such secondaries must be quantified experimentally and validated by simulation since they have a non-negligible contribution to the total volumetric dose. This subject is currently an active topic of research in carbon ion therapy.

As it concerns the experimental physicist, the presence of nuclear interactions offers a number of unique possibilities for *in-vivo* dosimetry using imaging detectors since some of the secondary particles escape the body carrying information about their primary interaction vertex. In proton and carbon ion therapy, the particles which have potential to escape the body and are suitable for detection include prompt gammas, elastically-scattered secondary protons and charged ions, and various decay products of excited

nuclear isotopes which are produced within the patient tissues by irradiation with the therapeutic beam.

Reconstructing the delivered dose through detection of these secondaries is not an easy task to achieve even with modern detector technologies and reconstruction techniques derived from HEP. For illustration, charged particles are produced in higher abundance before the Bragg peak, where they still have enough energy to escape the body, limiting the spatial resolution at the distal fall-off at the end of the beam range where it is most important. Furthermore, the reconstruction accuracy is limited by the Multiple Coulomb Scattering (MCS) of the charged particles before they exit the patient. On the other hand, prompt gammas don't suffer from MCS, however, using them for imaging purposes is challenging because the necessary collimation creates a trade-off between spatial resolution and detection efficiency. Here, the use of Compton cameras could be an asset. In both cases of charged particles or prompt gammas, a selection of the detection modality is required by the hardware, since both types of particles are emitted simultaneously at the moment of beam delivery. Also in these cases of prompt modalities, a high neutron background pervades the measurements leading to very challenging detector requirements. Though simulations and experiments are illuminating the path towards a solution, more research is required to validate the use of prompt gammas or scattered charged particles for doing accurate dosimetry. These prompt modalities are being actively explored by several research groups, within the framework of the European project ENVISION (European NoVel Imaging System for ION therapy) under grant agreement number 241851 [65].

Detection of the decay products of $\beta+$ isotopes created from nuclear interactions between the ion beam and tissue during irradiation, visualized by the use of PET detectors, is one modality very promising for *in-vivo* dose monitoring. One reason it is attractive over prompt methods (carried out during irradiation) is that the half-life of the $\beta+$ isotopes typically produced by proton and carbon-ion beams incident on biological tissue is on the order of seconds and minutes, making it possible to acquire data when the beam is off and when the radiation from the prompt modalities is minimal. Since the isotope concentration is built up in the patient over the course of treatment, an accurate picture of the total delivered dose can be made by interpreting the PET data both throughout the course of treatment and in the minutes which follow. Because of this fact, different technical implementations of PET dosimetry can be applied: a dedicated scanner can be integrated into the treatment room around the patient with space for the patient bed and the beam-line (in-beam PET), or the patient can be moved to a PET scanner nearby after treatment, either in the treatment room (in-room PET) or in another room of the hospital facility (off-line PET). Figure 6.1 shows a sketch of the $\beta+$ activity induced in the patient over the time-scale of a typical ion-therapy irradiation. The different implementations of PET have

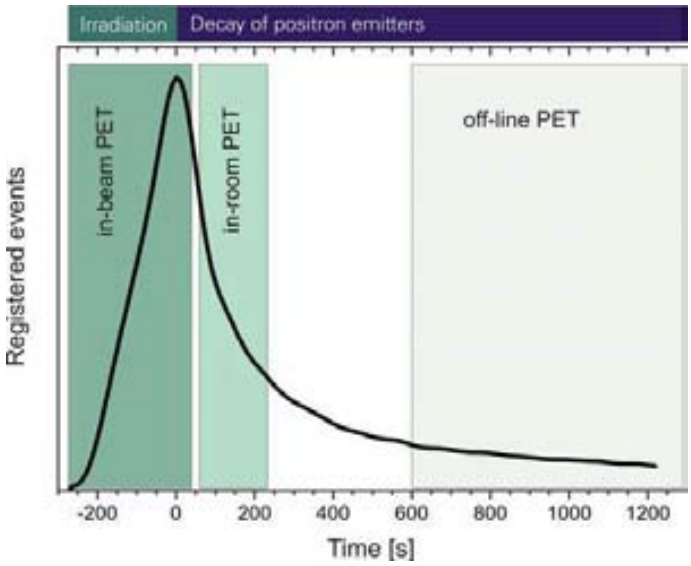

Figure 6.1: A sketch of the time dependance of the $\beta+$ activity induced in the patient by the proton or carbon-ion beam during and shortly after irradiation.

been indicated; in-beam PET is carried out during irradiation as the dose is accumulated, while in-room and off-line PET are carried out after treatment when the total activity is decaying.

At present, PET is the only modality for *in-vivo* dosimetry which has been tested clinically with patients receiving proton and carbon-ion therapy. A dedicated PET scanner has been integrated into the treatment room at the *Gesselschaft fur Schwerionenforschung* (GSI), in Darmstadt Germany [66] and at the Heavy Ion Medical Accelerator (HIMAC) in Chiba, Japan [67, 68]. Commercial scanners are also being used off-line as in one recent study made at the Massachusetts General Hospital (MGH) in Boston. Thanks to the experience gained, in-beam PET is at a more advanced stage of development as compared with the other prompt modalities, at least from a clinical perspective. The availability of real clinical data is certainly a drawing point for researchers wishing to develop a PET camera for this specialized application. However, the choice to use PET is motivated for another important reason: PET is already a mature technology in medical imaging and nuclear medicine with commercial PET systems in everyday clinical use in thousands of hospitals the world over. This allows in-beam PET developers to draw upon existing knowledge in the field of PET for nuclear medicine. Furthermore, PET research is still improving upon existing technologies, with new crystal and photodetector hardware soon to found in commercial devices which out-perform the present-day standards.

The fact that PET research is thriving is fortunate for the hadronther-

apy community. As we shall see, new improvements in PET technology, especially towards time-of-flight PET (TOF-PET), have the potential to overcome the challenges that a PET application would face for performing *in-vivo* dose monitoring in proton or carbon ion therapy. Outlining the specific challenges of in-beam PET is one purpose of this chapter. Before we delve into the specifics of the specialized application to hadrontherapy, however, we first discuss the basic features of PET detectors in case the reader is not already familiar. With those principles in mind, a few selected examples of PET detector designs will be described which illustrate the latest trends and state-of-the-art in PET research. The chapter then concludes with the specific challenges faced by an in-beam PET application including a look at some of the clinical experience that has been gained at GSI and MGH during *in-vivo* dosimetry studies with patients.

6.1 Basics of PET Imaging

The fundamental principle of Positron Emission Tomography (PET) is the detection of the two collinear photons produced by the annihilation of a positron emitted from the decay of a $\beta+$ isotope. Detection of both of the back-to-back photons within a short time window (coincidence) allows for the reconstruction of the origin of the positron annihilation along a line-of-response (LOR), the straight line connecting the two points of detection. By collecting a large number of emitted photon pairs over a large number of LORs, the spatial concentration of the positron-emitting substance can be reconstructed within the field-of-view (FOV) of the PET detector. The accuracy of the 3D reconstruction is limited by the positron's range in the material and the fact that the photons are not perfectly collinear of the photons, the latter due to the non-zero momentum of the positron at the moment of annihilation.

In the clinical practice of nuclear medicine, positron-emitting isotopes are attached to chemicals with biological functionality. These radio-labeled chemicals, also called radio-pharmaceuticals or radio-tracers, are then injected into the patient where they follow a certain biological pathway. The diffusion of the substance through the body can then be studied by PET imaging during the life-time of the radio-tracer until statistics are limited by its physical or biological decay. An overview of the major components of a typical PET system is shown in figure 6.2. Because the radio-tracer follows a metabolic pathway specific to its chemical role in the human body, PET is known as a functional imaging modality.

Nowadays, PET is often combined with anatomical imaging such as X-ray CT, in a single machine capable of carrying out both imaging modalities at the same time. The combination of the PET data with the anatomical data allows for a precise localization of the radio-pharmaceutical with re-

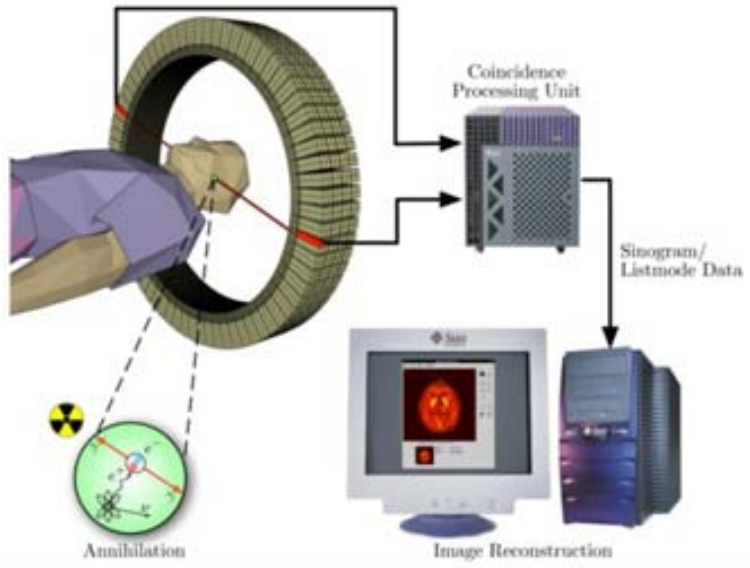

Figure 6.2: Overview of a positron emission tomography system used in nuclear medicine [69].

spect to the patient's tissues. In PET/CT, the PET image is usually superimposed onto the CT image as shown in figure 6.3. In this way, clinicians can study the diffusion of the selected radio-tracer precisely since the two data sets are accurately co-registered.

The combination of PET data with anatomical data also serves another important purpose. Because a fraction of the 511keV photons will be either absorbed or scattered by the patient tissue as they exit the body, the PET reconstruction must be corrected for attenuation according to the tissue morphology. This correction allows the PET data to qualitatively reflect the exact concentration of the isotope which is of much greater value to clinicians. Inclusion of CT allows for precise co-registration to the PET data which is needed for computing the attenuation correction accurately. A high resolution of the tissue morphology is also desirable and has prompted research into the challenging field of PET/MRI.

An absolute measurement of the $\beta+$ activity is especially important in oncology where FDG, a radio-tracer chemically analogous to glucose, is injected into a cancer patient to be subsequently absorbed in cells at a rate proportion to their metabolic activity. Since tumour cells by their nature are highly metabolizing, the actual concentration of FDG within the tumour after a given time is the information required by oncologists for determining the living volume of a cancer, the extent of its progression towards degenerative disease, and the efficiency of treatment. In the fight against cancer, PET/CT is arguably one of the oncologist's most powerful tools in the di-

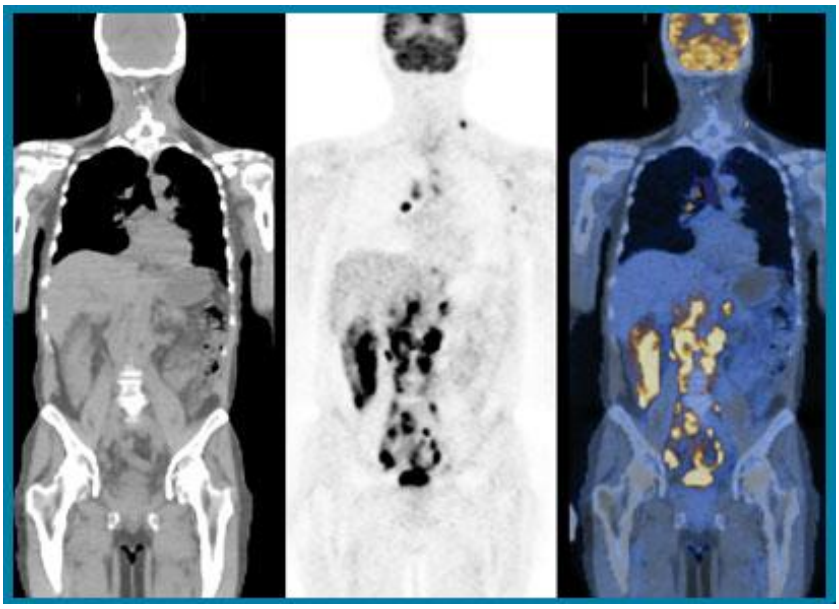

Figure 6.3: The concept of PET/CT. Shown left is the CT image and shown center the PET image. On the right is the fused image of both PET and CT displayed for clarity in a false color scale [70].

agnostic, treatment planning, and follow-up phases of therapy.

PET/CT and PET/MRI are known as functional imaging modalities because they provide quantitative and temporal information about chemical processes in the human body. Commercialized PET/CT machines are now common place in many hospitals and it would be fair to say that PET imaging has revolutionized the fields of nuclear biology and medicine since the initial development by David Townsend at the Geneva University Hospital in 1985 [71].

6.1.1 $\beta+$ emitters with relevance to medicine

Elements of biological relevance, such as carbon, nitrogen, oxygen, and fluorine, have several positron-emitting isotopes. Table 6.1 shows the $\beta+$ emitting isotopes most widely used in nuclear medicine along with several of their characteristics.

The half-life and the positron range are the most relevant parameters in the clinical practice of nuclear medicine. The half-life determines how the isotope can be handled: a shorter lifetime allows the image to be obtained in a shorter time thus reducing the exposure of radiation to the patient. This also creates logistical complications, explaining why most PET isotopes must be produced on-site by means of dedicated accelerators. The positron range, on the other hand, limits the spatial resolution of the PET image:

Isotope	Half-life (min)	Endpoint energy (MeV)	Average range in water (mm)
^{11}C	20.3	0.96	1.7
^{13}N	9.97	1.19	2.0
^{15}O	2.03	1.70	2.7
^{18}F	109.8	0.64	1.4
^{68}Ga	67.8	1.89	1.7
^{82}Rb	1.26	3.15	-

Table 6.1: Properties of positron emitting radioisotopes commonly used in nuclear medicine.

the shorter the range, the better the potential accuracy of the reconstruction and the quality of the image.

6.1.2 Sources of noise in PET

The most common sources of noise in a PET detector arise from accidental coincidences between two non-correlated photons and from scattering within the body of one or both of the photons before their arrival to the detector. Figure 6.4 illustrates how both scatter and random coincidences arise in a PET detector. In dealing with PET scanners, the fraction of total events corrupted by these sources of noise is typically quantified by two values, the scatter fraction (SF) and the signal-to-noise ratio (SNR). Noise arising from scattered and random events, if not rejected before reconstruction, leads to a degradation of the image quality, including image artifacts which are even more obtrusive for clinicians.

In PET detectors, the rate of randoms is dependent on the rate of single events in each detector element and on the width of the time window used to select coincidences; the higher the single rate and the larger the coincidence window the more likely for a random to occur. In a simplified case of two detectors having single rates R_1 and R_2 the random rate can be shown to be

$$R_{random} = 2R_1R_2\tau$$

where τ is the time window used to select coincidences. When considering full-ring scanner geometries, all possible contributions of randoms between individual detector elements with unique LORs must be considered. In practice, the random rate can be measured by applying a delayed coincidence window in the electronics chain. In this way, true coincidences are not recorded and a sampling of the random rate over the entire scanner is made instead.

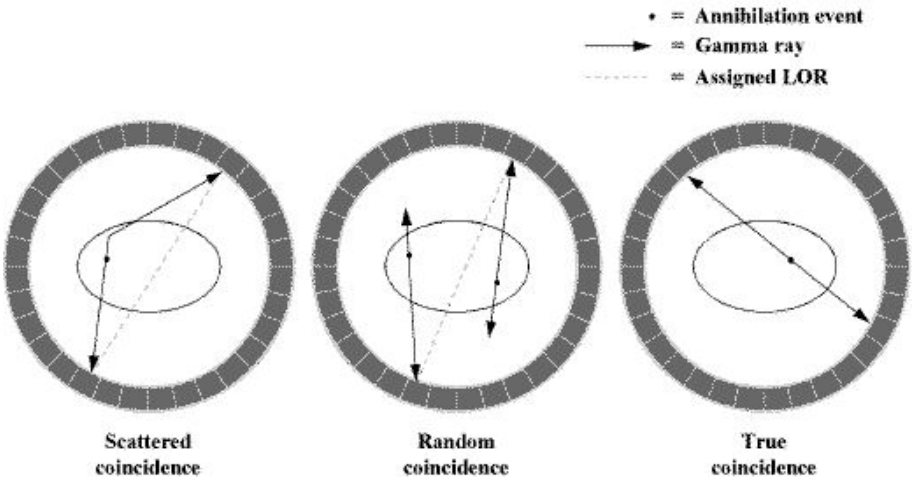

Figure 6.4: Sources of noise in a PET detector. Scatters occur when one of both photons interacts within the patient body before being detected by the detector (left). Randoms occur when two photons are detected which do not originate from the same positron annihilation (center). Only true coincidences should be accepted (right).

6.1.3 Choice of crystal and photodetector

Photons at the characteristic energy of PET have a rather low attenuation in biological tissues, which is what allows them to escape the body for detection. This same property makes them rather difficult to detect and for this reason, nearly all PET scanners make use of inorganic scintillator crystals which have a high absorption coefficient for 511 keV gammas. The crystals are coupled to a suitable photodetector which converts the scintillation light into an electronic pulse.

For the best PET performance, the scintillator should have a high density or Z, a short decay time, a high light output and a low attenuation to its own scintillation light. These properties ensure a good detection efficiency and light collection by the photodetector which should have similar or better timing properties than the scintillator, a linear gain over a wide dynamic range, and a high quantum efficiency in the emission spectrum of the scintillation photons.

The electronics for PET scanners are also important for the PET performance. Fast front-end electronics which provide a measurement of the energy deposited as well as the time of interaction must be connected to a DAQ system which evaluates coincidences in the detector modules and applies a threshold to select only 511 keV events. The dead-time of the acquisition chain must also be kept to a minimum since the longer a detector element is blind from the previous event, the higher the potential for a good

event to be missed, thereby reducing the effective sensitivity of the scanner.

The choice of crystal and photodetector is ultimately what will determine the overall sensitivity of the scanner but it also has a strong impact on the contribution from noise events. Specifically, the crystal should have a high efficiency for *photo-electric* absorption of the 511 keV photons and a good energy resolution. This allows a efficient rejection of energy-degraded photons which have scattered in the body prior to detection. In addition, the crystal must have a short decay time allowing a narrow coincidence window to be applied leading to a reduction of the number of randoms and therefore a better SNR.

In response to these requirements, the tendency in PET detector instrumentation has been to choose high density inorganic crystals with high light output coupled to an suitable photodetector with good timing properties and low noise. Traditionally, BGO and photo-multiplier tubes (PMTs) have been used in PET scanners, built-up from a large number of crystal-PMT assemblies. These were later replaced with larger BGO crystals which have been partially segmented to act as a waveguide. This allows the scintillation light from each segment of the block to be collected on several PMTs in a special way. By applying Anger logic, one can deduce in which segment of the crystal the interaction occurred by interpreting the ratio of signals in each PMT. Figure 6.5 shows a crystal-PMT assembly which uses the Anger logic principle. A 2" by 2" crystal block is coupled to four 1" square photomultiplier tubes. The BGO crystal block in this example has been machined into 64 segments each 6 mm square.

6.1.4 Image Reconstruction

The image reconstruction for PET imaging starts with the acquisition of coincidences occurring along LORs inside the camera's field-of-view; each pair of detected photons adds a count to a specific LOR in the detector. Upon the collection of a large amount of data over a large number of LORs, the concentration of the positron-emitting isotopes can be reconstructed by applying a mathematical method known as back-projection. This can be carried out either through an analytical computation or an iterative approach. The method most widely employed in analytical reconstructions is the filtered back-projection. This is often combined with an iterative method which uses a prediction of the current image fed back into the reconstruction to refine its quality on each step. The most common of these iterative reconstructions is the Maximum Likelihood approach combined with an Expectation Maximum algorithm. Many other possible techniques exist and more efficient and accurate algorithms are being studied in the field of PET image reconstruction, particularly as novel PET geometries become more commonplace in the field.

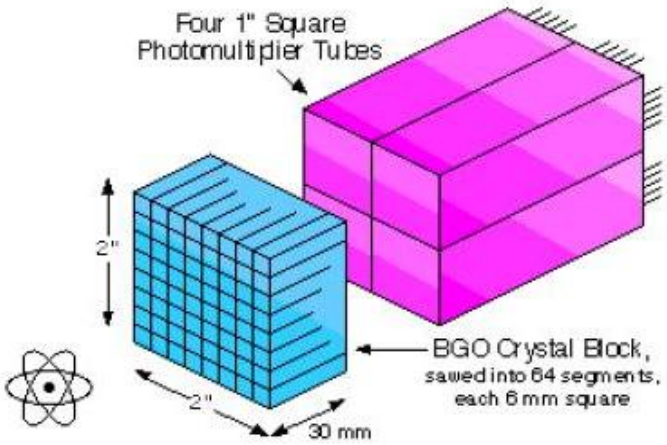

Figure 6.5: Traditional PET module consisting of a BGO block and four photomultiplier tubes. The BGO is specially cut to serve as a waveguide such the light produced by photon absorption is shared over all 4 PMTs. Using Anger logic the initial interaction can be located within the BGO block segments from the ratio of signals in the 4 PMT block assembly coupled to the crystal.

6.1.5 Evaluating PET Performance

When comparing the parameters of a PET detector, several concrete indicators are useful. The most commonly cited, and the most important in the scope of this dissertation, are the PET sensitivity and the spatial resolution.

The spatial resolution of a PET image is defined as the accuracy in localizing the positron emitting isotope within the FOV of the scanner. In principle, the spatial resolution is limited by the range of the positron, but in practice it depends mainly on the precision in determining the point of interaction of the photons in the crystal of the PET modules. This governs the accuracy of the determination of the LOR and therefore the accuracy of the reconstruction. Since the positron range for most isotopes used in clinical practice is on the order of a mm in tissue, this put a lower limit on the spatial resolution for all PET systems.

The PET sensitivity can be defined as the total probability of the PET scanner to record a valid coincidence, usually expressed in units of cps/kBq (counts-per-second per 1000 decays of the radio-pharmaceutical). The sensitivity depends in a complex way on many parameters of the PET scanner design. Generally speaking, the sensitivity will depend on the absorption co-efficient of the crystals and their length as well as the solid angle coverage of all crystals in the ring scanner design. Since an energy selection is made on events in each unit detector, the specific photoelectric absorption

probability of the crystal to 511 keV gammas is also important. Present-day commercial full-body PET scanners based on LSO scintillator typically have a sensitivity in the range of 5-10 cps/kBq.

As has already been mentioned, the width of the coincidence window and the dead-time during event readout also play a crucial role in determining the performance of a PET scanner. A larger time window worsens the SNR since more randoms will be recorded. A larger dead-time leads to a loss in sensitivity since the likelihood of missing a good event while blind from scatters or randoms increases. In general, faster systems result in a higher effective sensitivity, which is of considerable importance for the overall PET performance.

6.2 New advances in PET technology

Despite the pervasiveness of PET imaging in medicine and a solid and successful 20 years of the clinical application of commercial PET/CT scanners, PET technology is still evolving. The end goal is to obtain images faster and of higher accuracy, improving the relevance of the PET image and allowing for a lower dose to the patient, an inescapable consequence of every PET scan. The introduction of higher sensitivity PET cameras with better performance into the clinical world is very desirable: time is precious in any hospital environment yet even more so is the well-being of patients. Not surprisingly then, PET research is very active and competitive in striving to improve upon existing PET technologies. Nowadays, the trend in PET research is towards crystals with higher density, higher light yield, and faster timing properties; photodetectors with better energy resolution, quantum efficiency, and higher signal-to-noise; and improved electronics and acquisition systems.

6.2.1 DOI localization

The majority of commercial scanners employ unit PET detectors which make use the Anger logic technique described above to localize the interaction position of the 511 keV gamma within the scintillator crystal. One drawback of the Anger logic approach is the fact that differences in the depth-of-interaction (DOI) of the photon within the crystal change the ratio of signals on the PMTs, thereby degrading the localization and leading to a loss in spatial resolution since the LOR is less well defined [72]. In addition, without a measurement of the DOI, the PET system suffers from parallax errors for LORs that intersect the crystal at an angle, usually near the edge of the camera's FOV. Figure 6.6 demonstrates the error in the LOR determination when the DOI is not known.

Without a measurement of the DOI, the PET scanner suffers from a significant degradation in spatial resolution and resolution uniformity [73].

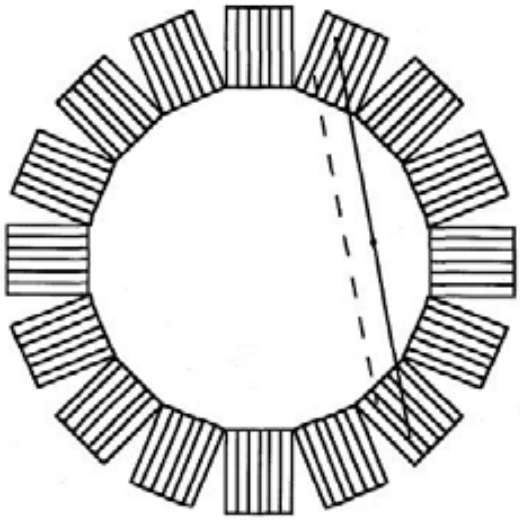

Figure 6.6: A schematic diagram of a typical PET geometry showing the error in LOR determination induced when no depth-of-interaction (DOI) measurement is possible. The false LOR is shown as the dotted line while the true LOR is shown as the solid line [75].

This puts limitations on the design of the crystal modules and the overall ring design. For example, the use of shorter crystals reduces parallax errors and LOR uncertainties but at the expense of sensitivity. Because of this, scanners must be larger than needed (and therefore more expensive) since the loss of spatial resolution at the edge of the FOV introduced by parallax makes wide-angle FOV images - wide with respect to the scanner diameter - too distorted to be useful to clinicians. If new technologies are introduced capable of measuring the DOI with some precision, this will allow PET scanners to be built with smaller ring diameters and greater axial extent at the same cost, resulting in gains in sensitivity. Similarly, for specialty high-resolution (<2 mm FWHM) PET scanners, hardware with DOI localization can lead to much higher sensitivity since the crystals can be made longer [74].

Many ideas have been proposed to allow for a measurement of the DOI within the scintillating crystal. Some solutions involve using two types of crystal coupled in a special way such that the light shared between the two depends on the DOI and can be measured [75]. Another method, illustrated in figure 6.7, is to use photodetectors on both ends of the crystal in which the ratio of light collected at each end can be used to extract the DOI along the crystal [76]. More creative ideas are also being explored. For example, the AxialPET group, a collaboration of over 9 institutes (including CERN),

Figure 6.7: A proposed PET design where the DOI information is extracted from the ratio of signals recorded by photodetectors at each end of the crystal.

proposes to use long axially-oriented bars of LYSO coupled orthogonally to strips of WLS material in a regular and repeated matrix. A schematic of one block of the AxialPET matrix is shown for illustration in figure 6.8. Both scintillator bars and WLS strips are read out on both sides by SiPMs allowing for a precise transverse and DOI localization of the photon interaction [77]. Already, a dual-head demonstrator made of 95 LYSO bars and 312 WLS strips has been built and tested by the collaboration. Their results with phantoms and FDG imaging in rodents has demonstrated an improved sensitivity and spatial resolution as compared with traditional Anger logic technologies.

Another method for measuring the DOI is to use a single large monolithic crystal coupled to a photodetector with position sensitivity. Such photodetectors, usually referred to as multi-anode PMTs, have become commercially available in recent years and in large surface areas. In the monolithic approach, the light from a gamma absorption in the crystal is shared over many anodes of the photodetector and the response from all anodes read out simultaneously. For each photon interaction the light response over the anodes is analyzed numerically. In this way it is possible not only to determine the transverse (XY) position of the interaction with a precision better than modules using Anger logic, but also the DOI from the shape of the distribution: interactions close to the photodetector produce a narrower peak (less sharing over anodes) and those far from the photodetector are wider (more sharing). Figure 6.9 illustrates this principle assuming a position-sensitive photodetector having 16 anodes.

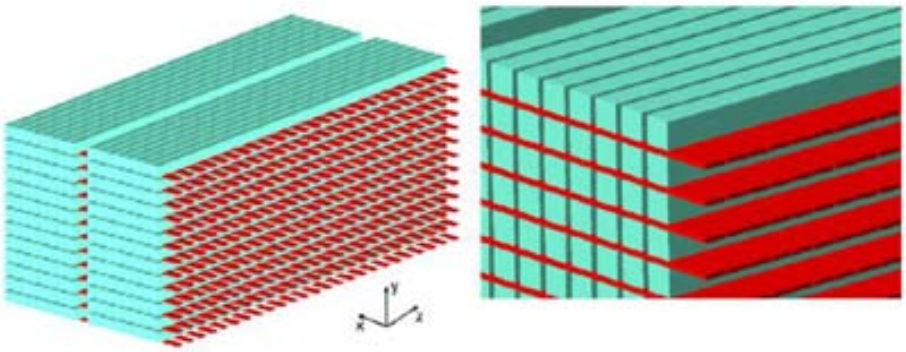

Figure 6.8: A schematic diagram of the proposed AxialPET matrix of orthogonally read out LYSO bars and WLS strips [77].

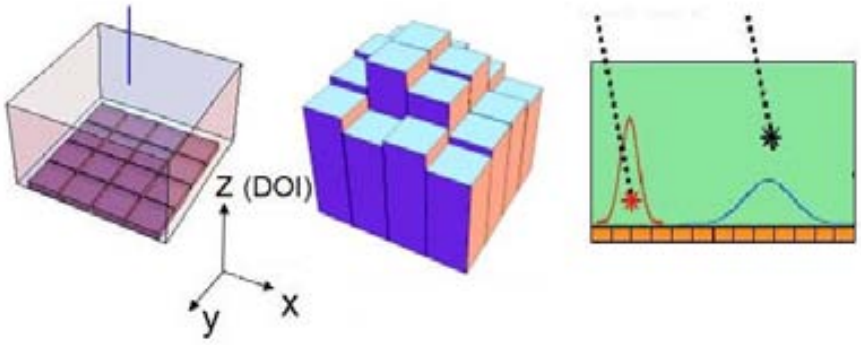

Figure 6.9: An illustration of the idea to use a single monolithic crystal coupled to position-sensitive photodetectors for determining the DOI from the distribution of light on the anodes [80].

This monolithic approach has already been proven by other research groups active in the field of nuclear medicine. Using a 64-anode PMT and a crystal slab of 50x50x8 mm^3 a spatial resolution of <1.4 mm has been achieved along with 1 bit of DOI data [78]. In addition, simulations studies suggest that a DOI determination of less than 5 mm is feasible, even in thicker slabs of monolithic scintillator [79].

6.2.2 TOF-PET

The quality of PET reconstruction is degraded by noise events arising from scattered photons and randoms. In particular, scattered photons, which result in the wrong LOR being recorded, can lead to image distortions and artifacts in the PET image. Though not a serious problem when imaging small volumes, full-body PET scans suffer from a high fraction of scattered

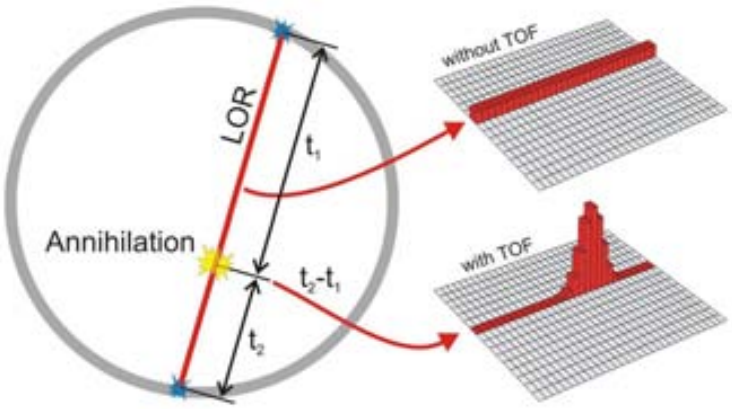

Figure 6.10: The principle behind time-of-flight PET.

events, expressed as a high SF. In crystal-based scanners, the energy resolution of the 511 keV photo-peak is largely what determines the efficiency of the scatter rejection and thus the SF, for a given patient volume in the scanner's FOV.

One solution to reduce the contribution of scattered events and randoms is to measure the time-of-flight (TOF) between the 511 keV coincidences. Knowing the TOF allows for a precise localization of the origin of the positron annihilation along the LOR. This principle is illustrated in figure 6.10. In measuring the TOF between coincident detectors, the resolution which one can localize the annihilation along the LOR is determined by the accuracy at which one can measure the difference in arrival time between the photons, specifically

$$\triangle t = 2\triangle x/c$$

where c is the speed of light and x the position along the LOR. For illustration, a TOF resolution of 600 ps allows to constrain the annihilation position to a region along the LOR of about 9 cm FWHM. A 100 ps TOF resolution corresponds to a displacement of 1.5 cm along the LOR.

In TOF-PET reconstruction, instead of computing the overlapping of hit LORs, one makes the convolution of a position expectation over a small segment of the LOR. Algorithms which incorporate the TOF information can achieve images of equivalent quality using fewer statistics than conventional PET scanners and with a better spatial resolution [81]. In addition, with some assumption about the expected position of the radio-pharmaceutical (anywhere *inside* the body), localization along the LOR allows the rejection of a large number of scattered events which is of particular importance for full-body PET [82]. The use of fast PET hardware also allows the application of a shorter coincidence time window which has a direct impact on the

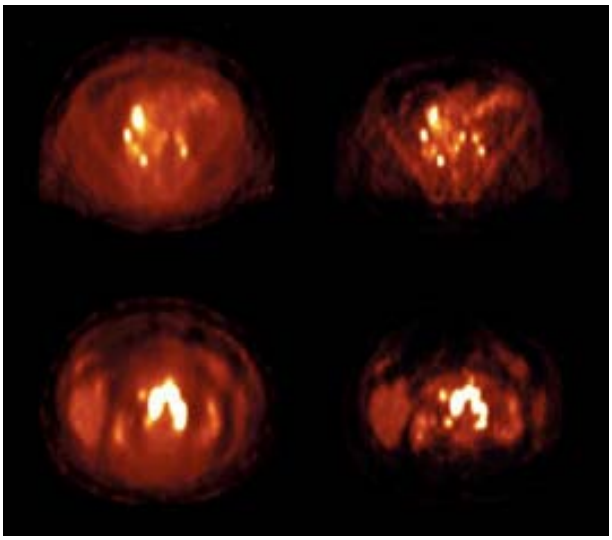

Figure 6.11: PET reconstructions without (left) and with (right) a time-of-flight determination of the coincident photons [84].

number of randoms recorded. In general, the TOF resolution has a large impact in rejecting randoms and scatters, leading to an increase in the SNR and a thus an improvement of the quality of the PET image. One needs only look to the example of a real PET image made with a commercial scanner with and without TOF (shown in figure 6.11) to appreciate how TOF-PET leads to better, more clinically relevant images. In addition to better quality images, the inclusion of the TOF information results in a reconstruction which requires less statistics, has a higher spatial resolution, and which reduces the sources of background noise improving the overall detector response [83].

In TOF-PET, the TOF resolution is determined predominantly by the intrinsic timing achievable in the crystal-photodetector modules. Faster scintillators and photodetectors are needed to obtain sub-nanosecond resolutions which allow a precise localization along the LOR. Although the front-end electronics must also be adapted for fast timing, the main challenge lies in choosing the right combination of crystal and photodetector which has the fastest timing characteristics. Since the performance of a PET scanner depends on other factors as well, the TOF resolution must be optimized without sacrificing on conversion efficiency or energy resolution. For example, the photo-fraction and light-yield of the scintillator must be considered as well as the matching between its spectral output and the photocathode of the photodetector. In practice, choosing the fastest combination of crystal and photodetector is not synonymous with optimizing the scanner's performance. For illustration, shorter crystals give better timing

Crystal	ρ (g/m^3)	Z_{eff}	Prob. p.e. abs (%)	Light output (γ/MeV)	Decay time (ns)	Scint. emission wavelen. (mm)	Hygr.
BGO	7.1	75	40	9000	300	480	No
LSO	7.4	66	32	30000	40	420	No
NaI:Tl	3.7	51	17	41000	230	410	Yes
CsI:Tl	4.5	52	21	66000	900	565	Slight
GSO	6.7	59	25	8000	60	440	No
LYSO	7.1	60	32	32000	41	420	No
LuAP	8.3	65	30	12000	18	365	No
YAP	5.5	33.5	4.2	17000	30	380	No
$LaBr_3$	5.3	47	-	65600	25	370	No
LuAG	6.7	63	27	18000	21	510	No

Table 6.2: Properties of crystals most commonly used for PET and those with potential for TOF-PET.

resolutions but are also less efficient in converting 511 keV gammas.

Since a detailed discussion about these concepts is beyond the scope of this thesis, we will instead discuss a few of the most important developments in crystal and photodetector technology which have appeared in recent years as well as referencing some of the most recent results from literature which provide a framework for approaching the problem of PET for *in-vivo* dosimetry.

New crystals

The requirements of TOF-PET have resulted in the investigation of new scintillators having shorter decay times. The other parameters required for TOF-grade scintillators are the same as in conventional PET: a high density, a high Z of the material, a high light output, and a low attenuation to the scintillation light. In table 6.2 the various parameters for several scintillator crystals used in PET imaging are summarized. The most relevant for TOF-PET are: LSO, LYSO, YAP, LuAG, and $LaBr_3$ because of their short decay times and high density and light output. In particular, scintillators based on lutetium and doped with cerium impurities (LSO:Ce and LYSO), are currently the best crystals for TOF-PET applications.

New photodetectors

In order to profit from fast and bright scintillators for TOF-PET applications, the photodetector must have a high-quantum efficiency to the emission

spectrum of the crystal and a low transit-time-spread (TTS). Also desirable as in conventional PET, are a good energy resolution, a high gain, and low noise.

Traditionally, photo-multiplier tubes (PMTs) have been used as the photodetector of choice in commercial PET cameras. Even today, PMT technology is still improving. More efficient photo-cathodes and shorter transit-time-spreads (hundreds of ps) are examples of some of the advances being made. Manufacturers are also producing arrays of PMTs housed in a single vacuum tube, an idea which has been exploited in novel detector designs like the ClearPET small animal scanner [85] developed by the Crystal Clear Collaboration (CCC)[86].

However, recent advances in alternative photodetector technologies have spurned the use of devices other than PMTs in PET systems. Micro-channel plates (MCP), and even more recently solid-state photo-multipliers are both examples of photodetectors that are generating excitement in the PET research community. MCPs are especially interesting for fast timing applications because of their very short TTS (several ps) and because they can be produced in large areas. Solid state photodetectors, especially SiPMs, are intriguing because of their excellent energy resolution, timing properties and because they have recently become very cheap to produce. Their small surface areas generally limited to 3x3 mm^2, however, are one drawback, although arrays of multiple SiPMs integrated onto a single chip offer a solution and are receiving more and more attention. Since prices are expected to fall as these devices become mainstream in the photodetector industry, we can also expect that MCPs and SiPMs will gradually replace PMT technologies in modern PET camera hardware.

Current status of TOF-PET research

With the appearance of new crystal and photodetector technologies with fast timing characteristics, interest in TOF-PET has renewed in recent years. In fact, commercial PET scanners which make use of TOF principles are already available on the market. The Philips Gemini PET/CT scanner, for example, makes use of 4x4x22 mm^3 LYSO crystals coupled to large PMTs and achieves a coincidence timing resolution of 585 ps [87]. Already with this modest TOF resolution, a significant improvement in the quality of images and acquisition speed is observed by clinicians, especially for full-body 3D imaging of heavy patients.

The TOF performance of currently available commercial scanners, however, is not representative of the best results from current state-of-the-art research. In fact, resolutions as low as 100 ps can be expected in the near future as current technologies are integrated into commercial devices. With this motivation many groups have conducted experimental tests on a variety of different combinations of crystals and photodetectors in order to optimize

their performance for TOF-PET. The approach favored by most groups has been to measure the achievable TOF resolution with single crystal-photodetector modules in coincidence and then to extrapolate those results through simulation in order to predict the performance of a full-sized scanner based on the same individual elements [88].

Many of the scintillators in table 6.2 have been characterized in this way and a good review using small sized crystals is published in reference [89]. In this study LSO is determined the best TOF-PET candidate because of its short decay time, high stopping power and high light output. A similar study has also been carried out by the CCC at CERN, with the inclusion of various types of photodetectors. Using small 2x2x10 mm^3 LSO crystals and SiPMs, they report a coincidence TOF resolution as low as 220 ps FWHM [90]. In another study focused on comparing several types of modern and fast PMTs, a single detector timing resolution of 200 ps FWHM has been achieved using LSO crystals having 10x10x5 mm^3 dimensions [91]. Even more encouraging, some groups are reporting coincidence TOF resolutions below 100 ps using small $LaBr_3$ crystals doped with cerium and coupled to SiPMs [92].

6.3 The challenges for *in-vivo* PET dosimetry

$\beta+$ emitters produced in biological tissues during ion therapy, through their decay of a positron and its subsequent annihilation, produce two collinear photons which can emerge from the body both during and in the minutes following irradiation. These collinear photons can be detected using the conventional PET technologies described above though the technique is more challenging than in the clinical practice of nuclear medicine.

In proton and carbon-ion therapy, the $\beta+$ emitting isotopes that occur in the greatest abundance are ^{11}C, ^{15}O, and ^{10}C which decay with a half-life of 20 min, 2 min and 20 s, respectively. The other isotopes contribute to less than 3% of the total yield and are generally disregarded. In carbon ion therapy the activity is dominated by ^{11}C and ^{10}C isotopes from projectile fragments which accumulate close to the end of beam range. Figure 6.12 sketches roughly the distribution of $\beta+$ emitters induced by a carbon ion beam (shown along with the Bragg peak dose profile shown for illustration). In proton therapy only the target nuclei are activated, occurring when sufficient energy is available above the nuclear reaction threshold, leading to a characteristic drop a few millimeters before the Bragg peak.

In both cases of proton and carbon ion therapy, the $\beta+$ activity distribution is not directly correlated to the delivered dose. Generally speaking, it is highly dependent on the tissue morphology and composition and the particle species and energy. For this reason, simulation studies are fundamental for correctly interpreting the PET data, which must be compared

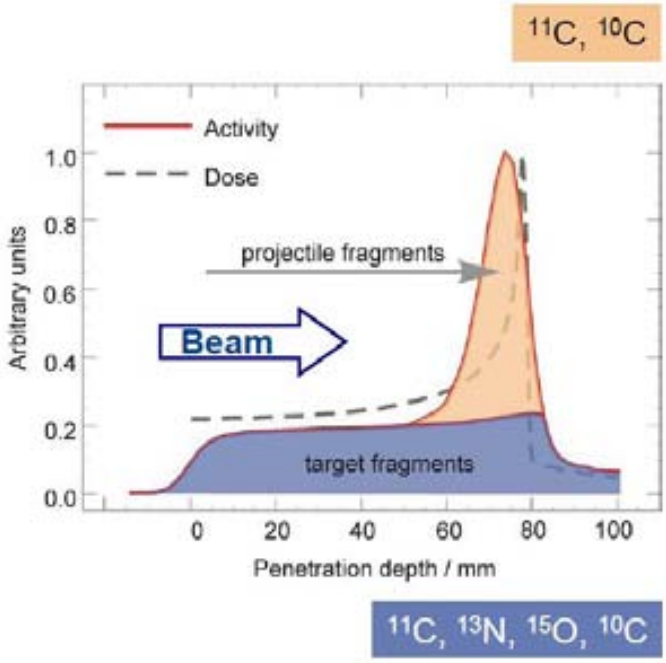

Figure 6.12: Illustration of the induced $\beta+$ activity by target and projectile fragments for ^{12}C ion therapy. The Bragg curve is shown for comparison [93].

to a prediction of the $\beta+$ activity calculated from simulations that use the treatment plan and planning CT as input. Many Monte-Carlo studies exist [94] [95] [96] [97] [98] to study the production of these isotopes for carbon and proton beam irradiations typical of therapy. The results of simulation studies, which have been confirmed experimentally with tests using PMMA targets, highlight that the total activity induced, on the order of about 1kBq for 10^6 incident ^{12}C ions and about 100 Bq for 10^6 incident protons, is typically 50 to 500 times smaller than in the case of standard nuclear medicine applications [93].

In addition to simulation and phantom studies, our understanding of the problem has been greatly enhanced by several key clinical trials in which in-beam PET and off-line PET have been performed with human patients receiving proton or carbon-ion therapy. In addition to confirming the low activation, these studies have been important in highlighting the challenges for clinical in-beam PET, one of which is the biological washout of the $\beta+$ emitters caused by the blood-flow in diffuse tissues which occurs in the minutes following treatment, which further limits the useful $\beta+$ activity. Two of these clinical studies, the pilot in-beam PET project at GSI and the off-line PET measurements carried out at MGH Boston, are described in the following sections.

6.3.1 The GSI experience

The in-beam PET technique has been applied in clinical studies made with patients undergoing carbon ion therapy at GSI in Darmstadt, Germany. Their scanner, named BASTEI, has a dual-head geometry and has been assembled from BGO-based detector components and integrated into the carbon-ion treatment room (see figure 6.13). Each head of the BASTEI scanner consists of 32 detector blocks generating over 4.2 million LORs.

Figure 6.14 shows a sample of the data acquired by the BASTEI during a carbon-ion irradiation of a patient at GSI. During the beam delivery from the GSI synchrotron, which lasts about 2 seconds followed by a 3 second pause, the data contains a large background from the particles which are emitted promptly during irradiation [100]. Since the data during the beam spill is corrupted by this background noise, the system records the status of irradiation (beam on/off) along with the PET data, as well as the characteristics of the beam such as its energy, lateral dimensions, and intensity. This information allows not only to reject noise-corrupted data, but also to improve the accuracy of the activity predication by including the complex time-dependent activity signal (which depends on the time structure of the beam and the mixed isotope production) into the simulations [99].

In the GSI approach, the positron distribution is first predicted by performing a Monte-Carlo simulation which uses the treatment plan and planning CT as input. The expected $\beta+$ activity distribution is then compared

Figure 6.13: The BASTEI scanner at the heavy ion treatment center at GSI Darmstadt.

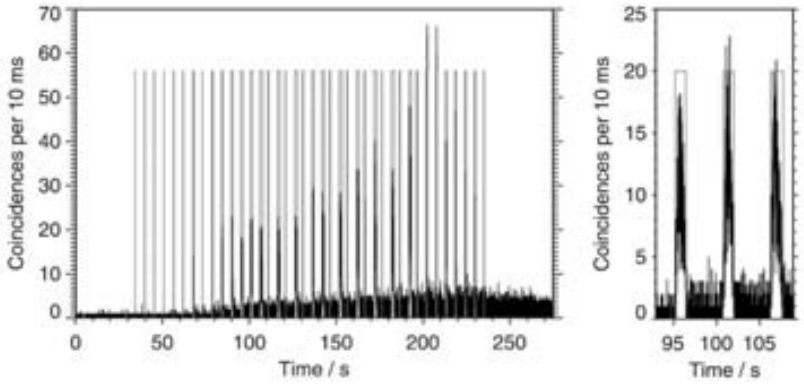

Figure 6.14: Coincidence rate measured with the BASTEI scanner during a carbon-ion irradiation of a patient at GSI. The spill structure from the GSI synchrotron, which have a 2 s duration followed by a 3 s pause, is visible in the data [100].

with a measurement made using the BASTEI scanner. Any significant deviations are investigated and if needed, a computer-aided interactive approach can be used to provide insights as to the discrepancy [101]. In rare cases, counteractive measures can be taken by clinicians, such as a performing a new planning CT scan, a recalculation of the treatment plan, or prescribing medication for adverse effects of the erroneous treatment. The reconstruction software uses a Maximum Likelihood Expectation Maximization (MLEM) algorithm which has been adapted to the dual-head configuration [66].

At GSI between 1997 to 2008, a pilot study was performed using the BASTEI scanner involving approximately 430 patients receiving carbon therapy for cancers mainly in the head and neck region. Figure 6.3.1 shows the planning CT with dose over the treatment plan, the predicted $\beta+$ activity distribution, and the actual PET reconstruction obtained by the BASTEI scanner in one of the patient studies. The study showed that in about 10% of cases, a modification to the treatment plan was necessary due to random errors such as patient misalignment, patient motion or organ motion, and density changes within the irradiated volume [102]. In addition, systematic discrepancies between the measurements and calculations were observed leading to improvements to the calibration between proton and CT data which are now used in clinical practice [103].

Stopped in 2008 with the closure of the GSI clinical program and the opening of the HIT, the GSI study has been nevertheless fundamental in validating the merit of the in-beam PET approach and in highlighting the opportunities for clinicians who wish to perform quality assurance in proton and carbon-ion therapy.

6.3.2 Off-line PET at MGH Boston

A commercial full-ring PET/CT scanner is being studied for *in-vivo* dosimetry with patients undergoing proton therapy at the Massachusetts General Hospital (MGH) in Boston. The use of a PET/CT scanner rather than PET alone allows for a better co-registration between the planning and imaging positions, an improvement over the manual co-registration employed during the GSI pilot study. It also benefits from the improved sensitivity over limited-angle in-beam PET geometries and the fact that the scanner is already available nearby.

In the initial study, 9 consenting patients suffering mainly from head-and-neck and para-spinal tumours were walked to a PET/CT scanner nearby immediately following a single session of fractionated radiotherapy using protons [104]. Patients received total doses of 1.8 to 3 GyE per fraction delivered in either 1 or 2 fields. The time between the end of treatment and the beginning of the PET scan was between 13-20 min, with the PET scan lasting an additional 30 min. Patients receiving two fields were scanned

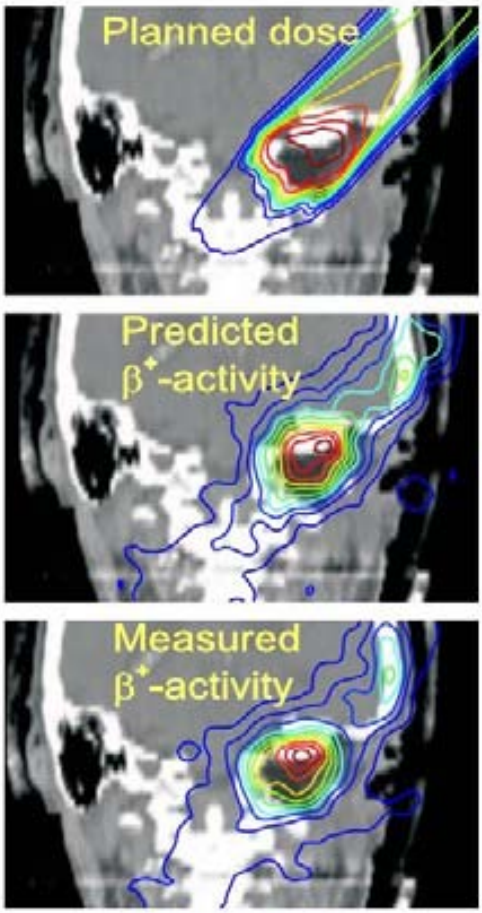

Figure 6.15: The dose distribution expected from a treatment plan (top), the simulated $\beta+$ activity distribution (middle) and the measured $\beta+$ activity (bottom) in a patient at GSI Darmstadt [97].

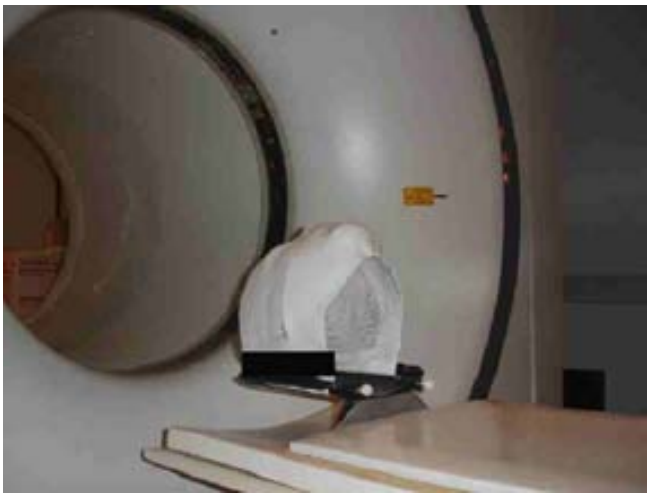

Figure 6.16: Setup for *in-vivo* dose monitoring using an off-line commercial PET/CT at MGH Boston. Also shown is the immobilization device for a patient with cranial tumour, carried along with the patient to improve co-registration [**?**].

after each irradiation in the same manner. In 7 out of 9 cases, the treatment immobilization device was carried along with patients and used for fixation of the patient at the remote PET/CT scanner. Shown in figure 6.16 is the commercial PET/CT scanner and patient bed as well as one of the fixation devices carried along with one of the patients suffering from a cranial tumour.

In analyzing the PET data, a similar procedure to that used at GSI has been followed, with the added ease of computer-aided co-registration made possible by the PET/CT. The patient-specific and field-specific $\beta+$ activity were first calculated from the treatment plan using Monte-Carlo. The simulations were also designed to dynamically model the biological washout of the activity distribution caused by blood flow through the tissues in the time elapsing from the treatment to the end of the PET scan. The PET image was then visually compared with the simulated ones with special attention to the position of the distal fall-off of the activity at the end of the beam range. In addition, the delivered dose was calculated back from the measured PET data for comparison with the original from the treatment plan. Shown in figure 6.17 is the data set for one patient of the MGH study suffering from clival chordoma. As this patient received two irradiation fields (of 0.96 GyE each), the data from both PET scans, carried out 26 and 16 min after each beam delivery, are superimposed. The upper two images display the planned dose delivery (left) and its Monte-Carlo recalculation (right). Shown below is the measured PET image (left) along with the Monte-Carlo expectation (right).

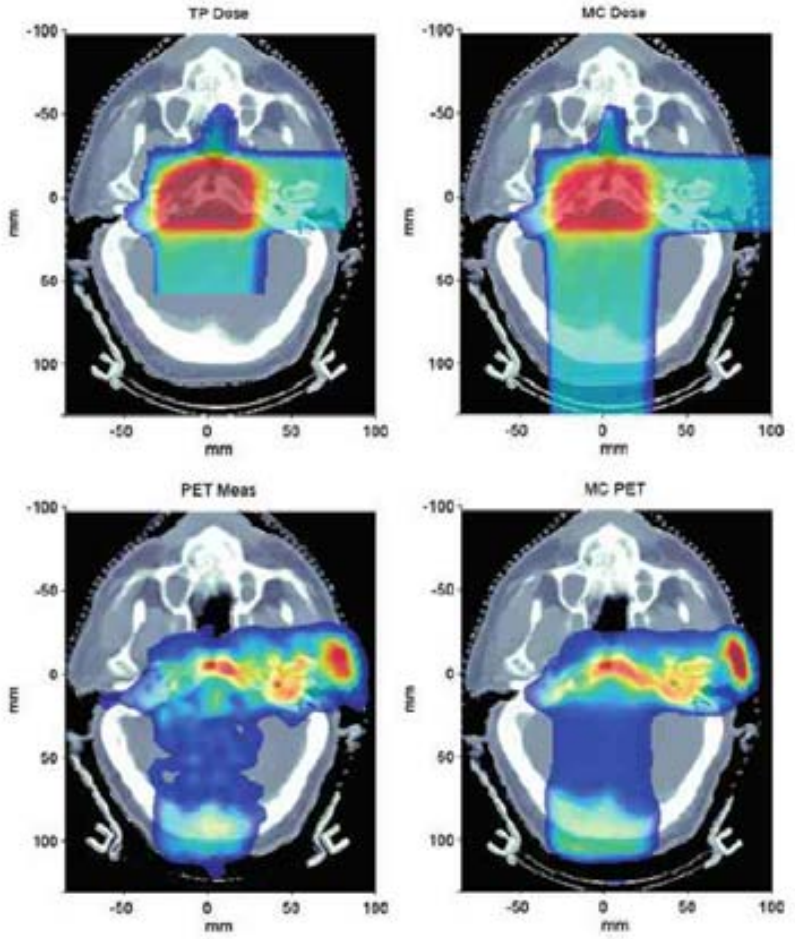

Figure 6.17: Image set for one chordoma patient at the MGH Boston. The planned dose delivery (left) and its Monte-Carlo recalculation (right) are displayed at the top while shown below is the measured PET image (left) along with the Monte-Carlo expectation (right). [104].

This study has been important in validating the off-line approach to *in-vivo* PET monitoring although a few of the challenges were also highlighted. Because of the long delay between irradiation and the PET acquisition, only the contribution from long-lived emitters (mainly ^{11}C) was registered. Tissues with high blood perfusion could not be imaged accurately because of the washout of the $\beta+$ activity. In addition, some limitations from fixation and co-registration issues were reported for ocular and extra-cranial sites. Despite these issues, the study has demonstrated a good spatial correlation and quantitative agreement within 30% between measured and expected $\beta+$ activity distributions. Furthermore, an accuracy in range monitoring as low as 1-2 mm has been achieved in tissues well co-registered and with low blood perfusion [105]. These results are very promising and have prompted interest in extended clinical studies which aim to improve performances and investigate additional indications that could benefit from off-line PET monitoring.

6.3.3 TOF-PET for hadrontherapy dosimetry

As discussed at the beginning of this chapter, the actual implementation of PET for hadrontherapy dosimetry can be either in-beam, in which a limited-angle scanner is dedicated to the treatment room, or in-room or off-line, in which a conventional full-ring PET scanner can be employed. Regardless of the specific implementation, the main challenge is the low activity which arises from a typical proton or carbon ion irradiation, which is further complicated by the biological washout.

For in-beam PET, the mechanical restrictions imposed by the beam-line and patient bed limit the angular coverage that the scanner can have and therefore its sensitivity. In addition, the high background flux of secondary particles produced exactly at the time of beam delivery, particularly in the forward beam direction, makes it practically impossible to operate when the beam is on. For in-beam PET, the data acquisition must be gated on the beam spill-structure in order to reduce this background noise. Fortunately, this is possible with many present-day proton and carbon-ion accelerators which make use of synchrotrons and has already been proven feasible during the GSI pilot study. Also, since an in-beam PET scanner must be dedicated to the treatment room, each particular scanner design must be tailored to the physical space requirements of the treatment room that it serves. This precludes the use of existing commercial PET systems and demands a substantial research investment.

In-room or off-line techniques can profit from the availability of full-ring commercial scanners and make use of their high sensitivity. In addition, for in-room and off-line techniques, PET/CT is also an option, facilitating the co-registration of the reconstructed PET image to the planning CT. However, the main drawbacks of these approaches are the loss of short-lived

isotopes such as ^{10}C and that the total activity is rapidly falling with each minute which passes between the moment of irradiation and the beginning of the PET scan. This is why in-room PET should be performed rather than off-line PET, especially if the scanner is located a long distance from the treatment room.

Choosing the optimum solution for a PET scanner built to perform *in-vivo* dose monitoring in hadrontherapy is a challenging endeavor and currently a topic of debate in the scientific community. Nevertheless, the clinical experience gained during patient studies clearly demonstrate the feasibility of range monitoring with a PET apparatus, either dedicated to the treatment room or nearby in the hospital. Thanks to the pioneering efforts, there is a growing interest in *in-vivo* treatment verification using PET [106]. With the advent of new crystal and photodetector technologies in the field of conventional PET for nuclear medicine, it seems likely that the main challenge of low statistics inherent in the application can be at least partially overcome as modern PET detector with high TOF resolutions become increasingly available. In fact, because TOF leads to an effective gain in sensitivity, there is currently a drive in the hadrontherapy community to develop a next generation TOF-PET scanner developed specifically for in-beam PET application. The European project ENVISION, in addition to exploring the use of the prompt detection modalities, is largely geared towards developing a PET demonstrator which makes use of the latest TOF technologies and could be used for *in-vivo* dosimetry in hadrontherapy. The experimental work on novel detector hardwares presented in the rest of this thesis are in line with this goal and have been partially funded in the framework of the ENVISION project.

Chapter 7

Results with TOF-PET prototypes

For the application of in-beam PET for *in-vivo* range monitoring and dosimetry in hadrontherapy, the TERA foundation has built novel PET camera modules and measured their performance in the laboratory using a source of ^{22}Na, a $\beta+$ emitter. Two main types of technologies have been developed, those which are based on the traditional combination of crystal-photodetector and those which make use of multi-gap Resistive Plate Chambers (MRPCs). In this chapter, we present in detail the results of the experimental work which has been carried out by the AQUA group using these two main classes of technologies. Before we describe the designs in detail as well as the results of measurements which have been performed, we first provide a short discussion about the motivation for our choices.

Crystal-PET

Following the trends of commercial PET technology, we have developed a unit PET camera block which makes use of an inorganic scintillator crystal coupled to a photodetector. Unlike traditional designs using Anger logic, it is based on a block of large crystals read out by a single position-sensitive multi-anode PMT, where the interaction localization is interpreted from the light distribution detected across a group of anodes beneath each crystal. This geometry allows not only for a measurement of the DOI, but also to maximize the packing fraction. It is hoped that this geometry will lead to a high detection efficiency with good spatial resolution while being able to reduce the effects of parallax error since the DOI is known.

Though having many similarities to the monolithic crystal designs presented in the previous chapter, TERA's proposal makes use of LYSO crystals and an alternative photodetector, a multi-anode MCP-PMT. A sub-nanosecond timing resolution is expected due to the excellent timing properties of LYSO crystals and MCP technology. Our design also differs from

other monolithic designs in that it is semi-monolithic: the crystal block coupled to the multi-anode photodetector is built not of a single crystal slab, but of five individual crystals. The crystals can be tightly packed into a unit and coupled to the surface of the MCP-PMT with little dead-space between.

MRPC-PET

The second class of PET detector studied by the AQUA group makes use of a technology called Multi-gap Resistive Plate Chambers (MRPC). Already used extensively in HEP, MRPCs are gas-filled detectors consisting of relatively cheap materials which makes them popular for charged particle tracking over large surface areas. In these applications, excellent position resolution and ultra-fast timing resolutions have been reported, making their application to PET, and particularly TOF-PET, very desirable.

The use of MRPCs in PET, however, is not evident, their very low conversion efficiency to 511 keV gammas being their main drawback. The reason is due to the physics: to be detected, the gamma must first interact in the bulk of the electrode material of the MRPC and then an energetic electron (either the Compton electron itself or a must escape into the gas gap where it can initiate electron avalanche in the high electric field in the gap. This principle is illustrated in figure 7.1.

Since common RPC electrode materials (glass, ceramic, or Bakelite) have a low density as compared to crystals, it follows that single-gap RPCs have a limited and tiny efficiency. Increasing the electrode thickness is of no use since the limited electron range restricts the volume of the electrode that can contribute to detection ($\sim$300 μm for glass). MRPCs, on the other hand, allow to improve the detection efficiency with each gap, without increasing the number of electronics channels. Because they are cheap and easy to build, one can envision realistically stacking large numbers of MRPC modules with large surface areas in order to reach an efficiency high enough for a PET application. This is the main goal of the simulation work presented in the final chapter of this thesis.

Another potential drawback for RPCs in a PET application is their inability to extract an energy measurement of the initial photon interaction. This is important in rejecting photons scattered in the body before detection which lead to false coincidences. Since RPCs operate in Geiger mode, the signal induced on the electrodes is saturated and non-proportional to the primary ionization. Even if it were possible to operate the MRPC in proportional mode, the primary interaction mechanism for 511 keV photons in glass is Compton scattering, therefore an unknown portion of the photon's energy is imparted to the ionizing electron, which follows a chaotic path before entering the gas gap. Rejecting non-scattered photons after they have been detected, therefore, is impossible for a scanner making use of MRPCs. It follows then that an MRPC-PET scanner would suffer from a high scatter

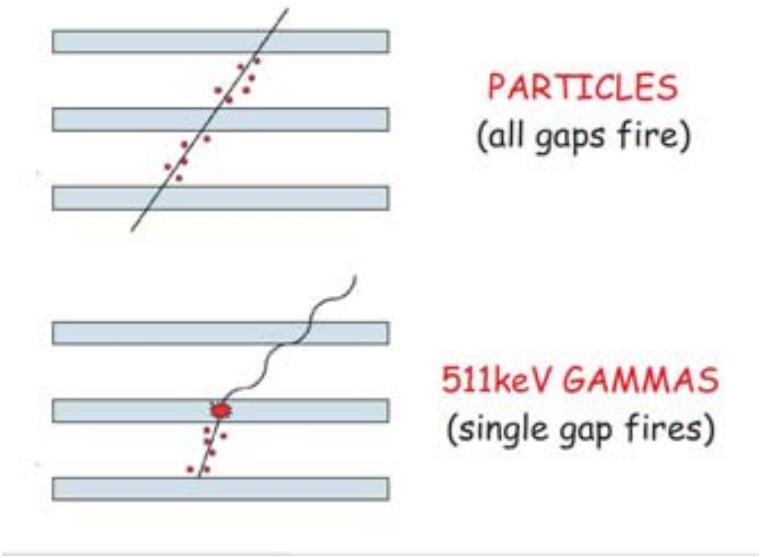

Figure 7.1: Detection principle of MRPC for charged particles (above) and for 511 keV photons (below).

fraction for full-body PET and potentially in hadrontherapy dosimetry as well. We shall see, however, MRPCs actually have an intrinsically higher detection efficiency for 511 keV photons than lower energy ones, which partially compensates for this drawback. This issue will be explored in more detail in the final chapter devoted to simulation work.

As it concerns MRPC-PET, both potential drawbacks, a low intrinsic sensitivity and lack of energy resolution, have solutions. The main reason MRPCs are attractive to PET, however, is because they can be used in TOF-PET, where a measurement of the time-of-flight between the collinear 511 keV gammas results in a higher effective sensitivity and signal-to-noise. In fact, the time resolutions that are typically achieved with MRPCs for charged particle detection in HEP are much better than those obtained with the state-of-art TOF-PET hardware based on crystal scintillators. In detecting 511 keV photons, the coincidence timing resolution of single-gap RPCs has already been measured by other groups to be 300 ps FWHM [107], which is better than existing commercial TOF-PET scanners based on LYSO or $LaBr_3$. The same group has also recently built a dual-head RPC-PET demonstrator and reports a spatial accuracy of 0.6 mm in their reconstruction of point sources [108].

In addition to a TOF measurement, a PET scanner based on MRPCs can also provide a DOI measurement. This arises naturally because in order to have a high enough sensitivity: an MRPC-PET scanner must consist of many single MRPC modules stacked one on top of the other in the radial

direction. Each module must be read out individually, and so the DOI is known at a resolution of the spacing between modules. This makes it feasible to build a PET scanner with a smaller patient bore diameter, which would result in an improved sensitivity at an equal cost, or the ability to increase the number of modules (also improving the sensitivity) without an increase of the total scanner size.

There have been several purposes for performing the experimental work with MRPCs which will be presented in this chapter. The first has been to investigate whether we can successfully build MRPC modules in a way that is suitable for large-scale production. Since a full MRPC-PET scanner would require many hundreds of modules, this step is critical in demonstrating that the unit detectors can be produced in the volumes needed for a PET application. The second has been to test whether our MRPCs deliver the excellent timing resolutions and other characteristics expected when detecting 511 keV photons. A final purpose has been to develop front-end readout electronics that can perform the data acquisition that would be required for a full MRPC-PET scanner.

7.1 LYSO-MCP

7.1.1 Choice of crystal-photodetector

A schematic representation of the proposal by the AQUA group for a unit PET module based on crystal scintillator (LYSO blocks and an MCP-PMT) is shown in figure 7.2. The MCP window is covered by 5 LYSO crystals having dimensions 60x30x12 mm^3 each. Such a geometry allows modules to be packed tightly with a minimum of dead-space over the entire active area of the MCP-PMT. In addition, because the total crystal size is larger than the photodetector housing, additional modules could be packed tightly together into compact detector heads while allowing enough room for mechanical support.

LYSO crystals

Five Prelude™ crystals having dimensions 12x30x60 mm^3 were purchased from Saint Gobain Crystals. Prelude™ is a lutetium-based inorganic scintillator with cerium doping very similar to LYSO. The crystals were characterized for light output and energy resolution using the available resources at the Crystal Clear lab at CERN. To perform the tests, each crystal was wrapped on 5 sides using Teflon tape to provide the best light collection. A picture of two of the crystals is shown in figure 7.3, one after wrapping in Teflon and another with an additional black tape wrapping which ensures no light enters from the exterior. The average light yield, recorded on a calibrated PMT setup was 27,500 γ/MeV with not more than a 5% variation

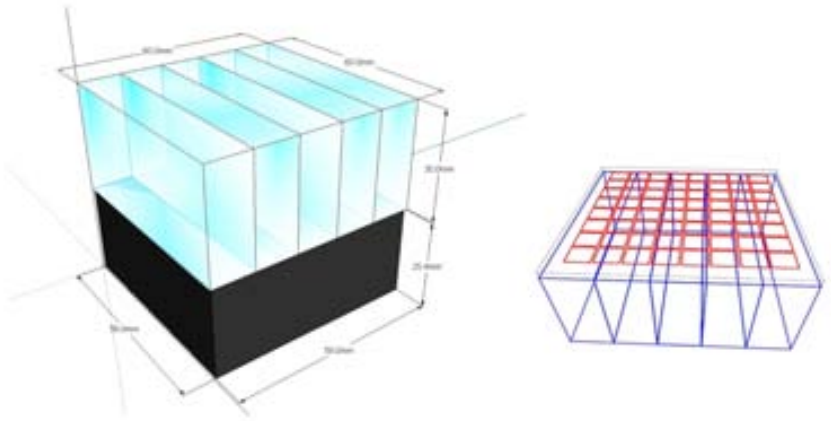

Figure 7.2: AQUA's proposal for a crystal-based TOF-PET unit module. The design is semi-monolithic: 5 crystals are read out by a multi-anode PMT and the light distribution is analyzed to find the interaction localization and the DOI.

between samples. In addition, the energy resolution was measured as 7% FWHM [94].

Photonis MCP-PMT

The Photonis XP85013 "Planacon" MCP-PMT was selected as photodetector and two devices were purchased for our studies. A photograph of one of them is shown in figure 7.4. The device consists of two MCPs having 25 μm pore size oriented in dual chevron configuration suspended above an 8x8 pixelated anode. The MCPs and anode readout are enclosed in a vacuum tube with a photocathode on the interior of the entrance window.

In addition to an individual readout for each of the 64 anodes, the Planacon also has a global output signal produced by the extraction of charge from the MCP plates themselves. Unlike the anode signals, the MCP-OUT signal is positive in polarity. Also, because the MCPs cover the entire anode structure, the MCP-OUT signal corresponds to the sum of the total signal collected by all 64 anodes. This feature allows for convenient triggering over all anodes simultaneously and has been used frequently in our experimental tests.

The Planacon MCP-PMT was selected for its good light-conversion efficiency and fast timing characteristics. The most relevant parameters taken from the vendor datasheet of the Photonis Planacon are summarized in table 7.1. The anode structure is 8x8 where each anode is 5.9x5.9 mm^2 arranged at 6.5 mm pitch covering a total active area of 53x53 mm^2. (In our design, the corresponding mapping between crystals and anodes is shown in

Figure 7.3: Two of the LYSO crystals wrapped in Teflon then black tape for mounting on photo-multiplier.

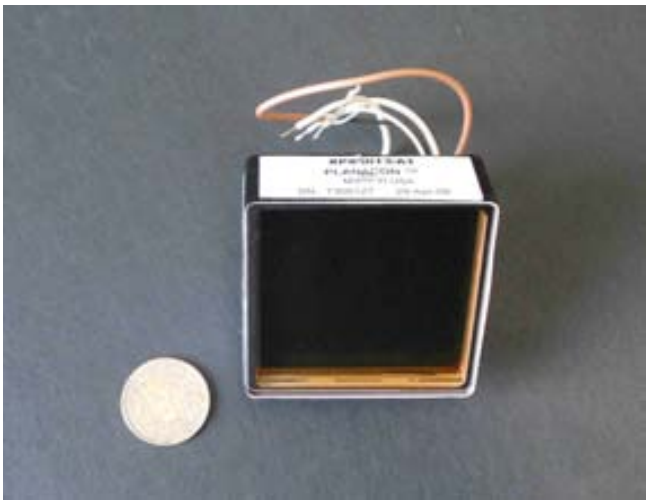

Figure 7.4: The multi-anode MCP-PMT XP85013 Planacon selected as photodetector for crystal-based PET module design.

Photonis XP85013	Typ. value	Max value
Peak sensitivity	400 nm	-
Anode structure	8x8 square	-
Active area	53x53 mm	-
Anode size	5.9 mm	-
Anode pitch	6.5 mm	-
Gain	6 x 10^5	-
Anode dark current @ 10^5 gain	1 nA	5 nA
Rise time	600 ns	-
Pulse width	1.8 ns	-
Anode uniformity	1 : 1.5	1 : 2.5 max

Table 7.1: Specifications of the Photonis Planacon XP85013 multi-anode MCP-PMT selected as photodetector for experimental tests.

the right of figure 7.2.) The photocathode is bialkali having roughly 25% quantum efficiency at the peak of 400 nm, well matched to the emission spectrum of LYSO. Also the device can achieve a very high gain, up to 6x10^5 at a maximum operating voltage of -2400 V. Both the photocathode spectral sensitivity and the MCP's gain curve are shown in figure 7.5, taken from the manufacturer's datasheet.

7.1.2 Anode calibration of MCP-PMT

One drawback of the Photonis MCP-PMT is the rather large non-uniformity of anode response, quoted as 1 to 2.5 maximum on the vendor's datasheet. The anode uniformity has consequences for the monolithic approach since the interaction localization within the crystal depends on correctly fitting the light distribution over the anodes beneath the crystal. Any variations in anode response and the localization could be degraded significantly. This property of the Photonis MCP-PMT made it necessary to study the anode response in an independent way such that any variation could be corrected for.

To make this calibration we devised an experimental setup in which the image of a UV diode is focused onto the MCP-PMT window and then precisely scanned across its surface. The diode used was a 3 mm diameter UV diode (type LED3-UV-400-30) which emits at 400 nm very close to the peak sensitivity of the MCP-PMT photocathode. In order to focus the light accurately onto the MCP-PMT window, the LED was encapsulated inside a plastic cylinder (with a long 3 mm diameter hole for partial collimation) and placed in the eyepiece of a microscope. The LED was pulsed with a 30 ns square wave from a function generator at a rate of 1 kHz. Next, the MCP-PMT was mounted in the microscope's focal plane, on an XY table

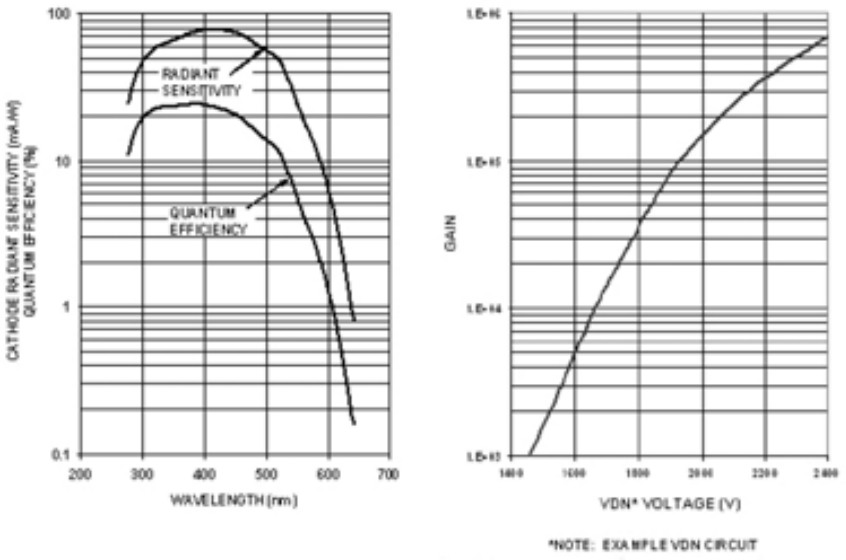

Figure 7.5: MCP-PMT QE of the photocathode and gain curve taken from the Photonis datasheet. (VDN = voltage divider network)

which can be adjusted with 0.3 mm precision. This setup is shown in figure 7.6.

With the MCP-PMT off and the UV diode on, the image of the UV diode was first focused onto the window of the MCP-PMT by adjusting the height of the microscope stage and observing the sharpness of the spot on the detector window. Once correctly focused, the size of the spot was roughly 2 mm in diameter, less than half the size of the anodes. The entire system was then covered by a opaque cloth and a voltage of -2200 V applied to the MCP-PMT.

Using standard NIM and CAMAC electronics, the response of the anodes was measured while scanning the UV light across the surface of the photodetector. The MCP-OUT signal was sent by a linear fan-out (LeCroy 428F) to a discriminator (LeCroy 821CL) allowing the generation of a gate needed for digitizing the anode signal using an ADC (LeCroy 2249A). A 160 ns gate was deemed sufficient to collect all the charge in the anode pulse and a delay of about 30 ns was added to the anode signal to bring it in time with the gate. The MCP-OUT pulse was also digitized in the same manner. The entire system was controlled by a CAMAC Wiener CC-USB with a custom software written in LABVIEW.

For each position, 5000 events were recorded. On each run, the pedestal of the ADC was estimated and subtracted from the response in the analysis. Scans were made moving the light spot by 1 mm and 2 mm in the Y and X directions, respectively. Shown in figure 7.7 is the response of one of the

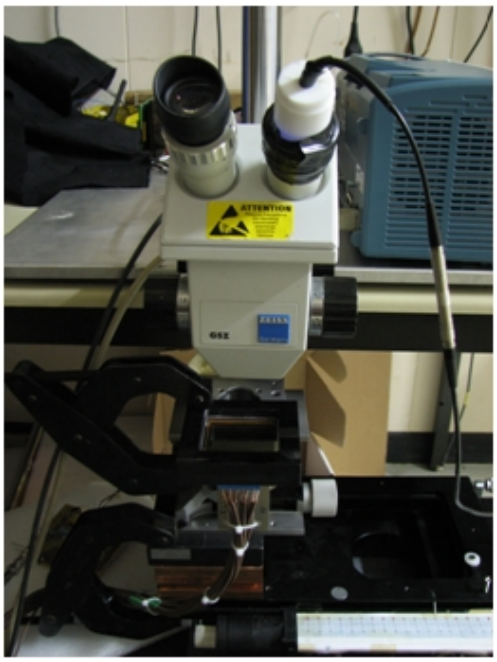

Figure 7.6: Setup for calibrating the MCP-PMT anode response. A UV diode, enclosed in a white plastic cylinder is place in the eyepiece of a microscope allowing an image of UV light to be focused on the window of the MCP-PMT. The MCP-PMT is mounted on a precision XY stage so that the light can be scanned across the MCP-PMT window.

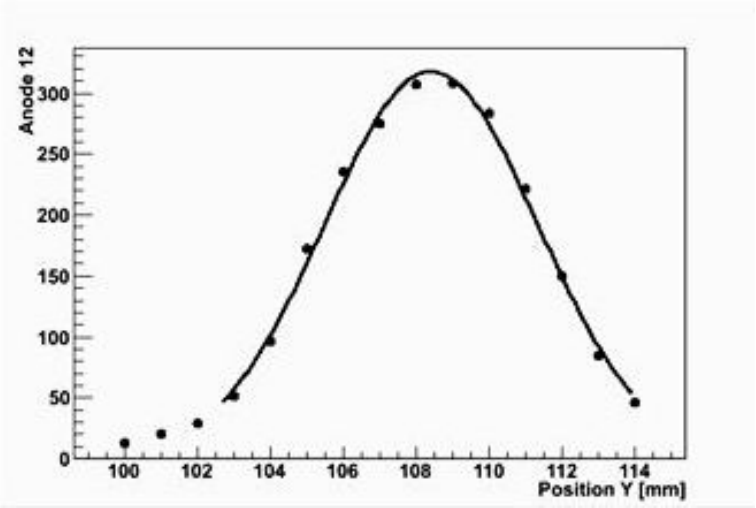

Figure 7.7: A single anode response to UV diode light scanned across surface of MCP-PMT. By fitting the response of each anode we were able to calibrate the relative response of 2 neighboring rows of 8 anodes (Courtesy of P. Solevi).

anodes to a scan in the Y-direction. By fitting the response of each anode in both X and Y we were able to deduce the center of its maximum response. The XY table was then moved to the position of the maximum and a new acquisition of 5000 events made which was used for the calibration.

This procedure was repeated for 16 anodes in two neighboring rows near the middle of the MCP-PMT. Shown left in figure 7.8 is the result with arbitrary units on the vertical scale. A maximum variation from the mean of 7% was observed. Shown on the right in the figure are the corresponding labels for the 16 anodes that were calibrated as well as their location with respect to the full 8x8 matrix.

7.1.3 Mechanical assembly

For all subsequent testing purposes, a single LYSO crystal was coupled along its 12x60 mm^2 face to the MCP-PMT window, directly over the set of 16 anodes that were calibrated by the UV diode procedure described above. The crystal was wrapped with Teflon and black tape and coupled to the MCP-PMT window using optical grease.

The crystal-photodetector assembly was then mounted in an aluminum box complete with a simplistic mechanics to hold the assembly in place with the crystal oriented precisely above two rows of anodes. A moderate pressure to ensure good optical contact between the crystal face and the detector window. One of the final prototypes is shown in figure 7.9.

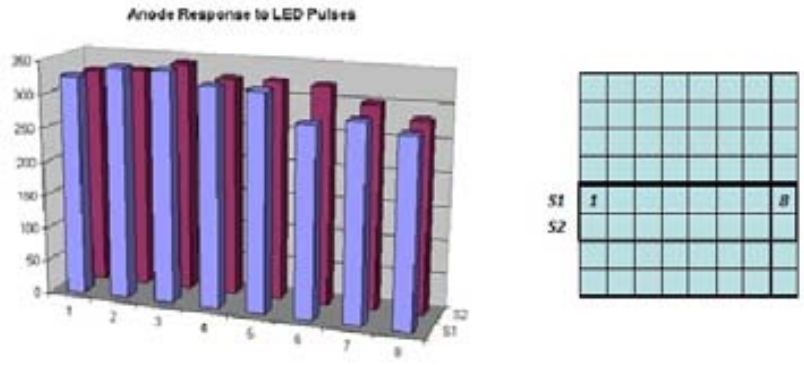

Figure 7.8: Relative anode response from UV light pulsing (left) used for calibration of the anode signals. The maximum variation of 7% from the mean. Also shown (right) is the location of the 16 anodes calibrated, which correspond to the location of a single LYSO crystal in future tests.

A light cap made of dark PMMA plastic and machined 3 mm thick (so as not to contribute to scatter) was also created to protect the detector from light leaks. In the rear of the box, an HV powering circuit was enclosed and the MCP output and HV routed to rear panel connectors for convenience (see figure 7.10). The anodes output pins, corresponding to the illuminated anodes beneath the crystal, were connected individually to coaxial cables.

Two such modules were assembled, each having only one LYSO crystal coupled over 2 rows of 8 anodes. This was done since only 5 LYSO crystals were purchased for initial testing, too few to equip both detector heads completely. Although this geometry is a simplification to the final one proposed for a compete module (in which 5 crystals are distributed over all 8 rows of 8 anodes) it was considered a good starting point for initial tests and proof-of-concept studies.

7.1.4 Experimental Results

LYSO background activity

LYSO is naturally radioactive due to the isotope ^{176}Le which emits a β- to the 597 keV excited state of ^{176}Hf. This state decays by triple gamma cascade having 88, 202 and 307 keV energies. Absorption of these gammas within the crystal produces scintillation light leading to a signal which is present even in the absence of a source. This background activity has important consequences for PET but, for experimental testing, it allows for a quick and easy way to verify the optical coupling of the crystal to photodetector and to check the proper functioning of the photodetector and readout electronics.

Figure 7.9: Single LYSO crystal and MCP-PMT mounted in an aluminum box for testing. Each of the 16 anodes illuminated by the crystal have been routed to a coaxial cable.

Figure 7.10: The aluminum box assembly opened and showing the rear-panel connection of the HV and MCP-OUT signals and 16 coaxial cables.

For the first test we verified that we could correctly measure the LYSO background activity and obtain a good energy spectrum from the MCP-OUT signal, indicating a good optical coupling and light collection. In addition, we wished to verify that the summed response of all 16 anodes beneath the crystal matched that of the MCP-OUT. To accomplish this, all 16 anode signals were digitized using the same NIM and CAMAC electronics described for the anode calibration above. In this test, however, all 16 anodes were digitized simultaneously using two CAMAC ADC modules (each LeCroy 2249A has only 12 channels). Trigger and gate generation was also made using the MCP-OUT signal and the NIM discriminator.

Digitizing the anode signals in this way proved challenging from a timing perspective. Previously, the anode signal was delayed in order to bring it within the timing of the gate signal, generated by the slower rising MCP-OUT which must also be inverted in order to be compatible with the NIM level discriminator. Delaying all 16 anodes simultaneously, however, proved to be impractical and is one reason we chose rather long coaxial cables connected to each anode. Even with these 50 ns cables we observed that the anode signals arrive before the opening of the ADC gate, introducing some uncertainty in the digitization. Shown in figure 7.11 is the timing of the gate with respect to the MCP-OUT signal and one of the anodes as seen on the oscilloscope. The anode signal arrives 15 ns earlier despite the inclusion of the 50 ns coaxial cables.

Figure 7.12 shows the pulse-height spectrum of recorded events from the MCP output and from the sum of the 16 anodes after subtraction of the ADC pedestal and application of the anode calibration. The reference spectrum taken from the LYSO vendor's datasheet is shown on the right for comparison. The spectrum from the MCP output matches closely the expected one. Even the spectrum obtained by summing the values of the 16 anodes is in good agreement though with a slightly poorer resolution. This could be the result of the imperfect gating of the anode signals.

The count rate of the background activity was also measured and found to be about 6 kBq for the single crystal. Taking the volume and density of the crystal, this is in agreement with the stated value of 39 Bq/g taken from the manufacturer datasheet.

Interaction localization

In order to test the resolution of the transverse localization and the depth-of-interaction measurement of the modules to 511 keV photons, the setup shown schematically in figure 7.13 was adopted. The MCP-PMT was placed in a vertical position on a stage which could be adjusted precisely in the X and Z directions and set in coincidence with a BGO-PMT assembly. The BGO crystal is cylindrical and measures 2.54 cm in diameter and in depth. The PMT (Hamamatsu R9980) has a spectral response between 300-650 nm

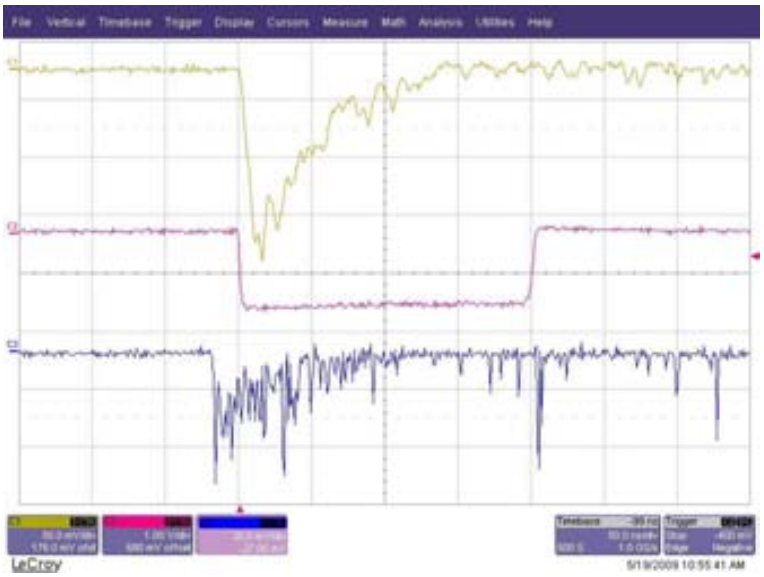

Figure 7.11: Timing of the MCP-OUT and anode digitization for the LYSO-MCP tests. From top to bottom: the MCP-OUT analogue signal, the gate passed to the ADC, and the analogue signal from one of the anodes. The anode signals arrive 15 ns before the gate despite the use of long 50 ns cables.

and a 34 mm diameter photocathode, well matched to the properties of the BGO crystal.

A ^{22}Na point-source was placed roughly 1 cm from the LYSO crystal and the BGO-PMT assembly placed about 50 cm from the source ensuring a narrow geometrical collimation of photons coincident between the two detectors on the LYSO crystal. A block of lead 5 cm thick with a hole of 5 mm diameter was also added between the BGO-PMT assembly and source to add an additional physical collimation and to reduce the background events in the BGO crystal. Since the source is contained in a disk of plastic and the positron's range is very short (<0.5 mm), the origin of the 511 keV photons can be considered point-like. In this configuration the size of the collimated spot on the LYSO crystal was estimated to be about 2 mm in diameter.

For the MCP-PMT, the same electronics chain was used as in the calibration tests described above. For the BGO-PMT assembly, the setup was similar, with the inclusion of a shaping preamplifier (Ortek 474 Timing Filter Amplifier) to integrate the charge arriving on the output of the PMT which was otherwise erratic due to the slow decay time of the BGO crystal. An integration time of 100 ns was used leading to a nicely shaped pulse and a good energy resolution. A NIM coincidence unit (LeCroy 465), receiving the discriminated MCP-OUT and BGO-PMT signals as input, was used to

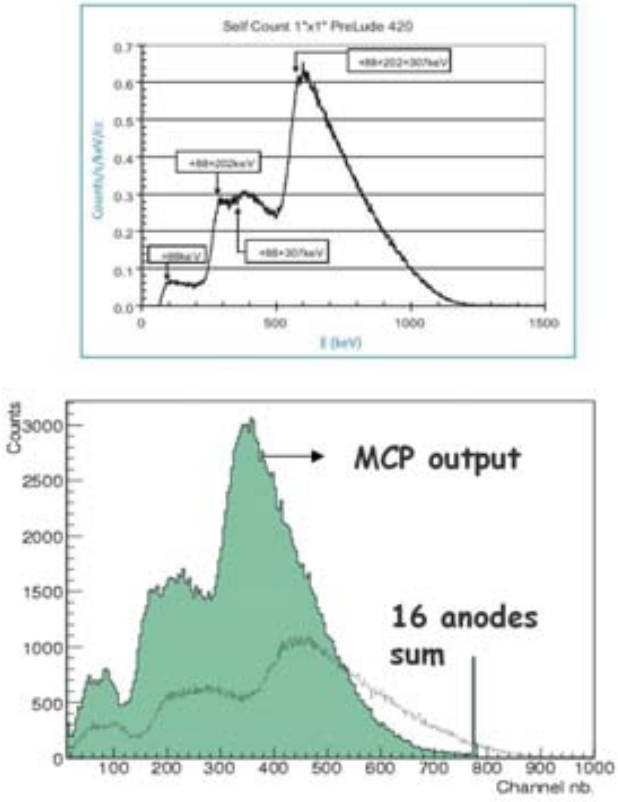

Figure 7.12: Measured spectra of the background activity of a single LYSO crystal (left) using both the MCP output and by summing the response from 16 anodes after calibration. The background energy spectrum of Prelude™ scintillator taken from St. Gobain datasheet is shown (right) for comparison.

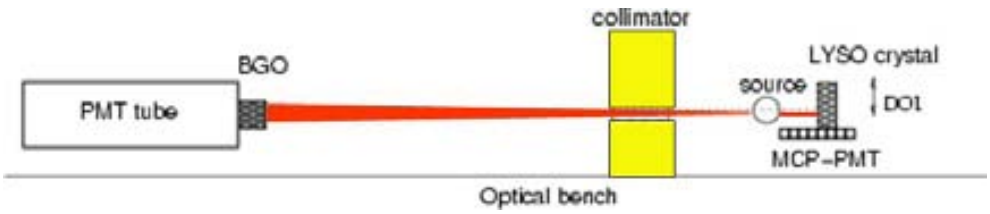

Figure 7.13: Schematic of experimental setup to measure the spatial resolution and depth-of-interaction resolution of gamma interactions in the crystal. A point-source of ^{22}Na has been used along with a 2.54 cm diameter BGO crystal coupled to PMT for selecting coincidences. The LYSO-MCP assembly can be moved precisely in both X and Z directions.

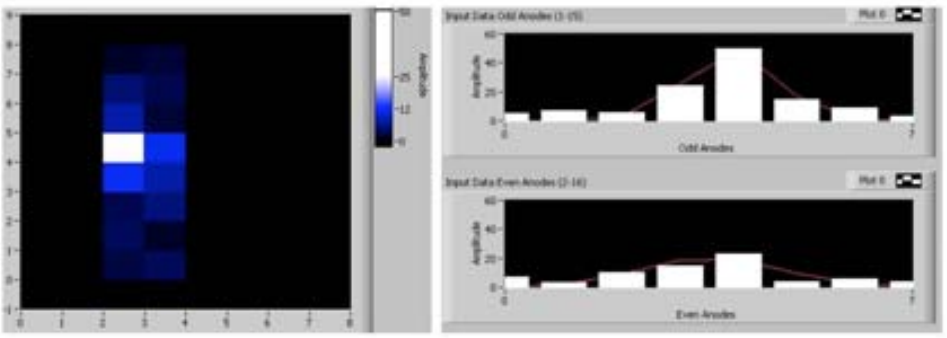

Figure 7.14: An example of a single event recorded by the LYSO-MCP assembly and analyzed with a simple LABVIEW program which fits the light response over each row of 8 anodes beneath the crystal.

produce the coincidence trigger between detectors. This trigger was then used to generate a gate of 200 ns for the anode signal digitization and a gate of 1000 ns for the BGO-PMT signal.

Four measurements were made along the transverse direction of the crystal, at X=15 mm, X=25 mm, X=35 mm and X=40 mm from the edge. The position in the Z direction was set to about 11 mm from the MCP-PMT window. Approximately 5000 coincidence events were acquired for each transverse position. For each event in each data set, the light response over both rows of 8 anodes beneath the crystal was fit with a Gaussian and the center and width of the fit recorded for all events. Figure 7.14 shows the LABVIEW analysis program which was created for this purpose. The light distribution over all 16 anodes beneath the crystal is shown for convenience in the intensity plot (shown left) as are the individual anode responses for each row of 8 anodes beneath the crystal (shown right). The Gaussian fit to the anode response in each row is also shown.

Taking the average of both center values from each row of 8 anodes and plotting the result for all events in each data set in a histogram, the measured transverse position was computed by a fit to the distribution. Figure 7.15 shows the result for all four measurements (left) as well as the distribution for the X=40 mm data set (right). The plot of the real transverse position as a function of the measured position is linear indicating that the transverse interaction position within the crystal can be accurately determined. The standard deviation of each distribution, which is roughly 1.2 mm sigma for each data set, defines the localization uncertainty for a single event that can be achieved using this method.

Following a similar procedure as the one described above, three measurements were made for different values of DOI: Z=27 mm, Z=18 mm and Z=2 mm, where Z=0 was defined at the upper surface of the LYSO crystal

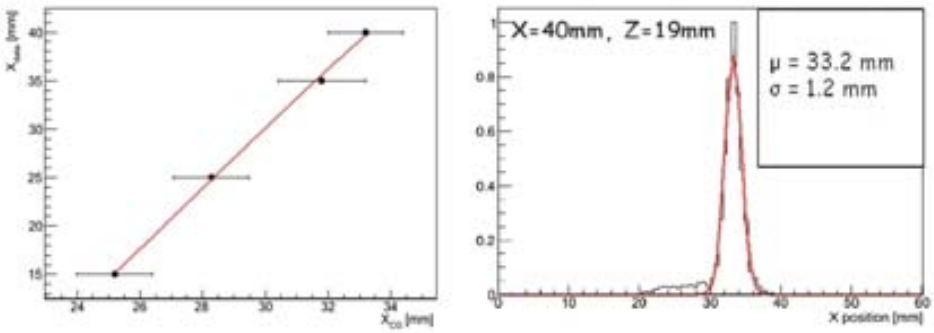

Figure 7.15: The measured and actual transverse interaction position of the LYSO-MCP assembly (left). The measured position, inferred by fitting the light response over the anodes beneath the crystal, is linear with the actual position as expected. The distribution of all events from one of the data sets (right) is also shown for illustration. The uncertainty of the localization using this technique, given by the width of the distributions, is about 1.2 mm sigma (courtesy of P. Solevi).

far from the MCP-PMT window. For each event in each data set, the width of the Gaussian fit to the anode response was used to infer the DOI. Figure 7.16 shows the results for the three different DOI locations. The actual DOI position, Z_{data}, has been plotted (on the left) as a function of the mean width of each data set, $\langle\sigma\rangle$. Also shown (on the right) is the distribution of the widths, σ, from each data set.

Some observations can be made regarding the results of these DOI measurements. First, the mean width of the anode response increases the further the interaction is from the surface of the MCP-PMT (Z decreasing by our convention). This is in line with expectations since the further the interaction is from the photodetector, the more the light will be spread over all anodes beneath the crystal. Although the relationship between the DOI and the mean width is not linear, it is sufficiently correlated to allow some amount of DOI localization. In the plot of the left of figure 7.16, error bars have been included derived from the standard deviations of the distributions of each data set. Also, the three data points have been fit with an exponential function which is a good approximation to the results obtained by simulation work previously carried out by the AQUA group [94]. The second observation that can be made is that at Z=27 mm and Z=18 mm, the distributions have well-resolved peaks (looking to the data at the right of figure 7.16). Because the two peaks can be distinguished from each other, we can say that it is possible to resolve the DOI at least at a resolution corresponding to the separation in Z between them, which in this case is 9 mm. However, for the measurement furthest from the MCP-PMT window,

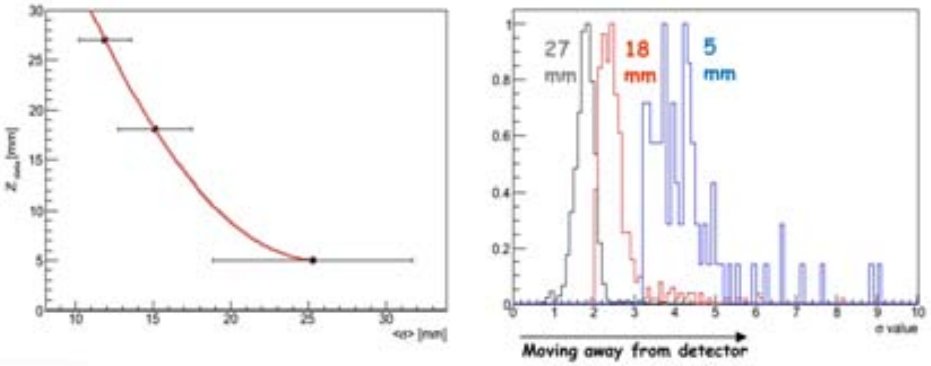

Figure 7.16: The actual DOI position as a function of the mean width of the response on the anodes beneath the crystal (left). Also shown (right) are the distributions of the widths for each of the three data sets. The DOI is well correlated to the DOI position for the two measurements at Z=27 mm and Z=18 mm, where the interaction is close to the MCP-PMT window. Far from the window, however, the data is less well behaved and the DOI localization deteriorated.

at Z=5 mm, the shape of the distribution is visibly degraded and without a well-defined peak. This makes it difficult to resolve the DOI with any accuracy when the interaction is far from the photodetector.

Although the results are not ideal, some information regarding the DOI can still be obtained using our semi-monolithic unit PET detector. Near the middle of the crystal and towards the MCP-PMT window, the DOI resolution is roughly 10 mm sigma and probably not better than 15 mm in the upper half far from the window. This DOI resolution is sufficient to reduce the effects of parallax as compared to crystal-based PET detectors that have no DOI resolution at all.

Coincidence tests

In order to measure the energy resolution of the AQUA LYSO-MCP modules to 511 keV photons, two identical modules were mounted facing each other in a coincidence configuration with the ^{22}Na point source placed directly between. An optical rail was used to ensure a precise alignment and each detector (as well as the source) was mounted on a stage whose height could be precisely adjusted. Figure 7.17 shows the two prototype crystal modules mounted on the coincidence test bench along with the ^{22}Na source.

The second MCP-PMT module was equipped with the same electronics chain as the first: the MCP-OUT signal was sent to a linear fan-out (LeCroy 428F) followed by a discriminator (LeCroy 821CL). Two additional ADC modules (LeCroy 2249A) were included for digitizing the 16 anodes of the

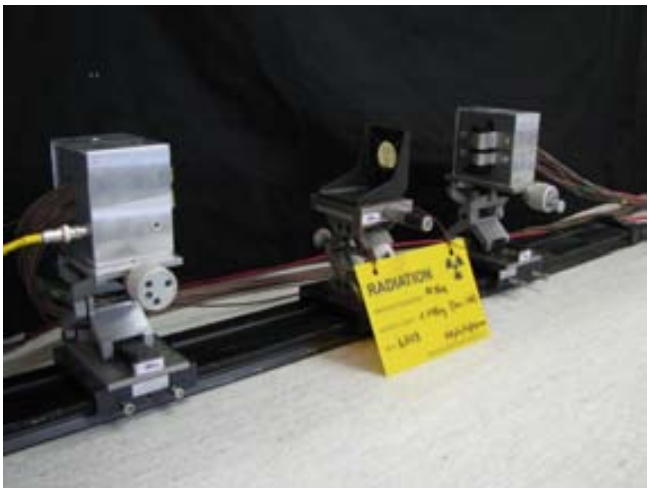

Figure 7.17: Two MCP-PMT modules mounted in a coincidence setup with a ^{22}Na point source. Only one LYSO crystal is coupled above 16 anodes on each of the modules.

second module. The same coincidence module used previously (LeCroy 465) was used directly to gate all four ADC modules reading all 16 anodes from each detector, 32 in total. The width of this gate was set to 200 ns for proper collection of the charge from all 32 anodes. The width of the discriminated MCP-OUT pulses, input to the coincidence unit, were shortened to about 20 ns for a total effective coincidence window of 40 ns.

About 10^3 coincidence events were acquired with this setup. The energy spectrum for each module, made in analysis by summing the signal of all 16 anodes beneath each crystal, is shown in figure 7.18. The energy resolution of the photo-peak in the two spectra was found to be 13% and 15% FWHM. It should be mentioned that the anode calibration was performed only on the first module and not on the second. Despite this fact, the energy resolution is only slightly worse on the module where the correction has not been applied. Although the anode correction may not have a dramatic effect on the energy resolution, it is likely to have a significant impact on the transverse and DOI localization resolution. For this reason, the anode calibration should be performed for future studies.

Coincidence timing studies

The timing resolution that can be achieved with the MCP-PMT modules has also been measured using the coincidence setup. Feeding the MCP-OUT signals from each module to an auto-walk constant-fraction discriminator (CAEN N415) the time difference between a sample of 10^3 events has been measured and the result is shown in figure 7.19. The distribution has been

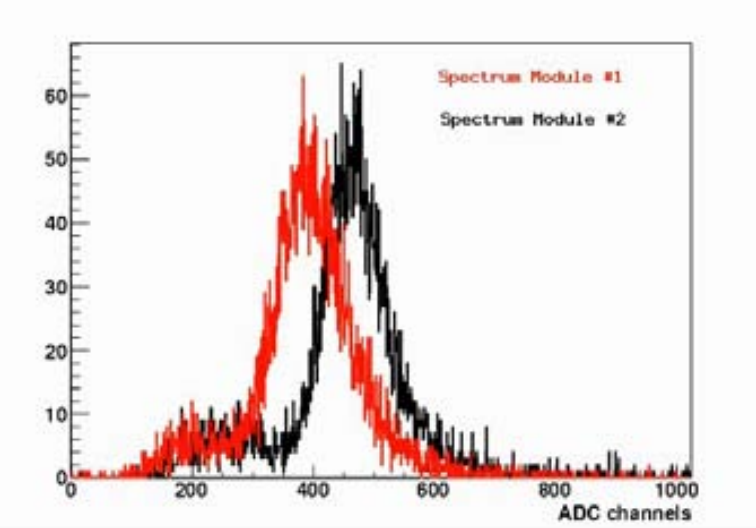

Figure 7.18: Spectra from both the MCP-OUT of both modules in coincidence with a ^{22}Na source. The peak corresponds to the 511 keV photoelectric events. The energy resolutions at the photo-peaks are 13% and 15% FWHM.

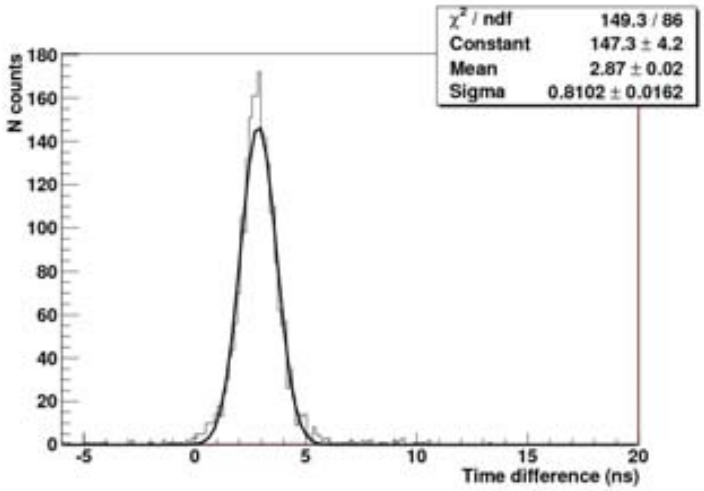

Figure 7.19: Timing resolution between two LYSO-MCP modules in coincidence with a ^{22}Na source and using constant-fraction discriminators. The coincidence timing resolution is 810 ps sigma.

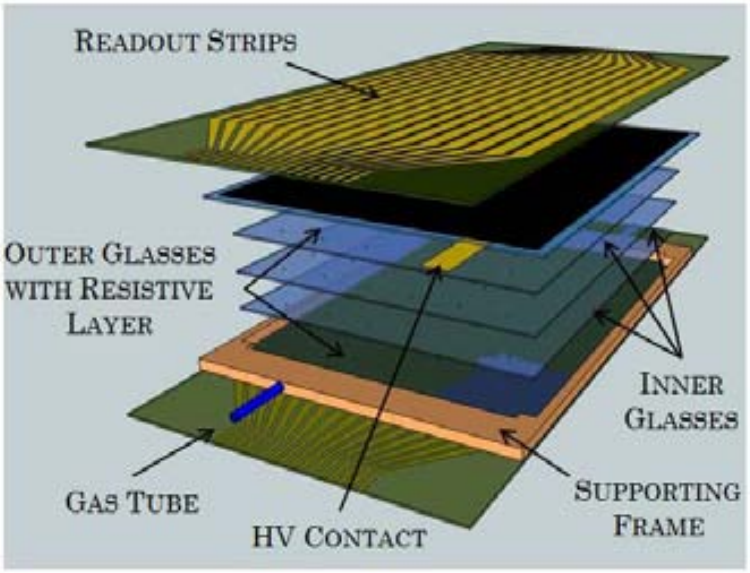

Figure 7.20: Exploded schematic drawing of the proposed 4-gap MRPC module for PET applications.

fit with a Gaussian and the standard deviation is 810 ps. No selection of events or calibration of the anodes has been performed.

7.2 MRPC-PET

In order to evaluate the merit of MRPC-PET we have studied various properties of custom-built MRPC modules. In this section, we describe in detail the materials and methods used to construct the MRPC prototypes as well as the results of extensive experimental tests that have been performed.

7.2.1 Generalities on MRPC designs

A schematic drawing of TERA's proposal for a compact and easy to assemble MRPC module designed for a PET application is shown in figure 7.20. The assembly consists of glass plates glued inside a low-density glass-epoxy frame. The frame itself is narrow (3 mm) along the axial edge in order to maximize the angular coverage and reduce unwanted scatter. The outermost glasses are coated with a resistive layer which allows application of the HV. A pair of strip-readout electrodes patterned onto flexible polyimide foils are placed above the resistive layers bringing the induced signal to the front-end electronics.

Figure 7.21: Insulating spacers produced from photo-sensitive polyimide patterned on glass. Spacers are 300 μm in height and 300 μm diameter.

Materials

All MRPC prototypes tested experimentally and reported in this thesis make use of regular soda-lime float glass as the material for the resistive plates. Soda-lime glass is composed typically of 15% sodium oxide, 70% silica (SiO_2) and 9% lime (CO) and is a common material in MRPC devices used in high-energy physics experiments. Although the use of lead glass in our MRPC modules would have been of interest in our studies due to its higher conversion efficiency to 511 keV gammas, it was excluded because of a difficulty of procurement of this material. Quotations from various suppliers have been obtained, yet so far, the prices for samples with the desired thickness and surface quality make this option unrealistic for a PET application which requires the use of many hundreds of MRPC modules. Float glass, on the other hand, is inexpensive and readily available for purchase in the thicknesses required for our MRPC design. Although 100-150 μm would be optimal, we have procured 400 μm thick glass because it is more easily available commercially and is relatively easy to handle in the laboratory.

Mechanical spacers

In many MRPC designs for high-energy physics, nylon fishing line is used as the mechanical spacer between electrodes [109]. We have chosen instead to use a production technique commonly found in the printed circuit board (PCB) industry which makes use of photo-sensitive polyimide film used for protecting and electrically insulating PCB and flex circuits. By photolithographic means, the polyimide film is laminated onto the glass and then selectively etched in any image desirable. For our purposes we have chosen a pattern of cylindrical spacers having 300 μm diameter and 300 μm height covering the glass surface at 1 cm separation.

A picture of the spacers, patterned on glass is shown in figure 7.21. The spacers greatly simplify the assembly process of our MRPC modules and

also allow us to reduce unwanted material outside the active area previously needed for fixing the fishing line. Because it is already an established industrial technology, producing the spacers on a volume of glasses is expected to be economically feasible.

Resistive Coating

In order to apply the high-voltage across the stack of glass plates, a resistive layer must be added to the outer surfaces of the module. The material chosen for our developments, and subsequently used in most of the following tests, is a colloidal graphite emulsion which is first applied to the glass surface and then allowed to dry forming a thin resistive layer. We have obtained layers having 150 k$\Omega/\Box$, 800 k$\Omega/\Box$, and 1 M$\Omega/\Box$ patterned over the entire surface of our glasses. The 1 M$\Omega/\Box$ has been made by making the layer as thin as possible, without compromising on uniformity. Values of resistivity above 1 M$\Omega/\Box$ have been deemed unacceptable for our purposes because of large visible variations in quality of the layer over the surface of the glass.

Gas circulation

In our experimental studies of MRPCs, pure tetrafluoroethane (TFE) gas, $C_2F_4H_2$ (R134a Freon), has been circulated through the detectors at a rate of a few L/hr.

The operation of MRPCs in pure TFE results in the onset of streamer formation at lower voltages as compared with gas mixtures using a small percentage of C_2H_4 and/or SF_6. This makes it more difficult to operate in the region of limited proportionality where a higher rate can be achieved. Because the detection efficiency of MRPCs to 511 keV gammas is low, however, a low rate (10-100 kHz/cm^2) is not foreseen to be a challenge for our MRPC-PET application. In fact, the use of pure TFE has been shown to give equivalent timing resolutions as compared with gas mixtures for charged particle tracking: using an MRPC with 10 gaps of 250 μm, a timing resolution of 50 ps at full efficiency has been demonstrated [110].

HV stability

Each time a new MRPC configuration was tested, the stability of the high voltage was monitored for the first several minutes. A dual-channel HV supply (CAEN N471A) was used which allows a maximum voltage of 6000 V and precision monitoring of the current down to 1 nA. Using both channels of the single supply, we applied +6000 V and -6000 V to each side of the resistive layer for a total of 12 kV. Because this was the maximum available voltage on the HV module, we limited our studies to 4-gap MRPCs (with 400 μm glass and 300 μm gaps). During correct operation, our chambers operate with less than 5 nA leakage current at the maximum voltage.

7.2.2 Initial studies with prototyping gas chambers

During the early stage of development of MRPC research carried out by the AQUA group, a number of aspects of the design required investigation. Instead of testing compact and sealed MRPC modules immediately (such as those proposed for a real PET application and described above), we have started by mounting MRPC prototypes inside larger gas chambers which can be easily disassembled. This affords us the flexibility to easily alter the configuration and has allowed us to study various aspects of the MRPCs without the need of a large amount of assembly work. Some of the properties that have been tested in this way include the effect of the resistive layer on the charge distribution, as well as the detection efficiency and TOF resolution to 511 keV gammas. Depending on the study, we have made use of different strip-readout configurations as well as different front-end electronics and DAQ. Each of these are described in detail in the following discussion along with the results of these preliminary investigations.

Charge distribution with different resistive layers

The value of resistivity of the resistive layer requires consideration in the design of MRPC detectors. In MRPC designs for charged particle tracking applications, the resistivity is usually on the order of 100 k$\Omega/\square$. In detecting gammas, however, we expect to have less overall charge induced on the electrodes of our MRPC chambers since only 1 gap fires rather than many. It follows that a too low resistivity could limit the detection efficiency (and timing resolution) since the charge induced on a single channel is decreased the more the charge is spread. At any rate, the width of the charge distribution is important in determining the optimal readout strip pitch, which in our design for compact modules, has been chosen as 4 mm.

In order to investigate the effect of the resistivity on the charge distribution, we have used a gas chamber containing an XY readout plane having strips at 400 μm pitch, fine enough to allow the shape of the induced signals to be recorded precisely. The gas chamber is essentially identical to that used to house the triple-GEM detectors of the PRR10 described in chapter 5 (see figure 5.14). Glasses of 7x10 cm^2 in size, patterned with insulating pillars, were placed above the active area of the XY readout plane building up RPC and MRPC stacks as desired. Both single-gap and multi-gap RPC stacks have been tested along with two types of the colloidal graphite resistive layer having 150 k$\Omega/\square$ and 1 M$\Omega/\square$. For reference, a single-gap RPC without resistive layer (where the upper layer was biased using a plane of copper tape and the lower layer left floating) was also tested. Insulation from the readout strips was made by including a 50 μm thin-film of Mylar placed between the lower resistive layer of the RPC stack and the XY readout plane.

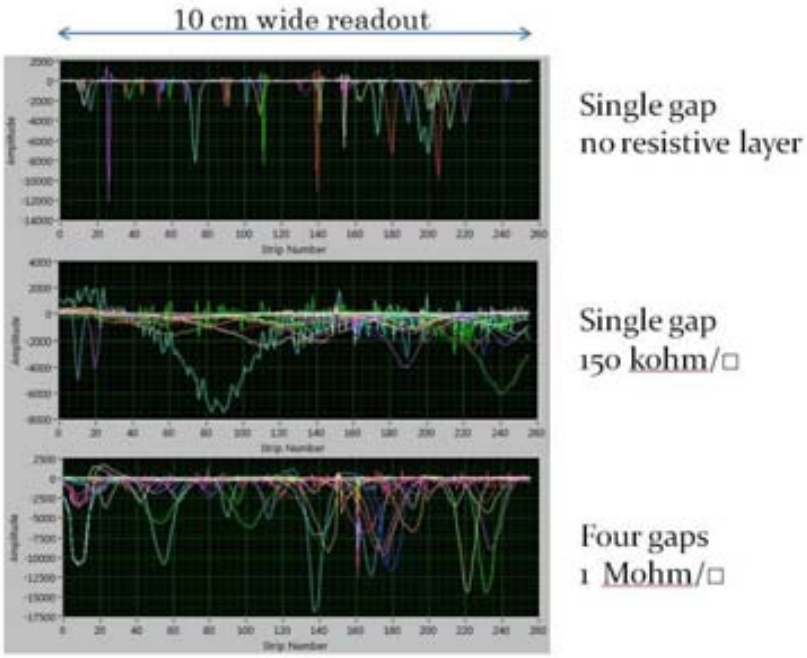

Figure 7.22: Signals recorded for three different MRPC configurations recorded using a 400 μm pitch readout

Once the desired stack had been assembled, the chamber was sealed and the gas allowed to flow for several hours before applying the HV. The readout strips of a single axis were read out with the DP-GP5 front-end electronics (see chapter 5). Data acquisition was performed in self-triggering mode with the GP5 thresholds trimmed above the electronic noise. With the HV applied (typically around 2.8 kV per gap), we recorded events in the detector with the ^{22}Na source placed on the window of the gas chamber.

Figure 7.22 shows a collection of events for three different RPC configurations: *without* resistive coating, and for two values of resistivity, 150 k$\Omega/\Box$ and 1 $M\Omega/\Box$. A drastic spreading of the signal with the lower resistivity coating of 150 k$\Omega/\Box$ can be easily observed (shown in the center of figure 7.22): the pulses typically have a width of $\sim$10 mm FWHM. The events recorded using the 1 M$\Omega/\Box$ surface resistivity and a 4-gap MRPC stack, shown in the lower image, are more in line with our requirements: the pulses are typically about 4 mm FWHM wide.

The observations made during this study demonstrate the effect of the layer's resistivity on the shape of the signals induced on the electrodes. For instance, the 150 k$\Omega/\Box$ resistive layers are less suited to a PET application since they lead to a very wide charge distribution over the electrodes. Instead, the 1.5 M$\Omega/\Box$ layer gives a charge distribution whose width is closely matched to our choice of strip pitch, 4 mm, thereby increasing the available

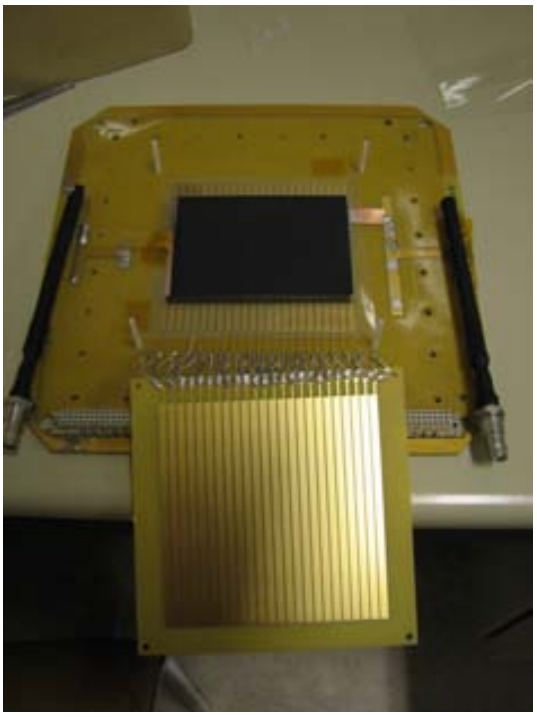

Figure 7.23: One of the gas chambers used for initial prototyping studies of MRPCs. The chamber is opened showing the MRPC stack which has been assembled above the strip readout plane. The upper plane, which fixes the stack in place mechanically, is shown before the final assembly. The readout strips 3.5 mm wide and at 4 mm pitch, are visible on both the lower and upper planes.

signal in the channels of the readout electronics.

Efficiency studies

To carry out realistic efficiency studies we produced new gas chambers which are mechanically similar to the XY readout chambers used previously except with a readout pattern that has been adapted to match more closely our proposal for compact MRPC modules: the XY strip pattern is uni-directional and the readout is differential, made possible by an upper PCB which is also patterned with a strip plane identical to the lower one. The pitch is 4 mm and the strips are 3.5 mm wide. Each pair of strips (24 in total), is routed to a connector which is matched to a front-end readout solution for MRPCs built for the ALICE experiment (described below). The glasses used are 7x10 cm^2. A picture of one of the opened gas chambers with MRPC stack used in the following studies is shown in figure 7.23.

Data acquisition has been achieved using a front-end readout electronics

Figure 7.24: The 24-channel NINO card designed for the ALICE experiment and used in our tests.

board produced for the ALICE collaboration and based on the NINO multichannel amplifier-discriminator ASIC [111]. Shown in figure 7.24 is the 24-channel ALICE TOF NINO front-end card (holding 3 NINOs). The card also delivers a fast-OR output of all 24 channels which we have used for this efficiency study.

The experimental setup for the efficiency studies, shown in figure 7.25, involves placing the MRPC under test (housed inside the gas chamber) in coincidence with a BGO scintillator coupled to a PMT (R980), the same assembly used to measure the depth-of-interaction localization of the crystal-based modules (described in the previous section of this chapter). The ^{22}Na point-source was positioned precisely between the detectors and the entire setup mounted on an optical rail to ensure a correct geometrical alignment. Since the BGO crystal measures 2.54 cm in diameter, placing the source half way between the MRPC and crystal ensures that no losses to the efficiency occur from the geometry. This is because in this configuration, every 511 keV photon seen by the BGO crystal must have a corresponding collinear 511 keV photon passing through the active area of the RPC (which is 7x10 cm^2).

^{22}Na is a $\beta+$ emitter which decays with a half-life of 2.6 years. The positron, when emitted, quickly annihilates producing two collinear 511 keV photons. The ^{22}Ne nucleus, left over from the $\beta+$ decay of ^{22}Na, is often left in an excited state which will quickly de-excite with the emission of a 1.27 MeV gamma. Because of the short-time scales involved, the gamma is emitted simultaneously along with the pair of 511 keV photons.

Because the emission of the 1.27 MeV gamma is isotropic and not collinear

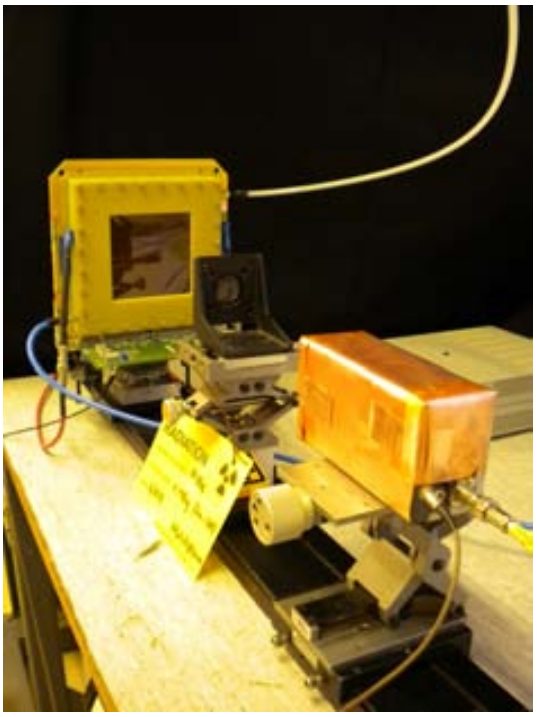

Figure 7.25: Experimental setup for measuring the MRPC efficiency to 511 keV photons. A ^{22}Na source is placed precisely between the MRPC under test and a BGO-PMT assembly.

with the 511 keV photons, it must be accounted for when measuring the efficiency of the MRPC chamber. This can be achieved by making a selection on only photoelectric events recorded in the BGO-PMT assembly. In this way, the efficiency can be defined as the number of events counted in both the MRPC and the BGO-PMT (coincidences) divided by the total number of events counted in the BGO, or

$$\epsilon = \frac{N_{coincidence}}{N_{BGO}}$$

The procedure followed was to trigger the data acquisition with each event in the BGO crystal, simultaneously digitizing the pulse from the BGO-PMT and recording whether a coincidence occurred in the MRPC by looking to the fast-OR output of the NINO board. The time window used for selecting coincidences was chosen at 50 ns to accommodate the fairly slow rising signal of the BGO-PMT assembly (caused by the long decay time of BGO scintillator). A gate of 350 ns was used to fully digitize the pulses in the BGO-PMT. Energy selection of the data in the BGO-PMT was made in analysis, after the acquisition of a large number of events (10^6). Because the efficiency of a single MRPC module is very low (<1%), this required running our measurements for long periods of time and in some cases, through an entire night.

The energy spectrum recorded by the BGO-PMT assembly of one of our measurements is shown in figure 7.26. A sharp peak corresponding to photoelectric absorption 511 keV photons is clearly visible at the center of the spectrum. Also visible is the photo-peak of the 1.27 MeV gammas. The broad peak below the 511 keV photo-peak is due to Compton interactions in the crystal or in the bulk material of the experimental setup, which are scattered before detection. The energy selection window which has been applied in the analysis is highlighted in blue. The 1.27 MeV as well as the Compton scattered events are thus excluded from the data before calculating the detection efficiency.

Using this technique the detection efficiency of the MRPCs to 511 keV gammas has been measured as a function of the applied HV. Figure 7.27 summarizes the results for both single and 4-gap RPCs having both two different types of resistive layer, 150 kΩ/□ and 1 MΩ/□. In order to aid the comparison between single-gap and 4-gap RPCs, the voltage per gap is plotted rather than the total.

For the single-gap structures, the efficiency reaches a plateau at a value of about 0.18±0.01% while for 4-gap modules, the plateau is found to occur at roughly 0.66% (with a statistical error of ± 0.01%), only slightly less than four times the single-gap efficiency. In both cases, the 1 MΩ/□ modules arrive at the plateau at lower voltages. This is most likely due to the fact that the signal in the readout electronic board must exceed a certain threshold on a single channel in order to be registered. As we have seen with the spatial

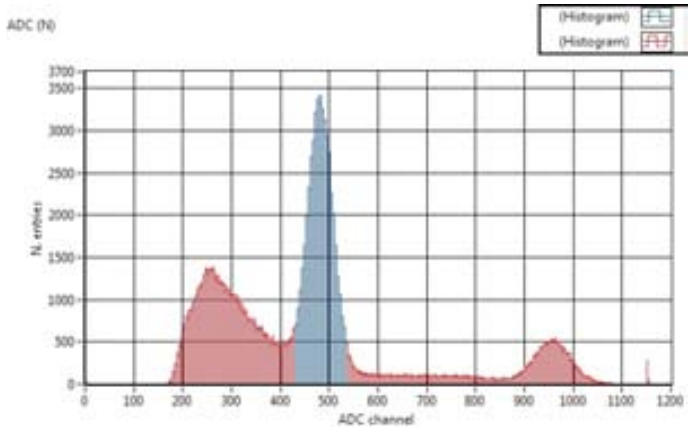

Figure 7.26: The energy spectrum of events recorded by the BGO-PMT assembly. Shown in blue are the fraction of events used in the efficiency measurement which belong to the 511 keV photo-peak.

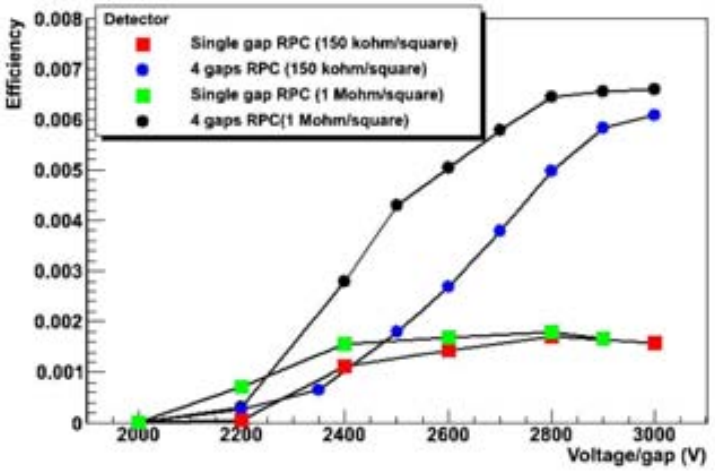

Figure 7.27: The measured efficiency of different RPC and MRPC constructions as a function of the voltage applied per gap. The 4-gap MRPC design reaches a efficiency plateau of $(0.66 \pm 0.01)\%$.

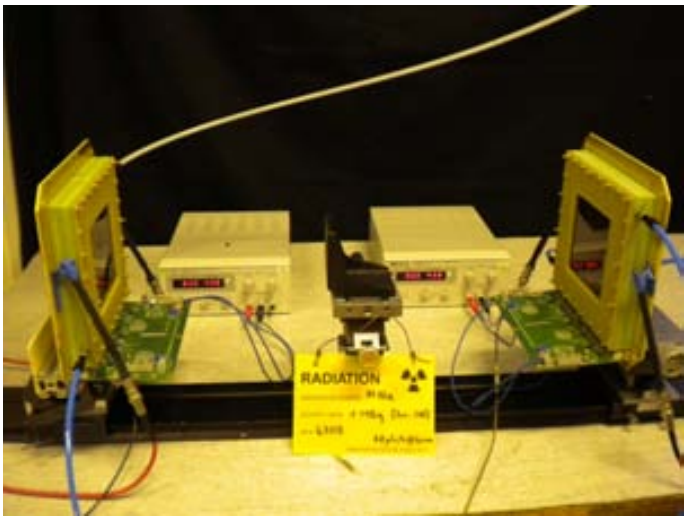

Figure 7.28: The experimental setup for detecting coincident 511 keV photons in two RPC detectors. The ^{22}Na point-source is placed precisely between the two modules.

resolution tests, the 150 k$\Omega/\square$ resistivity causes a large spreading of the charge over many channels. This results in a decrease in detection efficiency simply due to the signal-to-noise limitations of the electronics chain: more charge spreading results in less charge per channel, thus a lower likelihood of being over the noise threshold in that channel.

Timing studies

For timing studies two identical MRPC modules enclosed in identical gas chambers with 4 mm differential readout were placed in coincidence about the ^{22}Na source. The setup in the laboratory is shown in figure 7.28. Two of the ALICE NINO front-end boards were used, one for each detector.

The fast-OR output from each of the NINO boards, after translation to NIM level, were fed to a CAMAC TDC (LeCroy 2228A) having 100 ps time resolution. In our configuration, one MRPC detector gives the START signal and the other, delayed by a 50 ns cable, the STOP signal. Because triggering is made using a single MRPC detector and no coincidence selection is applied during data taking, we also acquired a very large number of events (10^6) in order to have a significant sample of coincidences ($\sim$1%) in the data set.

The results of measurements with a single-gap and 4-gap RPC module (both having 1 M$\Omega/\square$ resistive layers) are shown in figures 7.29 and 7.30, respectively. The standard deviation of the distribution of the time-difference for the single-gap RPC is 443 ps and 525 ps for the 4-gap RPC module. This translates into a single detector time resolution of 310 ps and 370 ps

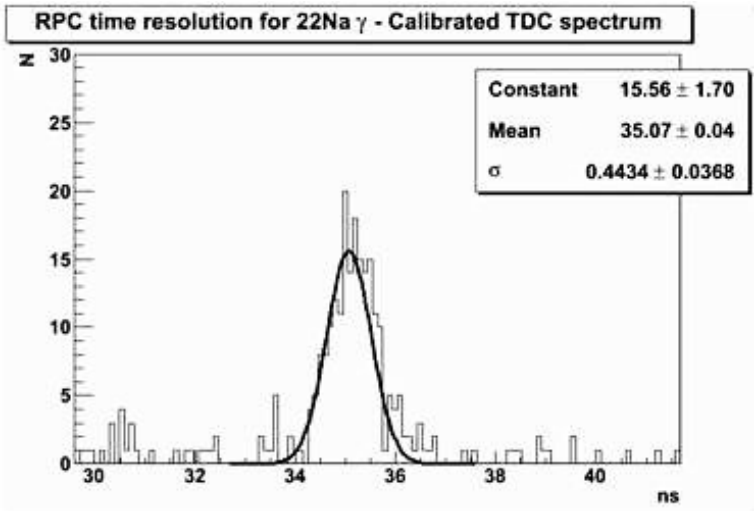

Figure 7.29: The distribution of the time delay between events recorded by two single-gap RPC chambers having 1MΩ/□ resistivity. The peak corresponds to the coincident detection of 511 keV photons and the timing resolution is 443 ps sigma.

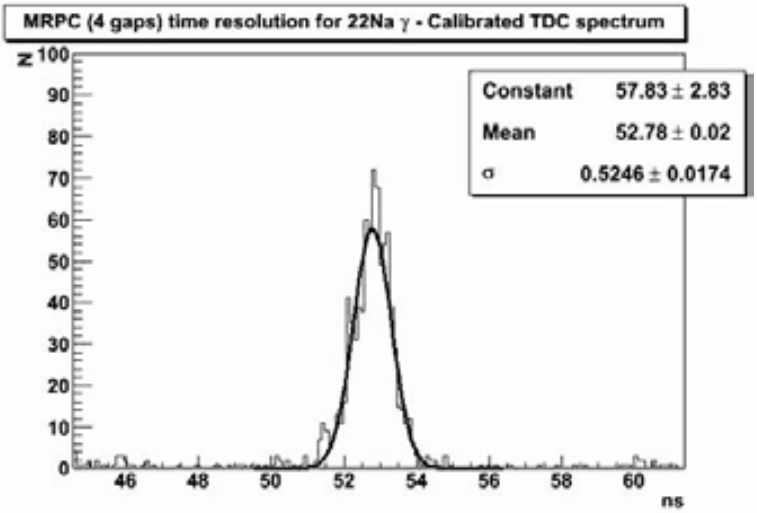

Figure 7.30: The distribution of the time delay between events recorded by two four-gap RPC chambers having 1 MΩ/□ resistivity. The peak corresponds to the coincident detection of 511 keV photons and the timing resolution is 525 ps sigma.

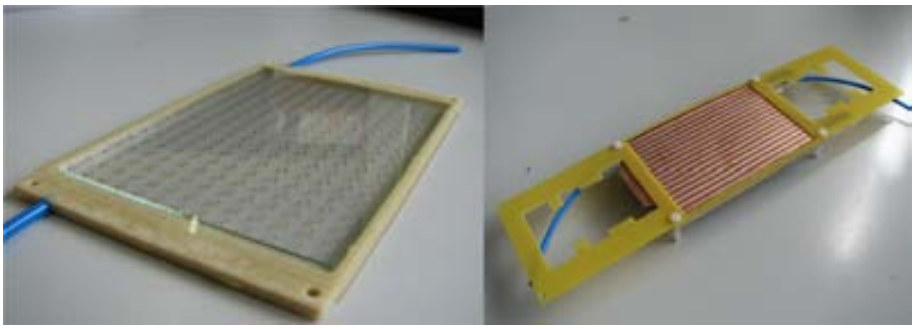

Figure 7.31: A 4-gap MRPC module with low material budget developed by TERA. Its active area is 7x10 cm^2. Shown left is the module after sealing the gas volume but before the resistive layer has been applied. On the right is the module completed and awaiting front-end readout electronics.

for the single-gap and 4-gap modules, respectively.

7.2.3 Measurements with compact MRPC modules

Having carried out the preliminary studies of MRPC prototypes, a compact and glued MRPC module having 7x10 cm^2 active area have also been constructed and tested experimentally. Figure 7.31 shows the 4 gas-gap module in two intermediate stages of assembly. Shown left is the module after the glasses have been glued inside the frame and before the resistive coating is applied. Shown right is the complete assembly with the resistive coating (not visible), readout strips and front-end electronics support. The modules use the same 400 μm soda-lime glass and 300 μm height polyimide spacers and make the assembly work easy as required for a PET application. Also, the modules are only 3.2 mm thick, making it feasible to stack many of them vertically with a minimum of space in between, a necessary constraint for achieving a high detection efficiency in a scanner configuration.

In order to determine the interaction localization along the axial extent of the active area, each module must be equipped with a minimum of two front-end boards. Because the ALICE NINO board used in the initial tests was not suited for this purpose, a new front-end readout board, also based on the NINO ASIC, was produced for our tests with the sealed MRPC modules.

The new NINO board makes use of nearly the same schematic as the ALICE NINO front-end board, except only one NINO ASIC per board is included for a total of 8 channels. Although this is insufficient to read out the entire 7x10 cm^2 module (16 strips at 4 mm pitch cover the 7 cm width), it was considered a good starting point for the tests described here. A 16-channel NINO card, which will be used to read out the entire active area of our 7x10 cm^2 is currently being developed.

Another difference between our NINO board and the ALICE board is

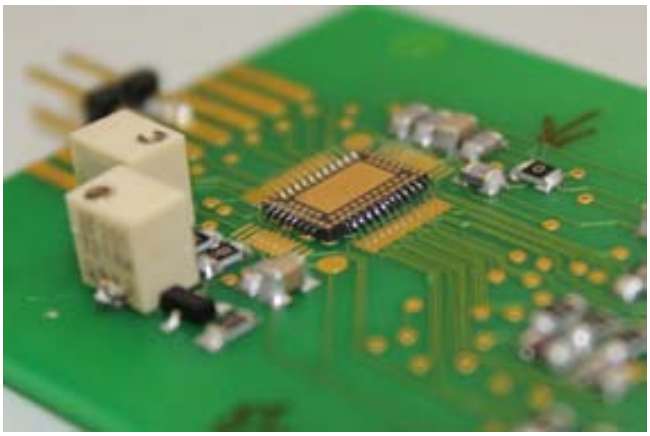

Figure 7.32: The custom-built NINO board used in the tests of compact MRPC modules.

that the NINO chip has been flipped and wire-bonded to the PCB, rather than soldering the packaged ASIC which requires high-resolution PCB technologies and assembly techniques. This avoids potential production complications and has limited expenses allowing us to proceed more rapidly in our developments. Figure 7.32 shows a close-up of the NINO ASIC wire-bonded to our custom-built PCB.

Trim-potentiometers have been used for setting the threshold and other values required by the NINO. In the future, these trim-pots will be replaced with surface mount (SMD) resistors such that the total profile of the board is less than 2 mm in height, allowing a tight stacking of MRPC modules.

A picture of one of the 7x10 cm^2 compact MRPC modules is shown in figure 7.33 after full assembly. Two of the custom-built NINO boards have been connected on either side of 8 readout strips which cover half of the active area.

In order to perform timing measurements with a higher precision than the CAMAC TDC system described previously, an Agilent Technologies oscilloscope (DSO9254A) has been used. The scope allows to digitally sample waveforms and perform a wide variety of measurements which can be recorded on a PC using LABVIEW software. We have measured an intrinsic resolution of $\sim$10 ps sigma by charge injection using this system, a significant improvement over the 100 *ps* resolution CAMAC system used in the prototyping studies.

Another new development has been to record the exact channel (or channels) which are triggered along with the fast-OR on each NINO board. This has been accomplished using the central-DAQ board (the same as used in the PRR10) connected by a cable to all 8 outputs of both NINO boards at either end of the MRPC module. A unique firmware program has been written for this purpose which records the channel (or channels) hit in each

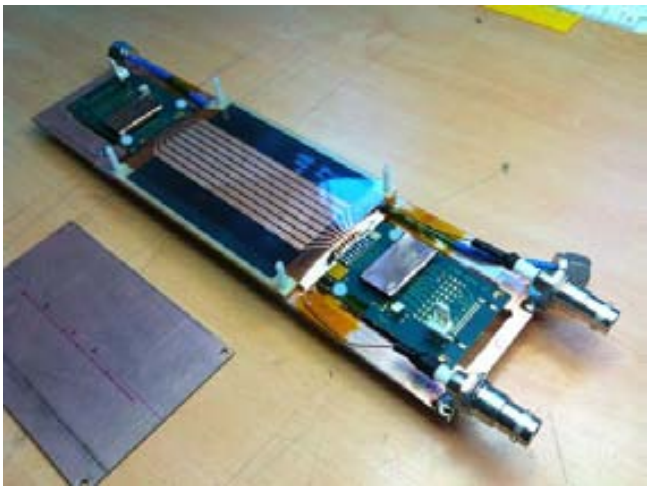

Figure 7.33: One of the 7x10 cm^2 compact MRPC modules equipped with two NINO front-end cards and HV polarization resistors.

NINO, as well as whether the events are in coincidence with the LYSO-SiPM assembly. The LABVIEW software used to interface with the Agilent scope has been modified to include this information along with the time difference between the fast-ORs.

The development of our custom-built NINO board as well as its integration with an FPGA-based DAQ solution has allowed us not only to make more accurate timing measurements (presented in the following discussion), but also constitutes a major step forward on the path towards developing a larger-sized MRPC-PET demonstrator.

Axial interaction localization

In the compact MRPC module designed for PET application, localization of the interaction along the axial length of the module is achieved by measuring the time-difference of arrival of the pulse at both ends of the readout strip. This technique has already been proven for MRPCs detecting charged particles: a resolution of a few mm has been achieved while maintaining a TOF resolution of the system of 50 ps [112].

In order to measure the axial resolution of our own MRPC prototypes, we measured the difference in arrival times between pulses on the same strip, seen by each of the NINO boards on either end of the module. One of the fully assembled 7x10 cm^2 modules was placed in coincidence with a small 3x3x20 mm^3 LYSO crystal coupled to a 3x3 mm^2 SiPM (Hamamatsu S10362-33-100C). The ^{22}Na source was placed close to the LYSO-SiPM assembly and a 5 cm thick lead block with 2 mm diameter hole placed between the LYSO-SiPM and the MRPC module. In this way the MRPC was irra-

Figure 7.34: Experimental setup for measuring the axial position resolution of the compact MRPC modules. A 3x3 cm^2 SiPM and 3x3x20 cm^3 LYSO crystal assembly is used to select coincidences. A 5 cm lead block with collimator ensure that only a narrow beam of 511 keV gammas from the ^{22}Na source are incident on the MRPC detector.

diated with a narrowly collimated beam of 511 keV photons which could be made incident at any position along the active area of the MRPC module. Figure 7.34 shows this experimental setup.

The fast-OR signal from each NINO was sent to the Agilent scope and the time-difference measured on the PC along with the channel address on each NINO board. One result that became apparent is that a significant time variation exists between the pairs of corresponding channels on each NINO board (possibly due to different routing within the chip itself). This has required us to calibrate the time difference for each strip (pair of NINO inputs) and has been carried out by scanning across all 8 strips of the module at a fixed axial position on the MRPC module and recording the relative time difference between pulses arriving on either ends of each strip. A maximum deviation of up to 200 ps difference between strips has been observed.

In order to test whether this time variation between channels can be corrected for, the Pb block with 2 mm diameter hole was replaced by two lead blocks separated by 1 mm, forming a vertical slit collimator. In this way, all 8 strips of the MRPC module were illuminated simultaneously by the ^{22}Na source and a correction for each pair applied in the data analysis. Figure 7.35 shows the result after the calibration has been applied for three different axial positions, -40 mm, -10 mm and +40 mm (the origin is defined as the center of the module). A double-Gaussian fit has been applied to each peak and the standard deviation of the central peak is 38 ps sigma.

Taking the center of each peak as well as the known locations of the axial

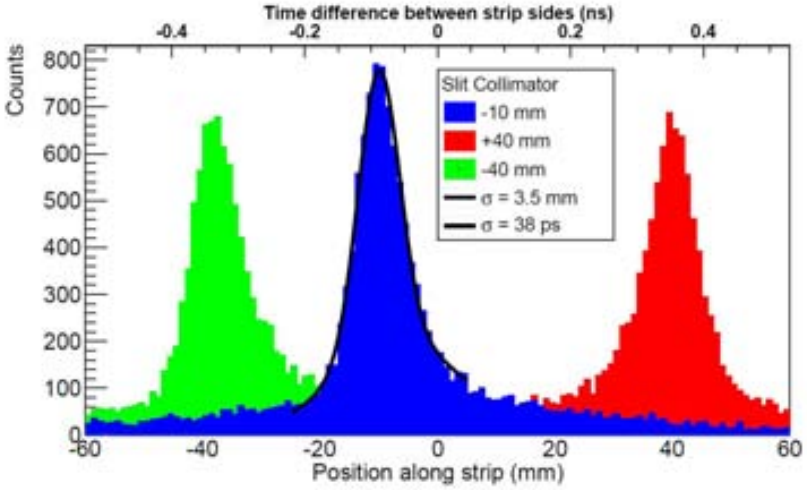

Figure 7.35: The time difference recorded between pulses on either end of the 7x10 cm^2 MRPC module. The timing resolution, obtained by a fit to the peak of each distribution, is 38 ps sigma. The known positions of all three peaks has been used to calculate the propagation velocity of the signal, equal to about 2/3 the speed of light. This allows to correlate the position of the interaction along the strip and the axial resolution which is 3.5 mm sigma.

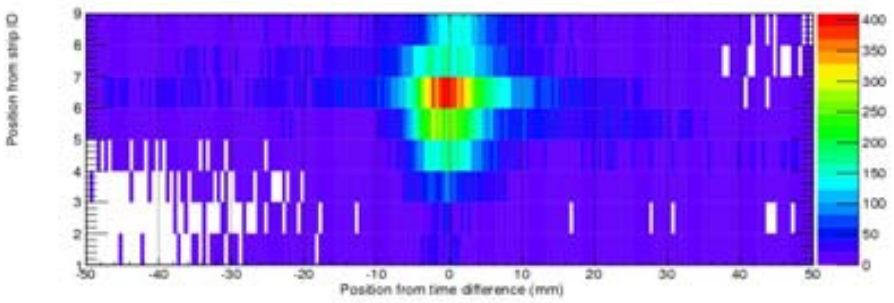

Figure 7.36: The 2D reconstruction of the 2 mm diameter beam of collimated 511 keV photons incident on the 7x10 cm^2 MRPC compact module. A timing calibration has been applied to each strip which is read by a pair of NINO channels at either end of the module.

position in each data set, the propagation velocity has been computed as 22.5 cm/ns, or about 2/3 the speed of light. This information has been used to translate the data into axial position and the same data, plotted with the horizontal axis in units of mm along the axial direction, is shown in figure 7.35. The peaks match well their expected positions and the uncertainty in axial localization is 3.5 mm sigma, sufficiently accurate for an MRPC-PET application.

Returning to the Pb block collimator with the 2 mm diameter hole in the experimental setup, an image of the 511 keV gamma beam, as seen by the 7x10 cm^2 compact MRPC module, has been acquired by recording data in coincidence with the LYSO-SiPM. Figure 7.36 shows a 2D intensity plot of the data after the timing calibration has been applied to all channel pairs, 8 strips in total. The image demonstrates that a correct identification of the hit channel (transverse direction) as well as the axial localization can be used to reconstruct events in our MRPC modules. Though this is a preliminary result, in which the readout strips cover only half the active area of the module, it is fundamental in proving that a good transverse and axial resolution for PET imagery can be achieved with MRPC technology.

Time-of-flight resolution

At the time of writing, in May 2013, a second compact 7x10 cm^2 MRPC module is being assembled and tested for gas tightness and HV stability in the laboratory. Using both modules the coincidence timing resolution will be measured using the new NINO boards and the Agilent scope DAQ system. Because of the excellent timing resolution measured between signals arriving on opposite ends of the compact module (38 ps) we expect to be able to measure a much lower coincidence TOF resolution as compared with

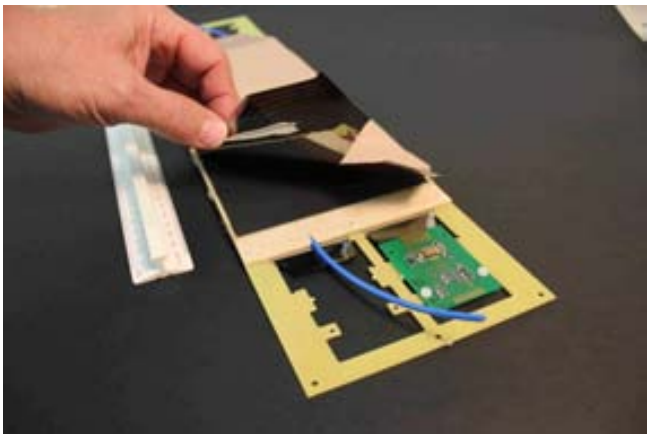

Figure 7.37: A full-size (30x12 cm^2 active area) compact MRPC prototype constructed for future testing.

that which was measured with the MRPCs housed inside the prototyping gas chambers. The main reason for our confidence in this prediction is that previously, no calibration was made to compensate for the time offset between channels of the NINO ASICs. Since we have recently observed a maximum deviation of 200 ps between strips on the compact modules, it is very likely that our previous result of 443 ps and 525 ps sigma coincidence, for the single-gap and 4-gap detectors respectively, was largely dominated by this dispersion and not the intrinsic timing capabilities of the MRPC technology itself. A further reason is that the physics principles which govern the timing characteristics of MRPCs when detecting charged particles are essentially identical to those when detecting 511 keV gammas, except that a single gap fires instead of many. This difference affects the signal-to-noise and could be improved with the use of more sensitive electronics but the dynamics of the avalanche formation is similar. It is expected that this will soon be verified experimentally in our laboratory measurements with a TOF resolution of ∼150 ps made with our compact 7x10 cm^2 MRPC modules.

7.2.4 Full-sized compact prototype

In the simulation studies that are presented in the final chapter of this thesis, the target size for the MRPC modules has dimensions 30x12 cm^2 and consists of five layers separated by four 300 μm gas-gaps. We have acquired float-glass having this size (and 400 μm thick) and production of glued MRPC modules of this dimension is underway. Pattering of the insulating spacers has already been proven on the larger glasses and one full-size (30x12 cm active area) MRPC module has also been recently built, shown in figure 7.37.

Though we intend to verify that these larger prototypes can achieve

the same efficiency and timing characteristics of the smaller modules, they have so far only been studied with the desire to validate the production procedure and mechanical construction. This is important in considering a possible MRPC-PET demonstrator which would require a large number of the larger MRPC modules to be assembled. In addition, a new NINO board having 16 channels, which would allow to record events across the entire active area of the 7x10 cm^2 modules and the larger 30x12 cm^2 modules, is currently under development by the AQUA group.

Chapter 8

Simulation studies

In order to asses their merit for a realistic in-beam PET application, we have carried out a series of Monte-Carlo simulation studies based on the proposed PET technologies tested experimentally in the framework of the AQUA group and presented in the previous chapter of this thesis. The goal was both to validate the experimental results obtained with the prototypes using basic simulations and to use those results as a basis for larger studies of full-ring and partial-ring scanners based on these novel technologies.

The main geometrical and material characteristics of the MRPC and LYSO-MCP prototypes have been modeled into our simulations. In the LYSO-MCP studies, the unit geometry is identical to the experimental prototype 5 LYSO crystals cover the entire MCP-PMT active area symmetrically. In the case of MRPC-PET, we have chosen the unit MRPC modules to have the same dimensions as the larger prototypes that were mechanically assembled in the lab, 12x30 cm^2 active area.

Although we have made some studies of crystal-based PET systems, most of our work focuses on MRPCs since their application to PET is most uncertain, due to the inherent low efficiency of MRPCs to 511 keV gammas. For this same reason, the simulation studies presented in this chapter have been restricted to evaluating the sensitivity of MRPC-PET technology. The more challenging task of including the TOF resolution into image reconstruction and evaluating improvements in image quality is currently under study by the TERA Foundation and other collaborators in the framework of the ENVISION project. For the scope of the work presented here, this more challenging task has been considered secondary to a sensitivity optimization.

There are several reasons that limiting the scope of our studies to the sensitivity is a logical starting point. First, the main limitation for an in-beam PET application is the low statistics caused by the intrinsically low $\beta+$ concentration activated in the patient by the therapeutic beam, the need for partial-ring geometries which allow an opening for the beam line, and the complication of biological washout. All of these factors make the sen-

sitivity the most important performance parameter to be considered for an in-beam PET application. Second, despite the excellent timing performance of MRPC technology, current research suggests that even an exceptional TOF resolution cannot compensate for a very poor sensitivity. Considering that MRPCs are inherently inefficient to 511 keV gammas as compared with crystals, we should not assume that their potentially excellent TOF resolution can overcome this drawback. Instead, the reasoning is that if we can optimize the sensitivity of an MRPC-PET scanner such that it has a near-equivalent sensitivity to crystal-based scanners, then we can only expect improvements when adding the better TOF resolution into the reconstructions, which should be carried out after the optimal MRPC-PET geometry is known.

One fact that does require consideration and which is discussed in some detail in the studies presented here, is the scatter fraction. Since the signals from MRPCs contain no energy information we expect a high fraction of scattered photons to be present in the data set. Although it is impossible to know whether events have scattered prior to detection in a real scanner, in simulation we can take into account their effect and this point will be reported along with the sensitivity results presented here.

In an initial phase of study, which we shall refer to as the basic studies, the focus has been to optimize the detection efficiency of MRPC-based detectors to a (imaginary) beam of 511 keV photons. For each set of simulations, various parameters, including the electrode thickness, electrode composition, and the number of modules in the stack, have been explored independently. This has been important not only for our own learning of the benefits and limitations of MRPC-PET technology, but also in validating the accuracy of our simulations in comparison to the experimental data.

Following upon the basic studies, we have also modeled full-ring and partial-ring PET scanners based on unit block detectors identical to the experimental MRPC and LYSO-MCP prototypes. The scanners have been assessed for their sensitivity to several sources which produce back-to-back 511 keV photon pairs. In order to benchmark the results and validate the simulation code, two types of commercial full-body PET scanners have also been simulated, the Philips Gemini and the Siemens HiRez scanners. The BASTEI dual-head scanner, used for in-beam PET studies with patients at GSI, has also been reproduced in simulation in order to serve as a benchmark for partial-ring geometries.

In all scanner studies, several different sources and phantoms have been simulated: a ^{22}Na point source, the same point source inside a cylindrical water phantom, and the NEMA2001 protocol which is the industry standard used for assessing the sensitivity of commercial full-body PET scanners.

The results of the basic studies as well as the full-ring and partial-ring scanner studies will be described in detail in this chapter.

8.1 The GATE Monte-Carlo software

The OpenGATE software has been chosen for the simulation work presented in this chapter. As defined on their web page, "GATE is an advanced open-source software developed by the international OpenGATE Collaboration and dedicated to numerical simulations in medical imaging and radiotherapy" [113]. In essence, it is a simple script-like programming language build on top of GEANT4, which allows all the parameters of the simulation and its execution to be described in a simple text script. It has been designed specifically for performing simulations of PET, SPECT, CT [114, 115]. Recently, GATE has also been used to preform treatment planning simulations of pencil beams for proton therapy applications [116].

In GATE simulations, similar to GEANT4, the user is required to specify the physics list, the detector and phantom geometries and materials, the digitization parameters, the visualization parameters (if desired), the source description, the simulation output and execution parameters. However, instead of manipulating GEANT4 classes in C++, the user simply adheres to the conventions of the GATE script language to define all aspects of the simulation.

The power of GATE lies in not only in its user-friendly interface, but also in that many aspects of the simulation, that would be otherwise time consuming to set-up in GEANT4, are already established and can be put to use by invoking the correct syntax in the text macro file which GATE interprets at run-time and communicates to the GEANT4 engine. For example, predefined *systems* specific to medical physics applications allow the user to execute complex PET and SPECT experiments and obtain the desired outputs without spending a lot of time programming. Another nice feature of GATE is the *digitizer* which allows the possibility to model the response of the detector (its efficiency, energy resolution, spatial resolution, dead time, etc.) as if it were a real instrument. The parameters given to the *digitizer* are reflected in the data output which can be saved as either as a simple text or formatted ROOT file.

8.1.1 Conventions

Detector and phantom geometry

In GATE, all geometrical parameters of the detectors must be described by the user. The *world* volume is first defined which sets a limit to the spatial extent of the simulation. Next, the detector is described which requires the specification of the geometry and placement of the various detector elements in the *world* volume. A complete set of instructions is available to build objects and move them precisely, as well as for performing rotations and repetitions of defined objects. The process follows the conventions of GEANT4, except that the GATE scripting language is followed instead.

RPCGlass: d=2.4 g/cm3; n=4; state=Solid
+el: name=Oxygen; f=0.4598
+el: name=Sodium; f=0.0964
+el: name=Silicon; f=0.3365
+el: name=Calcium; f=0.1073

Tetrafluoroethane: d=0.004275 g/cm3; n=3; state=gas
+el: name=Carbon; n=2
+el: name=Fluorine; n=4
+el: name=Hydrogen; n=2

RPCLeadGlass: d =4.2 g/cm3; n=7; state=Solid
+el: name=Oxygen ; f=0.6245
+el: name=Silicon ; f=0.2097
+el: name=Boron ; f=0.0544
+el: name=Aluminum ; f=0.0104
+el: name=Lead ; f=0.0425
+el: name=Magnesium ; f=0.0515
+el: name=Zinc ; f=0.0070

Ceramic: d =3.72 g/cm3; n=2; state=Solid
+el: name=Aluminum ; n=2
+el: name=Oxygen ; n=3

Table 8.1: Custom material definitions added to the GATE material database for our MRPC simulations.

Materials

All geometrical volumes must be defined with a certain material which are needed by the GEANT4 engine in calculations throughout the course of the simulation. GATE comes equipped with a large database of materials which reside in a text file which is referenced at the beginning of the macro. Most materials common to detector design are available along with many materials relevant to medical applications (such as tissues and plastics).

In addition to the extensive list of pre-defined materials, the user is free to define new materials in the database or modify existing entries. We have added several materials for our simulations, including float glass (named "RPCGlass"), lead glass (named "RPCLeadGlass"), tetrafluoroethane (TFE) gas ($C_2F_4H_2$) and ceramic (Al_2O_3). The density and elemental composition of these materials as entered in the GATE material database are given in table 8.1.

Physics List

GATE comes with several pre-defined physics lists which are regarded as sufficiently accurate for most imaging and radiotherapy applications. For our simulations we have used a physics list based on only a limited set of electromagnetic processes since we are dealing only with the interactions of photons, electrons and positrons in our simulations. [1]

CrystalSD and PhantomSD

In GATE, PET simulations are made simpler by the use of a *system*, defined usually as a cylindrical volume declared just after the definition of the *world* volume. Once the *system* is defined, daughter volumes inside the *system* can be made to register the energy deposition of interactions, leading to *hits* and *singles* which are processed by the digitizer. In GATE, this is set up in a straight-forward way by attaching the *CrystalSD* (sensitive detector) to the volume that will register detected events. In our simulations, the *CrystalSD* is attached to the crystals in the case of crystal-based scanners and to the gas volumes filled with TFE in the case of the MRPC scanners. In addition, the *PhantomSD* can be attached to any volume(s) allowing to track whether photons had first interacted in non-sensitive volumes before being detected.

Production cuts

In GATE, whenever an interaction occurs within the *world* volume, it leads to energy deposition but also to the possibility of secondary particle production, depending on the physics of the interaction mechanism. Although the energy deposition is accounted for regardless of the outcome (though only registered in the data output in the *CrystalSD*), the generation of secondary particles depends upon a value known as the production cut. These cuts must be defined by the user for all volumes and for all particle types. The production cuts are specified in units of range but are translated by GATE into equivalent kinetic energy at the beginning of the simulation, a conversion which depends on the material definition for each volume. During run-time in which the particles are tracked through the geometry, secondary particles are only produced if their kinetic energy exceeds the production cut.

Although the production cut must be applied to all particles, it is most important to understand its influence on the generation of secondary electrons, which in reality are produced in abundance as the result of electromagnetic interactions by ionizing radiation. In most GATE simulations, 1

[1] For simulations of the $\beta+$ activation, for example, which is produced in materials (or tissues) as a result of irradiations with hadron beams, a more complex physics lists is required. Such radiotherapy simulations are currently a subject of study within the AQUA group as part of the ENVISION project but are not presented in this thesis.

mm is the standard production cut for all particles used throughout the *world* volume. Tracking electrons below this range usually does not alter the outcome of the simulation significantly, since the majority of secondary electrons go on to deposit their kinetic energy in the same bulk detector material in which they were produced. Decreasing the range cut on electrons, however, does increase the processing time of the simulations dramatically making a higher cut more desirable. In some cases, reducing the production cut for electrons can be important for obtaining accurate results. For example, if the $e-$ production cut is on the order of the size of the detector elements, then the energy recorded in the detector volume may be over-estimated because, in reality, a significant number of secondary electrons whose range falls below the production cut would escape the detector volume carrying away energy.

In the case of our MRPC simulations, the production cut for electrons has an influence on the detection efficiency. This is because the mechanism for gamma detection with RPCs requires an energetic electron to escape into the gas-gap, and this electron most likely originates in the surface of the glass electrodes. If the escaping electron is in fact a secondary electron, produced by ionizations from the energetic Compton electron (or other secondary electrons), a higher cut will reduce the detection efficiency since some of the short-range secondary electrons may escape into the gas-gap and lead to avalanche multiplication. Investigation of this point has been one of our initial aims and will be discussed in the results with basic MRPC simulations.

8.1.2 Simplifications and assumptions

In simulations of MRPC (and crystal-based) detectors, several simplifications and assumptions have been made. The most important of these has been that the avalanche mechanism has been completely ignored. Instead, any energy deposition recorded within the gas-gap of an MRPC module has been deemed as a positive detection. This is reasonable considering that MRPCs operate in limited-proportional or streamer mode where even a single free-electron has a high likelihood of leading to avalanche multiplication. In any case, the detection efficiency derived from our basic simulations, using the assumption that any electron escaping into the gas gap results in detection, matches the experimental data to within $\sim$15%. This result was the first to be reproduced since it is fundamental in validating the rest of our simulation work and is presented below in the section on basic studies with single-module MRPC detectors.

8.2 Basic simulations with gamma beams

In these basic studies, a source of photons has been generated at the origin with a direction parallel to the +Z direction. The photon beam passes through various glass-gas absorber layers, and the detection efficiency as well as other characteristics have been studied. Different glass-gap configurations have been considered, including a single absorber plate with forward and backward gas volumes, a single 4 gas-gap MRPC module having 5 absorbers, and a stack of many such MRPC modules which could serve as a possible compact MRPC-PET detector head.

8.2.1 Single-plate studies

A single glass plate was first modeled in simulation, having 400 μm thickness and surrounded by two 300 μm gas volumes (forward and backward) containing pure TFE. One million 511 keV gammas have been generated from the source for each run.

Energy spectra of electrons produced in the glass absorber and released into the gas-gap

The energy spectrum of electrons entering into the gas-gap both upstream and downstream of the glass absorber is shown in figure 8.1. The majority of the interactions are Compton, with only very few photoelectric, as expected for glass absorber.

There are 2115 events in the distribution which gives the detection efficiency for this single plate RPC detector, or 0.21%. Less than 10% of the total are detected in the upstream gas volume. This result matches within 15% the one obtained experimentally (0.18%) for our single-gap RPC made of 400 μm float glass.

Effect of e- production cut

Using the same single absorber geometry described above, the effect of the $e-$ production cut on the simulation output has been investigated. The simulation was repeated setting different values for the $e-$ production cut in the glass absorber on each run. One million 511 keV photons were generated from the source. Shown in figure 8.2 is the number of *singles* recorded for the four different runs, using 100, 10, 1 and 0.1 μm cuts. An increase in the number of *singles* obtained of about 8% was observed when decreasing the production cut from 100 μm to 0.1 μm.

For all subsequent simulations, a 1 μm $e-$ production cut has been applied to all volumes inside the *world* volume. All other particles use a 10 μm production cut.

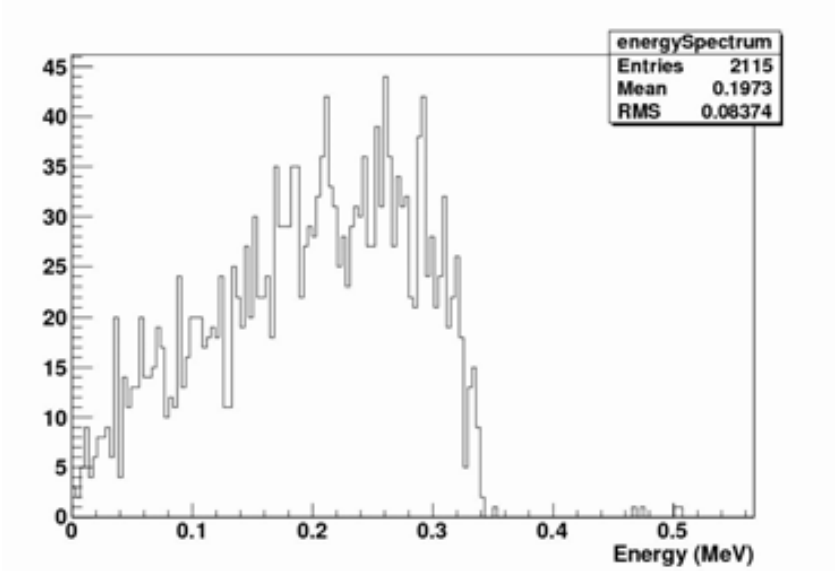

Figure 8.1: The energy spectra of electrons which are produced by interaction of the 511 keV gammas within a 400 μm plate of glass and then escape into an forward and backward gas volume.

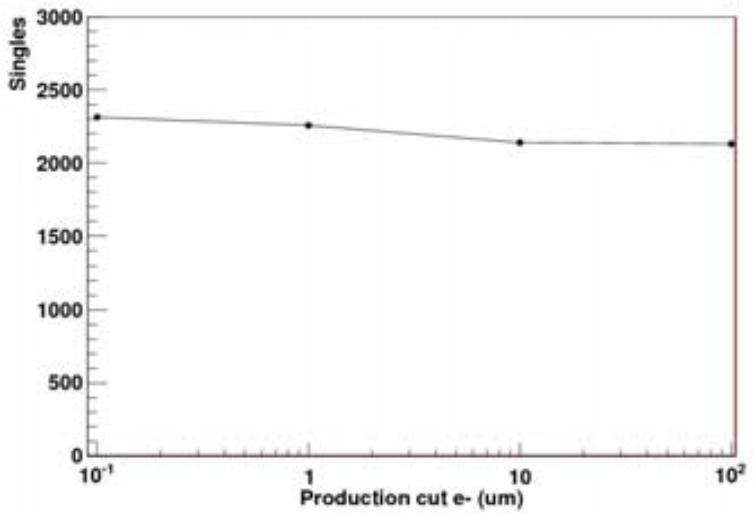

Figure 8.2: Number of singles as a function of the e- production cut applied to the glass plate volume. Between the lowest (0.1 μm) and highest cut (100 μm) there is only a difference of 8%. A 1 μm cut has been used for all subsequent simulations.

8.2.2 Single MRPC module simulations

A single MRPC module was modeled next, composed of 5 absorber plates having 400 μm thickness and 4 gas gaps of 300 μm filled with pure TFE. One million 511 keV gammas have been generated from the source for each run. The detection efficiency of the single module has been studied as a function of the thickness of the absorber and with different absorber materials.

Detection efficiency vs absorber thickness

In using MRPCs to detect 511 keV gammas, as required for a PET application, the detection efficiency is expected to depend strongly on the absorber thickness. This is due to the unique detection mechanism which requires an energetic electron (produced by Compton interaction by the photon in the absorber) to escape into the gas volume where it will lead to avalanche. If the absorber is too thick, electrons produced in the center will not escape due to their limited range. It follows then, that above a certain thickness we expect the efficiency to reach a plateau.

This has been confirmed in simulation using a single 4 gas-gap MRPC modules having absorbers of different thickness and made of different materials. Shown in figure 8.3 is the result where the thickness of the absorber has been varied for each run. The study includes various absorber materials: float glass, lead glass, and ceramic. An absorber made of pure lead has also been included for curiosity even though conductive materials cannot be used in MRPC designs. A beam of 1 million 511 keV gammas has been used giving a statistical uncertainty of $\sim$1% on the detection efficiency.

In glass, the efficiency plateau at 0.77% is reached at an absorber thickness of 300 μm, while for lead glass and ceramic, the plateau is reached at 200 μm. In pure lead, the maximum efficiency is reached already at 50 μm. The thickness at which the maximum is reached reflects the limited range of the Compton electron, shorter for denser materials. The value of the maximum reached in the plateau on the other hand, is only partially reflected by the higher conversion efficiency of the denser materials: lead glass and ceramic are barely 5% better than float glass and lead only a factor of 2 (despite being many times more absorbing to 511 keV photons). This later point suggests an interesting trade-off: a much higher number of Compton interactions may occur in denser materials, but at the expense of the volume that will effectively contribute. This is another justification for our choice of regular float glass over lead glass in our MRPC experimental work. Having said that, a factor of 2 in efficiency would be very welcome in MRPC-PET, but until resistive layers with conversion efficiencies comparable to lead can be found, the use of moderately higher density materials such as lead glass and ceramic is hardly justifiable considering their much higher cost.

Although the result above highlights some interesting physics, it also

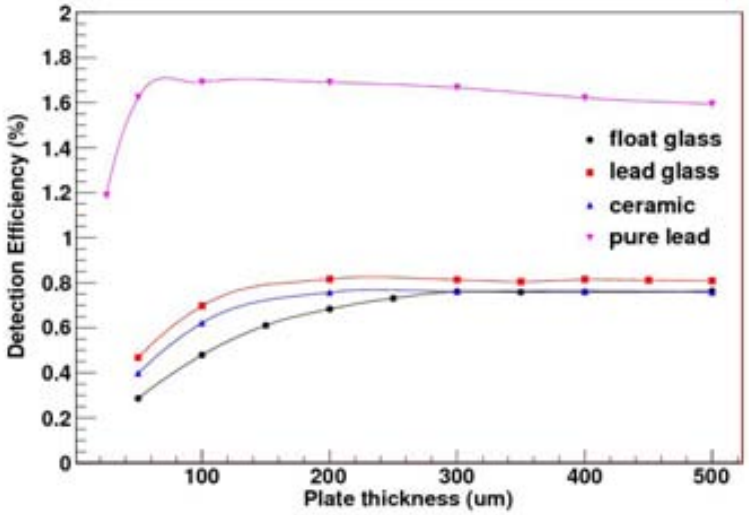

Figure 8.3: Detection efficiency as a function of plate thickness for single MRPC modules having 4 gas-gaps and made of absorbers of different materials. The gas thickness is always 300 μm and filled with tetrafluoroethane gas ($C_2F_4H_2$).

agrees closely with the efficiency that we have measured experimentally with our own MRPC prototypes (presented in the previous chapter). Specifically, the efficiency measured in simulation with the 4-gap 400 μm glass single MRPC, (0.77±0.01)%, matches the experimental result of (0.66±0.01)% within ∼15%. These results also match very closely the simulated and measured detection efficiency to 511 keV gammas of 4-gap MRPCs reported by other groups [117].

8.2.3 Multi-module MRPC stack simulations

The final group of simulations performed as part of the basic studies with a single gamma beam consist of a stack of MRPC modules, each composed of 5 absorber plates composed of float glass and 4 gas gaps of 300 μm filled with pure TFE. Stacks of 60, 80, 100, and 120 modules have been described, spaced uniformly at 8 mm. As before, one million 511 keV gammas have been generated from the source for each run.

Glass thickness optimization

Using the description of a full MRPC-PET head composed of a number of 4-gap MRPC modules, the effect of the absorber thickness on the detection efficiency to 511 keV gammas has been revisited. Unlike in a single MRPC

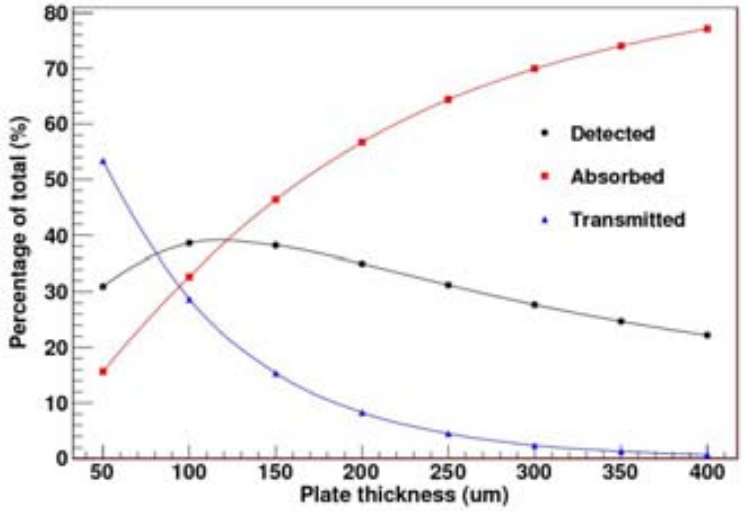

Figure 8.4: Different detection outcomes for a stack of 120 MRPC modules having glass absorbers of different thicknesses. The stack has been irradiated with a beam of 511 keV photons.

module where the efficiency reaches a plateau, here we expect the efficiency to reach a maximum and then to fall as the absorber thickness is increased. This is due to the shielding effect of the upstream modules on the downstream ones, which progressively attenuates the gamma beam leaving fewer photons available for detection to the modules deeper in the stack.

To investigate this precisely, rather than look only at the number of events detected by the stack (defined before as an energy deposition in any of the gas volumes within the modules), we have included a phase-space actor located in a plane directly following the full MRPC stack. By filtering on 511 keV photons entering into the phase-space, we can record also the number of photons which pass through all MRPCs without interacting (transmitted). This has been carried out with 60, 80, 100, and 120 module stacks, having different glass thickness between 50 and 400 μm. Shown in figure 8.4 is the result for the 120 module stack: the percentage of detected, transmitted, and absorbed (without detection) events is shown for each run with different plate thickness. At 400 μm, equal to the thickness of the glass in our experimental prototypes, the detection efficiency is 22% while the number of photons which do not interact are less than 1% of the total; over 77% have been absorbed without detection. At 100 μm thickness the efficiency is 39%, nearly a factor of 2 higher than at 400 μm, indication of the increased shielding caused by thicker absorbers.

The shielding effect can be seen in another way by analyzing the *singles*

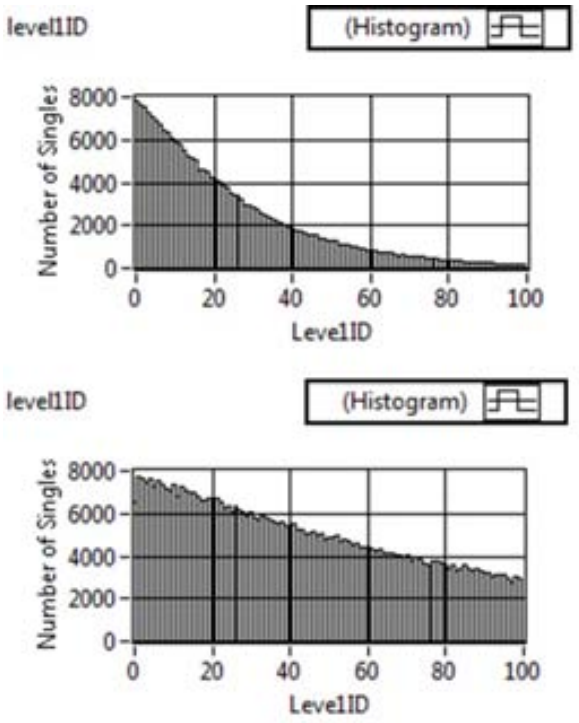

Figure 8.5: The distributions of *singles* recorded in a 100-module MRPC stack having 400 μm (above) and 150 μm thick glass absorbers (below). The shielding effect caused in the case of the 400 μm example is clearly visible; additional modules above 80 do not improve the detection efficiency. For the 150 μm example, however, the addition of extra modules is still useful to increase the total efficiency.

data for each simulation run. Shown in figure 8.5 is the *singles* distribution in each of the individual modules of a 100 module stack, having both 400 μm (above) and 150 μm (below) thick glass absorbers. The attenuation of the gamma beam caused by the shielding effect is clearly visible in both cases. In the 400 μm example, the addition of modules beyond about the 60^{th} contribute very little to the overall efficiency since the beam is already more than 90% attenuated at this point. Instead for 150 μm stack, not only is the overall efficiency increased (due to the higher number of *singles* in the downstream modules), but 20% of the photons are transmitted leaving the possibility to add more modules.

A summary of the detection efficiency as it varies with glass absorber thickness is shown in figure 8.6 for the 60, 80, 100, and 120 module MRPC stacks. Very little improvement in the efficiency is made by adding more than 60 modules when the glass is 400 μm thick. On the other hand, the maximum efficiency increases from 27% to 39% when going from 60 to 120

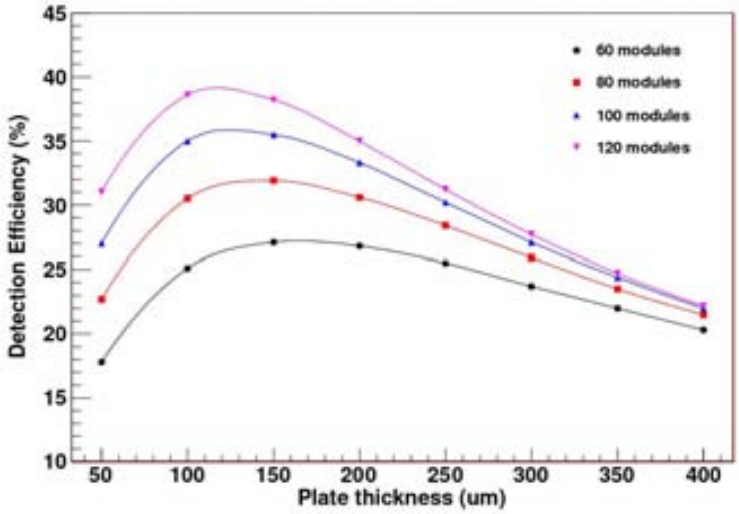

Figure 8.6: Single detection efficiency of a multi-module MRPC stack to 511 keV gammas as a function of the glass thickness.

modules and occurs at the optimum glass thickness of 150 and 100 μm, respectively.

Although these results indicate the path towards optimizing an MRPC for PET application, they should be compared with similar simulations made with crystals. For example, 20 mm of LYSO give a detection efficiency of 80% to 511 keV gammas, still a factor of 2 better than our 120-module MRPC stack at the optimum thickness. This translates into a factor of 4 lower sensitivity in coincidence, which is the true modality for any PET application.

Double interactions in multi-module MRPC stack

The probability for the photon to interact twice in two different MRPC modules of the stack has also been investigated. For the 60, 80, 100 and 120 module geometries the percentage of positive detections which actually contain 2 *singles* has been recorded while varying the glass absorber thickness. Shown in figure 8.7 is the result for 120 modules. The result is identical for the other geometries with fewer modules. In all cases, at 400 μm glass thickness, less than 2% of the detected photons have interacted twice. This percentage increases to 5% at 100 μm.

In crystal-based PET scanners, events which have interacted twice in the same detector head are normally rejected during data acquisition since the first interaction (which contains the correct information on the LOR) cannot be distinguished from the second (whose LOR is incorrect). Both have an

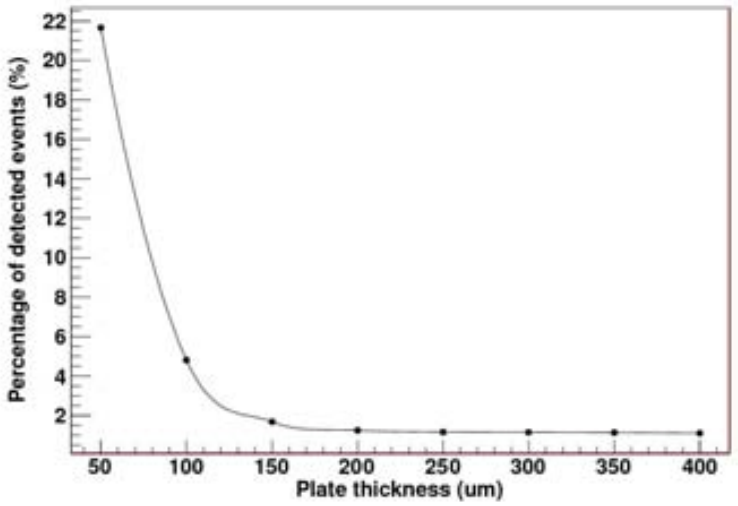

Figure 8.7: Percentage of detected events which have interacted in more than one MRPC module in a 120-module stack.

energy below the Compton edge thus are rejected by the energy threshold applied. In an MRPC scanner, however, rejection of these events is not necessarily mandatory since the majority of Compton-scattered photons are emitted in the forward direction and the DOI is known, making a selection on the first hit (inner-most) module an alternative. This point could be studied in future second-order MRPC sensitivity studies and could offer an improvement of about 10% in sensitivity for a scanner with 100 μm absorbers. Because the aim of the studies of MRPC scanners presented in the next section of this chapter is to optimize the sensitivity over a much larger range, coincidences which contain a double event in one or both detector heads have also been rejected in our analysis.

Intrinsic scatter-rejection of MRPC-PET

In general when considering a PET application, events which have scattered in the patient (or elsewhere in dead detector materials) must be rejected in order to maximize the signal-to-noise ratio (SNR) leading to better quality PET images. One challenge with full-body PET imaging, and especially with larger patients, is that the probability for either of the two collinear 511 keV photons to undergo a Compton interaction before emerging from the patient is quite high. Our own analysis of crystal-scanner simulations using a point source and a 20 cm diameter cylindrical water phantom shows that roughly 70% of the detected *singles* (before energy selection) have scattered prior to detection.

In crystal-based PET scanners, a good energy resolution is required for rejecting Compton-scattered events, however, full-body systems with very good energy resolutions (∼10% FWHM at 511 keV) suffer degradation of image quality since not all scattered photons can be rejected. Because MRPCs operate in saturated avalanche mode, no energy selection can be made on scatter events, and thus at first glace, an MRPC-PET scanner would suffer from a very high fraction of false coincidences and consequently a very poor SNR.

As it turns out, MRPCs are actually intrinsically less sensitivity to lower-energy photons, which partially compensates for their lack in energy resolution. This fact, which has been studied by other groups [107], arises from the physics of their unique detection mechanism to photons: interactions of lower energy photons in the absorber results in the production of an energetic electron with a shorter range which will only escape into the gas volume if produced closer to the surface of the absorber.

In order to investigate this ourselves, we have recorded the probability for detection of our stack of MRPC modules to a beam of photons having a range of energies between 50 and 511 keV. Shown in figure 8.8 is the result for a 60-module stack of 4-gap MRPC modules (400 μm glass). In each run, 10^6 photons have been delivered from the source. Shown for comparison in figure 8.9 is the result for a cubic 20x20x20 mm^3 block of both LYSO and LSO scintillator in which 10^4 photons have been delivered. In the crystal, the efficiency at 511 keV is roughly 80% and increases steadily towards 100% at lower energy with full efficiency reached at 200 keV.

The energy sensitivity of the stack of MRPC modules is characteristically different to crystal. Rather than being more efficient at lower energies, the MRPC stack is less sensitive, implying a natural energy selection on higher energy photons. This result is fortunate for the use of MRPCs in PET, since no selection on energy can be made after the photon has been detected. If this were not the case, RPCs would suffer heavily from a very high scatter fraction, even for small volume patients. Even so, the natural selection is not sharp enough to completely filter out lower energy photons. As we shall see if the scanner studies presented in the next section, this results in a significant higher SF for an MRPC-PET detector as compared with crystal-based scanners.

8.3 Results of full-ring scanner configurations

This section presents a series of simulation studies in which the sensitivity of full-ring MRPC-PET scanners are compared to full-ring PET scanners based on conventional crystal technology. Although full-ring scanner geometries are not relevant for the application of in-beam PET for hadrontherapy dosimetry (where a partial ring geometry is required because of the presence

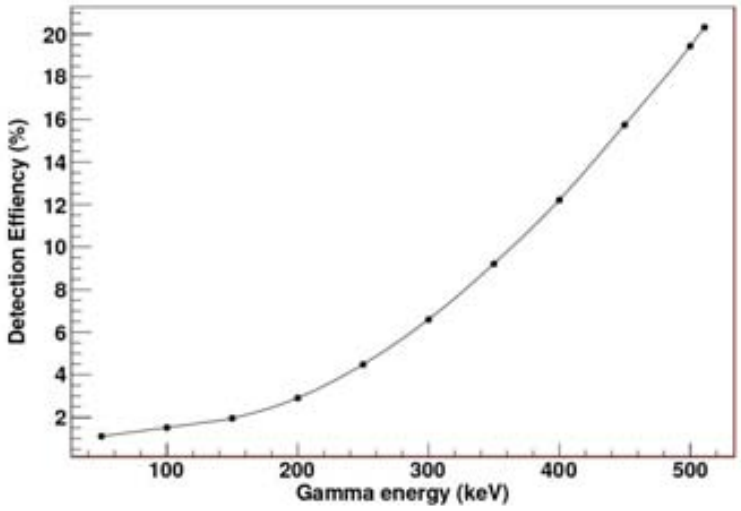

Figure 8.8: Detection efficiency of a 60 module stack of 4-gap MRPC modules to a narrow beam of gammas having energies between 50 keV and 511 keV.

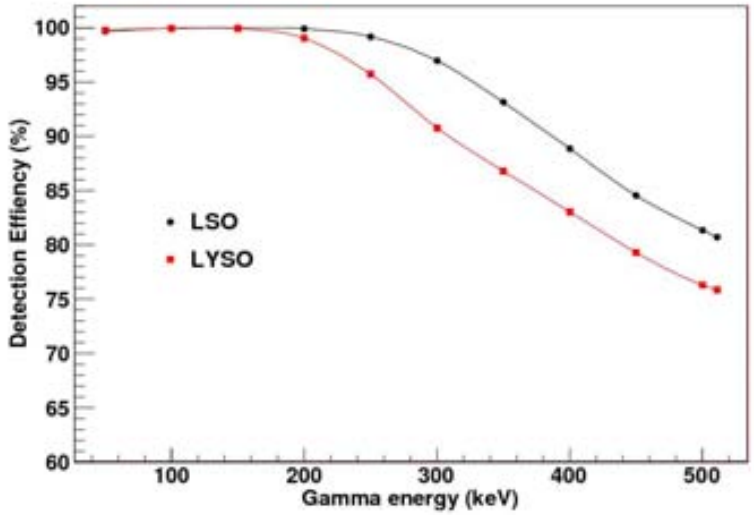

Figure 8.9: Detection efficiency for a cubic block of 20x20x20 mm^3 LSO and LYSO scintillator to a narrow beam of gammas having energies between 50 keV and 511 keV.

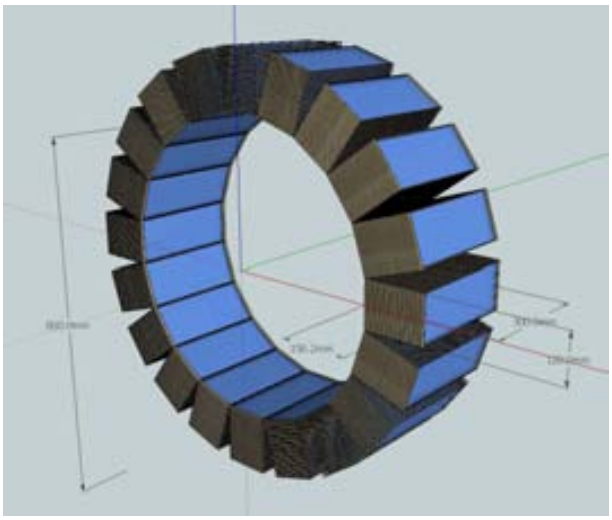

Figure 8.10: One of the full-ring (20 heads) MRPC-PET scanner configurations described in simulation as part of the sensitivity studies. In this example, each head consists of 20 module spaced at 8 mm pitch in the radial direction. Each module contains 5 glass absorbers of 400 μm with 4 gas gaps of 300 μm filled with pure TFE. The internal diameter of the scanner is 80 cm.

of the hadron beam line), a full-ring scanner geometry could be used for in-room or off-line PET, during the minutes immediately following irradiation with the therapeutic beam. In addition, a full-ring design based on either the MRPC or LYSO-MCP technologies can have relevance in the field of nuclear medicine; although hadrontherapy QA is the main topic of this thesis, the possibility of using MRPC technology for full-body PET imaging must not be forgotten, especially considering the potential reduction in cost that such technology provides.

Using the dimensions of both the MRPC and LYSO-MCP experimental prototypes as unit detectors and building up hypothetical full-ring PET scanner geometries, we have studied the sensitivity that can be achieved using these technologies. In the case of full-ring MRPC-PET scanners (having 20 heads in a ring configuration as shown in figure 8.10), an additional aim has been to optimize the sensitivity by tuning several geometrical parameters. These include: the number of MRPC modules per head, their spacing within the head (separation in the radial direction), the glass absorber thickness in each module, and the axial extent of the modules. Other aspects are common to all the MRPC scanner geometries: each MRPC module has 5 absorbers and 4 gas gaps, the absorbers are made of float glass, the gas gaps are 300 μm and filled with pure TFE, and the internal diameter of the scanner is 80 cm.

Many different geometrical configurations have been simulated in the following study aimed at optimizing the sensitivity of full-ring MRPC-PET scanners. In order to make the task of describing each geometry simpler, a reference-code convention has been adopted and will be used for the rest of this thesis. The code sums up the various parameters that have been modified systematically and will be written as follows

[modules per head (#)] - [glass thickness (μm)] - [module spacing (mm)] - [axial length (cm)]

For example, a full-ring MRPC scanner having 20 modules per head, 400 μm glass absorbers, 8 *mm* module spacing and 30 cm axial length is referred to as MRPC 20-400-8-30. Figure 8.10 shows a drawing of a full-ring MRPC 20-400-8-30 scanner which has been the starting point for our studies.

8.3.1 Analysis Parameters

Analysis of the *singles* data returned by GATE for each simulation run is required for computing coincidences and extracting the measured sensitivity. Although coincidence sorting can be carried out within GATE itself, a custom-built software based on LABVIEW has been written for this purpose, allowing to change the analysis parameters quickly (without needing to re-run the simulation) and for visualizing the simulation output. Shown in figure 8.11 is a screen-shot from the LABVIEW analysis program in which the *singles* data for a full-ring MRPC-PET scanner having 60 modules per head is displayed.

In performing our analysis of the simulation output, we have first filtered the *singles* data by applying an energy blurring (in the case of the crystal scanners) followed by an energy selection before selecting coincidences. Shown in figure 8.12 is the energy distribution of the *singles* data for one of the crystal scanners before (above) and after (below) an energy blurring of 11.5% FWHM has been applied. This energy blurring is needed in the analysis of crystal-based scanners in order to accurately model the true output produced by a real scanner and obtain the correct sensitivity.

Table 8.2 summarizes the parameters used in the analysis of the scanner geometries. For both crystal scanners using LYSO crystal (the Gemini and our MCP-PMT), we have used an energy blurring of 11.5% FWHM and an energy selection window of 440-665 keV. These values have been derived from the measured performance of the real Gemini scanner [87]. For the scanners using LSO crystal (the HiRez and BASTEI) we have used an energy blurring of 15% and a window of 425-650 keV following the results used in previous studies of the HiRez scanner [94].

In the case of the MRPC scanners, we have not applied any energy blurring and have filtered the *singles* data above a lower threshold value

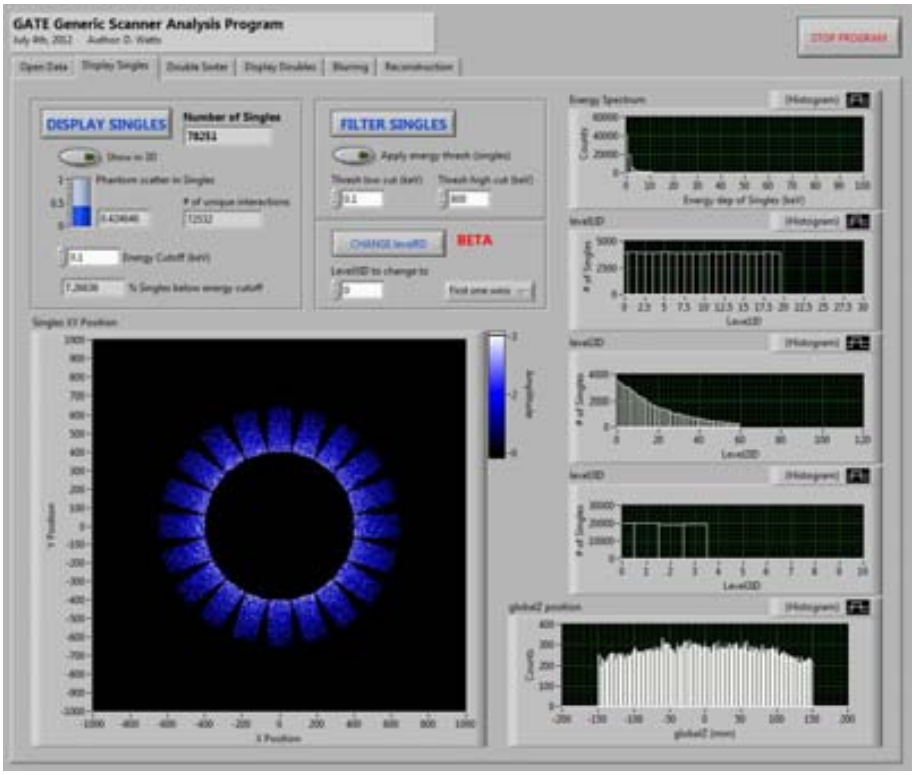

Figure 8.11: A screen-shot of the LABVIEW software built for analysis of the GATE simulation output. In this example, the *singles* data for a full-ring MRPC scanner is shown.

Scanner	Energy Blur.	Energy win.	Time win.	FOV Filter
	(% FWHM)	(keV)	(ns)	(#Sect/minSectDiff)
MRPC-PET	-	> 0.100	1.0	20 / 5
LYSO-MCP	11.5	440 - 665	3.8	40 / 10
HiRez	11.5	425 - 650	3.8	48 / 12
Gemini	15.0	440 - 665	3.8	28 / 7
BASTEI	15.0	425 - 650	3.8	2 / 1

Table 8.2: Various parameters applied in the data analysis.

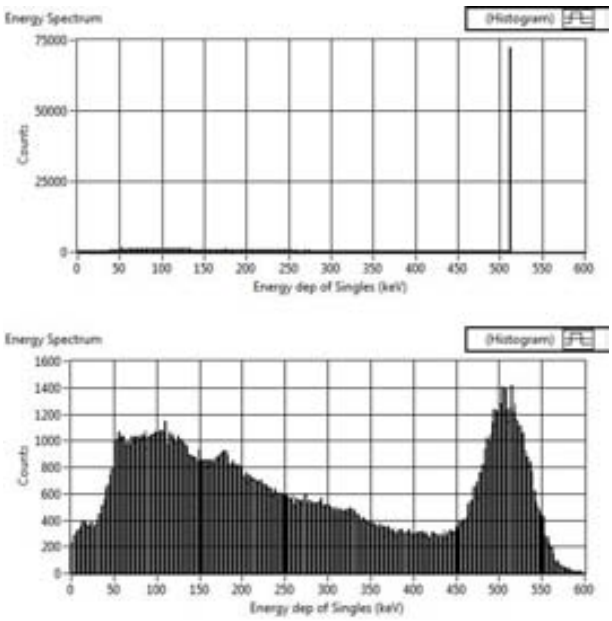

Figure 8.12: Above: the energy of *singles* data returned from GATE for one of the crystal-based scanners using the point source with water phantom. The large fraction of events have exactly 511 keV energy. Below: the same data after energy blurring has been applied in the LABVIEW analysis software.

chosen at 0.1 keV. This was done not because it reflects the true physics of the MRPC detection mechanism, but rather because it removes roughly 15% of the *singles* from the data set, bringing the simulated detection efficiency of a single 4-gap MRPC module with 400 μm glass in line with that which has been measured experimentally with the real module.

After filtering the *singles*, coincidences have been sorted using a time window of 1.0 ns or 3.8 ns, for the MRPC and crystal scanners, respectively. No time blurring has been applied to the single data since our study focuses only on the sensitivity and not on reconstructions using TOF information. Finally, for all scanner types, a FOV filter has been applied to the sorted coincidences in order to reject LORs outside of the FOV or caused by double interactions of a single photon in neighboring detectors heads. Following the convention used in the GATE *digitizer*, the minimum separation between heads (*minSectDiff*) is defined in order to reject coincidences outside the FOV. The number of heads (*#Sect*), which depends on the full-ring scanner geometry, must also be specified in the analysis software in order for the FOV filter to be computed correctly. These two values are also summarized for each scanner type in table 8.2.

8.3.2 Sources used in scanner studies

Three distinct source configurations have been used in the scanner simulation studies: a point source (having 1 mm diameter spherical volume), the same point source surrounded by a 20 cm diameter cylindrical water phantom of 30 cm length, and a water-filled line source following the NEMA NU2-2001 protocol for full-body PET scanners [118].

Pilot point source with and without phantom

The point source has been generated using the *back-to-back* source available in the GATE toolkit. The energy has been set at 511 keV and the source is spherical in dimension with 1 mm diameter. The activity has been set at 1 MBq such that for each decay from the source, two 511 keV photons which are collinear are emitted spontaneously from the source. In most simulations, and unless stated otherwise, the source is placed at the origin in the *world* volume, center in the transverse and axial FOV of the scanners.

The point source on its own is not realistic for PET applications since the presence of the patient leads to Compton-scattering of a large number of the photons before detection [2]. This has a significant impact on the scanner sensitivity, be it crystal-based or MRPC-based, since scattered photons are rejected either by the energy window applied by the electronics during acquisition (in the case of crystal scanners), or by the intrinsic insensitivity

[2] Our own simulations show that about 70% of 511 keV photons emitted at the center of a 20 cm diameter water phantom will undergo Compton scattering before exiting.

Sleeve number	Inside dia.	Outside dia.	Length
	(mm)	(mm)	(cm)
1	3.9	6.4	70
2	7.0	9.5	70
3	10.2	12.7	70
4	13.4	15.9	70
5	16.6	19.1	70

Table 8.3: Aluminum sleeves of the absolute sensitivity measurement according to the NEMA NU-2 2001 protocol.

to low energy photons in the case of MRPC detectors. To have a source which is more realistic, we have also made simulations with the inclusion of a cylindrical water phantom having 20 cm diameter and 30 cm axial length, centered over the point source at the origin. Inclusion of the water phantom also gives an indication of the scatter fraction.

NEMA2001

One of the sources used in our simulation studies has been derived from the National Electrical Manufacturers Association (NEMA) NU2-2001 publication and used in the nuclear medicine industry for measuring the conventional imaging performance of commercial PET scanners [118]. Although the protocol describes measurements which can be used to compare all the necessary performance characteristics of the scanner (scatter fraction, random fraction, position resolution, etc.) only the absolute sensitivity procedure has been adopted in our own studies.

In the NEMA sensitivity protocol performed with real PET scanners, a 70 cm long 3.9 mm diameter tube is filled with water mixed with a positron source of a given activity and placed at the center of the scanner along the axial direction. An aluminum sleeve is placed around the tube to ensure that all positrons annihilate before escaping the cylinder. Because the aluminum sleeve also results in some scattering of the emerging photons, additional sleeves are added allowing the absolute sensitivity with no sleeves to be extrapolated [119]. The dimensions of the aluminum sleeves are given in table 8.3.

The NEMA absolute sensitivity measurement protocol has been reproduced in simulations and tested with most of the scanner configurations presented in this chapter. In addition the use of a *back-to-back* line source of the same dimensions (3.9 mm diameter water-filled cylinder 70 cm long) but without aluminum sleeves has also been used and validated to give the same results as the absolute sensitivity extrapolated using the NEMA protocol. This has allowed us to proceed more rapidly in testing various MRPC

scanner geometries without the need to do 5 separate simulations with different aluminum sleeve thicknesses.

8.3.3 Philips Gemini scanner

As a benchmark for comparing the results with our own proposals for MRPC and MCP-PMT PET scanners, and also to validate our simulation code, we have chosen to model the Philips Gemini PET/CT detector. At the time of writing, the Gemini is one of the latest TOF-capable PET scanners to appear on the market, employing fast crystal and PMT technology and capable of a TOF resolution of 585 ps [87].

The PET ring of the Gemini scanner is made up of 28 flat module heads, each a 23x44 array of 4x4x22 mm^3 LYSO crystals. Each head is read out by 18 PMTs of 39 mm diameter using hexagonal Anger logic, an approach developed previously to the Gemini for GSO-based brain PET scanners [120]. The total axial FOV of the Gemini is 18 cm and the inner diameter of the crystal ring is 90.34 cm.

The Gemini crystal geometry has been described in GATE for our simulations. Figure 8.13 shows a composite drawing of the different elements of the scanner: a single LYSO crystal, one 23x44 crystal block (head) and the 28-head full ring. The position of the PMT windows for each head (shown as white circles) has been sketched to give a rough idea of the crystal-to-photodetector geometry of the hexagonal Anger logic approach, however, only the crystals have been included in simulation. The levels of the digitizer have been defined as follows for the generic *scanner* system: head (level1ID), crystal (level2ID). Readout is performed on the head level (depth 1).

The first source to have been used is the 70 cm long line source. Following the NEMA protocol for an absolute scanner sensitivity measurement, five separate runs have been made surrounding the line-source by progressively thicker sleeves of aluminum. Figure 8.14 shows the sensitivity for each run after applying energy blurring (11.5% FWHM) and energy selection (440-665 keV) to the singles data and then filtering coincidences within the 3.8 ns time window. The FOV filter (minimum sector difference: 7, number of sector: 28) has then been applied to the coincidences.

In order to determine the absolute sensitivity (the sensitivity for no aluminum sleeve), the sensitivity is extrapolating to 0 mm aluminum thickness from the results from each run. We achieve 6.57 cps/kBq, in agreement with the value of 6.6 cps/kBq made with the real Gemini scanner and published by other groups [87].

In addition to the NEMA source, we have also determined the sensitivity of the Gemini to the point source both with and without the cylindrical water phantom. For the point source, simulations return the sensitivity of 52.1 cps/kBq while for the same point source with water phantom the sensitivity drops to 9.33 cps/kBq, an indication of the large number of photons

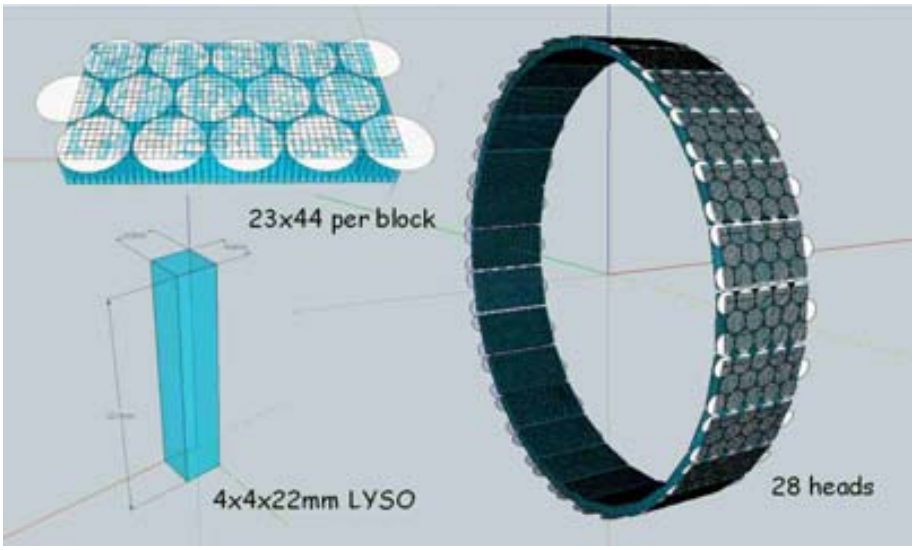

Figure 8.13: A composite drawing of the Philips Gemini geometry used in simulation studies. The rull-ring scanner is formed by 28 heads (or blocks), each consisting of 23x44 LYSO crystals having 4x4x22 mm^3. The hexagonal Anger logic readout geometry made by PMTs is sketched along with the drawing of the 23x44 crystal head.

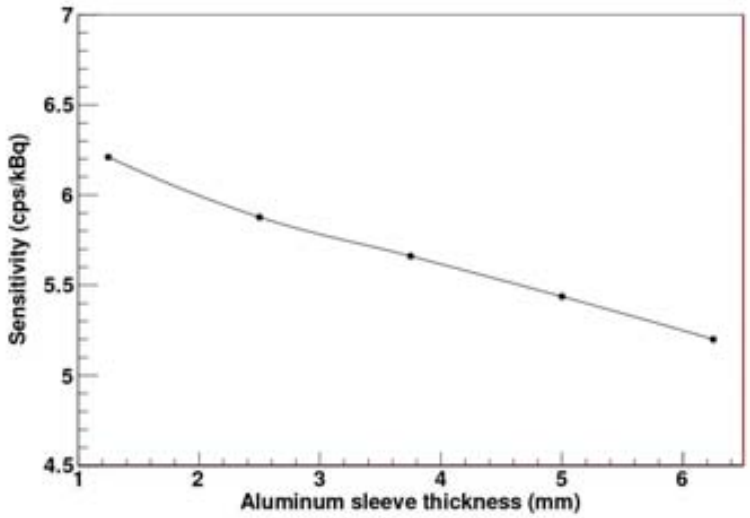

Figure 8.14: Simulated sensitivity of the Philips Gemini using the NEMA2001 protocol phantom. Five simulations have been run, each with different thickness of aluminum sleeve surrounding the 1 MBq line source. Extrapolating the curve to 0 mm gives the absolute sensitivity.

Philips Gemini	Sensitivity	Scatter Fraction
	(cps/kBq)	(%)
Point	52.1	0
Point /w phantom	9.33	17.9
NEMA source	6.57	-

Table 8.4: Sensitivity and scatter fraction of the LYSO-based Gemini full-ring scanner to the three different sources.

Siemens HiRez	Sensitivity	Scatter Fraction
	(cps/kBq)	(%)
Point source	69.8	0
Point source /w phantom	12.7	20.2
NEMA source	7.69	-

Table 8.5: Sensitivity and scatter fraction of the LSO-based HiRez full-ring scanner to the three different sources.

which scatter in the phantom and are then rejected by the application of the energy window between 440 and 665 keV. Because of the non-perfect energy resolution, some of the scattered events remain in the final data set,

8.3.4 Siemens Hi-Rez scanner

Another commercial scanner, the HiRez produced by Siemens, has also been simulated as part of the benchmark studies. The HiRez geometry has been already been validated in GATE simulations during a previous study carried out by the TERA Foundation [94]. These results have been reproduced to further validate the code and also to provide an alternative benchmark to the Gemini with a scanner based on a different crystal type and slightly different geometry.

The HiRez scanner is composed of 48 heads, each consisting of 3 unit block detectors arranged in the axial direction. Each unit block is an array of 13x13 LSO crystals, 4x4x20 mm^3 in size. The axial extent of the scanner is 16.2 cm and the ring diameter is 83 cm. This geometry has been described in GATE, shown as a composite drawing in figure 8.15. The levels of the digitizer for the HiRez simulations have been set as follows: head (level1ID), block (level2ID) and crystal (level3ID). Readout is performed on the block level (depth 2).

The NEMA line-source and the point source both with and without water phantom have been simulated. The results are summarized in table 8.5. Compared with the Philips Gemini, the sensitivity to all three sources is ∼15-30% higher, an indication of the higher stopping power of LSO as compared with LYSO.

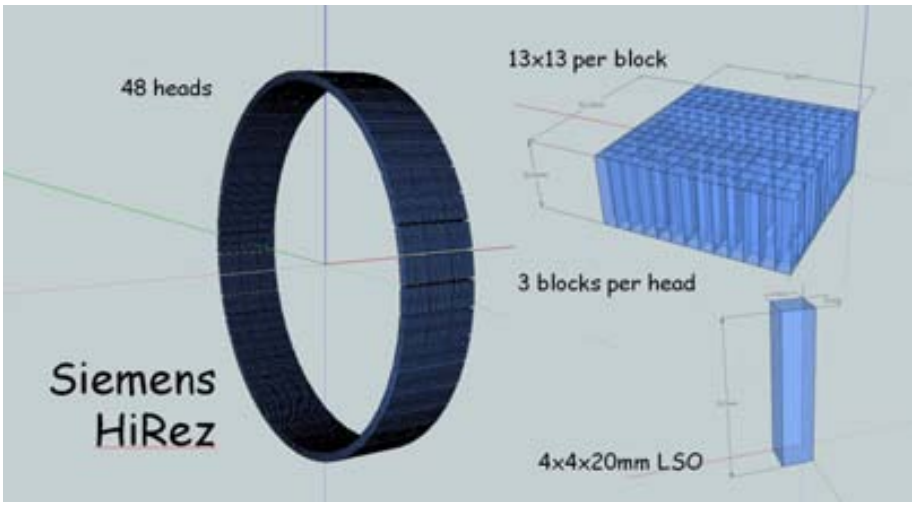

Figure 8.15: A composite drawing of the Siemens HiRez geometry used in simulation studies. The rull-ring scanner is formed by 48 heads where each head is made up of 3 detector blocks in a linear (axial) configuration. Each unit block consists of 13x13 LSO crystals each being 4x4x20 mm^3.

8.3.5 TERA LYSO-MCP scanner

A full-ring scanner based on the geometry of the MCP-PMT prototypes has been modeled in simulation. The unit detector block has the dimensions of the proposal outlined in the previous chapter, each multi-anode MCP-PMT is coupled to five LYSO crystals, each with dimensions 12x30x60 cm^3. No wrapping material has been described and so the effective crystal volume per block is 60x60x30 cm^3. A drawing of the unit block MCP-PMT module is shown on the left in figure 8.16. In the scanner geometry, 3 unit blocks make up a single head and 40 heads cover a full-ring with 80 cm bore diameter. A drawing of the full-ring MCP-PMT geometry is shown on the right of figure 8.16. Although the MCP-PMT is shown in the drawing for clarity, it has not been included in the geometric description of the detector in these simulation studies.

Simulations have been performed with all three sources and the results summarized in table 8.6. The results are rather promising, the sensitivity to the NEMA source being 57% and 35% higher than the Gemini and HiRez, respectively. This is certainly due to the fact that the depth of the the crystals is larger, 30 mm for the LYSO-MCP and only 22 and 20 mm for the Gemini and HiRez, respectively. This is one advantage of our proposed crystal geometry: because a DOI localization can be made within the crystal, longer crystals can be used without a degradation in spatial resolution caused by parallax errors.

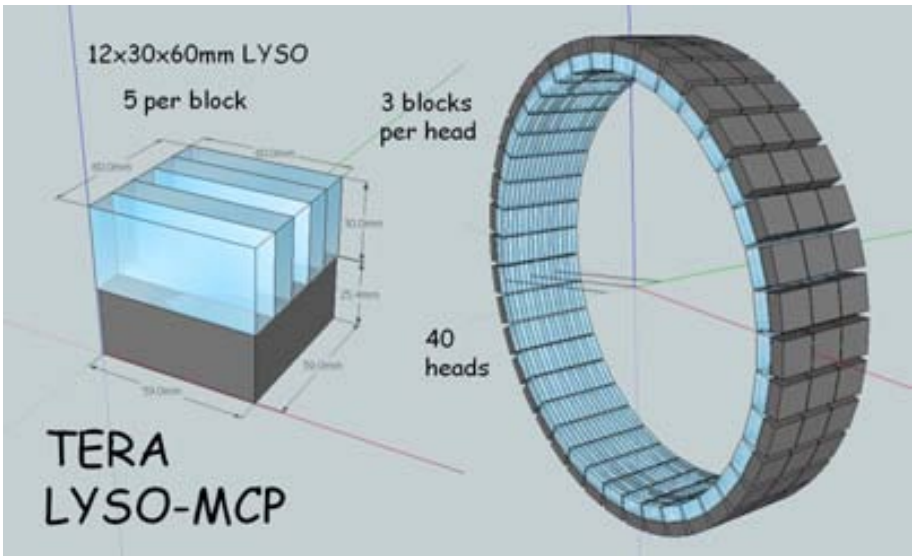

Figure 8.16: A drawing of the LYSO-MCP scanner geometry simulated in our studies. The dimensions of the unit block detector are the same as the experimental prototype built and tested by the AQUA group.

LYSO-MCP	Sensitivity	Scatter Fraction
	(cps/kBq)	(%)
Point source	82.4	0
Point source /w phantom	14.69	20.0
NEMA source	10.37	0.72

Table 8.6: Sensitivity and scatter fraction of the TERA LYSO-MCP scanner to the three different sources.

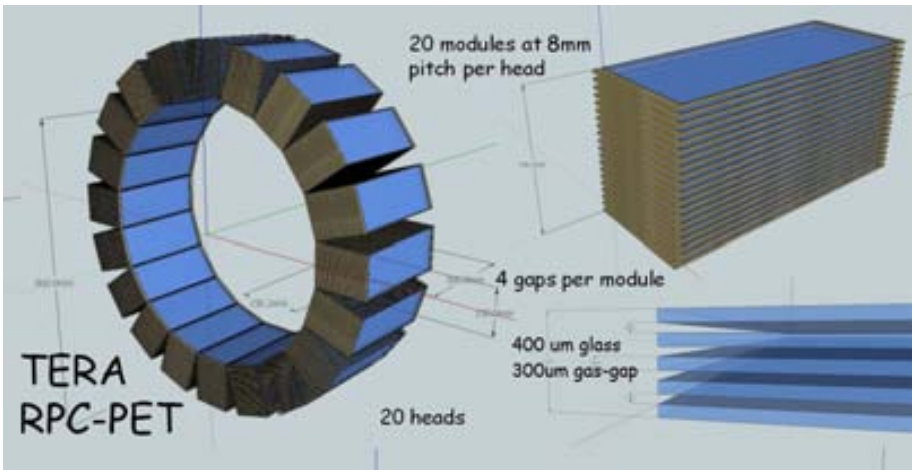

Figure 8.17: A composite drawing of one of the the full-ring MRPC-PET geometries used in simulation studies. All simulations use 4-gap modules with 300 μm gas-gaps filled with tetrafluoroethane gas ($C_2F_4H_2$). Other parameters, such as the glass thickness, number of modules, and module spacing, have been systematically varied in our studies. This example shows a 20 head MRPC scanner having 20 modules per head, 400 μm glass and 8 mm spacing between each module in the radial direction.

8.3.6 Full-ring MRPC-PET

A drawing of an MRPC 20-400-8-30 full-ring scanner geometry is shown in figure 8.17. Shown on the right of the scanner drawing is a close-up of a single MRPC module (with 400 μm glass and 300 μm gas gap) as well one of the multi-module heads, which has 20 modules spaced at 8 mm.

Initial geometry with 400μm glass absorbers

The geometry shown in figure 8.17, the MRPC 20-400-8-30, was our inital starting point for simulations but was found to have a sensitivity an order of magnitude lower than any of the crystal-based scanner presented previously for each of the 3 sources. Instead, an MRPC 60-400-4-30 full-ring scanner geometry was simulated, having 60 heads and in which the spacing between modules within each head was reduced to 4 mm. Such a geometry is feasible since a 4 gap 400 μm absorber MRPC module is 3.2 mm thick.

The results for the 3 sources for the MRPC 60-400-4-30 are reported in table 8.7. Even with the reduced module spacing of 4 mm, the MRPC 60-400-4-30 geometry has a $\sim$3 times lower sensitivity with the NEMA source as compared with the crystal-based scanners and $\sim$6 times lower sensitivity with the point source without water phantom.

Full-ring MRPC	Sensitivity	Scatter Fraction
60-400-4-30	(cps/kBq)	(%)
Point source	9.01	0
Point source /w phantom	2.11	42.4
NEMA source	2.03	-

Table 8.7: Sensitivity and scatter fraction of the MRPC 60-400-4-30 scanner to the three different sources.

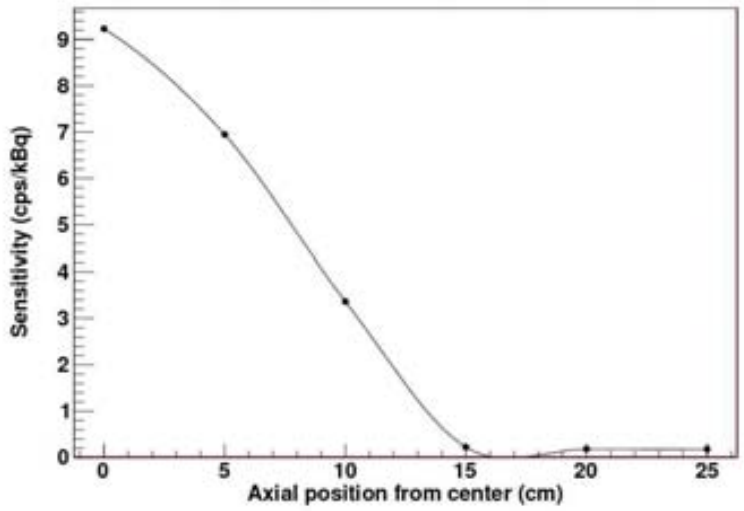

Figure 8.18: Sensitivity of the MRPC 60-400-4-30 to the point source moved off-axis in the axial direction.

Off-axis point-source sensitivity

Using the MRPC 60-400-4-30 geometry, the sensitivity while moving the point source away from the center of the scanner FOV, in both radial and axial directions, has been studied. Shown in figure 8.18 is the result for the axial direction at steps of 5 cm. As expected, the sensitivity drops rapidly as the source is moved from the center of the axial FOV and goes to zero when outside the active area of the scanner at Z $>$ 15 cm.

Shown in figure 8.19 is the result when moving the source in the radial direction (and centered in the axial FOV). A loss in sensitivity of 15% can be observed at the position X=5 cm. At this location the point source lies just between two MRPC heads when considering vertical LORs.

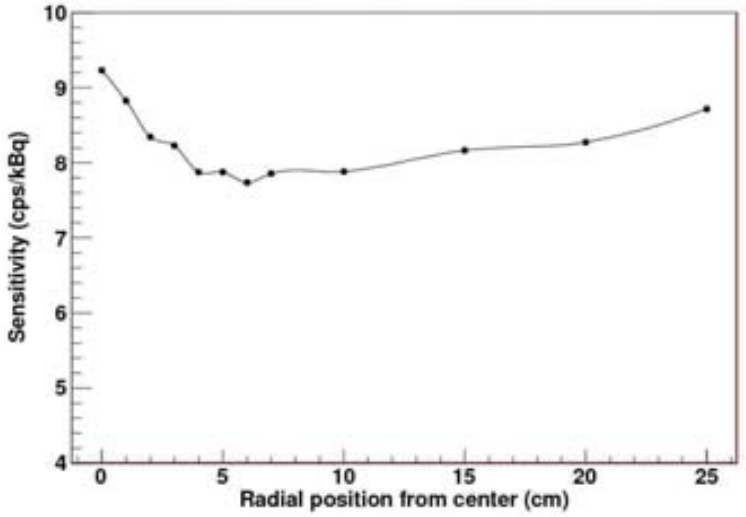

Figure 8.19: Sensitivity of the MRPC 60-400-4-30 to the point source moved off-axis in the radial direction.

Improved geometries with 150μm glass absorber

The MRPC geometries simulated in the previous section make use of glass absorbers of 400 μm, far from the optimum thickness as observed in the basic simulations studies. In order to quantify the improvement in sensitivity for a full-ring scanner, an MRPC 60-150-4-30 scanner has been described, where all glass absorbers are 150 μm. (In this configuration, each MRPC module is only 1.95 mm thick, making it possible to stack modules more closely than 4 mm within each head, a possibility that is investigated below.)

With the 400 μm glass absorbers, 60 modules was the maximum number that could be used within a single head since the shielding effect resulting in near complete attenuation of the photons, observed in the basic studies with collimated 511 keV gamma beams (recall figure 8.5). With the 150 μm absorbers, however, a large fraction of the photons are transmitted through the 60-module head making it beneficial to add more modules. This has been done for a full-ring configuration having 120 modules per head, the MRPC 120-150-4-30.

The results for the 3 different sources with the MRPC 60-150-4-30 and MRPC 120-150-4-30 scanners are given in tables 8.8 and 8.9. The sensitivity of the MRPC 120-150-4-30 is only 66% that of the Gemini scanner when using the NEMA source (see table 8.4).

Full-ring MRPC	Sensitivity	Scatter Fraction
60-150-4-30	(cps/kBq)	(%)
Point source	12.5	0
Point source /w phantom	2.93	45.6
NEMA source	2.95	-

Table 8.8: Sensitivity and scatter fraction of the MRPC 60-150-4-30 geometry (having 150 μm glass absorbers) to the three different sources.

Full-ring MRPC	Sensitivity	Scatter Fraction
120-150-4-30	(cps/kBq)	(%)
Point source	20.0	0
Point source /w phantom	4.44	37.8
NEMA source	4.37	-

Table 8.9: Sensitivity and scatter fraction of the MRPC 120-150-4-30 geometry (having 150 μm glass absorbers) to the three different sources.

Increased axial FOV MRPC-PET scanners

A very attractive feature of the proposed MRPC technology is that modules are scalable in the axial direction without any increase in the number of electronic channels required. Apart from the excellent TOF and spatial resolutions, this feature is one of the main reasons why MRPC-PET is an exciting alternative technology for PET since the sensitivity can be increased dramatically without a substantial increase in material cost.

The effect on the sensitivity of increasing the axial FOV of the MRPC-PET scanners has been made by simulating full-ring MRPC scanners which are 60 cm in axial length. This has been done for scanner geometries having both 60 and 120 modules per head always with the optimized 150 μm glass absorber thickness. Figure 8.20 summarizes the results for the NEMA source and includes the results for the 30 cm axial FOV MRPC scanner for comparison. Figure 8.21 summarizes the results for the point source without water phantom for the same series of MRPC scanner geometries.

In adjusting various parameters of the MRPC-PET scanner geometries, it is important to keep in mind the overall physical size that each scanner will have. Even though we can simulate geometries with an unlimited number of modules per head, the geometry must be feasible to build physically, such that it can be included comfortably in a hospital facility. In the case of a nuclear medicine application, the geometrical requirement are much less stringent than in a hadrontherapy application.

Shown in table 8.10 are the some of the mechanical dimensions of the full-ring MRPC scanners (using the optimized 150 μm thick absorbers) which have been described in the simulation study presented in this chapter. Figure

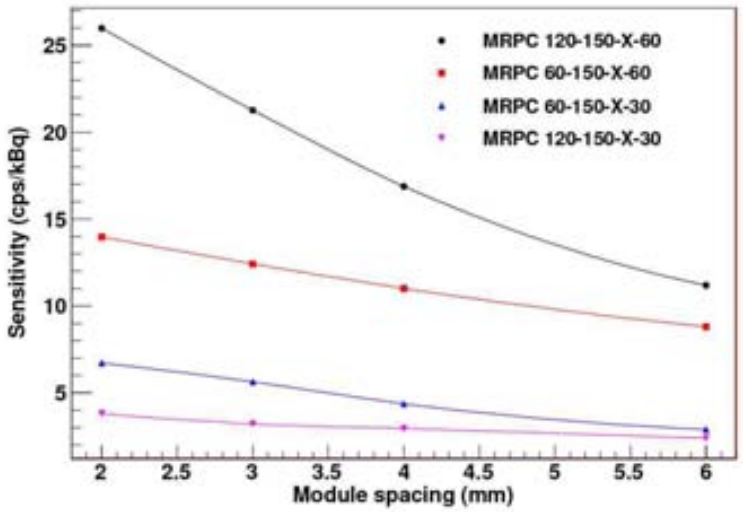

Figure 8.20: Sensitivity study of full-ring MRPC scanner geometries having 150 μm absorbers to the NEMA source. Both 30 and 60 cm axial length scanners are shown as well as scanners having 60 or 120 modules per head. For each geometry the sensitivity has been measured for different module spacings from 2 to 6 mm.

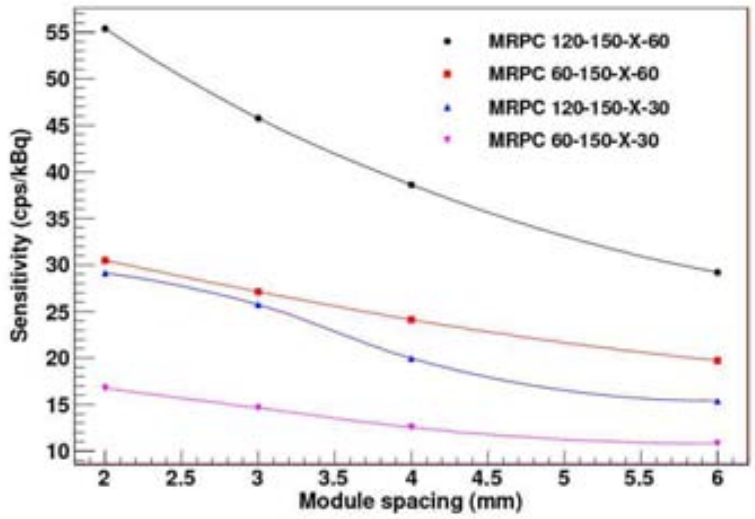

Figure 8.21: A similar sensitivity study using the same set of full-ring MRPC scanner geometries (having 150 μm absorbers and either 60 or 120 modules, and either 30 or 60 cm axial length) to the back-to-back point source.

Modules/head	Module spacing	Depth of head	Outer ring dia.
	(mm)	(cm)	(cm)
60	2	12	104
	3	18	116
	4	24	128
	6	36	152
120	2	24	128
	3	36	152
	4	48	176
	6	72	224

Table 8.10: An overview of the dimensions of simulated full-ring MRPC-PET scanner geometries described in the sensitivity optimization study.

Scanner type	Sensitivity			Scatter Fr.
	NEMA	Point	Point w phan.	Water phan.
	(cps/kBq)	(cps/kBq)	(cps/kBq)	(%)
MRPC 60-400-4-30	2.03	9.01	2.11	42.4
MRPC 120-150-4-30	4.37	20.0	4.44	37.8
MRPC 60-150-4-60	11.0	24.1	6.6	52.8
MRPC 120-150-4-60	18.7	38.6	10.4	52.7
LYSO-MCP	10.4	82.4	14.7	20.0
Gemini	6.6	52.1	9.3	17.9
HiRez	7.7	69.8	12.7	20.2

Table 8.11: Sensitivities of some of the MRPC scanner geometries and the crystal-based scanners for all three sources used. The scatter fraction is also reported for the point source with water phantom of 30 *cm* length and 20 *cm* diameter.

8.22 gives a visual summary of 6 of the proposed geometries as seen in the visualization of the GATE simulations.

8.3.7 Comparison of MRPC-PET results to crystal-based scanners

Table 8.11 shows the sensitivity results for selected MRPC configurations and all the crystal-based scanners for the 3 different sources used. The sensitivities of the MRPC configurations improve with each change to the geometry: first the use of 150 μm absorbers, second the increase from 60 to 120 modules per stack, and finally the extension to 60 cm axial length. All configurations given here use 4 mm spacing between modules within each head, which should be reasonably easy to build mechanically. However, if it could be possible to stack the modules more closely, at say 2 or 3 mm, then

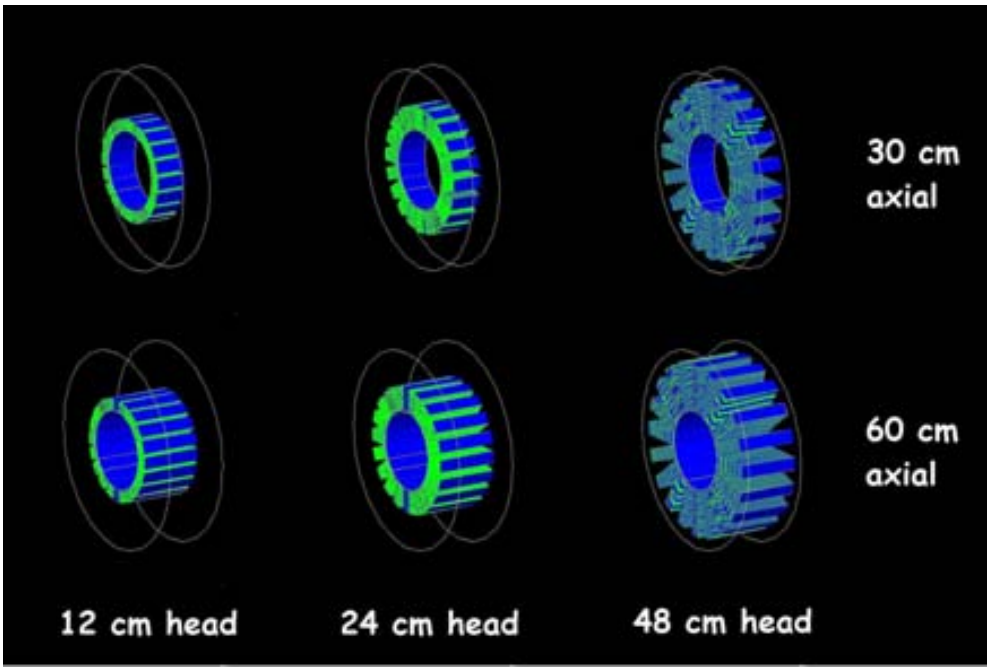

Figure 8.22: GATE visualizations of 6 of examples of full-ring MRPC scanners having different head sizes (determined by the number of modules and module spacing) and either 30 or 60 cm axial length.

we can expect even higher sensitivities (as given in figures 8.20 and 8.21).

As it stands, the best MRPC scanner configuration given in table 8.11, the MRPC 120-150-4-60, compares reasonably well with the crystal-based scanners when considering the point source with water phantom [3]. In fact, it is 12% better than the Gemini, and only 18% worse than the HiRez. For our LYSO-MCP scanner, the sensitivity is 57% better than the Gemini, however, this solution will surely be as expensive as commercial scanners since it makes use of roughly the same volume of scintillator crystal. The MRPC 120-150-4-60 scanner, on the other hand, is likely to be less expensive than any of the crystal-based scanners simply because the price of glass is orders of magnitude cheaper than crystal. This point should be quantified in future developments once a supplier which can produce the glass absorbers patterned with polyimide spacers in massive quantities has been found.

The scatter fraction for the point source with water phantom is also shown for comparison. Because of the selective sensitivity of MRPC to higher energy photons, the MRPC scanner suffer only a factor of 2 to 2.5 worse scatter fraction than the crystal-based scanners, for the point source with water phantom. Despite this drawback, it is expected that the an excellent TOF resolution will largely compensate since it results in an increase in the signal-to-noise. This issue should be examined in detail in future studies which compare the true quality of images obtained from MRPC-based PET scanners to those based on crystals.

In the case of the results with the NEMA phantom, the best MRPC-PET scanner shows a much better absolute sensitivity than the crystal-based ones, a factor of $\sim$2.5 as compared with the Gemini and HiRez commercial scanners. The reason the results are much better with the NEMA sources as compared with the point source is clearly due to the fact that the NEMA source is 70 cm long: most of it lies completely outside the axial FOV of the crystal scanners, therefore, the 60 cm long MRPC scanners have a huge advantage. Instead, the axial FOV, which is limited by cost in crystal-based scanners, is essentially unlimited in an MRPC scanner since it can be extended with only a minor increase in materials and no increase in the number of electronic channels.

Although we can extend our MRPC scanner beyond 60 cm, we see that already this technology offers a dramatic increase in sensitivity as compared with crystal technology. Considering also that MRPCs are expected to yield a better position resolution and TOF resolution, this result is extremely interesting in the field of nuclear medicine and especially for whole-body PET imaging.

[3] The sensitivity to the point source *without* the water phantom is more of a novelty and is completely unrealistic since every PET scan includes at least some tissue-equivalent volume around the $\beta+$ activity. It has been included for curiosity.

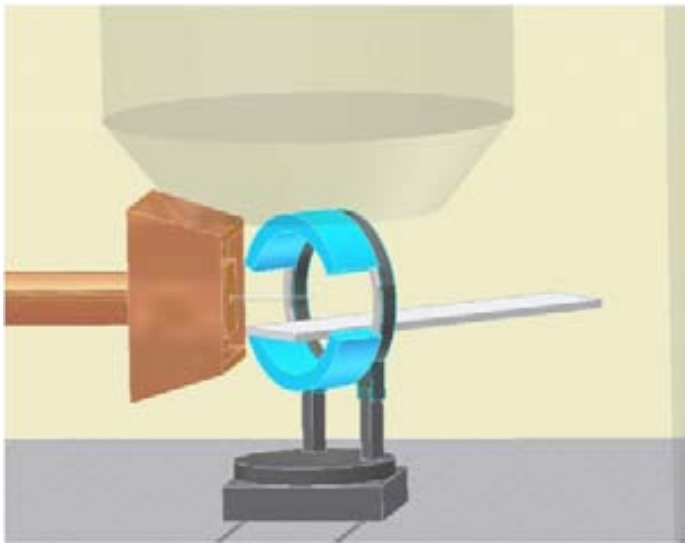

Figure 8.23: A drawing of a hypothetical in-beam PET apparatus proposed by the TERA Foundation. The geometry of the horizontal beam-line is modeled according to one of the treatment rooms at the CNAO which uses a horizontal hadron beam for therapy [94].

8.4 Partial-ring geometries for in-beam PET

Partial-ring PET scanner designs based on MRPC technology have also been investigated in light of a potential application to in-beam PET for *in-vivo* dosimetry, in which the presence of the hadron beam-line excludes the possibility of a full-ring scanner. Shown for example in figure 8.23 is a previous proposal by the TERA Foundation for a partial-ring in-beam PET scanner based on LSO crystals which could be used in a treatment room at the CNAO where a horizontal beam line is available for therapy [94] [4].

8.4.1 BASTEI dual-head scanner

In order to have an alternative in-beam PET scanner to compare our MRPC results to, we have first simulated the BASTEI dual-head scanner which was used for in-beam PET dosimetry with patients at GSI.

Each head of the BASTEI scanner consists of 4x8 unit detector blocks having 54x54x20 mm^3 arranged in a spherical configuration [66]. Each block is made up of 8x8 individual BGO crystals of 6.75x6.75x20 mm^3. The inner diameter is 80 cm. The BASTEI geometry has been described in GATE and

[4] In addition to the requirement of open-ring (or dual-head) scanner designs, the limitations imposed by the beam line nozzle (shown in brown) and other devices within the treatment room are also important when considering the overall scanner size.

BASTEI dual-head	Sensitivity	Scatter Fraction
	(cps/kBq)	(%)
Point source	39.9	0
Point source /w phantom	7.0	19.7

Table 8.12: Sensitivity and scatter fraction of the BASTEI dual-head scanner to the point source with and without phantom.

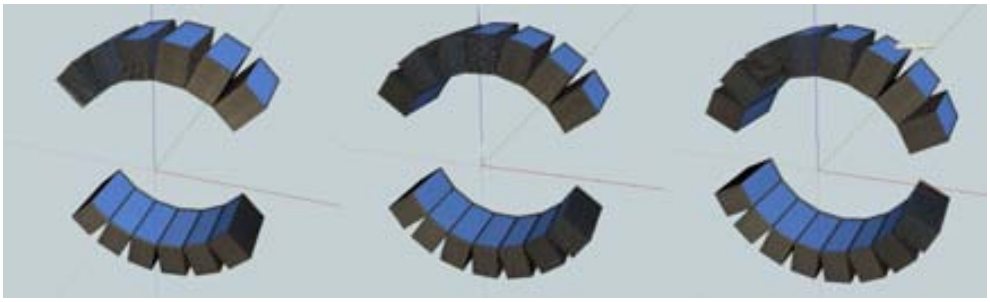

Figure 8.24: Drawings of the 3 different partial-ring MRPC scanners for illustration of the geometry. From left to right, a 12 head, 14 head, and 16 head open-ring designs are shown each with 20 modules per head.

the two point sources simulated. Table 8.12 gives the results of the BASTEI simulations for the two sources.

The NEMA source, has not been included in these partial-ring studies since in the application of *in-vivo* dosimetry the general location of the activity within the patient is known and not likely distributed along the axial axis of the scanner. The point source (with phantom) is perhaps not entirely realistic either, since the activity distribution caused by a therapeutic beam is expected to be spread out over the treatment volume. [5]

8.4.2 Partial-ring MRPC-PET

Circular partial-ring geometries

Three simple partial-ring MRPC-PET scanner geometries have been simulated, having 12, 14 and 16 heads with an internal ring diameter of 80 cm (see figure 8.24). The partial-ring designs are essentially identical to the full-ring designs presented previously except that several of the detector heads have been removed allowing for passage of the therapeutic hadron beam.

Rather than re-simulate all possible geometric variations of the MRPC-PET scanner for all three partial ring geometries, we have instead selected

[5]The task of comparing reconstructed images made from simulated patient data using the BASTEI and other in-beam PET scanners based on MRPC technologies is currently a subject of study within the ENVISION project.

Source	MRPC-PET	Sensitivity	% of full-ring
	120-150-4-60	(cps/kBq)	(%)
Point source	20 head	38.6	100
	12 head	23.3	60.3
	14 head	27.1	70.1
	16 head	30.9	80.1
Point w phan.	20 head	10.4	100
	12 head	5.67	54.5
	14 head	6.53	62.7
	16 head	7.81	75.0

Table 8.13: A summary of the sensitivity results for partial-ring MRPC geometries using the point source without phantom. Each head is composed of 120 modules, with 150 μm glass absorbers spaced at 4 mm pitch and 60 cm axial length.

the MRPC 120-150-4-60 geometry and simply removed heads to produce the partial-ring configurations. The point source both with and without phantom has been simulated and the results for each partial-ring configuration given in table 8.13. The results for the full-ring scanner geometry are also given for comparison along with the percentage of the full-ring sensitivity for each of the partial-ring geometries.

As can be seen from the data, the 16 head partial-ring MRPC scanner is nearly 12% more sensitive to the point source with water phantom than the BASTEI dual-head scanner. Considering the excellent spatial resolution and timing resolutions that are expected with MRPC technology, it can be expected that this MRPC partial-ring geometry would perform better than the BASTEI while being cheaper to produce. Future studies which include the TOF resolution and the spatial resolution in reconstruction, and which use the $\beta+$ activation from real patient data, will be required to resolve this issue definitively. [6]

Planar partial ring geometries

In order to present an alternative to the partial-ring geometries presented in the previous section, we have also simulated a dual-head planar scanner geometry based on MRPC technologies. Because of the axial scalability of the MRPC technology we have considered a scanner which is 2 m in axial length, in order to asses the gain in sensitivity that can be achieved. Such studies have already been carried out by other groups and a dual-head (and even 4-head) planar MRPC-PET scanner are being investigated [117, 121].

The exact geometry that has been simulated here is a dual-head planar

[6] Such studies are currently being carried out in the ENVISION project.

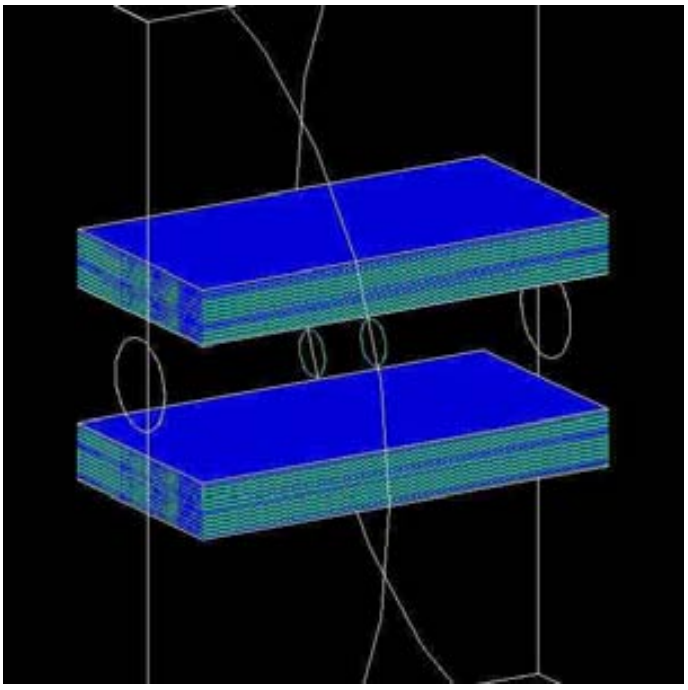

Figure 8.25: The simulated dual-head planar MRPC-PET geometry as seen by the GATE visualization. The modules are 1 m in width and 2 m long in the axial direction. Each head is composed of 60 modules spaced at 4 mm where modules are composed of 150 μm glass absorbers. The space between heads is 60 cm.

configuration where each head consists of 60 MRPC modules (each with 150 μm glass absorbers) and each with 1x2 m^2 active area. The two heads are separated by 60 cm, enough to allow a patient to lie comfortably in between. Figure 8.25 shows this geometry in the GATE visualization.

All three sources have been simulated and the results are given in table 8.14. The results are 8% better than the BASTEI with the point source and 72% better with the point source with water phantom. However, the scatter fraction is nearly 3 times higher, as seen previously. The result with the NEMA source must be compared with the NEMA results for the commercial crystal-based scanners, and not with the BASTEI, since the NEMA source has relevance in whole-body PET for nuclear medicine. In this case the dual-planar MRPC-PET geometry is ∼6.5 times better than the Gemini and ∼5.5 times better than the HiRez. It should be mentioned that the dual-head planar geometry presented here has not been completely optimized; with 120 modules per detector head, the gain in sensitivity over commercial crystal-based scanners will be even larger. As it stands, however, the sensitivity obtained with this geometry clearly demonstrates the potential advantage of the MRPC technology as it applies to whole-body human PET imaging.

Dual-head planar MRPC 2x1 m^2 60 modules	Sensitivity (cps/kBq)	Scatter Fraction (%)
Point source	43.1	0
Point source /w phantom	12.1	54.5
NEMA source	42.8	-

Table 8.14: Sensitivity and scatter fraction of the 1x2 m^2 dual-head planar MRPC scanner to the three different sources.

Chapter 9

Conclusions

Hadrontherapy is a relatively new technique in cancer radiotherapy allowing to obtain highly conformal dose distributions as compared with photon beams used in conventional radiation therapy. The characteristic sharp rise of energy loss at the end of the hadron range, known as the Bragg peak, allows a much lower dose to be given to healthy tissues both before and after the treatment volume making the technique highly desirable for treating deep-seated tumours, especially in the vicinity of organs at risk. Because they suffer minimal diffusion while traversing matter, hadrons can be delivered in narrow beams whose position and range can be adjusted to accurately target even complex tumour volumes. Also, the use of light-ions, such as carbon, which leads to high-density ionizations in the region of the Bragg peak has a more devastating effect on tumour cells, quantified by an enhancement of the Radio Biological Effectiveness (RBE). For this reason light ions, such as carbon, are used to treat radio-resistant malignancies with promising results.

Recognized in the 40's for their beneficial use in radiotherapy, it is only in the last twenty years that hadrons are being routinely used in clinical practice. This is largely the result of improvements in accelerator technologies but also thanks to the pioneering clinical studies performed with patients in centers devoted to fundamental research. Today in 2013, thirty-five centers are in operation the world over and already 110,000 patients have been treated with hadrons, mainly protons and carbon ions.

Although hadrons are superior to photons in many cases of cancer therapy because of the characteristic Bragg-peak profile of dose deposition, this same characteristic also puts high requirements on the accuracy of the delivered treatment plan. Unlike irradiation with photons, any deviation between the expected and delivered range or position of the hadron beam can result in large increases in the dose given to healthy tissues as well as severe localized under-dosing of the tumour. Even if uncommon in routine practice, such errors not only undermine the advantage of using hadrons for ther-

apy, but can be more hazardous to patient well-being than similar errors in treatments with photons. Quality assurance (QA), therefore, is of particular importance in hadrontherapy, if the physical properties of hadrons are to be best exploited for the highest benefit of patients.

To response to this requirement, radiation detectors have been proposed, some of which are already in use in conventional radiotherapy and others which exploit the unique opportunities made possible by the presence of the hadron beam. This thesis describes an expansive study of novel radiation detectors which are under development by the Advanced QUality Assurance (AQUA) group of the TERA Foundation for QA in clinical hadrontherapy.

Drawing from the field of detector instrumentation for high energy physics (HEP), the detectors have been tailored to this unique medical application. Three distinct detector solutions have been proposed and developed.

The first is an instrument capable of performing proton range radiography (PRR) for patient setup and treatment planning verification. It makes use of a diagnostic beam of protons delivered from the particle accelerator in the moments prior to treatment. This project reached a very advanced stage of development and has been the main focus of the AQUA group during the years of research covered by this thesis. The second and third detector solutions are both designed to perform in-beam PET dosimetry during irradiation with the therapeutic beam. Two solutions have been investigated, each employing very different technologies: inorganic scintillator crystals and Multi-gap Resistive Plate Chambers (MRPCs).

PRR10 & PRR30

Proton radiography can be used as a validation of the patient setup immediately prior to irradiation with the therapeutic beam, greatly enhancing the ability of clinicians to check for positioning errors or density changes in the patient which can otherwise go undetected during the course of therapy, especially if treatment is performed over many fractions. More importantly, the information obtained with PRR images can be used directly in calculations of the stopping power of the patient's morphology, needed to accurately predict the range of protons and light-ions in the tissues of the patient. This is highly desirable in hadrontherapy treatment planning which currently depends on the conversion from X-ray CT data and is characterized by a small but non-negligible uncertainty.

The PRR10 detector, designed and built by the AQUA group as a proof-of-principle prototype, has an active area of 10x10 cm^2 and can cover a residual proton range of nearly 10 cm water-equivalent. Developed for the purpose of performing 2D PRR images, the PRR10 also constitutes an important first step towards full 3D proton CT, considered by many researchers to be the future of hadrontherapy treatment planning. Beam tests with protons at the Proton Irradiation Facility at the Paul Scherrer Institute and on

a horizontal beam line at the *Centro Nazionale di Adroterapia Oncologica* (CNAO) have shown that the PRR10's imaging capabilities are sufficiently good to be used for QA in clinical applications with real patients. The PRR10 prototype detector currently sits in the CNAO hospital in Pavia where it is scheduled for tests with patients once the center is in full operation.

Construction of a new PRR telescope, based on the same technology as the PRR10 but with a larger active area, is also nearing a final stage of development. The new device, called the PRR30, will be capable of obtaining PRR images over a full 30x30 cm^2 and a residual range of nearly 15 cm, a substantial improvement over the PRR10 prototype. To allow a fast data acquisition to be performed over the entire 30x30 cm^2 active area, an entirely new front-end readout electronics, the GEMROC, has been designed and implemented. This upgrade has been necessary to obtain full-size PRR images within a timescale realistic for clinical studies. Development of the GEMROC and a fast DAQ solution, which has potential applications in high-energy physics and other medical fields, has been carried out in collaboration between TERA and the AGH University of Science and Technology in Krakow, Poland. A 1.6 MHz total event through-put on a 30x30 cm^2 GEM detectors has already been demonstrated and the PRR30 instrument is scheduled for testing with diagnostic protons beams at PSI by the end of the year 2013.

Semi-monolithic LYSO-MCP

For the application of in-beam PET dosimetry during irradiation with the therapeutic beam, a special PET camera design has been proposed by the TERA Foundation based on crystal scintillator technology. The design builds upon the trends of state-of-the-art techniques in current PET research, a convenient choice since the requirements on PET hardware for hadrontherapy QA are essentially the same as for nuclear medicine. Our design for a unit PET detector consists of 5 large LYSO crystals packed into a 60x60x30 cm^3 block and coupled to multi-anode MCP-PMT having 8x8 anode configuration.

This semi-monolithic geometry has been selected to allow the depth-of-interaction (DOI) to be measured within the crystal block, a technique which has been shown to improve the spatial resolution in PET scanners at the edge of the transverse FOV. PET hardware which is DOI-capable leads to better spatial resolutions over the full extent of the FOV but also to higher sensitivities for the same volume of crystal in the scanner, highly beneficial considering the costs of the crystals themselves is usually the limiting factor in PET performance.

In addition to a DOI measurement, LYSO and MCP photodetector technologies have good timing properties, allow to resolve the time-of-flight

(TOF) of arrival between the coincidence 511 keV gammas. TOF-PET is currently a hot topic in PET research for nuclear medicine since it greatly reduces the contributions of noise events in PET systems leading to a higher effective sensitivity and dramatically better quality images. The benefit of TOF-PET is especially high in full-body imaging where a large fraction of the emitted photons, and thus the available signal, are scattered within the patient before arriving to the detection. Considering the application to hadrontherapy *in-vivo* dosimetry, TOF-PET is especially desirable since the main challenge is the limited $\beta+$ activity produced in the patient by the therapeutic hadron beam.

To validate that our PET camera design performs as expected, two such prototypes have been assembled with a single crystal each and tested in the laboratory with a source of ^{22}Na, a positron emitter. The energy resolution has been measured to be 13% FWHM after a calibration of the anode response beneath the crystal. An excellent localization of the 511 keV photon interaction within the crystal has been demonstrated, 1.2 mm in the transverse direction and $\sim$15 mm DOI. The coincidence timing resolution made with both modules has been measured as 810 ps, not quite as good as the latest TOF-PET scanners recently becoming available on the market, but better than most standard PET systems. It should be pointed out this result has been made using the global output signal from each MCP-PMT, which limits the number of time-to-digital (TDC) channels required for a larger PET system. However, a better TOF resolution may still be possible if the timing is derived from the signals acquired on individual anodes, a point which is to be investigated in future studies of this technology.

MRPC-PET

In addition to the crystal-based proposal, for this thesis we have extensively investigated the use of MRPC technology as an alternative solution for an in-beam PET application. Commonplace in HEP instrumentation, MRPCs are highly uncommon in PET, since high-density materials (such as inorganic scintillators) are used to efficiently detect 511 keV photons. This fact has required us to start from scratch in most of our developments and it should be stated that a great deal of the efforts over the course the research period covered by this thesis has been spent in developing this technology towards a PET application.

The first step in the research has been to construct compact and easy to assemble MRPC modules in light of the requirements for large production volumes required if ever an MRPC-based PET demonstrator is to be built with high enough sensitivity, the main requirement for nuclear medicine application and especially for hadrontherapy QA. Improving upon techniques used in MRPC designs for HEP, a new method of producing polyimide spacers by photo-lithographic means has been developed to maintain the

mechanical support between the glass layers. Such spacers make the task of assembling the multi-gap modules less laborious and also minimizes the amount of mechanical supporting material required.

The unit MRPC-PET detector built is made of thin (400 μm) absorbers made of float glass patterned with the insulating spacers (300 μm) stacked into a 4-gap module filled with pure tetrafluoroethane. Both 7x10 cm^2 and 10x30 cm^2 active area prototypes have been constructed, validating the assembly procedure and paving the way for larger production volumes.

The 7x10 cm^2 module has been tested extensively with a front-end electronics board, designed specifically for our purposes and based on the NINO amplifier-discriminator, a fast-timing ASIC used in HEP experiments for fast tracking of charged particles. The sensitivity to 511 keV gammas for a single 4-gap module has been measured as (0.66$\pm$0.01)%, only $\sim$10% less than that predicated by Monte-Carlo simulation. We have also measured a timing resolution of 38 ps between pulses arriving on either end of the module's readout, giving an axial position localization of the detected gamma of 3.5 mm. For MRPCs stacks composed of the same base materials as the compact modules and housed inside of prototyping gas chambers, the single-detector TOF resolution has been measured for single-gap and 4-gap configurations as 310 ps and 370 ps, respectively.

At the time of completion of this thesis, the TOF measurement with compact 7x10 cm^2 modules is still ongoing. A second 7x10 cm^2 MRPC module has already been assembled and is currently being tested, soon to be place in coincidence with an identical module and the ^{22}Na source. It is is hoped that we will soon publish a coincidence timing resolution of $\sim$150 ps, close to the best results currently being reported in TOF-PET research with small crystal-photodetector assemblies and vastly superior to the resolutions of the latest TOF-PET scanner currently on the market.

The experimental results obtained with the compact MRPC prototypes, as well as the validation of their assembly and production, constitute a major step forward in the use of MRPC technology in TOF-PET. To place the experimental findings on a firm footing, an extensive sensitivity optimization of hypothetical MRPC-PET scanner geometries has also been performed using the GATE Monte-Carlo toolkit using crystal-based scanners as benchmark. The aim has been to optimize the sensitivity of a full-ring MRPC-PET scanner by tuning several geometrical parameters of the unit MRPC module design and the overall scanner configuration. We have focused on the sensitivity rather than on the quality of reconstructed images, since the other properties of MRPCs (excellent timing and spatial resolutions) are expected to be similar, if not better, than current state-of-the-art crystal-based PET hardware.

In addition to the sensitivity, the scatter fraction (SF) has also been extracted from our simulations. Although the effect of the SF on the quality of reconstructed PET images has been postponed to future study, the intrinsic

insensitivity to lower energy photons characteristic of MRPCs has been seen to at least partially compensate for this drawback. That being said, the SF is still at least twice are large for MRPC-based scanner as for those based on crystal, a point which must be carefully considered in studies which involve image reconstruction.

In terms of sensitivity, the simulation results clearly demonstrate that the low sensitivity of single MRPC detectors to 511 keV photons can be overcome by the use of hundreds of individual MRPC modules. In fact, if the detection efficiency of multi-module MRPC stacks is optimized by the use of thinner glass absorbers (100-150 μm) and the axial extent of the modules extended to 60 cm, then a scanner based on MRPC technology can largely compete with existing crystal technologies and possibly even outperform them. Even more importantly, the results with the 70 cm long NEMA source show that, for whole-body PET imaging, our optimized full-ring MRPC-PET scanner has nearly an order of magnitude higher sensitivity than existing commercial scanners based on crystal. If the TOF resolution can be measured in line with our expectations, then the true performance of an MRPC-based PET scanner will by far surpass that of crystal scanners and potentially at a fraction of the cost.

Clearly, the next steps are to confirm the excellent timing and spatial resolutions of compact MRPC modules and to develop a dual-head MRPC-PET demonstrator which will unequivocally prove the advantages of this technology in PET, whether for nuclear medicine or hadrontherapy. This will demand that a large number of MRPC modules be produced, a requirement which will surely involve the participation of industrial partners in the production and assembly process. At that time, a realistic cost estimation for a full-ring or partial-ring scanner can be made, the final deciding factor in bringing this technology to market.

Although the aim of the research presented in this thesis has been to develop detectors for quality assurance in clinical hadrontherapy, we should emphasize that MRPC technology has enormous potential in the field of whole-body imaging in nuclear medicine. At present, the sensitivity of the best commercial PET scanners on the market makes it undesirable to carry out whole-body PET scans on patients regularly, since a rather large dose is given to the patient as a consequence of the PET scan itself. Even when the latest results emerging from state-of-the-art PET research with crystal technology are implemented into commercial systems, it is likely that this fact will remain unchanged. However, if an order of magnitude increase in sensitivity can be made, which seems feasible with the use of MRPC technology after a lot of development work, then it may be possible to increase the frequency of whole-body scanning, something which would allow doctors to routinely screen the population for particular cancers, leading to earlier tumour detection and therefore important advances in the fight against cancer.

Bibliography

[1] U. Amaldi, *Nuclear physics applications in diagnostics and cancer therapy*, Nuclear Physics A 751 (2005) 409c - 428c

[2] Sistema AQUA: Advanced Quality Assurance for CNAO, http://project-aqua.web.cern.ch/project-aqua

[3] TERA Foundation, *Sistema AQUA 'Advanced QUality Assurance' per il Centro Nazionale di Adroerapia Oncologica,* 2008

[4] GLOBOCAN 2008 (IARC 2010) Section of Cancer Information

[5] World Health Organization, Cancer Fact Sheet N 297, February 2012

[6] U. Amaldi. *Cancer therapy with particle accelerators*, Nuclear Physics A, 654(1-2):C375

[7] G. Kraft and J. Debus, *Cancer situation as presented by EC 1991*, available at: www.nupecc.org/iai2001/report/B31.pdf

[8] Eric J. Hall, Amato J. Giaccia, *Radiobiology for the Radiologist, Sixth Edition,* Lippincott Williams & Wilkins, 2006

[9] E.B. Podgorsak, *Radiation Oncology Physics: a Handbook for Teachers and Students*, IAEA, 2005.

[10] Example from the image gallery on the Varian Medical Systems website: http://varian.mediaroom.com/image-gallery?mode=gallery&cat=2477

[11] Bortfeld, T. and Schlegel, W., *An Analytical Approximation of Depth - Dose Distributions for Therapeutic Proton Beams*, Physics in Medicine and Biology, 1996, 41(8):1331.

[12] U. Amaldi and G. Kraft, *Radiotherapy with beams of carbon ions*, 2005, Reports on Progress in Physics, 68(8):1861

[13] G. Kraft, *Tumor Therapy with Heavy Charged Particles*, Progress in Particle and Nuclear Physics, 45 (2000) S473-S544

[14] M. Kraemer and M. Scholz, *Treatment planning for heavy ion therapy,* Physics in Medicine and Biology, 2000, 45 3319–30

[15] Robert Wilson, *Radiological use of fast protons,* 1946, Radiology 47 487–91

[16] PTCOG Patient Statistics March 2nd, 2009 http://www.ptcog.com

[17] National Institute of Standards and Technology (NIST) website: http://physics.nist.gov/PhysRefData/contents.html

[18] Particle Data Group, 2001, http://pdg.web.cern.ch/pdg/2011/reviews/rpp2011-rev-passage-particles-matter.pdf

[19] C. Caso, et al., *Review of Particle Physics,* The European Physical Journal C3 (1998) 1

[20] F. Sauli, *Principles of operation of multiwire proportional and drift chambers*, CERN Geneva, CERN Academic Training Lectures, 81, 1977

[21] P. Rice-Evans, *Spark, Streamer, Proportional and Drift Chambers*, The Richelieu Press, London, 1974

[22] G. Charpak et al., *The use of multiwire proportional counters to select and localize charged particles*, Nuclear Instruments and Methods in Physics Research A 62, 1968, pp 262

[23] A. Oed, *Position-sensitive detector with microstrip anode for electron multiplication with gases*, Nuclear Instruments and Methods in Physics Research A 263, 1988, pp 351

[24] Y. Giomataris, Ph. Rebourgeard, J.P. Robert, and G. Charpak, *MICROMEGAS: a high-granularity position-sensitive gaseous detector for high particle-flux environments*, Nuclear Instruments and Methods in Physics Research A 376, 1996, pp 29-35

[25] F. Sauli, *GEM: A new concept for electron amplification in gas detectors*, Nuclear Instruments and Methods in Physics Research A 386, 1997, pp 531-534

[26] S. Bachmann, A. Bressan, L. Ropelewski, F. Sauli, A. Sharma, and D. Mormann, *Charge amplification and transfer processes in the gas electron multiplier* Nuclear Instruments and Methods in Physics Research A 438, 1999, pp 376-408

[27] V. Peskov, P. Fonte, M. Danielsson, C. Iacobaeus, J. Ostling, M. Wallmark, *Fundamentals of gas micropattern detectors* arXiv:physics/0106016v1, 2001

[28] R.K. Carnegie, M.S. Dixit, J. Dubeau, D. Karlen, J.-P. Martin, H. Mes and K. Sachs, *Resolution studies of cosmic-ray tracks in a TPC with GEM readout,* Nuclear Instruments and Methods in Physics Research A 538, 2005, pp 372-383

[29] A Bressan. M. Hoch, P. Pagano, L. Ropelewski, F. Sauli, S. Biagi, A. Buzulutskov, M. Gruwe, G. De Lentdecker, D. Moermann, and A. Sharma, *High rate behavior and discharge limits in micro-pattern detectors,* Nuclear Instruments and Methods in Physics Research A 424 (1999) 321-342

[30] F. Sauli, L. Ropelewski, and P. Everaerts, *Ion feedback suppression in time projection chambers* Nuclear Instruments and Methods in Physics Research A 560, 2006, pp 269-277

[31] R. Santonico and R. Cardarelli, *Development of resistive plate counters,* Nuclear Instruments and Methods in Physics Research, Vol. 187, pp 377-380, 1981

[32] R. Santonico and R. Cardarelli, *Progress in resistive plate counters,* Nuclear Instruments and Methods in Physics Research A 263: 20-25, 1988

[33] Christian Lippmann, *Detector Physics of Resistive Plate Chambers,* Doctoral thesis, Johann Wolfgang Goethe-Universitat, 2003

[34] E. Cerron Zeballos et al., *A new type of resistive plate chamber: the multigap RPC,* Nuclear Instruments and Methods in Physics Research A, 374 (1996) 132-135

[35] ATLAS muon spectrometer technical design report, CERN LHCC-97-22, ATLAS TDR 10, CERN, 1997

[36] CMS muon technical design report, CMS TDR 3, CERN/LHCC 97-32, 1997

[37] E. Scapparone, et al., *The Time-of-Flight detector of the ALICE experiment,* Journal of Physics G: Nuclear and Particle Physics, 34 (2007) S725-S728

[38] U. Schneider, J. Besserer, P. Pemler, M. Dellert, M. Moosburger, E. Pedroni, B. Kaser-Hotz, *First proton radiography of an animal patient,* Med. Phys. 31 (5), May 2004

[39] U. Schneider, E. Pedroni, A. Lomax, *The calibration of CT Hounsfield units for radiotherapy treatment planning,* Phys. Med. Biol. 41 (1996) 111-124

[40] U. Schneider, E. Pedroni, *Proton radiography as a tool for quality control in proton therapy,* Med. Phys. 22 (4), April 1995

[41] G.A.P. Cironne, *Monte Carlo studies of a proton computed tomography system,* IEEE Vol. 54 (2007)

[42] M. Petterson, N. Blumenkrantz, J. Feldt, J. Heimann, D. Lucia, A. Seiden, D. C. Williams, H. F.-W. Sadrozinski, Member, IEEE, V. Bashkirov, R. Schulte, M. Bruzzi, D. Menichelli, M. Scaringella, C. Talamonti, G. A. P. Cirrone, G. Cuttone, D. Lo Presti, N. Randazzo, V. Sipala, *Proton radiography studies for proton CT,* 2006 IEEE Nuclear Science Symposium Conference Record

[43] N. Randazzo, V. Sipala, D. Lo Presti, G.A. Pablo Cirrone, G. Cottone, F. Di Rosa, V. Bashkirov, R. Schulte, *Residual energy measurements for proton computed tomography,* 2007 IEEE Nuclear Science Symposium Conference Record

[44] H. F.-W. Sadronzinski, V. Bashkirov, B. Colby, G. Coutrakon, B. Erdelyi, D. Fusi, F. Hurley, R. P. Johnson, S. Kashiguine, S. McAllister, F. Martinez-McKinney, J. Missaghian, M. Scaringella, S. Penfold, V. Rykalin, R. Schulte, K. Schubert, D. Steinberg, A. Zatserklaniy, *Detector development for proton computed tomorgraphy (pCT),* 2011 IEEE Nuclear Science Symposium Conference Record

[45] P. Pemler et al, *A detector system for proton radiography on the gantry of the Paul Scherrer Institute,* Nuclear Instruments and Methods in Physics Research A, 432, 483, 1999

[46] Saint-Gobain Crystals website: http://www.detectors.saint-gobain.com/

[47] Hamamatsu website: http://www.hamamatsu.com

[48] QuickUSB website: http://www.quickusb.com

[49] B. Ketzer, M. C. Altunbas, K. Dehmelt, J. Ehlers, J. Friedrich, B. Grube, S. Kappler, I. Konorov, S. Paul, A. Placci, L. Ropelewski, F. Sauli, L. Schmitt, and F. Simon, *Triple GEM Tracking Detectors for COMPASS*, IEEE Transactions on Nuclear Science, Vol. 49, No. 5, October 2002, pp 2403-2410

[50] L. Dick, N. Malakhov, R. De Oliveira, D. Watts, *First results of FGLD gas detector with multi-channel self-triggering readout electronics,* Nuclear Instruments and Methods in Physics Research A 572 (2007) 205-207

[51] L. Dick, N. Malakhov, R. De Oliveira, D. Watts, *Results of a prototype imaging system using the FGLD technology and self-triggering discharge-protected readout electronics,* Nuclear Instruments and Methods in Physics Research A 581 (2007) 279-282

[52] D. Watts, N. Malakhov, L. Ropelewski, J. Samarati, F. Sauli, *Performance of MPGDs with Portable Readout Electronics,* 2008 IEEE Nuclear Science Symposium Conference Record

[53] IDEAS website: http://www.ideas.no

[54] E. Noschis, G. Anelli, G. Cervelli, M. Eraluoto, K. Kurvinen, R. Lauhakangas, L. Ropelewski, and W. Snoeys, *Protection circuit for the T2 readout electronics of the TOTEM experiment,* Nuclear Instruments and Methods in Physics Research A 572, 2007, pp 378-381

[55] A. Bianchi, *Detectors for Quality Assurance in Hadrontherapy Centers,* Master's Thesis, Universita Degli Studi di Milano - Bicocca, 2009-2010

[56] U. Grossner, W. Hajdas, K. Egli, R. Brun, R. Harboe-Sorensen, *Proton Irradiation Facility at the PROSCAN project of the Paul Scherrer Institute,* 2008, http://pif.web.psi.ch/Reports/

[57] U. Amaldi, *CNAO - The Italian Center for Light Ion Therapy,* Radiatherapy and Oncology, 2002

[58] U. Amaldi and G. Magrin, *Path to the Italian Center for Ion Therapy,* Mercurio Edizioni (2010)

[59] T. Fiutowski, et al., IEEE NSS/MIC (2011) 1540, http://dx.doi.org/10.1109/NSSMIC.2011.6154366

[60] Eljen Technology website: http://www.eljentechnology.com/

[61] A. Brogna et al, *MSGCROC - an ASIC for High Count Rate Readout of Position Sensitive Microstrip Gas Chambers for Thermal Neutrons,* 2008 IEEE Nuclear Science Symposium Conference Record

[62] RD51 Webpage: http://rd51-public.web.cern.ch/rd51-public

[63] M. Bucciantonio, U Amaldi, R. Kieffer, N. Malakhov, F. Sauli, D. Watts, *Fast readout of GEM detectors for medical imaging,* Nuclear Instruments and Methods in Physics Research A (2012), http://dx.doi.org/10.1016/j.nima.2012.10.046

[64] K. Mueller, Z. Liang, T. Li, F. Xu, J. Heimann, L. Johnson, H. Sadronzinski, A. Seiden, D. Williams, L. Zhang, S. Peggs, T. Satogata, V. Bashkirov, R. Schulte, *Reconstruction for Proton Computed Tomography: A Practical Approach,* 2004, IEEE.

[65] ENVISION website: http://envision.web.cern.ch/envision/Default.htm

[66] W. Enghardt et al, *Charged hadron tumour therapy monitoring by means of PET,* Nuclear Instruments and Methods in Physics Research A 525 (2004) pp 284-288.

[67] K. Yoshikawa et al., *The initial imaging of C-11 distribution yielded by auto activation of C-12 beams in the heavy ion therapy,* J. Nucl. Med. Technol. 24, 167-8

[68] T. Tomitani et al., *Washout studies of ^{11}C in rabbit thigh muscle implanted by secondary beams of HIMAC,* Phys. Med. Biol. 48 (2003) 875-889

[69] J. Langner, *Development of a Parallel Computing Optimized Head Movement Correction Method in Positron Emission Tomography,* M. Sc. thesis, University of Applied Sciences Dresden and Research Center Dresden-Rossendorf, Germany, 2003

[70] Future Diagnostic webpage: http://www.futurediagnosticgroup.com/services.php

[71] D. Townsend, *Combined PET/CT: the historical perspective,* Semin Ultrasound CT MR, 2008 August, 29 (4), 232-235

[72] M. Korzhik et al, *Development of scintillation materials for PET scanners,* NIMA 571 (2007) 122-125

[73] V. Astakhov, P. Gumplinger, C. Moisan, T.J. Ruth, V. Sossi, *Effect of depth of interaction decoding on resolution in PET: a simulation study,* IEEE 2003.

[74] T Ling, T.K. Lewellen, R. S. Miyaoka, *Depth of interaction decoding of a continuous crystal detector module,* Phys. Med. Biol. 52 (2007) 2213-2228

[75] R. S. Miyaoka et al, *Design of a Depth of Interaction (DOI) PET Detector Module,* IEEEtransactions on Nuclear Science, Vol 45, No 3, June 1998, pp 1069-1073.

[76] A. Braem et al, *Novel design of a parallax free Compton enhanced PET scanner,* Nuclear Instruments and Methods A, 524 (2004) 268-274.

[77] A. Braem et al, *High precision axial coordinate readout for an axial 3-D PET detector module using a wave length shifter strip matrix*, Nuclear Instruments and Methods A, 580 (2007) 1513-1521.

[78] T. Lewellen, *Recent developments in PET detector technology,* Phys. Med. Biol. 53 (2008) R287-R317

[79] C. W. Lerche et al, *Depth of γ-ray interaction within continuous crystals from the width of its scintillation light-distribution,* IEEE Transactions on Nuclear Science, Vol 52, No 3, June 2005, pp 560-572.

[80] P. Dendooven, *$LaBr_3$ and LYSO monolithic crystals coupled to photosensor arrays for TOF-PET,* Oral presentation, Physics for Health in Europe Workshop, Feb. 2-4, 2010, CERN, Geneva

[81] M. Conti, *State of the art and challenges of time-of-flight PET,* Physica Medica (2009) 25, 1-11

[82] S. Surti, J. Karp, L. Popescu, M. Daube-Witherspoon, M. Werner, *Investigation of Time-of-Flight Benefit for Fully 3-D PET,* IEEE Transactions on Medical Imaging, Vol. 25. No. 5, May 2006

[83] R. M. Manjeshwar, Y. Shao, and F. P. Jansen, *Image quality improvements with time-of-flight positron emission tomography for molecular imaging*, in IEEE International Conference on Acoustics, Speech, and Signal Processing 2005 (ICASSP05) Proceedings, March 18-23, 2005, vol. 5, pp. 853-856.

[84] Philips Gemini TruFlight PET/CT promo brochure, website: www.medical.philips.com

[85] K. Ziemons, E. Auffray, R. Barbier et al., the Clear Collaboration, *The ClearPET project: development of a 2nd generation high-performance small animal PET scanner,* Nuclear Instruments and Methods in Physics Research A 537, 307-311 (2005)

[86] Crystal Clear Website: http://crystalclear.web.cern.ch/crystalclear/

[87] S. Surti, A. Kuhn, M. E. Werner, A. E. Perkins, J. Kolthammer, J. S. Karp, *Performance of Philips Gemini TF PET/CT Scanner with Special Considerations for its Time-of-Flight Imaging Capabilities,* J Nucl Med 48 (2007) 471-480

[88] F. Daghighian et al., *Evaluation of Cerium Doped Lutetium Oxyorthosilicate (LSO) Scintillation Crystal for PET,* IEEE Transactions on Nuclear Science, Vol 40, No 4, August 1993

[89] M. Conti, L. Eriksson, H. Rothfuss, and C. Melcher, *Comparison of Fast Scintillators with TOF PET Potential,* IEEE Transactions on Nuclear Science, Vol 56, No 3, June 2009, pp 926-933.

[90] S. Gundacker, et al, *A Systematic Study to Optimize SiPM Photodetectors for Highest Time Resolution in PET,* IEEE Transactions on Nuclear Science, Vol 59, No 5, October 2012

[91] T. Szczesniak, M. Msozynski, L. Swiderski, A. Nassalski, A. Syntfeld-Kazuch, A-G. Dehaine, M. Kapusta, *A comparative study of fast photomultipliers for timing experiements and TOF PET,* IEEE Transactions on Nuclear Science, Vol. 56, No. 3, June 2009

[92] S. Seifert et al, *Ultra Precise Timing with SiPM-Based TOF PET Scintillation Detectors,* 2009 IEEE Nuclear Science Symposium Conference Record, J01-4, pp 2329 - 2333

[93] F. Fiedler, et al., *The Feasibility of In-Beam PET for Therapeutic Beams of ^{3}He,* IEEE Transactions on Nuclear Science Vol. 53, No. 4 (2006) 2252

[94] P. Solevi, *Study of an in-beam PET system for CNAO, the National Centre for Oncological Hadrontherapy,* Doctoral Thesis, Univerista degli studi di Milano, Facolta di Scienze Matematiche, Fisiche e Naturali, 2008

[95] P. Solevi, *Monte Carlo simulations for in-beam PET,* Nuclear Physics B (Proc. Suppl.) 172 (2007) pp 97-100.

[96] F. Sommerer, *In-beam PET monitoring of mono-energetic ^{16}O and ^{12}C beams: experiments and FLUKA simulations for homogenous targets,* Phys. Med. Biology. 54 (2009) pp 3979-3996.

[97] K. Parodi, *On the feasibility of dose quantification with in-beam PET data in radiotherapy with ^{12}C and proton beams,* Doctoral Thesis, Technischen Universitat Dresden, 2004

[98] P. Crespo, *Optimization of In-Beam Positron Emission Tomography for Monitoring Heavy Ion Tumor Therapy,* Doctoral Thesis, Technischen Universitat Dresden, 2005

[99] F. Ponsich, et al., *The modelling of positron emitter production and PET imaging during carbon ion therapy,* Physics in Medicine and Biology, 49 (2004) 5217

[100] K. Parodi, P. Crespo, H. Eickhoff, T. Haberer, J. Pawelke, D. Schardt, W. Enghardt, *Random coincidences during in-beam PET measurements at microbunched therapeutic ion beams,* Nuclear Instruments and Methods in Physics Research A 545 (2005) 446-458

[101] W. Enghardt et al, *Dose Quantification from In-Beam Positron Emission Tomography,* Radiother. Oncol. 73 (suppl. 2) (2004) S96

[102] F. Fiedler, *On the effectiveness of ion range determination from in-beam PET data,* Phys. Med. Biol. 55 (2010) pp 1989-1998.

[103] E. Rietzel, D. Schardt, T. Haberer, *Range accuracy in carbon ion treatment planning based on CT-calibration with real tissue samples,* Radiation Oncology, 2 (2007) 14

[104] K. Parodi, H. Paganetti, H. Shih, S. Michaud, J. Loeffler, T. Delaney, N. Liebsch, J. Munzenrider, A. Fischman, A. Knopf, T. Bortfeld, *Patient study of in-vivo verification of beam delivery and range, using positron emission tomography and computed tomography imaging after proton therapy,* Int J Radiat. Oncol. Biol Phys. 2007 July 1, 68(3) 920-934

[105] K. Parodi, T. Bortfeld, W. Enghardt, R. Fiedler, A. Knopf, H. Paganetti, J. Pawelke, G. Shakirin, H. Shih, *PET Imaging for treatment verification of ion therapy: Implementation and experience at GSI Darmstadt and MGH Boston,* Nuclear Instruments and Methods in Physics Research A 591 (2008) 282-286

[106] P. Crespo, *On the detector arrangement for in-beam PET for hadron therapy monitoring,* Phys. Med. Biol. 51 (2006) pp 2143-2163.

[107] A. Blanco et al., *Perspectives for positron emission tomography with RPCs,* Nuclear Instruments and Methods in Physics Research A 508 (2003) 88-93

[108] A. Blanco et al., *An RPC-PET prototype with high spatial resolution*, Nuclear Instruments and Methods in Physics Research A 533 (2004) 139-143

[109] M. Abbrescia et al, *Performance of a six-gap MRPC built for large area coverage*, Nuclear Instruments and Methods in Physics Research A 593 (2008) 263-268

[110] K. Doroud, D. Hatzifotiadou, D.W. Kim, M.M. Kim, J. Seo, M.C.S. Williams, A. Zichichi, *Performance of Multigap Resistive Plate Chambers with pure Freon 134a,* Nuclear Instruments and Methods in Physics Research Section A 629, 1, p. 106-110

[111] F. Anghinolfi, et al., *NINO: An ultrafast low-power front-end amplifier discriminator for the time-of-flight detector in the ALICE experiment*, IEEE Trans. Nucl. Sci., Vol. 51, No. 5, pp. 1974-1978, Oct. 2004

[112] K. Doroud et al., *MRPC-PET: A new technique for high precision time and position measurements*, Nuclear Instruments and Methods in Physics Research A 660 (2011) 73-76

[113] OpenGATE Collaboration webpage: http://www.opengatecollaboration.org

[114] K. Assie et al., *Monte Carlo simulation in PET and SPECT instrumentation using GATE*, Nuclear Instruments and Methods in Physics Research A 527 (2004) 180-189

[115] I. Buvat and D. Lazaro, *Monte Carlo simulations in emission tomography and GATE: An overview*, Nuclear Instruments and Methods in Physics Research A 569 (2006) 323-329

[116] L. Grevillot et al., *Optimization of GEANT4 settings for Proton Pencil Beam Scanning simulations using GATE*, Nuclear Instruments and Methods in Physics Research *B*, 268 (2010) 3295-3305 (2010)

[117] A. Blanco et al., *Efficiency of RPC detectors for whole-body human TOF-PET*, Nuclear Instruments and Methods in Physics Research A 602 (2009) 780-783

[118] *NEMA Standards Publication NU2-2001: Performance Measurements of Positron Emission Tomographs,* Rosslyn, VA: National Electrical Manufacturers Association, 2001

[119] DL. Bailey, T. Jones, TS Spinks, *A method for measuring the absolute sensitivity of positron emission tomographic scanners,* Eur. J Nucl Med. 1991, 18, 374-379

[120] J. Karp, S. Surt, M. Daube-Witherspoon, R. Freifelder, C. Cardi, L-E. Adam, K. Bilger, G. Muehllehner, *Performance of a Brain PET Camera Based on Anger-Logic Gadonlinium Oxyorthosilicate Detectors*, Jounal of Nuclear Medicine, Vol. 44, No. 8, 2003 1340-1349

[121] M. Couceiro, P. Crespo, L. Mendes, N. Ferreira, R. Ferreira Marques, P. Fonte, *Spatial resolution of human RPC-PET system*, Nuclear Instruments and Methods in Physics Research A 661 (2012) S156-S158